# Quadratic magnetooptic Kerr effect spectroscopy of magnetic thin films with cubic crystal structure

by

Ing. Robin Silber

A thesis submitted in partial fulfillment for the
degree of *Doctor of Philosophy*
under joint supervision
in the

**BIELEFELD UNIVERSITY**
DEPARTMENT OF PHYSICS
Center of Spinelectronic Materials and Devices

*Supervisor:*
Prof. Dr. Günter Reiss
*Co-Supervisor:*
Dr. Timo Kuschel

**VŠB - TECHNICAL UNIVERSITY OF OSTRAVA**
FACULTY OF MATERIALS SCIENCE AND TECHNOLOGY
Nanotechnology centre

*Supervisor:*
doc. Dr. Ing. Michal Lesňák
*Co-supervisor:*
Mgr. Jaroslav Hamrle, Ph.D.

September 19, 2019

# Declaration of Authorship

I, Robin Silber, declare that this thesis titled, 'Quadratic magnetooptic Kerr effect spectroscopy of magnetic thin films with cubic crystal structure' and the work presented in it are my own. I confirm that:

- This work was done wholly or mainly while in candidature for a research degree at Bielefeld University and VŠB–Technical University of Ostrava.
- Where I have consulted the published work of others, this is always clearly attributed.
- Where I have quoted from the work of others, the source is always given. With the exception of such quotations, this thesis is entirely my own work.
- I have acknowledged all main sources of help.
- Where the thesis is based on work done by myself jointly with others, I have made clear exactly what was done by others and what I have contributed myself.

Signed: ________________________________

Date: ________________________________

*“The first principle is that you must not fool yourself and you are the easiest person to fool”*

Richard P. Feynman

# *Abstract*

The magnetooptic Kerr effect (MOKE) is a well known and long used tool for ferro-, ferri- and antiferromagnetic material characterization. MOKE is also utilized in optical communication e.g. in optical isolators and circulators or in planar waveguide structures. Many of the MOKE techniques rely solely on linear MOKE (LinMOKE), i.e. magnetooptic (MO) effects linear in magnetization $\boldsymbol{M}$ and neglect the contribution of higher orders. Nevertheless, a higher-order term being proportional to $\boldsymbol{M}^2$ and called quadratic MOKE (QMOKE) can be strong enough to additionally contribute to the overall MOKE signal. A technique known as 8-directional method separates LinMOKE and two constituent QMOKE contributions and is well known for (001) oriented cubic crystal structures, but is not yet developed for other cubic crystal orientations. The origin of (Q)MOKE can be described as the perturbation of the permittivity tensor by $\boldsymbol{M}$ of a magnetized sample. The permittivity tensor for a cubic crystal is fully described up to the second order in $\boldsymbol{M}$ by linear MO parameter $K$ and two quadratic MO parameters $G_s$ and $2G_{44}$. Although those parameters have been studied in the past, the systematic experimental technique that would effectively yield the spectral dependence of quadratic MO parameters is lacking. This work extends the 8-directional method to the crystal orientations (011) and (111). The theoretical equations that are derived through an approximative analytical description relating MOKE with the elements of the permittivity tensor (e.g. $K$, $G_s$ and $2G_{44}$) are compared to numerical simulations using Yeh's 4×4 matrix formalism and to the experimental measurements. We further present a novel approach to QMOKE spectroscopy of (001) oriented cubic crystal structures that is based on the classical 8-directional method, but using the combination of only four magnetization directions together with a sample rotation of 45°. By reproducing the measurement procedure numerically the spectral dependencies of the quadratic MO parameters $G_s$ and $2G_{44}$ are extracted from QMOKE spectroscopy in addition to the linear MO parameter $K$ that is extracted from LinMOKE spectroscopy. This new procedure is applied to prototypical ferromagnetic samples of Fe(001) thin films with various thicknesses grown on MgO(001) substrates and to the thin film samples of $Co_2MnSi(001)$ Heusler compounds with different annealing temperatures promoting different degree of $L2_1$ ordering. $G_s$ and $2G_{44}$ are experimentally determined in spectral range of 0.8–5.5 eV for both materials. In case of the bcc Fe we show that the dependence on Fe layer thickness is small, indicating small contribution of the interface. In case of the $Co_2MnSi$ Heusler compounds we found that higher amount of $L2_1$ ordering promotes interband contribution to the MOKE spectra.

# *Abstract (Czech version)*

Jev známý jako Magnetooptický Kerrův efekt (MOKE) je hojně využíván pro charakterizaci ferro-, ferri- a antiferromagnetických materiálů. Dále jsou na tomto jevu založeny optické prvky které jsou využívány v optických komunikacích, např. optické isolátory a cirkulátory. Ve většině těchto aplikací se uvažuje pouze lineární MOKE (LinMOKE), t.j. magnetooptický (MO) efekt linearní v magnetizaci $\boldsymbol{M}$, a příspěvky vyšších řádů se zanedbávají. Nicméně, příspěvek vyššího řádu, který je úměrný $\boldsymbol{M}^2$ a nazývá se kvadratický MOKE (QMOKE), je v mnoha případech dostatečně silný na to, aby do celkového MOKE signálu nezanedbatelně přispěl. Takzvaná 8-mi směrná metoda dokáže separovat LinMOKE od jednotlivých QMOKE příspěvků a je dobře známa pro kubické materiály s (001) orientovaným povrchem. Pro případ kubických materiálů s jinou orientací povrchu nebyla však tato metoda ještě zcela vynalezena. Původ (Q)MOKE jevu může být popsán jako porucha symetrie tenzoru permitivity v důsledku magnetizace materiálu. Změna tenzoru permitivity kubických struktur až do druhého řádu v magnetizaci může být popsána pomocí lineárního MO parametru $K$ a dvou kvadratických MO parametrů $G_s$ a $2G_{44}$. Ačkoliv byly tyto MO parametry v minulosti studovány, experimentalní technika, která by efektivně a systematicky dokázala získat spektrální závislosti kvadratických MO paramterů, stále chybí. Tato práce rozšiřuje 8-mi směrnou metodu na kubické materiály s orientací povrchu (011) a (111). Teoretické rovnice těchto metod jsou odvozeny z analytického vztahu, který spojuje tenzor permitivity s MOKE jevem. Tyto rovnice jsou dále porovnány s numerickým modelem založeným na 4×4 maticovém Yehově formalismu a také s experimentálním pozorováním. Práce dále prezentuje původní návrh QMOKE spektroskopické experimentální techniky pro měření kubických struktur s (001) orientovaným povrchem. Tato spektroskopická technika vychází z klasické 8-mi směrné metody, ale využívá pouze 4 směry magnetizace a otočení vzorku o 45°. Za pomocí numerických simulací dokážeme z experimentálních QMOKE spekter získat spektra kvadratických MO paramterů $G_s$ a $2G_{44}$ a z klasické LinMOKE spektroskopie spektra linearního MO parametru $K$. Tato metoda byla aplikována na sérii vzorků tenkých vrstev Fe(001)/MgO(001) s různou tlouštkou Fe vrstvy pro každý vzorek a dále na sérii tenkých vrstev Heuslerovy slitiny $\mathrm{Co_2MnSi}$, ve které se měnila teplota žíhání jednotlivých vzorků, což má za následek jiný stupeň $L2_1$ uspořádání. Parametry $G_s$ a $2G_{44}$ byly experimentálně určeny pro oba materiály v rozsahu $0.8 - 5.5\,\mathrm{eV}$. V případě Fe vzorku jsme zjistili, že závislost na tlouštce vrstvy je malá, což ukazuje na zanedbatelný příspěvek z rozhraní. V případě $\mathrm{Co_2MnSi}$ vzorků jsme zjistili, že vyšší stupeň $L2_1$ uspořádání ovlivňuje tzv. interband příspěvek k MO parametrům.

# *Abstract (German version)*

Der magnetooptische Kerr Effekt (MOKE) ist eine verbreitete und gut verstandene Technik zur Charakterisierung von ferro-, ferri- und antiferromagnetischen Materialien. MOKE wird auch in der optischen Kommunikation verwendet, z.B. in optischen Isolatoren und Zirkulatoren oder in planaren Wellenleiterstrukturen. Viele MOKE Techniken berücksichtigen ausschließlich magnetooptische (MO) Effekte, die linear von der Magnetisierung $\boldsymbol{M}$ abhängen, den sog. linearen MOKE (LinMOKE), und vernachlässigen demnach Beiträge höherer Ordnung. Die Terme, die proportional zu $\boldsymbol{M}^2$ sind, und quadratischer MOKE (QMOKE) genannt werden, können dennoch signifikante Anteile des gemessenen MOKE Signals ausmachen. Für kubische Kristalle können mit dem als 8-directional method bekannten Verfahren LinMOKE und QMOKE separiert werden, was bisher nur für (001) orientierte Kristalle funktionierte. Der Ursprung des (Q)MOKE kann als die Störung des Permittivitätstensors $\boldsymbol{\varepsilon}$ einer magnetischen Probe durch $\boldsymbol{M}$ beschrieben werden. Für einen kubischen Kristall wird $\boldsymbol{\varepsilon}$ bis zur zweiten Ordnung in $\boldsymbol{M}$ durch den linearen MO Parameter $K$ und die zwei quadratischen MO Parameter $G_s$ und $2G_{44}$ vollständig beschrieben. Obwohl $G_s$ und $2G_{44}$ schon früher untersucht wurden, gibt es bisher keine experimentelle Technik, mit der die spektrale Abhängigkeit von quadratischen MO Parametern gemessen werden kann. Die vorliegende Arbeit erweitert die 8-directional method auf die Orientierungen (011) und (111). Die verwendeten Gleichungen werden aus Näherungen der analytischen Beschreibung abgeleitet und so der MOKE mit $\boldsymbol{\varepsilon}$ in Beziehung gesetzt. Das Ergebnis wird mit experimentellen Daten sowie numerischen Simulationen unter Verwendung des $4\times4$ Matrixformalismus von Yeh verglichen. Wir präsentieren weiterhin einen neuartigen Ansatz zur QMOKE Spektroskopie von (001) orientierten kubischen Kristallen, der die Kombination von nur vier Ausrichtungen von $\boldsymbol{M}$ zusammen mit einer Probendrehung von 45° verwendet. Durch numerische Reproduktion des Messvorgangs werden die spektralen Abhängigkeiten der quadratischen MO Parameter $G_s$ und $2G_{44}$ zusätzlich zu dem linearen MO Parameter K ermittelt, der aus der LinMOKE Spektroskopie extrahiert wird. Dieses neue Verfahren wird an jeweils auf MgO (001) gewachsenen dünne Schichten aus Fe (001) verschiedener Dicke und aus $\mathrm{Co_2MnSi}$ (001) exemplarisch angewandt. Der Grad der $L2_1$ Ordnung des $\mathrm{Co_2MnSi}$ wurde durch Auslagerung bei verschiedenen Temperaturen eingestellt. $G_s$ und $2G_{44}$ werden jeweils im Spektralbereich von 0.8-5.5 eV experimentell bestimmt. Wir zeigen, dass die Abhängigkeit von der Fe Schichtdicke gering ist, was auf einen geringen Beitrag der Grenzfläche hinweist. Desweiteren verstärkt ein höherer Grad der $L2_1$ Ordnung in den $\mathrm{Co_2MnSi}$ Heusler Schichten den Interband Beitrag in den MOKE Spektren.

# Contents

# Chapter 1

# Introduction

In the 1960's the first silicon transistor was invented at Bell Labs. This was a milestone of unthinkable importance that started the automatization on the world-scale level and opened the door for the use of electronics in the private-customer sector. Thus, the digital revolution has started at the very end of the previous millennium and is still very alive today. Largest and wealthiest companies of the world, like Amazon, Apple, or Microsoft, have their success and business anchored in this digital revolution. Miniaturization of the transistor and other electrical components advanced to amazing levels. It's the year 2019 and Moore's law is slowly reaching its end, as the size of a transistor is approaching the limit given by the quantum tunnelling effect of the electron. While in the beginning of this silicon revolution people's question was: "Where will we place the computer?", today's question rather is: "Where have I left it?".

With this digital revolution, a new kind of business has emerged. In today's world, to process, handle, preserve and store information is one of the largest business, possibly larger than fossil fuels, pharmacy and monetary business combined. If not, soon it will be, as this branch of "silicon industry" is exponentially growing, where companies like Google or Facebook are undisputed proof of that.

Nevertheless, this astronomical amount of information that is pulsing everyday through the global network called the internet has actually to be stored somewhere. Therefore, there is a significant urge to store the data as compactly and as safely as possible. New methods and possibilities of data storage have been continuously searched for, examined and employed since the transistor discovery. While the first hard-drive disk (HDD) was so large that a single person was unable to move it, today's HDD is not much larger than a wallet, yet it's storage capacity is about million-times larger. This was possible by substantial effort that was put into the ferromagnetic (FM) materials research. To probe, understand and control magnetism in the material, multiple methods have to be employed and invented.

One very powerful tool vastly employed for the FM research is the magnetooptic Kerr effect (MOKE) [1, 2]. It manifests through the change of the polarization state of light upon reflection from a magnetized specimen. Main advantages are that it is a sturdy, easy to use and non-destructive method, while the needed equipment is cheap and without any special prerequisites. The MOKE itself was actually used in the past as the way to read out information on the magnetooptic disc, but this concept has been replaced by modern HDD, since the area of one bit of information is below the diffraction limit of visible light. Nevertheless, the MOKE setup is a fundamental piece of equipment in groups working in the magnetism research today. Furthermore, as electromagnetic (EM) wave propagation is nonreciprocal (i.e. unidirectional) in magnetooptic (MO) media, the MO effects are fundamental for design of optical isolators and circulators that are extensively used in optical communications [3].

Most of those applications usually utilize the approach of linear MOKE (LinMOKE), where only the MOKE contribution proportional to magnetization $\boldsymbol{M}$ is considered. But, as was shown in the last two decades, quadratic MOKE (QMOKE) which is the contribution proportional to $\boldsymbol{M}^2$, cannot be neglected [4–10] and must be properly taken care of [11–19]. Lately, it was also shown that QMOKE on its own have lots of perspectives [20–22].

The 8-directional method [13] is one of the techniques that can efficiently separate QMOKE from LinMOKE and analyze its contributions in the case of (001) oriented cubic crystal structures [23–29]. The focus of this thesis is QMOKE behaviour of cubic crystal structures. The theory of MOKE is treated here from the point of view of classical physics, and we use linear MO parameter $K$ and quadratic MO parameters $G_s$ and $2G_{44}$ [30] to describe LinMOKE and QMOKE contributions. The origin of equations of 8-directional method is analyzed and, as one of the main results, this method is extended to (011) and (111) oriented cubic crystal structures, which is done through derivation of theoretical equations and comparison to numerical calculations as well as to experimental measurements. The second main result of this thesis is the QMOKE spectroscopy of (001) oriented cubic crystal structures [31, 32]. Our approach is established on determining the spectra of quadratic MO parameters $G_s$ and $2G_{44}$ (together with linear MO parameter $K$), and was successfully applied to Fe thin films and $\mathrm{Co_2MnSi}$ Heusler compounds of differently strong $L2_1$ ordering. A more comprehensive introduction to this work will be given in Sec. 1.3 at the end of this introduction chapter.

## 1.1 Introduction to the magnetooptic Kerr effect

### 1.1.1 From simple idea to basic model

At start we will discuss some simple ideas, as it is useful to have a very simple model at hand. MOKE takes place in the extended visible spectral range i.e. from near infrared (NIR) to ultra violet (UV) light. Because of that, the response of the magnetic moments in the matter does not play any important role (resonant frequencies of magnetic moments are several orders of magnitude lower - atoms with their magnetic moments are too heavy to follow such a vastly oscillating magnetic field of the EM wave. Thus, MOKE must be connected with the change of the specimen response to an alternating electric field $\boldsymbol{E}$ of EM wave when a static magnetic field $\boldsymbol{B}_0$ is applied (and thus the specimen gets magnetized).

Let's start with a simple picture of a free charged particle. If such a particle will be struck by linearly polarized EM wave, the particle will oscillate in the plane of polarization of $\boldsymbol{E}$. We can imagine that the particle absorbs and reemits the EM wave at once[1] (which is a good imagination as the particle will truly serve as a scattering centre of the EM wave). Now, if we apply constant magnetic field $\boldsymbol{B}_0$ (such that $\boldsymbol{E} \times \boldsymbol{B}_0 \neq 0$), the Lorentz force acting on the particle will result in the circular-like oscillations of that particle. Such a circular motion could be thought of as superposition of two orthogonal linear oscillations. Therefore the reemitted wave will also be composed of two orthogonally linearly polarized waves, producing a somewhat different polarization state of the reemitted light when compared to the polarization state of the incoming light. Although this model is oversimplified, it is still an excellent first approximation.

Now, when the free charged particle is replaced by an electric dipole $\boldsymbol{p}$, the picture of interaction with EM wave in the static magnetic field $\boldsymbol{B}_0$ will not be that much different from the previous case. The oscillation of the electric dipole $\boldsymbol{p}$ will also be altered by the presence of the magnetic field $\boldsymbol{B}_0$. Further, in classical physics, the material can be actually well described as large quantities of such electric dipoles. For this we use polarization $\boldsymbol{P}$ of the material, being the number of electric dipoles $\boldsymbol{p}$ per unit volume. Thus, this material polarization $\boldsymbol{P}$, usually induced by the acting electric field $\boldsymbol{E}$, will be changed when magnetic field $\boldsymbol{B}_0$ is applied.

Nevertheless, the magnetic field $\boldsymbol{B}_0$ alone has rather small impact, observable only when the light is passing through the material at larger distance e.g. few millimetres (this is actually known as Faraday effect), or when the $\boldsymbol{B}_0$ is of enormous strength. But when reflection occurs, the light penetrates the material in the substantially lower depth

---

[1] A phase shift may be induced.

(no more than few dozens of nanometers), thus in the case of reflection the change of polarization will be rather observable only within FM materials that can get magnetized, which empowers the MO effect to large extent. The $\boldsymbol{B}_0$ will then serve us to induce the magnetization $\boldsymbol{M}$ of the material and keep it saturated, eventually driving $\boldsymbol{M}$ into the desired direction when needed. As we will discuss later, MOKE does change for different $\boldsymbol{M}$ directions. This fact is actually used for the MOKE measurement. If MOKE would be constant for all $\boldsymbol{M}$ directions, it would be technically hard to measure the change of polarization absolutely and separate it from other effects (e.g. strain). But if we posses the description of how the MOKE changes with $\boldsymbol{M}$ direction (described below and mainly in Chapter 2), we can use it to separate and analyze the MOKE signal. Otherwise, in case of FM material with zero net magnetization, contributions from various magnetic domains will zero-out.[2]

Thus, material polarization $\boldsymbol{P}$ will change with the magnetization $\boldsymbol{M}$ of the material. Roughly, we can write $\Delta\boldsymbol{P}_M \sim \boldsymbol{M} \times \boldsymbol{E}$, where $\Delta\boldsymbol{P}_M$ is the change of the material polarization with $\boldsymbol{M}$. Note that this is actually the similar condition as $\boldsymbol{E} \times \boldsymbol{B}_0 \neq 0$ introduced above for the Lorentz force acting on the oscillating charged particle in the static magnetic field. However, to quantify and describe the MO activity of the material, the polarization $\boldsymbol{P}$ is not the best option, as it does scale with the amplitude of the driving electric field $\boldsymbol{E}$. In our experiment, we do not always use the same intensity of the light – it is different at different wavelengths, or drops in time as a lamp gets older, etc. Thus we rather need a material parameter that is independent on the intensity of the light. For this, electric susceptibility $\boldsymbol{\chi}$ of material is suitable [33], where

$$\boldsymbol{P} = \varepsilon_0 \boldsymbol{\chi} \boldsymbol{E} \tag{1.1.1}$$

with $\varepsilon_0$ as the permittivity of vacuum. The electric susceptibility describe material properties itself and is independent on the electric field $\boldsymbol{E}$, i.e.

$$\boldsymbol{\chi} \neq \boldsymbol{\chi}(\boldsymbol{E}). \tag{1.1.2}$$

Note that Eq. (1.1.2) bound all this work to the realm of *linear optics*. If the intensity of the EM wave is too high[3], or in the case of some special materials (so-called non-linear media) Eq. (1.1.2) is not valid anymore, and we have to employ the theory of *non-linear optics*, where $\boldsymbol{\chi} = \boldsymbol{\chi}(\boldsymbol{E})$. Non-linear optics will not be used at any point in this work and we will strictly stick to Eq. (1.1.2).

---

[2] Of course, unless the light is focused onto a single domain state, which is something that would have to be achieved and is quite technically demanding rather than something that happens unintentionally without our intervention.

[3] ca. $> 10^7$ Vm$^{-1}$

In matrix notation, Eq. (1.1.1) writes

$$\begin{bmatrix} P_x \\ P_y \\ P_z \end{bmatrix} = \varepsilon_{\text{vac}} \begin{bmatrix} \chi_{xx} & \chi_{xy} & \chi_{xz} \\ \chi_{yx} & \chi_{yy} & \chi_{yz} \\ \chi_{zx} & \chi_{zy} & \chi_{zz} \end{bmatrix} \begin{bmatrix} E_x \\ E_y \\ E_z \end{bmatrix}. \tag{1.1.3}$$

If some of the off-diagonal elements $\chi_{ij}(i \neq j)$ of the electric susceptibility tensor $\boldsymbol{\chi}$ are non-zero, the material polarization $\boldsymbol{P}$ is not parallel to the driving electric field $\boldsymbol{E}$. Here, one can note the analogy to the charged particle that is in circular motion, although the driving electric field $\boldsymbol{E}$ is only linearly polarized.

But we will actually not use electric susceptibility $\boldsymbol{\chi}$ to describe the material, but rather relative permittivity $\boldsymbol{\varepsilon}_r$. The relation between those two is

$$\boldsymbol{\varepsilon}_r = \mathbf{1} + \boldsymbol{\chi}, \tag{1.1.4}$$

with $\mathbf{1}$ as the identity matrix. The difference is that the relative permittivity already contains the contribution of vacuum, whereas electric susceptibility does not. Later in the Chapter 2 we will show how to bind relative permittivity together with conductivity of the material (where conductivity at optical frequencies actually describes dissipation of EM wave inside the material) under so-called complex permittivity tensor $\boldsymbol{\varepsilon}$. This $3\times3$ complex permittivity tensor $\boldsymbol{\varepsilon}$ will be the quantity through which we will characterize all the samples and the materials from optical and MO point of view.

### 1.1.2 Change of polarization state of light upon reflection

Let's introduce two orthogonally linearly polarized waves: *s*- polarized wave and *p*-polarized wave. The electric field vector $\boldsymbol{E}$ of the *s*- polarized wave oscillates in the plane perpendicular[4] to the plane of incidence (plane defined by incident beam and surface normal. In the case of specular reflection, which is the case at hand, the reflected beam will also lay in plane of incidence). In the case of *p*- polarization the electric field vector $\boldsymbol{E}$ oscillates parallel to the plane of incidence. For a better grasp of our conventions, see Appendix A. Upon reflection of *s*-polarized wave from a magnetized specimen, the reflected wave will also contain a small *p*-polarized component and vice versa (see the sketch of Fig. 1.1). The superposition of those two polarization modes will produce

---

[4] In german language, perpendicular is *senkrecht*, therefore *s*- polarization.

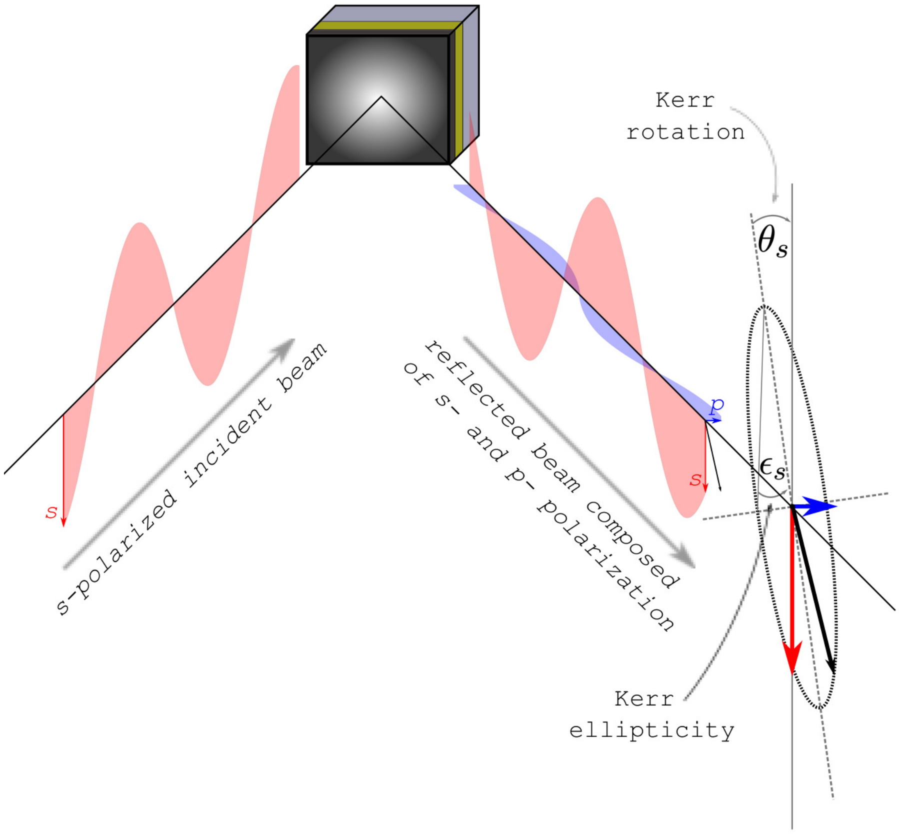

FIGURE 1.1: Sketch of the MOKE phenomenon. The $s$-polarized incident wave obtains small part of $p$- polarization upon reflection from the magnetized specimen. The $p$-polarized reflected wave has much smaller amplitude and also gains a phase shift compared to the reflected $s$- polarized wave. By the superposition of the $s$- and $p$- polarized waves we obtain elliptically polarized light that is described by the Kerr rotation $\theta$ and Kerr ellipticity $\epsilon$.

elliptically polarized light.[5] Elliptical polarization is the most general polarization state of light and can be described by its rotation $\theta$, being the angle between the major axis of ellipse and given axis in our coordinate system and by its ellipticity $\epsilon$, being the arctan of the ratio of major and minor axis (see Fig. 1.1). Therefore, MOKE is defined through so called Kerr rotation and Kerr ellipticity and together called complex Kerr angles or Kerr amplitude $\Phi$. The Kerr angles [33]

$$\Phi_s = \theta_s + i\epsilon_s, \qquad \Phi_p = \theta_p + i\epsilon_p \tag{1.1.5}$$

define the polarization state of the reflected light, where incident light is $s$-polarized, $p$-polarized, respectively.

---

[5] Note that we could actually use an arbitrary set of two orthogonal polarization modes. For some applications - for example in order to measure some MO effects in the x-ray part of the spectrum - left circular polarization (LCP) and right circular polarization (RCP) is chosen as a set of polarization eigenmodes. Though, for our use, the $s$- and $p$- polarization is much wiser choice, as those are the eigenmodes used to probe the sample.

The Kerr angles are given by the ratio of the amplitudes and the phase shift of the reflected $s$- and $p$- polarized waves. These attributes are described within four reflection coefficients of the sample[6], $r_{ss}$, $r_{pp}$, $r_{sp}$ and $r_{ps}$, which can be ordered into the Jones reflection matrix [34]

$$\boldsymbol{R} = \begin{bmatrix} r_{ss} & r_{sp} \\ r_{ps} & r_{pp} \end{bmatrix}. \tag{1.1.6}$$

The first subscript refer to the polarization of the reflected light and the second to the polarization of the incident light. Hence, the off-diagonal elements of the reflection matrix actually describe the conversion between one polarization state to the another one. The Jones formalism is used to describe propagation and interaction of fully polarized light with the sample and other optical elements and it will be discussed and introduced in the Sec. 2.4.2, where we will also show that Eq. (1.1.5) can be actually written as

$$\Phi_s = -\frac{r_{ps}}{r_{ss}} = \theta_s + i\epsilon_s, \qquad \Phi_p = \frac{r_{sp}}{r_{pp}} = \theta_p + i\epsilon_p. \tag{1.1.7}$$

### 1.1.3 MOKE and the permittivity tensor

The reflection coefficients for a single interface can be described through the Fresnel formulae [34] that stem directly from the index of refraction of both materials forming the interface and from the angle of incidence (AoI). The index of refraction $n$ is directly bound to the permittivity as $n = \sqrt{\varepsilon}$. In the case of a thin film multilayer system, a more computation demanding approach must be used to obtain the reflection coefficients, yet AoI and permittivity of layers still play a crucial role. As can be deduced from the text above, the permittivity

$$\boldsymbol{\varepsilon} = \begin{bmatrix} \varepsilon_{xx} & \varepsilon_{xy} & \varepsilon_{xz} \\ \varepsilon_{yx} & \varepsilon_{yy} & \varepsilon_{yz} \\ \varepsilon_{zx} & \varepsilon_{zy} & \varepsilon_{zz} \end{bmatrix} \tag{1.1.8}$$

is a 3×3 tensor of second rank, with element $\varepsilon_{ij}$ describing what is the response of the material in the direction $i$ when $\boldsymbol{E}$ is applied in the direction $j$.

All MO effects, including MOKE, could be actually phenomenologically described by the change of the permittivity tensor with $\boldsymbol{M}$. For optically isotropic material, e.g. cubic crystal structures, the tensor of permittivity without the contribution of $\boldsymbol{M}$ is described as $\varepsilon\mathbf{1}$, where $\mathbf{1}$ is identity matrix and $\varepsilon$ is a scalar. This will result in $r_{sp} = r_{ps} = 0$ and, thus, there will be no change of polarization upon reflection. When the cubic crystal

---

[6] Those reflection coefficients describe reflection of fully polarized light and, thus, depolarization is not considered.

| PMOKE | LMOKE | TMOKE |
|---|---|---|
| 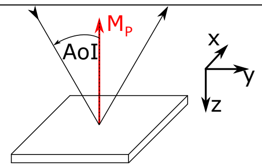 | 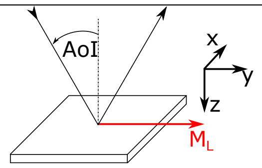 | 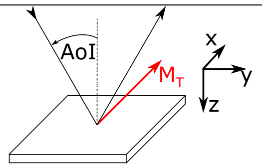 |
| $\begin{bmatrix} \varepsilon_d & -\varepsilon_1(M_z) & 0 \\ \varepsilon_1(M_z) & \varepsilon_d & 0 \\ 0 & 0 & \varepsilon_d \end{bmatrix}$ | $\begin{bmatrix} \varepsilon_d & 0 & \varepsilon_1(M_y) \\ 0 & \varepsilon_d & 0 \\ -\varepsilon_1(M_y) & 0 & \varepsilon_d \end{bmatrix}$ | $\begin{bmatrix} \varepsilon_d & 0 & 0 \\ 0 & \varepsilon_d & -\varepsilon_1(M_x) \\ 0 & \varepsilon_1(M_x) & \varepsilon_d \end{bmatrix}$ |
| $\begin{bmatrix} r_{ss} & r_{sp}(M_z) \\ r_{ps}(M_z) & r_{pp} \end{bmatrix}$ | $\begin{bmatrix} r_{ss} & r_{sp}(M_y) \\ r_{ps}(M_y) & r_{pp} \end{bmatrix}$ | $\begin{bmatrix} r_{ss} & 0 \\ 0 & r_{pp} + \Delta r_{pp}(M_x) \end{bmatrix}$ |

TABLE 1.1: Permittivity tensor and reflection matrix of a cubic crystal structure for PMOKE (1st column), LMOKE (2nd column) and TMOKE (3rd column) configuration. In the first row a sketch of the configurations itself is shown, depicting the sample surface, plane of incidence and direction of magnetization in the sample. In the second row, the permittivity tensor of the magnetized crystal is shown (only linear-in-magnetization contribution is considered here). In the last row we show the reflection matrix of the crystal and how it is change upon magnetization of the specimen.

gets magnetized, the tensor of permittivity will change its shape and the off-diagonal reflection coefficient will become non-zero.

We will provide a detailed description of how the permittivity tensor changes with magnetization in Sec. 2.2, but for now we will discuss a vastly used approach of LinMOKE. Thus, we will consider only changes of the permittivity tensor with the linear dependence on $\boldsymbol{M}$. Table 1.1 summarizes the shape of the permittivity tensor and the reflection matrix for three well known LinMOKE configurations. Each of those configurations describes the case when magnetization is aligned along one of the axes of the Cartesian coordinate system $xyz$. If the magnetization is parallel to the plane of incidence and normal to the surface, being direction parallel to axis $z$, we call this type of effect polar MOKE (PMOKE). Longitudinal MOKE (LMOKE) occurs when magnetization is parallel to the plane of incidence as well as to the surface of the sample, i.e. directed along the $y$-axis. In the case when magnetization is parallel to the sample surface but perpendicular to the plane of incidence (i.e. direction of $x$-axis), we talk about transversal MOKE (TMOKE). Thus we can write magnetization vector as

$$\boldsymbol{M} = \begin{bmatrix} M_x \\ M_y \\ M_z \end{bmatrix} = \begin{bmatrix} M_T \\ M_L \\ M_P \end{bmatrix}. \tag{1.1.9}$$

For a full description of the used conventions, of the coordinate system and of the sign conventions, please see Appendix A.

Note that PMOKE and LMOKE do manifest through a change of polarization upon reflection, but TMOKE manifests only through a change of intensity of the reflected $p$-polarized wave.[7]

### 1.1.4 Introduction to quadratic MOKE

Now we will introduce contributions of higher orders in magnetization to MOKE. The permittivity tensor of a magnetized crystal $\boldsymbol{\varepsilon_M}$ can be fully described as expansion [30]

$$\boldsymbol{\varepsilon_M} = \boldsymbol{\varepsilon}^{(0)} + \boldsymbol{\varepsilon}^{(1)} + \boldsymbol{\varepsilon}^{(2)} + \boldsymbol{\varepsilon}^{(3)} + \dots \quad , \tag{1.1.10}$$

where superscript in brackets denote the order of the contribution's dependence on magnetization $\boldsymbol{M}$. Thus, the examples of those three LinMOKE configurations described in Tab. 1.1 use actually the approximation $\boldsymbol{\varepsilon_M} = \boldsymbol{\varepsilon}^{(0)} + \boldsymbol{\varepsilon}^{(1)}$, when contributions of higher orders are neglected. At first sight this may look like quite severe approximation, but the contributions of higher orders are usually substantially smaller then the contribution of the first order, which is why the LinMOKE approach is sufficient in most cases. Very roughly, the contribution of the $n-$th order is about one order of magnitude smaller then the contribution of the $(n-1)$-th order, i.e. contribution of $\boldsymbol{\varepsilon}^{(3)}$ should be very roughly 1/10 of $\boldsymbol{\varepsilon}^{(2)}$ and 1/100 of $\boldsymbol{\varepsilon}^{(1)}$. Most of the conventional FM materials, like 3d metals and its alloys, or some Heusler compounds etc., have Kerr angles smaller than 1 degree. Thus, the higher orders contributions to MOKE are usually negligible and special techniques have to be employed to observe and separate them.

Nevertheless, the contribution of the $\varepsilon^{(2)}$, which is the origin of QMOKE, is usually strong enough to be clearly observed in the measurements. While LinMOKE is odd in magnetization, i.e. it does change sign upon magnetization reversal, the QMOKE is even in magnetization and, thus, does not change sign upon magnetization reversal. Such a behaviour can be easily recognized e.g. in the MOKE magnetization hysteresis curves. Nevertheless, note that it is not solely LinMOKE and QMOKE that is odd and even in magnetization, respectively. The Eq. (1.1.10) can be actually written as

$$\boldsymbol{\varepsilon_M} = \boldsymbol{\varepsilon}^{(0)} + \boldsymbol{\varepsilon}^{(\mathrm{odd})} + \boldsymbol{\varepsilon}^{(\mathrm{even})}, \tag{1.1.11}$$

---

[7] Under some combinations with other effects, the change of reflection coefficient $r_{pp}$ can actually result in a change of polarization of reflected light as well.

where

$$\boldsymbol{\varepsilon}^{(\mathrm{odd})} = \sum_{n=0}^{\inf} \boldsymbol{\varepsilon}^{(1+2n)} = \boldsymbol{\varepsilon}^{(1)} + \boldsymbol{\varepsilon}^{(3)} + \boldsymbol{\varepsilon}^{(5)} + \dots \quad , \tag{1.1.12a}$$

$$\boldsymbol{\varepsilon}^{(\mathrm{even})} = \sum_{n=0}^{\inf} \boldsymbol{\varepsilon}^{(2+2n)} = \boldsymbol{\varepsilon}^{(2)} + \boldsymbol{\varepsilon}^{(4)} + \boldsymbol{\varepsilon}^{(6)} + \dots \quad . \tag{1.1.12b}$$

Therefore, if the contribution of 3rd or 4th order would be strong enough they can as well contribute to the odd and even parts of the hysteresis loops, respectively.

However, in this work we will make the widely used approximation (e.g. [13, 17, 19, 23–29, 35, 36])

$$\boldsymbol{\varepsilon}^{(\mathrm{odd})} = \boldsymbol{\varepsilon}^{(1)}, \qquad \boldsymbol{\varepsilon}^{(\mathrm{even})} = \boldsymbol{\varepsilon}^{(2)} \quad \rightarrow \quad \boldsymbol{\varepsilon}_{\boldsymbol{M}} = \boldsymbol{\varepsilon}^{(0)} + \boldsymbol{\varepsilon}^{(1)} + \boldsymbol{\varepsilon}^{(2)}. \tag{1.1.13}$$

Note that the higher order contributions are not only of quantitative nature, but they induce as well some additional anisotropic behaviour (i.e. dependence on sample orientation) that is not present with contributions of the lower order. Each subsequent contribution in the row of Eq. (1.1.10) can lower the symmetry of $\boldsymbol{\varepsilon}_{\boldsymbol{M}}$. Thus, if the symmetry of the experimental data cannot be described through Eq. (1.1.13), one should consider possibility that some contributions of higher orders are involved.

In the case of samples with cubic crystal structure, the LinMOKE response is the same for all possible sample orientations and only depending on the $\boldsymbol{M}$ direction within our coordinate system. The QMOKE response on the other hand depends on the sample orientation as well as on the $\boldsymbol{M}$ direction.

This behaviour is actually used to analyze QMOKE and separate individual contributions. As will be shown in Chapter 2, we can describe $\boldsymbol{\varepsilon}^{(1)}$ and $\boldsymbol{\varepsilon}^{(2)}$ as $K_{ijk}M_k$ and $G_{ijkl}M_kM_l$, respectively. $K_{ijk}$ are elements of the linear MO tensor $\boldsymbol{K}$ whereas $G_{ijkl}$ are elements of the quadratic MO tensor $\boldsymbol{G}$. $M_k$ and $M_l$ are then individual components of the normalized magnetization $\boldsymbol{M}$ as introduced in Eq. (1.1.9). In our investigations of thin films, we consider only in-plane magnetization, i.e. $\boldsymbol{M} = [M_T, M_L, 0]$. The reason is that thin films are usually much harder to saturate out-of-plane than in-plane due to a large demagnetization field of the FM thin film layer [37]. Consequently, the experimental separation method used within this work, the so-called 8-directional method [13], is invented solely for the in-plane $\boldsymbol{M}$ MOKE measurements. However, some out-of-plane separation method could be developed from the equations of Ref. [38].

We can distinguish individual contributions to MOKE based on (i) different elements of the MO tensors and (ii) different dependence on $\boldsymbol{M}$. For cubic crystals in case of (i) we can distinguish linear MO parameter $K$ and two quadratic MO parameters $G_s$ and

$2G_{44}$. In case of (ii) we have contributions $M_L$, $M_L M_T$ and $M_T^2 - M_L^2$. All this will be well explained in the Chapter 2.

## 1.2 Putting MOKE into context

### 1.2.1 History of magnetooptics

It was Michael Faraday who recognized that electricity and magnetism are closely related and together with the colleagues of his time showed that change of one creates the other.[8] In the year 1845 the same man discovered that the azimuth of linearly polarized light is rotated when propagating through a flint glass rod in a magnetic field [39]. Today this is known as the Faraday effect. This discovery showed for the first time the interconnection between light and electromagnetism and finally led to to the conclusion that light is actually an EM wave.

31 years after the discovery of the Faraday effect, Reverend John Kerr has observed that there is also polarization rotation induced to light upon reflection from the polished pole of a permanent magnet (i.e. PMOKE)[1]. Two years later he also observed the same phenomenon for light reflected from the equatorial part of the permanent magnet (i.e. LMOKE)[9] [40]. Some years later it was recognized that polarization of the reflected light is not only rotated, but also posses some ellipticity [41], today known as the Kerr ellipticity. First quantitative measurements of the Kerr ellipticity was carried out by Zeeman [42], a well known physicist who discovered the splitting of spectral lines of an atom in the magnetic field [43]. He further discovered TMOKE [44], although it has been theoretically predicted by Wind [45].

The theoretical explanation of MO effects was given by Lorentz and Drude [46–48], but a proper microscopic explanation couldn't be provided until Quantum mechanics emerged. The understanding that MO effects stem from the interplay of spin-orbit coupling and exchange splitting was provided during 50's of the previous century [49–52].

In the second half of the 20th century, substantial technical improvements of the experimental equipment caused an abrupt rise in the experimental field of MOKE. Many experimental studies were carried out during this period, e.g. MOKE spectral dependencies of 3d transition ferromagnets and their alloys was provided by Krinchik *et al.* [53, 54] and Ferguson *et al.* [55]. The possibility to compare those spectra with a theoretical description was significantly boosted with the development of density-functional

---

[8] Later it was recognized that the magnetic field is actually just a relativistic correction of the electric field.

[9] Obviously in his time the nomenclature PMOKE or LMOKE was not introduced yet.

theory and the local spin-density approximation (LSDA) [56, 57]. Optical conductivity calculations from linear-response theory [58] also played an important role. This made it possible to calculate spectra of diagonal and off-diagonal elements of the permittivity tensor by first principle (so-called ab-initio) calculations. Nevertheless, the agreement between experimental and theoretical spectra was not very good, due to some difficulties with the MO spectra evaluation. MOKE also become an important tool for investigations of magnetic properties of thin magnetic films through hysteresis curves measurements, where even single monolayer films can be probed successfully [59].

### 1.2.2 Recent history, history of QMOKE and state of the art

In the 90's the ab-initio calculations were significantly improved by Peter M. Oppeneer *et al.* [60, 61], which allowed to describe the experimental results of MOKE spectroscopy much more precisely. The experimental research in MOKE spectroscopy does continue to present days [62–69], where experimental results are commonly accompanied with ab-initio calculations. The vast amount of experimental data together with ab-initio spectra produced until the end of the previous millennium are summarized by Buschow in the book *Handbook of magnetic materials* with the chapter about MOKE spectroscopy written by Peter M. Oppeneer [70].

The first publication concerning quadratic MO effect was published already in 1965 [71]. In the 80's the description of the shape of $\boldsymbol{\varepsilon}^{(1)}$ and $\boldsymbol{\varepsilon}^{(2)}$ was provided for various crystallographic structures by Štefan Višňovský [30]. Though, the experimental measurement of QMOKE have not been done so far. Then, at the beginning of the 90's unexpected symmetric contributions to the hysteresis loops of Ni-Fe bilayers were reported [4, 5] and, later on, explained as QMOKE contributions to the overall MOKE signal [6–10]. Since then, several methods have been proposed for the separation of QMOKE contributions from the LinMOKE signal including the ROTMOKE method [11, 12], the 8-directional method [13], the sample rotation by 180° [14], and the rotation field method [19].

In the recent years the characteristic capabilities of MOKE were largely improved, which can be partly credited to the understanding of QMOKE contribution. As example we can mention the precise vectorial MOKE magnetometry [17, 18] as well as some other studies where QMOKE was extracted from the hysteresis loop measurements [15, 16]. Nevertheless, QMOKE itself was also successfully used in the Heusler compounds research a few years ago [16, 23–29], where mostly 8-directional method was used to characterize the QMOKE contribution.

Thus, MOKE does obviously serve very well for the FM material characterization. Nevertheless, it has also found its irreplaceable position in the cutting edge research area of spintronics and spincaloritronics. Here, MOKE can be used e.g. for spin accumulation detection [72, 73], or to detect exchange bias - an effect vastly employed in the magnetoresistive devices that occur when the magnetization of a thin FM layer is pinned by an adjacent antiferromagnetic (AFM) thin layer [74]. The QMOKE itself can be used e.g. for investigation of spin-orbit torques in metallic as well as insulating magnetic heterostructures [20].

Further, MOKE gets a lot of attention recently in the AFM material investigations [22] as a new possibility to control AFM spin orientation by electric current was introduced based on spin-orbit torque effects [75, 76]. The characterization of AFM is well feasible also through MO effects in the x-ray part of the spectra, but this requires access to large synchrotron facilities. The attractiveness of MOKE is that it is a fast, cheap and easily accessible characterization method. Also, as the AFM lacks the net magnetization, a lot of methods that are classically used in FM research, like vibrating sample magnetometry (VSM), are not applicable to AFMs. This is actually also a problem with LinMOKE that is applicable only to canted AFMs and AFM dynamics [77–79]. This brings us to another quality of QMOKE, which is its applicability to fully compensated AFMs [21].

### 1.2.3 MOKE with respect to other magnetotransport effects

Magnetotransport effects describe how the transport properties of a given material change with the presence of the material's magnetization. We may distinguish transport of three different elements inside the material: (i) charge of the electron, (ii) spin of the electron, (iii) heat. All those three transports can actually intermix and affect each other. The discipline that studies the coupled transport of spin and charge is known as spintronics. Well known effects of spintronics are, e.g. giant and tunnel magnetoresistance [80], or the (inverse) spin Hall effect [81]. Spincaloritronics is the discipline that studies coupled transport of heat and spin. Here, we can find thermomagnetic effects such as the anomalous Nernst effect (linear in $\boldsymbol{M}$)[82–84] and the anisotropic magnetothermopower together with the planar Nernst effect (quadratic in $\boldsymbol{M}$) [85–87].

Although MOKE can be successfully employed for examination of lots of effects from realm of spin(calori)tronics, its origin fell solely into the part where we consider change of charge transport with the $\boldsymbol{M}$, thus, MOKE itself is a charge magnetotransport effect. Nevertheless, the charge magnetotransport effects have their own names according to the spectral region they are found in. The spectral region is given by the frequency of electric field $\boldsymbol{E}$, being the excitation force acting on the electron's charge, whose transport properties are then affected by the presence of the magnetization. From the d.c. part of the spectra we can name the anomalous Hall effect (AHE) [88], that is linear

| proportional to | d.c | Optics (NIR+Vis+UV) reflection | transmission | x-ray |
|---|---|---|---|---|
| $\sim \boldsymbol{M}$ | AHE | LinMOKE | Faraday effect | XMCD |
| $\sim M_L M_T$ | PHE | QMOKE | Voigt effect | XMLD |
| $\sim (M_T^2 - M_L^2)$ | AMR | QMOKE | Voigt effect | XMLD |

Table 1.2: Comparison of the magnetotransport effects in different spectral regions and with different dependencies on magnetization. In d.c. part of spectra there is the anomalous Hall effect (AHE), the planar Hall effect (PHE) and the anisotropic magneto resistance (AMR). In extended visible spectral range, i.e. from near infrared (NIR) over visible (Vis) to ultraviolet (UV) light, we have the LinMOKE and QMOKE with the Faraday and Voigt effect. In the x-ray part of the spectra there is the x-ray magnetic circular (XMCD) and linear dichroism (XMLD).

in $\boldsymbol{M}$ and the anisotropic magnetoresistance (AMR) [89] together with the planar Hall effect (PHE), both being quadratic in $\boldsymbol{M}$. From the x-ray family there is the well known x-ray magnetic circular (linear) dichroism and birefringence, being linear (quadratic) in $\boldsymbol{M}$ [90, 91]. The MOKE and Faraday effect are then charge-related magnetotransport effects from extended visible spectral range. In Tab. 1.2 we summarize most known charge-related magnetotransport effects from three well distinctable spectral regions. We also show the distribution into the linear and quadratic dependence on $\boldsymbol{M}$ here.

Note that in the d.c. part of the spectra those effects are usually described through magnetization driven changes of complex conductivity tensor $\hat{\boldsymbol{\sigma}}$, whereas in the optical and x-ray frequencies one use the complex permittivity tensor $\hat{\boldsymbol{\varepsilon}}$ . Nevertheless, those two quantities are fully interchangeable and what is described by one is also described by the other in the given spectral range. The relationship between those two is

$$\hat{\varepsilon}_{ij} = \frac{i}{\omega\varepsilon_0}\hat{\sigma}_{ij} \tag{1.2.1}$$

with $i$ as imaginary unit, $\omega$ as radial frequency of the EM wave and $\varepsilon_0$ as the vacuum permittivity. One way how to derive this relationship is from the wave equations of the EM wave, which will be given in Chapter 2.

## 1.3 Introduction to this work

### 1.3.1 Motivation

From what was written so far it is quite obvious that MOKE is a well utilized technique in condensed matter physics, and QMOKE becomes to be an inherent part of it and is getting on popularity. Our aim is to further examine and understand QMOKE behaviour and to help strengthen and anchor the utilization of QMOKE in the field of magnetic materials research. The 8-directional method [13] is developed for (001) oriented cubic crystal structures and was applied to many materials, so far. Yet, the equations and techniques of 8-directional method for (011) and (111) oriented cubic crystal structures are missing. Although there are some studies that are dealing with those cubic crystallographic orientations [26, 36], the equations are not developed in detail or the 8-directional method separation is not considered at all.

Further, we mentioned how wealthy amount of LinMOKE spectroscopy data is available, but in the field of QMOKE spectroscopy not so many systematic studies have been carried out so far [92, 93]. From our perspective the QMOKE spectroscopy together with ab-initio calculations is an appropriate combination to gain a better understanding of the microscopic origin of the quadratic MO effects.

In addition, QMOKE can be a suitable tool for AFM research as this technique could be easily adopted by any laboratory. In AFM research QMOKE is usually utilized through measurements of linear magnetic dichroism and birefringence - different propagation and absorbtion of two linearly polarized modes, one parallel to $\boldsymbol{M}$ (or in case of AFM, rather to the AFM vector $\boldsymbol{L}$, i.e. to the individual directions of the magnetic moments in the material) and other perpendicular to it. Yet, a more comprehensive approach through 8-directional method is available which takes into account also the anisotropy of QMOKE effects. Although we recognize that to apply this method on AFM would be considerably challenging as one has to be able to reorient the magnetic moments of the AFM to desired directions, it will not be in principle impossible. The reorientation of an AFM with an easy magnetic plane parallel to surface plane of the sample by magnetic field is possible [94] and there are also other approaches as polarization-dependent optical annealing [95] or the use of inverse MO effects [78, 96–98]. Nevertheless, before we get to the step of AFM investigations, we need to test and master the ideas and techniques of QMOKE spectroscopy based on 8-directional methods on FM materials, where we can simply orient the direction of $\boldsymbol{M}$ by a sufficient large external magnetic field and hence separate different QMOKE contributions.

### 1.3.2 Goals and content of this thesis

This work is focused on (i) the 8-directional method that is extended from (001) oriented cubic crystal structure to (011) and (111) oriented cubic crystal structures. The aim here is to provide theoretical equations in analogy with the equations of the 8-directional method of (001) oriented cubic crystal structures that are presented in Ref. [13]. Those equations are then compared to numerical simulations and experimental measurements.

(ii) The QMOKE spectroscopy of (001) oriented cubic crystal structures based on a modified 8-directional method. Our goal here is to fully develop the experimental technique through which we can systematically determine spectra of quadratic MO parameters $G_s$ and $2G_{44}$ in addition to the linear MO parameter $K$. To successfully achieve this, multiple steps have to be undertaken. First, the LinMOKE and QMOKE spectra stemming from individual MO parameters are separated directly from the experiment [31, 99]. To obtain the pure spectra of the MO parameters, we need to post-process our spectroscopic measurements by a numerical model. Development and optimization of this model was substantial part of this work, yet it is discussed just very briefly within the text. Note that we have to posses good knowledge about the measured sample (e.g. thickness and $\varepsilon^{(0)}$ of each layer in the sample) to successfully yield the MO parameters. Thus, the structural, magnetic and optical characterizations of the samples were also an inherent part of this task. As a final outcome, we compare each of the experimental spectra of the MO parameters with the ab-initio calculations [100, 101].

The QMOKE spectroscopy is first applied to Fe(001)/MgO(001) sample series, where the thickness of the Fe layer is varied [32]. The method is well tested and optimized on this sample set, which allow us to further use it for systematic studies of QMOKE spectra with other materials. The QMOKE spectroscopy is further applied to thin film sample series of $Co_2MnSi$ Heusler compounds. Each sample in the series was annealed at different temperature providing different degree of $L2_1$ ordering. The effect of ordering on linear and quadratic MO parameters is studied with this sample series. Moreover, comparison to ab-initio calculations is present for both sample sets.

The additional samples of Fe(011) grown on MgO(111) and Co(011) grown on MgO(011) were prepared to probe the 8-directional method of (011) oriented cubic crystal structures, but only Fe(011) samples were finally used as we were not able to saturate the Co(011) sample within our setup. For the purpose of 8-directional method of (111) oriented cubic crystal structures we prepared Ni(111) thin films grown on MgO(111) substrates.

### 1.3.3 Word of author

I hope that this text will serve as accessible and understandable way to introduce the field of MOKE and QMOKE to students that will choose to join the research in this area. Nevertheless, this work is also a key source for consideration if I, the author of this text and Ph.D. candidate, Robin Silber, will be granted to enter the scientific community. This work is obviously a collaboration of multiple co-workers and laboratories. Thus, at those lines I would like to specify what exactly was my sole work and what was the work of the co-workers.

My research was simultaneously settled at two universities: VŠB - Technical University of Ostrava and Bielefeld University. At Bielefeld University I prepared some of the samples investigated in this work [Fe(001), Fe(011), Co(011), Ni(111)] by magnetron sputtering. Further, I obtained all the structural and magnetic characterization at this University, together with the measurements of the 8-directional method. During my time at Technical University of Ostrava, I obtained all the LinMOKE and QMOKE spectroscopy measurements with an in-house developed setup [99] that I further upgraded from the side of hardware and software alike. I also conducted some of the optical characterization of the samples, i.e. ellipsometry measurements at the Technical University of Ostrava. Processing of all the data, coding of the numerical calculus and its optimization with further simulations was done by myself at both universities [32].

The preparation and structural characterization of Fe(001) samples prepared by molecular beam epitaxy were fully provided by my colleagues Jannis Thien, Olga Kuschel and Joachim Wollschläger from Osnabrück University. Those sample were prepared for comparison with the Fe(001) sample series prepared by myself by magnetron sputtering in Bielefeld. The PMOKE spectroscopy of the Fe(001) samples and ellipsometry of the $Co_2MnSi$ samples was provided by my colleagues from Charles University in Prague, Lukáš Beran and Daniel Král, respectively. The $Co_2MnSi$ samples were prepared by Takahide Kubota from Tohoku University in Sendai. Finally, all the ab-initio calculations presented in this work are sole work of my colleagues Ondřej Stejskal [101] from Technical University of Ostrava and Jaroslav Hamrle from Charles University in Prague.

Finally, if any of the original data presented in this work was not acquired or processed by myself, it will be clearly stated in the text or/and in the caption of the figures.

### 1.3.4 Layout of this work

In Chapter 2 all the necessary theory to understand our further experimental work will be provided. The theory of EM wave propagation in the multilayer stack (Yeh's formalism) is built here from the scratch and the formalism used to describe the permittivity of a magnetized crystal is explained as well.

Chapter 3 will then deal with all experimental techniques. The theory and techniques of the sample preparation, structural characterization as well as magnetic and optical characterization will be briefly discussed here. Further, the walkthrough of all MOKE setups, used for gathering the experimental data, will be described here. Finally, in the last part of this section, we will show and discuss the data of the structural, magnetic and optical characterizations of all the sample series investigated within this work.

In the subsequent Chapter 4 we will start our investigation of the 8-directional method. The chapter will first discuss the well known (001) surface orientation. We will compare those equations with our numerical model and experiments, and we will outline the utilization of QMOKE spectroscopy from 8-directional method here. Then, the derivation of equations for (011) and (111) orientation will follow. Again, the comparison to the numerical calculations and to the experimental measurements will be presented. The possibility to apply those equations for QMOKE spectroscopy will be discussed here as an outline for future work.

Chapter 5 will then handle the QMOKE spectroscopy technique. The measurement algorithm for separation of MOKE spectra stemming from individual MO parameters will be presented and put to work. The post processing in our numerical calculus, providing us with the pure spectra of MO parameters, will be discussed, together with some troubleshooting. The spectral dependencies of linear and quadratic MO parameters $K$,$G_s$ and $2G_{44}$ will be shown for Fe and $\mathrm{Co_2MnSi}$. Comparison of those results with ab-initio calculations and the literature (where available) will be presented as well.

# Chapter 2

# Classical theory behind magnetooptic effects

In the first section of this chapter we provide some basics of classical theory of electromagnetism and electromagnetic optics. We will discuss the Maxwell equations and derive the wave equation of the EM wave propagating in the anisotropic media, such as in magnetized cubic crystals. We will also explain what is the origin of the complex nature of the permittivity tensor. In Sec. 2.2 we will explain a formalism that is used for the description of the permittivity tensor of magnetized crystals. Here, we will introduce linear and quadratic MO parameters that are used to describe the MO activity of the material. Section 2.3 will introduce the so-called Yeh 4×4 matrix formalism, which describes the propagation of coherent EM waves through a multilayer stack. Note that as all of our samples studied in this work are actually thin films, this formalism is necessary to properly process our MOKE experimental data. Further, in Sec. 2.4 we will give a basic introduction into the description of polarized light by the Jones formalism. Finally, at the end of this chapter in Sec. 2.5 we will discuss the separation process of LinMOKE and QMOKE contributions known as the classical 8-directional method, although this separation process will be thoroughly revisited in Chapter 4.

## 2.1 Electromagnetic waves in matter

### 2.1.1 Maxwell's equations

Maxwell's equations, the brilliant set of four relations that governs the field of electromagnetism, empirically gathered by Faraday, Gauss, Ampère and summarized and extended by James Clerk Maxwell.[1] The equations come in two forms: microscopic and macroscopic. The microscopic Maxwell equations are suitable for use in vacuum or in the case when each charged particle can be tracked individually. Nevertheless, it is impossible to use them for macroscopic description of electromagnetism inside matter, as contribution of each single charge would have to be taken into account. Therefore, use of the macroscopic Maxwell equation is more suitable in this case. Response of the material to fields $\boldsymbol{E}$ and $\boldsymbol{B}$ is described by polarization $\boldsymbol{P}$ and magnetization $\boldsymbol{M}$, being defined as density of electric and magnetic dipoles moments per unit volume element, respectively.

$$\boldsymbol{P} = \frac{\mathrm{d}\boldsymbol{p}}{\mathrm{d}V}, \qquad \boldsymbol{M} = \frac{\mathrm{d}\boldsymbol{m}}{\mathrm{d}V}, \tag{2.1.1}$$

with $\boldsymbol{p}$ as electric dipole moment and $\boldsymbol{m}$ as magnetic dipole moment.

Inside the material, we can split the charge density $\varrho$ into two contributions. The charge density of free or free-like charges $\varrho_f$ and the density of bound charges $\varrho_b$ that is caused by the inhomogeneous polarization $\boldsymbol{P}$. The relation between bound charge and the material polarization can be derived through same way as Gauss's law [102] and hence

$$\varrho_b = -\boldsymbol{\nabla} \cdot \boldsymbol{P}. \tag{2.1.2}$$

Further, we can also split current density $\boldsymbol{J}$ in the matter into the three contributions: (i) $\boldsymbol{J}_f$, being the free current density (in our cases mostly current in metals, i.e. movement of free-like electrons), (ii) $\boldsymbol{J}_b$, being the bound current density, which is connected to movement of charge when there is change of polarization $\boldsymbol{P}$ in time and (iii) $\boldsymbol{J}_m$ being magnetic current density which we can imagine as current loop that describe magnetization in the material [102].

$$\boldsymbol{J}_f = \sigma \boldsymbol{E}, \qquad \boldsymbol{J}_b = \frac{\partial \boldsymbol{P}}{\partial t}, \qquad \boldsymbol{J}_m = \boldsymbol{\nabla} \times \boldsymbol{M}, \tag{2.1.3}$$

---

[1] Although, note that it was Oliver Heaviside, the self-taught mathematician and physicist, who gave the equations the shape we know and use today. He's supposed to also be the one who introduced use of complex numbers to the field of electromagnetism.

where $\sigma$ is the conductivity of the material. Then, the macroscopic Maxwell equations can be written as

$$\boldsymbol{\nabla}\cdot\boldsymbol{E}=\frac{\varrho_f+\varrho_b}{\varepsilon_0}=\frac{\varrho_f}{\varepsilon_0}-\frac{\boldsymbol{\nabla}\cdot\boldsymbol{P}}{\varepsilon_0},\tag{2.1.4a}$$

$$\boldsymbol{\nabla}\cdot\boldsymbol{B}=0,\tag{2.1.4b}$$

$$\boldsymbol{\nabla}\times\boldsymbol{E}=-\frac{\partial\boldsymbol{B}}{\partial t},\tag{2.1.4c}$$

$$\begin{aligned}\boldsymbol{\nabla}\times\boldsymbol{B}&=\mu_0\left(\boldsymbol{J}_f+\boldsymbol{J}_m+\boldsymbol{J}_b+\varepsilon_0\frac{\partial\boldsymbol{E}}{\partial t}\right)=\\&=\mu_0\left(\sigma\boldsymbol{E}+\boldsymbol{\nabla}\times\boldsymbol{M}+\frac{\partial\boldsymbol{P}}{\partial t}+\varepsilon_0\frac{\partial\boldsymbol{E}}{\partial t}\right),\end{aligned}\tag{2.1.4d}$$

where $\varepsilon_0$ and $\mu_0$ are vacuum permittivity and vacuum permeability. For the microscopic Maxwell equations we just set $\varrho_b=0$ and $\boldsymbol{J}_b=\boldsymbol{J}_m=0$. Origin of individual contributions in the Maxwell equations (2.1.4) can be well understood, but the shape is not very convenient for further operations. The response of the material can be also described through fields $\boldsymbol{D}$ and $\boldsymbol{H}$, where their constitutive relations are

$$\boldsymbol{D}=\varepsilon_0\boldsymbol{E}+\boldsymbol{P}=\varepsilon_0\varepsilon_r\boldsymbol{E},\tag{2.1.5a}$$

$$\boldsymbol{H}=\frac{1}{\mu_0}\boldsymbol{B}-\boldsymbol{M}=\frac{1}{\mu_0\mu_r}\boldsymbol{B},\tag{2.1.5b}$$

with $\varepsilon_r$ as relative permittivity and $\mu_r$ as relative permeability. From our point of view it is more suitable to stay with fields $\boldsymbol{E}$ and $\boldsymbol{B}$ and use $\varepsilon_r$, $\mu_r$ and $\sigma$ to describe response of the material[2], where we limit ourselves to homogenous materials and linear optics. For anisotropic materials $\boldsymbol{\varepsilon_r}$, $\boldsymbol{\mu_r}$ and $\boldsymbol{\sigma}$ are in a form of the second rank $3\times3$ tensor. Now, we can write Maxwell's equations as

$$\boldsymbol{\nabla}\cdot(\boldsymbol{\varepsilon_r}\boldsymbol{E})=\frac{\varrho_f}{\varepsilon_0},\tag{2.1.6a}$$

$$\boldsymbol{\nabla}\cdot\boldsymbol{B}=0,\tag{2.1.6b}$$

$$\boldsymbol{\nabla}\times\boldsymbol{E}=-\frac{\partial\boldsymbol{B}}{\partial t},\tag{2.1.6c}$$

$$\boldsymbol{\nabla}\times\boldsymbol{B}=\mu_0\boldsymbol{\mu_r}\boldsymbol{\sigma}\boldsymbol{E}+\mu_0\boldsymbol{\mu_r}\varepsilon_0\boldsymbol{\varepsilon_r}\frac{\partial\boldsymbol{E}}{\partial t}.\tag{2.1.6d}$$

By comparison of the Maxwell equations (2.1.6) with the Maxwell equations (2.1.4), one can get a grasp of what all is described by the relative permittivity $\boldsymbol{\varepsilon_r}$ and relative permeability $\boldsymbol{\mu_r}$.

---

[2] Note that $\boldsymbol{E}$ and $\boldsymbol{B}$ are the "real" fields that can be measured using charged particle, whereas fields $\boldsymbol{D}$ and $\boldsymbol{H}$ are only used for macroscopic description of matter, but from microscopic point of view they can't be defined.

Important result that stems from the Maxwell equations are the boundary conditions that describes continuity of the fields $\boldsymbol{E}$ and $\boldsymbol{B}$ through the interface.

$$\varepsilon_0 \left(\boldsymbol{\varepsilon}_r^{(1)} \boldsymbol{E}^{(1)} - \boldsymbol{\varepsilon}_r^{(2)} \boldsymbol{E}^{(2)}\right) \cdot \hat{\boldsymbol{n}} = q_i, \qquad \left(\boldsymbol{B}^{(1)} - \boldsymbol{B}^{(2)}\right) \cdot \hat{\boldsymbol{n}} = 0 \tag{2.1.7a}$$

$$\left(\boldsymbol{E}^{(1)} - \boldsymbol{E}^{(2)}\right) \times \hat{\boldsymbol{n}} = 0, \qquad \frac{1}{\mu_0}\left(\frac{\boldsymbol{B}^{(1)}}{\boldsymbol{\mu}_r^{(1)}} - \frac{\boldsymbol{B}^{(2)}}{\boldsymbol{\mu}_r^{(2)}}\right) \times \hat{\boldsymbol{n}} = \boldsymbol{J}_f \tag{2.1.7b}$$

with $\hat{\boldsymbol{n}}$ as normal unit vector of the interface. Superscript (1) and (2) refers to the two different materials that are forming the interface, respectively. Further, $q_i$ is the charge at the interface and $\boldsymbol{J}_f$ is the current density at the interface. Thus, we can see that normal component of the field $\boldsymbol{\varepsilon}_r \boldsymbol{E}$ (if the interface is not charged) and $\boldsymbol{B}$ does not change through the interface. Further, tangential components of the fields $\boldsymbol{E}$ and $\boldsymbol{B}/\boldsymbol{\mu}_r$ (if there is no current through the interface) are continuous through the interface. Note that the boundary conditions are the core of formalism that describes the EM wave propagation through the multilayer system.

### 2.1.2 Wave equation for anisotropic media

In our work we are interested in the response of the material to the monochromatic EM wave with electric and magnetic fields in a form

$$\boldsymbol{E}(\omega, \boldsymbol{k}) = \boldsymbol{E}_0 \exp\big\{-i\left(\omega t - \boldsymbol{k} \cdot \boldsymbol{r}\right)\big\}, \tag{2.1.8a}$$

$$\boldsymbol{B}(\omega, \boldsymbol{k}) = \boldsymbol{B}_0 \exp\big\{-i\left(\omega t - \boldsymbol{k} \cdot \boldsymbol{r}\right)\big\}, \tag{2.1.8b}$$

with $i$ as imaginary unit, $\omega$ as radial frequency of the wave, $\boldsymbol{k}$ as its wave vector and $\boldsymbol{E}_0$, $\boldsymbol{B}_0$ as the amplitude of the electric, magnetic field of the wave, respectively. This is EM wave in phasor notation[3]. As $\boldsymbol{E}$ and $\boldsymbol{B}$ are functions of $\omega$, the relative permittivity $\boldsymbol{\varepsilon_r}$, relative permeability $\boldsymbol{\mu_r}$ and conductivity $\boldsymbol{\sigma}$ are also treated as functions of $\omega$ [33].

$$\boldsymbol{\varepsilon_r} \rightarrow \boldsymbol{\varepsilon_r}(\omega), \qquad \boldsymbol{\mu_r} \rightarrow \boldsymbol{\mu_r}(\omega), \qquad \boldsymbol{\sigma} \rightarrow \boldsymbol{\sigma}(\omega). \tag{2.1.9}$$

Further, in the range of optical frequencies we can set $\boldsymbol{\mu_r} = \mathbf{1}$ as magnetic dipoles in the material can not follow such a vastly oscillating magnetic field of an EM wave.

Now, we will yield the wave equation of EM waves in anisotropic media. Taking the curl of Eq. (2.1.6c) and then rewriting its right side with use of Eq. (2.1.6d) providing

---

[3] The EM wave $\boldsymbol{E} = \boldsymbol{E}_0 \cos\left(\omega t - \boldsymbol{k} \cdot \boldsymbol{r}\right)$ can be equivalently written with use of Euler's formula as $\boldsymbol{E} = \boldsymbol{E}_0/2\left[e^{i(\omega t - \boldsymbol{k}\cdot\boldsymbol{r})} + e^{-i(\omega t - \boldsymbol{k}\cdot\boldsymbol{r})}\right]$. For linear systems one of the complex conjugate can be discarded. Note that our choice here will determine the sign convention with all complex variables used in optics. Although it is not a strictly followed rule, usually physicist in optics use convention $e^{-i(\omega t - \boldsymbol{k}\cdot\boldsymbol{r})}$.

us with

$$\boldsymbol{\nabla} \times (\boldsymbol{\nabla} \times \boldsymbol{E}) = -\mu_0 \boldsymbol{\sigma} \frac{\partial \boldsymbol{E}}{\partial t} - \mu_0 \varepsilon_0 \boldsymbol{\varepsilon_r} \frac{\partial^2 \boldsymbol{E}}{\partial t^2}. \tag{2.1.10}$$

Because we assume $\boldsymbol{E}$ to be in a form of Eq. (2.1.8a)

$$\boldsymbol{\nabla} \times \boldsymbol{E} = i\boldsymbol{k} \times \boldsymbol{E}, \tag{2.1.11}$$

$$\frac{\partial \boldsymbol{E}}{\partial t} = -i\omega \boldsymbol{E}. \tag{2.1.12}$$

Then, the Eq. (2.1.10) become[4]

$$\boldsymbol{k} \times (\boldsymbol{k} \times \boldsymbol{E}) - \frac{\omega^2}{c^2} \left( \boldsymbol{\varepsilon_r} + i \frac{\boldsymbol{\sigma}}{\varepsilon_0 \omega} \right) \boldsymbol{E} = 0. \tag{2.1.13}$$

Here the complex permittivity tensor $\hat{\boldsymbol{\varepsilon}}$ is defined.

$$\hat{\boldsymbol{\varepsilon}} = \left( \boldsymbol{\varepsilon_r} + i \frac{\boldsymbol{\sigma}}{\varepsilon_0 \omega} \right) = \begin{bmatrix} \varepsilon_{r,xx} + \frac{i}{\varepsilon_0 \omega} \sigma_{xx} & \varepsilon_{r,xy} + \frac{i}{\varepsilon_0 \omega} \sigma_{xy} & \varepsilon_{r,xz} + \frac{i}{\varepsilon_0 \omega} \sigma_{xz} \\ \varepsilon_{r,yx} + \frac{i}{\varepsilon_0 \omega} \sigma_{yx} & \varepsilon_{r,yy} + \frac{i}{\varepsilon_0 \omega} \sigma_{yy} & \varepsilon_{r,yz} + \frac{i}{\varepsilon_0 \omega} \sigma_{yz} \\ \varepsilon_{r,zx} + \frac{i}{\varepsilon_0 \omega} \sigma_{zx} & \varepsilon_{r,zy} + \frac{i}{\varepsilon_0 \omega} \sigma_{zy} & \varepsilon_{r,zz} + \frac{i}{\varepsilon_0 \omega} \sigma_{zz} \end{bmatrix}. \tag{2.1.14}$$

Now we can rewrite Eq. (2.1.13) in the matrix form as

$$\begin{bmatrix} k_y^2 + k_z^2 - \frac{\omega^2}{c^2} \hat{\varepsilon}_{xx} & -k_x k_y - \frac{\omega^2}{c^2} \hat{\varepsilon}_{xy} & -k_x k_z - \frac{\omega^2}{c^2} \hat{\varepsilon}_{xz} \\ -k_y k_x - \frac{\omega^2}{c^2} \hat{\varepsilon}_{yx} & k_z^2 + k_x^2 - \frac{\omega^2}{c^2} \hat{\varepsilon}_{yy} & -k_y k_z - \frac{\omega^2}{c^2} \hat{\varepsilon}_{yz} \\ -k_z k_x - \frac{\omega^2}{c^2} \hat{\varepsilon}_{zx} & -k_z k_y - \frac{\omega^2}{c^2} \hat{\varepsilon}_{zy} & k_x^2 + k_y^2 - \frac{\omega^2}{c^2} \hat{\varepsilon}_{zz} \end{bmatrix} \cdot \begin{bmatrix} E_{0x} \\ E_{0y} \\ E_{0z} \end{bmatrix} = 0. \tag{2.1.15}$$

Equation (2.1.15) is the Helmholtz form of wave equation for anisotropic material described by complex permittivity tensor $\hat{\boldsymbol{\varepsilon}}$. If we would consider isotropic case, i.e. $\boldsymbol{\varepsilon} = \varepsilon \mathbf{1}$, where $\mathbf{1}$ is identity matrix, and we would forbid charging of the material, i.e. $\boldsymbol{\nabla} \cdot \boldsymbol{E} = i(k_x E_x + k_y E_y + k_z E_z) = 0$, we will end up with

$$\nabla^2 \boldsymbol{E} - \frac{1}{c^2} \left( \varepsilon_r + i \frac{\sigma}{\varepsilon_0 \omega} \right) \frac{\partial^2 \boldsymbol{E}}{\partial t^2} = 0, \tag{2.1.16}$$

which is the familiar shape of wave equation of EM wave in isotropic materials.

---

[4] The vacuum permittivity and vacuum permeability are connected through speed of light $c$ as $1/(\varepsilon_0 \mu_0) = c^2$.

## 2.2 Permittivity tensor of a magnetized crystal

### 2.2.1 Complex permittivity, complex conductivity

During derivation of wave equation we defined complex permittivity tensor $\hat{\boldsymbol{\varepsilon}}$ as

$$\hat{\boldsymbol{\varepsilon}} = \left(\boldsymbol{\varepsilon_r} + i\frac{\boldsymbol{\sigma}}{\varepsilon_0\omega}\right) \tag{2.2.1}$$

However, through a similar way complex conductivity tensor can be defined.

$$\hat{\boldsymbol{\sigma}} = \boldsymbol{\sigma} - i\omega\varepsilon_0\boldsymbol{\varepsilon_r}\,. \tag{2.2.2}$$

From Eq. (2.2.1) and Eq. (2.2.2) we can see that complex permittivity and complex conductivity are interchangeable through relation

$$\hat{\boldsymbol{\varepsilon}} = i\frac{\hat{\boldsymbol{\sigma}}}{\varepsilon_0\omega}\,. \tag{2.2.3}$$

Now, we would like to address possible source of confusion connected within this nomenclature. Relative permittivity $\boldsymbol{\varepsilon_r}$ and conductivity $\boldsymbol{\sigma}$ are both purely real variables. The fact that we bind those two variables into the single complex variable is only our construct that is advantageous within our models using phasor notation of EM wave. As this is so widely adopted, the denomination of complex conductivity and permittivity with hat (ˆ) above is very rarely used. If this is further combined with denomination $\boldsymbol{\varepsilon} = \varepsilon_0\boldsymbol{\varepsilon_r}$, that is also sometimes used, Eqs.(2.2.1–2.2.3) could become confusing for the reader that is not well familiar with the use of complex valued permittivity or conductivity and the idea which of the permittivity and conductivity in the equations above is of real nature and which is of complex nature can easily jumble up.

Nevertheless, in optics where EM fields are treated according to Eq. (2.1.8), permittivity $\boldsymbol{\varepsilon}$ and conductivity $\boldsymbol{\sigma}$ are always understood as complex variables according to Eq. (2.2.1) and Eq. (2.2.2), respectively. Thus, we will as well restrain from denomination using a hat (ˆ), and from now onwards $\boldsymbol{\varepsilon} = \hat{\boldsymbol{\varepsilon}}$ and $\boldsymbol{\sigma} = \hat{\boldsymbol{\sigma}}$. Further, Eq. (2.2.3) is sometimes used as $\boldsymbol{\varepsilon} = \mathbf{1} + i\boldsymbol{\sigma}/(\varepsilon_0\omega)$. This is due to complex conductivity imaginary part, that is sometimes defined through electric susceptibility and not through relative permittivity. Finally, note that several different denominations for real and imaginary part of $\boldsymbol{\varepsilon}$ do exist, e.g. $\boldsymbol{\varepsilon} = \boldsymbol{\varepsilon}_1 + \boldsymbol{\varepsilon}_2$, or $\boldsymbol{\varepsilon} = \boldsymbol{\varepsilon}' + \boldsymbol{\varepsilon}''$, or $\boldsymbol{\varepsilon} = \boldsymbol{\varepsilon}_R + \boldsymbol{\varepsilon}_I$. In our case we will use very obvious denomination

$$\boldsymbol{\varepsilon} = \mathrm{Re}\{\boldsymbol{\varepsilon}\} + \mathrm{Im}\{\boldsymbol{\varepsilon}\}. \tag{2.2.4}$$

One more thing should be mention concerning the complex nature of the permittivity. The real and imaginary part of $\boldsymbol{\varepsilon}$ may seem unrelated at single photon energy, but from spectral point of view they are binded by so called Kramers-Kronig relations.

$$\mathrm{Re}\{\varepsilon_{ij}(\omega)\} = \delta_{ij} + \frac{2}{\pi}\mathrm{V.P.}\int_0^\infty \frac{\omega'\,\mathrm{Im}\{\varepsilon_{ij}(\omega')\}}{\omega'^2 - \omega^2}\,\mathrm{d}\omega'\,, \tag{2.2.5a}$$

$$\mathrm{Im}\{\varepsilon_{ij}(\omega)\} = -\frac{2\omega}{\pi}\mathrm{V.P.}\int_0^\infty \frac{\mathrm{Re}\{\varepsilon_{ij}(\omega')\}}{\omega'^2 - \omega^2}\,\mathrm{d}\omega'\,, \tag{2.2.5b}$$

where $\varepsilon_{ij}$ are the elements of the permittivity tensor $\boldsymbol{\varepsilon}$, V.P. stands for Cauchy principal value and $\delta_{ij}$ is Kronecker delta. Hence, the real (imaginary) value of the $\varepsilon_{ij}$ at photon energy $\hbar\omega$ can be computed from full spectral dependence of imaginary (real) part of $\varepsilon_{ij}$. Nevertheless, in the experiment we measure just limited part of the spectral dependence, and thus, the Kramers-Kronig relations have rather limited use here and must be used with care.[5] On contrary, Kramers-Kronig relations are heavily used in the ab-initio calculations, where they substantially speed up the calculations.

### 2.2.2 Magnetooptic tensors

The shape of the permittivity tensor stems from the crystallographic structure of the material. The triclinic crystal system do have all 9 elements of the permittivity tensor non-zero whit single symmetry $\varepsilon_{ij} = \varepsilon_{ji}$. In contrary, the cubic crystal structure has permittivity tensor described through single scalar as $\varepsilon_d \cdot \mathbf{1}$ with $\mathbf{1}$ as identity matrix.

The shape of the permittivity tensor $\boldsymbol{\varepsilon}$ can be further altered by magnetization of the material[6], being the origin of MOKE from phenomenological point of view. Permittivity tensor of magnetized specimen can be described by McLaurin power series [30, 33] as

$$\begin{aligned}\varepsilon_{ij} &= \varepsilon_{ij}^{(0)} + \left[\frac{\partial\varepsilon_{ij}}{\partial M_k}\right]_{\boldsymbol{M}=0} M_k + \frac{1}{2}\left[\frac{\partial^2\varepsilon_{ij}}{\partial M_k M_l}\right]_{\boldsymbol{M}=0} M_k M_l + \ldots \\ &= \varepsilon_{ij}^{(0)} + \underbrace{K_{ijk}M_k}_{\varepsilon_{ij}^{(1)}} + \underbrace{G_{ijkl}M_kM_l}_{\varepsilon_{ij}^{(2)}} + \ldots\end{aligned} \tag{2.2.6}$$

where $M_k$ and $M_l$ are components of the normalized magnetization $\boldsymbol{M}$. $K_{ijk}$ and $G_{ijkl}$ are the components of the so-called linear and quadratic MO tensors $\boldsymbol{K}$ and $\boldsymbol{G}$, which are 3×3 tensors of third rank and fourth rank, respectively. Einstein summation convention

---

[5] We can use them to some extent during data processing, e.g. in B-spline method. Also, if in the measured spectral range the imaginary part of the spectra will posses strong peaks, but real part of the spectra will be completely flat, something is obviously wrong.

[6] The shape of the permittivity tensor can be further altered by others perturbations, e.g. stress, but we do not consider these other effects in this work.

is used within Eq. (2.2.6). The general shape of those tensors is ($x$,$y$,$z$ = 1,2,3):

$$\boldsymbol{\varepsilon}^{(0)} = \begin{bmatrix} \varepsilon_{11}^{(0)} & \varepsilon_{12}^{(0)} & \varepsilon_{13}^{(0)} \\ \varepsilon_{21}^{(0)} & \varepsilon_{22}^{(0)} & \varepsilon_{23}^{(0)} \\ \varepsilon_{31}^{(0)} & \varepsilon_{32}^{(0)} & \varepsilon_{33}^{(0)} \end{bmatrix}, \tag{2.2.7}$$

$$\begin{bmatrix} \varepsilon_{11}^{(1)} \\ \varepsilon_{22}^{(1)} \\ \varepsilon_{33}^{(1)} \\ -- \\ \varepsilon_{12}^{(1)} \\ \varepsilon_{13}^{(1)} \\ \varepsilon_{23}^{(1)} \\ -- \\ \varepsilon_{21}^{(1)} \\ \varepsilon_{31}^{(1)} \\ \varepsilon_{32}^{(1)} \end{bmatrix} = \begin{bmatrix} K_{111} & K_{112} & K_{113} \\ K_{221} & K_{222} & K_{223} \\ K_{331} & K_{332} & K_{333} \\ -- & -- & -- \\ K_{121} & K_{122} & K_{123} \\ K_{131} & K_{132} & K_{133} \\ K_{231} & K_{232} & K_{233} \\ -- & -- & -- \\ K_{211} & K_{212} & K_{213} \\ K_{311} & K_{312} & K_{313} \\ K_{321} & K_{322} & K_{323} \end{bmatrix} \begin{bmatrix} M_1 \\ M_2 \\ M_3 \end{bmatrix}, \tag{2.2.8}$$

$$\begin{bmatrix} \varepsilon_{11}^{(2)} \\ \varepsilon_{22}^{(2)} \\ \varepsilon_{33}^{(2)} \\ -- \\ \varepsilon_{12}^{(2)} \\ \varepsilon_{13}^{(2)} \\ \varepsilon_{23}^{(2)} \\ -- \\ \varepsilon_{21}^{(2)} \\ \varepsilon_{31}^{(2)} \\ \varepsilon_{32}^{(2)} \end{bmatrix} = \begin{bmatrix} G_{1111} & G_{1122} & G_{1133} & | & G_{1112} & G_{1113} & G_{1123} & | & G_{1121} & G_{1131} & G_{1132} \\ G_{2211} & G_{2222} & G_{2233} & | & G_{2212} & G_{2213} & G_{2223} & | & G_{2221} & G_{2231} & G_{2232} \\ G_{3311} & G_{3322} & G_{3333} & | & G_{3312} & G_{3313} & G_{3323} & | & G_{3321} & G_{3331} & G_{3332} \\ -- & -- & -- & & -- & -- & -- & & -- & -- & -- \\ G_{1211} & G_{1222} & G_{1233} & | & G_{1212} & G_{1213} & G_{1223} & | & G_{1221} & G_{1231} & G_{1232} \\ G_{1311} & G_{1322} & G_{1333} & | & G_{1312} & G_{1313} & G_{1323} & | & G_{1321} & G_{1331} & G_{1332} \\ G_{2311} & G_{2322} & G_{2333} & | & G_{2312} & G_{2313} & G_{2323} & | & G_{2321} & G_{2331} & G_{2332} \\ -- & -- & -- & & -- & -- & -- & & -- & -- & -- \\ G_{2111} & G_{2122} & G_{2133} & | & G_{2112} & G_{2113} & G_{2123} & | & G_{2121} & G_{2131} & G_{2132} \\ G_{3111} & G_{3122} & G_{3133} & | & G_{3112} & G_{3113} & G_{3123} & | & G_{3121} & G_{3131} & G_{3132} \\ G_{3211} & G_{3222} & G_{3233} & | & G_{3212} & G_{3213} & G_{3223} & | & G_{3221} & G_{3231} & G_{3232} \end{bmatrix} \begin{bmatrix} M_1^2 \\ M_2^2 \\ M_3^2 \\ -- \\ M_1M_2 \\ M_1M_3 \\ M_2M_3 \\ -- \\ M_2M_1 \\ M_3M_1 \\ M_3M_2 \end{bmatrix}. \tag{2.2.9}$$

Note that the rank and dimensions of the MO tensors $\boldsymbol{K}$ and $\boldsymbol{G}$ are given through the way they construct contributions $\boldsymbol{\varepsilon}^{(1)}$ and $\boldsymbol{\varepsilon}^{(2)}$ to the permittivity tensor $\boldsymbol{\varepsilon}$ with the magnetization $\boldsymbol{M}$ (3×1 tensor of first rank, i.e. vector) and square of magnetization $\boldsymbol{M}^2$ (3×3 tensor of the second rank), respectively. We recall that $M_1$, $M_2$, $M_3$ are magnetization directions with respect to Cartesian coordinate system and not with respect to the crystallographic axes of the material. For details on our coordinate system, see

Appendix A.

### 2.2.3 Permittivity tensor of a cubic crystal structure

The most general shapes of the MO tensors introduced above can be substantially simplified through Onsager relation

$$\varepsilon_{ij}\left(\boldsymbol{M}\right) = \varepsilon_{ji}\left(-\boldsymbol{M}\right), \tag{2.2.10}$$

which enforce condition

$$\varepsilon_{ij}^{(1)} = K_{ijk}M_k = -K_{jik}M_k = -\varepsilon_{ji}^{(1)} \tag{2.2.11}$$

on the permittivity tensor $\boldsymbol{\varepsilon}^{(1)}$, wherefrom $K_{iik} = 0$ and $K_{ijk} = -K_{jik}$. Further, permittivity tensor $\boldsymbol{\varepsilon}^{(2)}$ must follow the condition

$$\varepsilon_{ij}^{(2)} = G_{ijkl}M_kM_l = G_{jikl}(-M_k)(-M_l) = \varepsilon_{ji}^{(2)}, \tag{2.2.12}$$

wherefrom $G_{ijkl} = G_{jikl} = G_{ijlk} = G_{jilk}$ [30, 33]. Those restriction provided by Onsager's relation are valid within all crystallographic classes, but there are further restrictions on the shape of those tensors, that are given by the symmetry arguments of the crystal. In this work we examine only cubic crystal structures (crystal classes 432, $\bar{4}3m$ and $m3m$). The symmetry arguments of those classes together with Onsager relation then provide following shape of tensors $\boldsymbol{\varepsilon}^{(0)}$, $\boldsymbol{K}$ and $\boldsymbol{G}$ (in the case when cubic crystal axes are aligned with axes of Cartesian coordinate system $xyz$):

$$\boldsymbol{\varepsilon}^{(0)} = \begin{bmatrix} \varepsilon_d & 0 & 0 \\ 0 & \varepsilon_d & 0 \\ 0 & 0 & \varepsilon_d \end{bmatrix}, \tag{2.2.13}$$

$$\begin{bmatrix} \varepsilon_{12}^{(1)} \\ \varepsilon_{13}^{(1)} \\ \varepsilon_{23}^{(1)} \\ -- \\ \varepsilon_{21}^{(1)} \\ \varepsilon_{31}^{(1)} \\ \varepsilon_{32}^{(1)} \end{bmatrix} = \begin{bmatrix} 0 & 0 & K_{123} \\ 0 & -K_{123} & 0 \\ K_{123} & 0 & 0 \\ -- & -- & -- \\ 0 & 0 & -K_{123} \\ 0 & K_{123} & 0 \\ -K_{123} & 0 & 0 \end{bmatrix} \begin{bmatrix} M_1 \\ M_2 \\ M_3 \end{bmatrix}, \tag{2.2.14}$$

$$\begin{bmatrix} \varepsilon_{11}^{(2)} \\ \varepsilon_{22}^{(2)} \\ \varepsilon_{33}^{(2)} \\ -- \\ \varepsilon_{12}^{(2)} \\ \varepsilon_{13}^{(2)} \\ \varepsilon_{23}^{(2)} \end{bmatrix} = \begin{bmatrix} G_{1111} & G_{1122} & G_{1122} & | & 0 & 0 & 0 \\ G_{1122} & G_{1111} & G_{1122} & | & 0 & 0 & 0 \\ G_{1122} & G_{1122} & G_{1111} & | & 0 & 0 & 0 \\ -- & -- & -- & & -- & -- & -- \\ 0 & 0 & 0 & | & 2G_{2323} & 0 & 0 \\ 0 & 0 & 0 & | & 0 & 2G_{2323} & 0 \\ 0 & 0 & 0 & | & 0 & 0 & 2G_{2323} \end{bmatrix} \begin{bmatrix} M_1^2 \\ M_2^2 \\ M_3^2 \\ -- \\ M_1 M_2 \\ M_1 M_3 \\ M_2 M_3 \end{bmatrix}. \tag{2.2.15}$$

Thus, we can see that for cubic systems permittivity $\boldsymbol{\varepsilon}^{(0)}$ is defined by scalar $\varepsilon_d$ and identity matrix $\mathbf{1}$. Linear MO tensor $\boldsymbol{K}$ is defined through one free parameter $K_{123} = K$ and quadratic MO tensor $\boldsymbol{G}$ is defined by $G_{1111} = G_{11}$, $G_{1122} = G_{12}$ and $2G_{2323} = 2G_{44}$. The Eqs.(2.2.13–2.2.15) are described more concisely as

$$\varepsilon_{ij}^{(0)} = \delta_{ij}\varepsilon_d, \tag{2.2.16a}$$

$$K_{ijk} = \epsilon_{ijk} K, \tag{2.2.16b}$$

$$G_{iiii} = G_{11}, \tag{2.2.16c}$$

$$G_{iijj} = G_{12}, \qquad i \neq j, \tag{2.2.16d}$$

$$G_{1212} = G_{1313} = G_{2323} = G_{44}, \tag{2.2.16e}$$

where $\delta_{ij}$ is Kronecker delta function and $\epsilon_{ijk}$ is Levi-Civita symbol. Further, $G_{11}$ and $G_{12}$ always contribute to MOKE signal in a form of their difference $G_s = G_{11} - G_{12}$. The parameter $\Delta G = G_s - 2G_{44}$ then describes anisotropy strength of the quadratic MO tensor $\boldsymbol{G}$ of cubic crystal structure [38].

### 2.2.4 Permittivity tensor with misaligned axes

So far, we described permittivity tensor $\boldsymbol{\varepsilon}$ of cubic crystal structures up to second order in magnetization, but only for the case when crystallographic axes are align with axes of Cartesian coordinate system $xyz$. Now, we need to extend this description for cubic crystal structure with general orientation in our coordinate system $xyz$. Such a permittivity tensor will be described as

$$\varepsilon'_{ij} = \varepsilon_{ij}^{(0)\prime} + K'_{ijk} M_k + G'_{ijkl} M_k M_l, \tag{2.2.17}$$

where

$$\varepsilon_{ij}^{(0)\prime} = a_{im} a_{jn} \varepsilon_{mn}^{(0)}, \tag{2.2.18a}$$

$$K'_{ijk} = a_{im} a_{jn} a_{ko} K_{mno}, \tag{2.2.18b}$$

$$G'_{ijkl} = a_{im} a_{jn} a_{ko} a_{lp} G_{mnop}. \tag{2.2.18c}$$

Here $a_{\nu,\omega}(\nu,\omega = x,y,z)$ are elements of 3×3 matrix $\boldsymbol{a}$ which represent the Cartesian vector transformations and can be expressed as product of three rotation matrixes

$$\boldsymbol{a} = \begin{bmatrix} \cos\vartheta_z & -\sin\vartheta_z & 0 \\ \sin\vartheta_z & \cos\vartheta_z & 0 \\ 0 & 0 & 1 \end{bmatrix} \begin{bmatrix} \cos\vartheta_y & 0 & \sin\vartheta_y \\ 0 & 1 & 0 \\ -\sin\vartheta_y & 0 & \cos\vartheta_y \end{bmatrix} \begin{bmatrix} 1 & 0 & 0 \\ 0 & \cos\vartheta_x & -\sin\vartheta_x \\ 0 & \sin\vartheta_x & \cos\vartheta_x \end{bmatrix}, \tag{2.2.19}$$

representing the rotation around $x, y, z$ axis of our coordinate system by angle $\vartheta_x, \vartheta_y, \vartheta_z$, respectively and strictly in that order. Thus, through $\boldsymbol{\varepsilon}'$ we can fully describe permittivity of cubic crystal structure with arbitrary orientation and up to second order in magnetization. Note that only quadratic MO tensor $\boldsymbol{G}$ is anisotropic here, i.e. it will change its shape upon transformation described by Eq. (2.2.18c). In contrary, $\boldsymbol{\varepsilon}^{(0)}$ and linear MO tensor $\boldsymbol{K}$ are isotropic and will not be affected by transformations described by Eq. (2.2.18a) and Eq. (2.2.18b), respectively. Nevertheless, with other crystal structures this may no longer hold true.

## 2.3 Propagation of electromagnetic waves in an anisotropic planar multilayer structure

The description of the Yeh's formalism in this section is inspired by Ref. [33]. Further, to prevent any confusion, we emphasise that upper index in the bracket denote here the position of the layer in the multilayer stack and not the order in $\boldsymbol{M}$. We will hold this nomenclature only through this single section.

Now, let's consider the case of a planar multilayer structure composed of $\mathcal{N}$ layers that are sandwiched between two halfspaces as sketched in Fig. 2.1. For our purpose, we will treat upper half space (0) as air, while the lower half space $(\mathcal{N}+1)$ is the substrate at which our multilayer stack has grown. Note that if the backside of the substrate would be polished and hence specular reflection would occur at the lower interface of the substrate, we couldn't treat the substrate as the semi-infinite halfspace, but as another (but thick) layer, where incoherent propagation of light occurs.[7] The theory on how to deal with

---

[7] The decision if the layer is thin or thick is actually made by the coherency of the probing light.

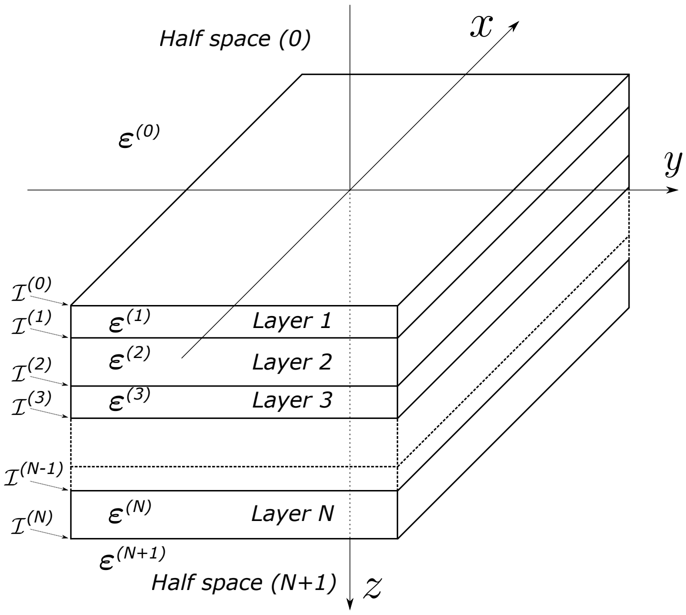

FIGURE 2.1: Sketch of a multilayer stack composed from the $\mathcal{N}$ layers and sandwiched between two semi-infinite half-spaces. The positive direction of $z$ axis, and thus positive direction of EM wave propagation, is downwards. The drawing is inspired by drawing in Ref. [33]

presence of optically thick layers in the multilayer stack is well explained in Ref. [103], but as this is not the case of any samples studied in this work the semi-infinite halfspace $(\mathcal{N}+1)$ can be safely described by the properties of the substrate.

The idea behind this formalism is as follow. We will solve wave equation (2.1.15) for each layer of the multilayer stack and its half-spaces. This will provide us with four solutions, i.e. four EM waves for each layer. One set of two waves is propagating upwards in the layer and other set of two waves is propagating downwards in the layer (with respect to $z$ direction). Those two waves of each set create a basis for arbitrary polarization state of light, i.e. they are proper polarization modes for the given medium. For case of isotropic, non-absorbing meterial (such as air – the upper halfspace), any set of two orthogonal polarization modes will do. For our purpose it is advantageous to chose $s$- and $p$- polarizations as the proper polarization modes for the upper halfspace (as in our experiments one of those polarization states is used to probe the sample). But in the $n$-th layer of the multilayer stack, where permittivity could be of general shape, the set of upwards or downwards propagating waves will be described by two orthogonal eigenmodes of general elliptical polarization. Their exact shape must be found from wave equation (2.1.15) and will be dependent on crystallographic anisotropy, direction of magnetization inside the layer and the angle of incidence (AoI) of EM wave on the multilayer stack. Then, we can describe propagation of the arbitrary polarization state of light through this layer by decomposition of this polarization state into the layer's polarization eigenmodes. With the use of boundary conditions we can treat the EM waves at the interface $\mathcal{I}^{(n)}$ and continue with propagation in the subsequent layer.

### 2.3.1 Proper polarization modes in the $n$-th layer

Let's start with the solution of the wave equation [Eq. (2.1.15)] for the $n$-th layer of the multilayer stack. The $n$-th layer is bounded by its upper interface $\mathcal{I}^{(n-1)}$ and lower interface $\mathcal{I}^{(n)}$ and is characterized by its permittivity tensor $\boldsymbol{\varepsilon}^{(n)}$ and thickness $d^{(n)} = z(\mathcal{I}^{(n)}) - z(\mathcal{I}^{(n-1)})$. The propagation vector in the $n$-th layer is

$$\boldsymbol{k}^{(n)} = \left(k_x^{(n)}\hat{\boldsymbol{x}} + k_y^{(n)}\hat{\boldsymbol{y}} + k_z^{(n)}\hat{\boldsymbol{z}}\right) = \frac{\omega}{c}\left(N_x^{(n)}\hat{\boldsymbol{x}} + N_y^{(n)}\hat{\boldsymbol{y}} + N_z^{(n)}\hat{\boldsymbol{z}}\right), \tag{2.3.1}$$

where $N_x^{(n)}, N_y^{(n)}$ and $N_z^{(n)}$ can be understood as directional components of the propagation vector in the $n$-th layer and $\hat{\boldsymbol{x}}$, $\hat{\boldsymbol{y}}$, $\hat{\boldsymbol{z}}$ are cartesian unit vecotrs. From the Snell law (boundary conditions), the parallel and planar components of the propagation vector to the interface must be constant through all layers in the multilayer stack[8] (pay attention to the superscripts in the following equation)

$$\boldsymbol{k}^{(n)} \cdot \hat{\boldsymbol{x}} = \frac{\omega}{c} N_x^{(0)} \cdot \hat{\boldsymbol{x}}, \qquad \boldsymbol{k}^{(n)} \cdot \hat{\boldsymbol{y}} = \frac{\omega}{c} N_y^{(0)} \cdot \hat{\boldsymbol{y}}. \tag{2.3.2}$$

In a wisely chosen coordinate system, being $xyz$ cartesian coordinate system with $yz$ plane parallel to the plane of incidence (where $z$ is pointing into the multilayer structure and $y$ have the same direction and sign as $k_y$ component of the propagation vector of the incident light), we can set

$$N_x^{(n)} = 0, \qquad N_y^{(n)} = N_y = N^{(0)} \sin\left(\mathrm{AoI}\right), \tag{2.3.3}$$

As we already mention above, the upper half space (0) from where is EM wave incident on the multilayer structure is treated as air here and, thus, we can set $N_y^{(n)} = \sin\left(\mathrm{AoI}\right)$.[9] Now, we can write wave equation (2.1.15) for anisotropic material in the $n$-th layer of the multilayer structure as

$$\frac{\omega^2}{c^2} \underbrace{\begin{bmatrix} N_y^2 + N_z^{(n)2} - \varepsilon_{xx}^{(n)} & -\varepsilon_{xy}^{(n)} & -\varepsilon_{xz}^{(n)} \\ -\varepsilon_{yx}^{(n)} & N_z^{(n)2} - \varepsilon_{yy}^{(n)} & -N_y N_z^{(n)} - \varepsilon_{yz}^{(n)} \\ -\varepsilon_{zx}^{(n)} & -N_y N_z^{(n)} - \varepsilon_{zy}^{(n)} & N_y^2 - \varepsilon_{zz}^{(n)} \end{bmatrix}}_{\boldsymbol{W}^{(n)}} \cdot \underbrace{\begin{bmatrix} E_{0x}^{(n)} \\ E_{0y}^{(n)} \\ E_{0z}^{(n)} \end{bmatrix}}_{\boldsymbol{E}_0^{(n)}} = 0. \tag{2.3.4}$$

---

[8] Note that this condition will not be valid for the multilayer stack with wedge-like layers in it.

[9] In our numerical code exact value of index of refraction of air was used.

Here, only unknown to us is the directional component $N_z^{(n)}$ of the propagating vector. To obtain a nontrivial solution determinant of $\boldsymbol{W}^{(n)}$ must be equal to zero. This condition will in general lead to polynomial equation of 4th order with four roots of $N_z^{(n)} = N_{zj}^{(n)}$, $j = 1, ..., 4$ (two double roots for the case of isotropic material).

Now, we can solve Eq. (2.3.4) for each $N_{zj}^{(n)}$ by finding the null-space of the matrix $\boldsymbol{W}^{(n)}$, i.e. we are looking for such $\boldsymbol{E}_{0j}^{(n)} = E_{0j}^{(n)} \boldsymbol{e}_j^{(n)}$ that $\boldsymbol{W}_j^{(n)} \cdot \boldsymbol{E}_{0j}^{(n)} = 0$, with $\boldsymbol{e}_j^{(n)}$ as the $j$-th proper polarization eigenmode of the $n$-th layer and $E_{0j}^{(n)}$ as its amplitude. Each of those four proper polarization modes propagate through the $n$-th layer without change of polarization, but each with different phase speed and different attenuation. Further, we are adopting here a widely used convention that directional components $N_{z1}^{(n)}$ and $N_{z3}^{(n)}$ define the downwards propagating eigenmodes (i.e. positive direction of $z$), whereas $N_{z2}^{(n)}$ and $N_{z4}^{(n)}$ define the upwards propagating eigenmodes (i.e. negative direction of $z$)[10]

The electric field vector of EM wave in the $n$-th layer can be therefore described as

$$\boldsymbol{E}^{(n)} = \sum_{j=1}^{4} E_{0j}^{(n)} \boldsymbol{e}_j^{(n)} \exp\left\{ -i \left( \omega t - \frac{\omega}{c} \left[ N_y y + N_{zj}^{(n)} \left( z - z\left(\mathcal{I}^{(n)}\right)\right)\right]\right)\right\}. \tag{2.3.5}$$

To obtain magnetic field of the proper polarization modes, we can simply apply Faraday law from Maxwell's equations [i.e. Eq. (2.1.6c)].

$$c\boldsymbol{B}^{(n)} = \sum_{j=1}^{4} E_{0j}^{(n)} \boldsymbol{b}_j^{(n)} \exp\left\{ -i \left( \omega t - \frac{\omega}{c} \left[ N_y y + N_{zj}^{(n)} \left( z - z\left(\mathcal{I}^{(n)}\right)\right)\right]\right)\right\}, \tag{2.3.6}$$

where

$$\boldsymbol{b}_j^{(n)} = \left( N_y \hat{\boldsymbol{y}} + N_{zj}^{(n)} \hat{\boldsymbol{z}} \right) \times \boldsymbol{e}_j^{(n)}. \tag{2.3.7}$$

---

[10] When one is putting this formalism in use, the way how $N_{zj}$ are sorted is a crucial part of the numerical calculs and extra care must be taken in this step.

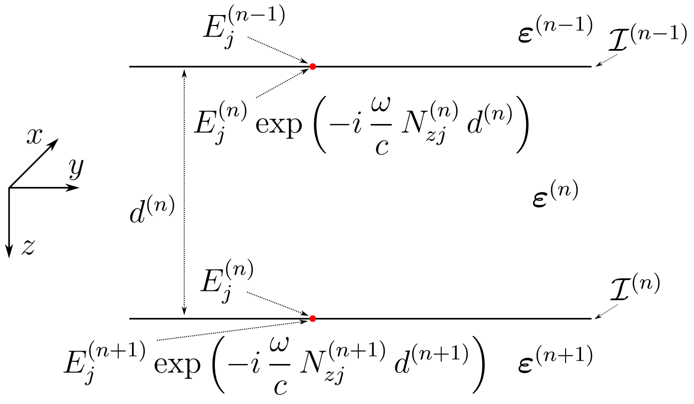

FIGURE 2.2: Sketch of the electric field amplitudes at the boundaries of the $n$-th layer.

### 2.3.2 Propagation through the whole multilayer stack - Yeh's formalism

From boundary conditions we know that the tangential field components must be continuous through the interface. Thus, at the interface $\mathcal{I}^{(n-1)}$

$$\sum_{j=1}^{4} E_{0j}^{(n-1)} \boldsymbol{e}_j^{(n-1)} \cdot \hat{\boldsymbol{x}} = \sum_{j=1}^{4} E_{0j}^{(n)} \boldsymbol{e}_j^{(n)} \cdot \hat{\boldsymbol{x}} \exp\left\{-i\frac{\omega}{c} N_{zj}^{(n)} d^{(n)}\right\}, \tag{2.3.8a}$$

$$\sum_{j=1}^{4} E_{0j}^{(n-1)} \boldsymbol{e}_j^{(n-1)} \cdot \hat{\boldsymbol{y}} = \sum_{j=1}^{4} E_{0j}^{(n)} \boldsymbol{e}_j^{(n)} \cdot \hat{\boldsymbol{y}} \exp\left\{-i\frac{\omega}{c} N_{zj}^{(n)} d^{(n)}\right\}, \tag{2.3.8b}$$

$$\sum_{j=1}^{4} E_{0j}^{(n-1)} \boldsymbol{b}_j^{(n-1)} \cdot \hat{\boldsymbol{x}} = \sum_{j=1}^{4} E_{0j}^{(n)} \boldsymbol{b}_j^{(n)} \cdot \hat{\boldsymbol{x}} \exp\left\{-i\frac{\omega}{c} N_{zj}^{(n)} d^{(n)}\right\}, \tag{2.3.8c}$$

$$\sum_{j=1}^{4} E_{0j}^{(n-1)} \boldsymbol{b}_j^{(n-1)} \cdot \hat{\boldsymbol{y}} = \sum_{j=1}^{4} E_{0j}^{(n)} \boldsymbol{b}_j^{(n)} \cdot \hat{\boldsymbol{y}} \exp\left\{-i\frac{\omega}{c} N_{zj}^{(n)} d^{(n)}\right\}. \tag{2.3.8d}$$

The tangential electric and magnetic fields of the wave in the layer $(n-1)$ at the interface $\mathcal{I}^{(n-1)}$ are equal to tangential electric and magnetic fields of the wave in the layer $(n)$ after propagation through the layer of thickness $d$ from interface $\mathcal{I}^{(n)}$ to interface $\mathcal{I}^{(n-1)}$.[11] The propagation of the $j$-th proper polarization mode through the $n$-th layer from interface $\mathcal{I}^{(n)}$ to interface $\mathcal{I}^{(n-1)}$ is described by the factor $\exp\left\{-i\frac{\omega}{c}N_{zj}^{(n)}d^{(n)}\right\}$. See the Fig. 2.2. The fact that in Eq. (2.3.8) the dependence on the position $z$ was substituted by the dependence on the layer thickness $d$ allow us to employ matrix formalism for description of EM wave propagation through the structure.

---

[11] Note that here our choice of time convention will play important role. We remind that we are using time convention $\exp\{-i\omega t\}$.

We can rewrite Eqs. (2.3.8)(a)-(d) as

$$\boldsymbol{D}^{(n-1)}\boldsymbol{E}_0^{(n-1)} = \boldsymbol{D}^{(n)}\boldsymbol{P}^{(n)}\boldsymbol{E}_0^{(n)}, \tag{2.3.9}$$

where

$$\boldsymbol{D}^{(n)} = \begin{bmatrix} \boldsymbol{e}_1^{(n)}\cdot\hat{\boldsymbol{x}} & \boldsymbol{e}_2^{(n)}\cdot\hat{\boldsymbol{x}} & \boldsymbol{e}_3^{(n)}\cdot\hat{\boldsymbol{x}} & \boldsymbol{e}_4^{(n)}\cdot\hat{\boldsymbol{x}} \\ \boldsymbol{b}_1^{(n)}\cdot\hat{\boldsymbol{y}} & \boldsymbol{b}_2^{(n)}\cdot\hat{\boldsymbol{y}} & \boldsymbol{b}_3^{(n)}\cdot\hat{\boldsymbol{y}} & \boldsymbol{b}_4^{(n)}\cdot\hat{\boldsymbol{y}} \\ \boldsymbol{e}_1^{(n)}\cdot\hat{\boldsymbol{x}} & \boldsymbol{e}_2^{(n)}\cdot\hat{\boldsymbol{x}} & \boldsymbol{e}_3^{(n)}\cdot\hat{\boldsymbol{x}} & \boldsymbol{e}_4^{(n)}\cdot\hat{\boldsymbol{x}} \\ \boldsymbol{b}_1^{(n)}\cdot\hat{\boldsymbol{y}} & \boldsymbol{b}_2^{(n)}\cdot\hat{\boldsymbol{y}} & \boldsymbol{b}_3^{(n)}\cdot\hat{\boldsymbol{y}} & \boldsymbol{b}_4^{(n)}\cdot\hat{\boldsymbol{y}} \end{bmatrix} \tag{2.3.10}$$

is so called 4 × 4 *dynamic matrix*,

$$\boldsymbol{P}^{(n)} = \begin{bmatrix} \exp\left\{-i\frac{\omega}{c}N_{z1}^{(n)}d^{(n)}\right\} & 0 & 0 & 0 \\ 0 & \exp\left\{-i\frac{\omega}{c}N_{z2}^{(n)}d^{(n)}\right\} & 0 & 0 \\ 0 & 0 & \exp\left\{-i\frac{\omega}{c}N_{z3}^{(n)}d^{(n)}\right\} & 0 \\ 0 & 0 & 0 & \exp\left\{-i\frac{\omega}{c}N_{z4}^{(n)}d^{(n)}\right\} \end{bmatrix} \tag{2.3.11}$$

is so called 4 × 4 *propagation diagonal matrix*, and

$$\boldsymbol{E}_0^{(n)} = \begin{bmatrix} E_{01}^{(n)} \\ E_{02}^{(n)} \\ E_{03}^{(n)} \\ E_{04}^{(n)} \end{bmatrix} \tag{2.3.12}$$

is four-component vector of the complex proper polarization amplitudes. Those matrixes were firstly introduced by Pochi Yeh [104]. The dynamical matrix serves us to relate amplitudes of the proper polarization modes from two adjacent layers, while propagation matrix describe propagation of proper polarization modes through the layer.

Then, we can bind proper polarization mode amplitudes from $(n-1)$-th layer at interface $\mathcal{I}^{(n-1)}$ with proper polarization mode amplitudes from $n$-th layer at interface $\mathcal{I}^{(n)}$ as

$$\boldsymbol{E}_0^{(n-1)} = \boldsymbol{T}^{(n-1,n)}\boldsymbol{E}_0^{(n)}, \tag{2.3.13}$$

where

$$\boldsymbol{T}^{(n-1,n)} = \left(\boldsymbol{D}^{(n-1)}\right)^{-1}\boldsymbol{D}^{(n)}\boldsymbol{P}^{(n)} \tag{2.3.14}$$

is so-called *transfer matrix.* This transfer matrix, that is describing the propagation from the $(n-1)$-th layer to the $n$-th layer, is the main building block of the Yeh's formalism. The propagation through the whole multilayer stack, i.e. relating the proper polarization mode amplitudes in upper half space (0) and lower halfspace $(\mathcal{N}+1)$, is described as

$$\boldsymbol{E}_0^{(0)} = \prod_{n=1}^{\mathcal{N}+1} \boldsymbol{T}^{(n-1,n)} \boldsymbol{E}_0^{(\mathcal{N}+1)} = \boldsymbol{M}\boldsymbol{E}_0^{(\mathcal{N}+1)} \tag{2.3.15}$$

where $\boldsymbol{M}$ is so-called *total matrix* of the whole multilayer structure. Note that if the multilayer stack would be reduced to single interface, i.e. $\mathcal{N}=0$, the total matrix $\boldsymbol{M}$ would be equal to transfer matrix $\boldsymbol{T}^{(0,1)}$ with its propagation matrix $\boldsymbol{P}=\mathbf{1}$, as thickness of the interface is $d=0$. Propagation matrix $\boldsymbol{P}=\mathbf{1}$ is also employed in the last transfer matrix in the multilayer stack to obtain proper polarization mode amplitudes in the lower hlafspace $(\mathcal{N}+1)$ at the interface $\mathcal{I}^{(\mathcal{N})}$.

### 2.3.3 Reflection from the multilayer stack

Let's assume that the multilayer stack is only irradiated by EM wave from the upper halfspace (0), which is in agreement with the experiment. Then we can set $E_{02}^{(\mathcal{N}+1)} = E_{04}^{(\mathcal{N}+1)} = 0$ (recall our convention on upwards and downwards modes) and we can write

$$\begin{bmatrix} E_{01}^{(0)} \\ E_{02}^{(0)} \\ E_{03}^{(0)} \\ E_{04}^{(0)} \end{bmatrix} = \begin{bmatrix} M_{11} & M_{12} & M_{13} & M_{14} \\ M_{21} & M_{22} & M_{23} & M_{24} \\ M_{31} & M_{32} & M_{33} & M_{34} \\ M_{41} & M_{42} & M_{43} & M_{44} \end{bmatrix} \begin{bmatrix} E_{01}^{(\mathcal{N}+1)} \\ 0 \\ E_{03}^{(\mathcal{N}+1)} \\ 0 \end{bmatrix} \tag{2.3.16}$$

Further, if we assume that the multilayer stack is illuminated with EM wave of single proper polarization mode of the upper half space (0), we can show that reflection coefficient of that multilayer stack are

$$r_{21}^{(0,\mathcal{N}+1)} = \left(\frac{E_{02}^{(0)}}{E_{01}^{(0)}}\right)_{E_{03}^{(0)}=0} = \frac{M_{21}M_{33} - M_{23}M_{31}}{M_{11}M_{33} - M_{13}M_{31}}, \tag{2.3.17a}$$

$$r_{41}^{(0,\mathcal{N}+1)} = \left(\frac{E_{04}^{(0)}}{E_{01}^{(0)}}\right)_{E_{03}^{(0)}=0} = \frac{M_{41}M_{33} - M_{43}M_{31}}{M_{11}M_{33} - M_{13}M_{31}}, \tag{2.3.17b}$$

$$r_{43}^{(0,\mathcal{N}+1)} = \left(\frac{E_{04}^{(0)}}{E_{03}^{(0)}}\right)_{E_{01}^{(0)}=0} = \frac{M_{11}M_{43} - M_{41}M_{13}}{M_{11}M_{33} - M_{13}M_{31}}, \tag{2.3.17c}$$

$$r_{23}^{(0,\mathcal{N}+1)} = \left(\frac{E_{02}^{(0)}}{E_{03}^{(0)}}\right)_{E_{01}^{(0)}=0} = \frac{M_{11}M_{23} - M_{21}M_{13}}{M_{11}M_{33} - M_{13}M_{31}}. \tag{2.3.17d}$$

The reflection of light from multilayer stack is then described by Jones formalism as

$$\begin{bmatrix} E_{02}^{(0)} \\ E_{04}^{(0)} \end{bmatrix} = \begin{bmatrix} r_{21}^{(0,\mathcal{N}+1)}, & r_{23}^{(0,\mathcal{N}+1)}, \\ r_{41}^{(0,\mathcal{N}+1)}, & r_{43}^{(0,\mathcal{N}+1)}. \end{bmatrix} \begin{bmatrix} E_{01}^{(0)} \\ E_{03}^{(0)} \end{bmatrix}. \tag{2.3.18}$$

As was told at the beginning of this section, in the upper halfspace (0) (air) we can choose arbitrary set of orthogonal polarization eigenmodes. For our purpose set of $s$- and $p$- polarized waves is needed, as this is the polarization state of light that we use to probe the samples in our experiments. From formalism then follows

$$\begin{aligned} r_{ss} &= r_{21} \qquad & r_{sp} &= r_{23} \\ r_{ps} &= r_{41} \qquad & r_{pp} &= r_{43} \end{aligned} \tag{2.3.19}$$

Nevertheless, if we would want to use this formalism to process, for example, some XMCD results, it would be wise to chose RCP and LCP waves as our set of proper polarization modes in the upper halfspace (0).

Finally, transmission coefficient of the multilayer stack can be easily deduct from total matrix $\boldsymbol{M}$ through the similar logic as the reflection coefficients of Eq. (2.3.17). As the transmission coefficient are not needed in this work we do not show them here.

## 2.4 Description of light polarization by the Jones formalism

Jones formalism is used to describe propagation of fully polarized light through the optical setup. This means that light is propagating through air – a homogenous isotropic medium. Whenever the light interacts with some optical element (polarizer, sample etc.) the interaction is handled by 2×2 Jones matrix, e.g. the reflection matrix of the sample.

### 2.4.1 Jones vectors

In the Jones formalism 2×1 Jones vector is used to describe polarization state of fully polarized light. One way how to describe general state of polarization through Jones vector is

$$\boldsymbol{J}_{\psi\delta} = \begin{bmatrix} \cos\psi \\ \sin\psi \cdot e^{i\delta} \end{bmatrix}, \tag{2.4.1}$$

where $\tan\psi = E_s/E_p$, where $E_s$, $E_p$ are amplitudes of $s$-, $p$- polarization eigenmodes, respectively and $\delta$ is a phase shift between them. Therefore, Jones formalism does not posses information about the amplitude of EM wave. If we choose cartesian basis for description of light (our case), those two eigenmodes of linearly polarized waves are

$$E_s = \begin{bmatrix} 1 \\ 0 \end{bmatrix}, \qquad E_p = \begin{bmatrix} 0 \\ 1 \end{bmatrix}. \tag{2.4.2}$$

In the circular basis, RCP and LCP eigenmodes are then describe by Jones vectors as

$$E_{\text{RCP}} = \frac{1}{\sqrt{2}} \begin{bmatrix} 1 \\ i \end{bmatrix}, \qquad E_{\text{LCP}} = \frac{1}{\sqrt{2}} \begin{bmatrix} 1 \\ -i \end{bmatrix}. \tag{2.4.3}$$

### 2.4.2 Description of optical elements by the Jones formalism

With the description of polarization state of light in hand, we now need to describe how such a polarization state of light is altered by an optical element. For this purpose 2×2 matrix is employed in Jones formalism. Examples of Jones matrixes for few optical elements are shown in Tab.2.1. Polarization state of incident light $\mathbf{J}_{(I)}$ is changed through optical element (described by Jones matrix $\boldsymbol{L}$) to polarization state of outgoing (reflected / transmitted) light $\mathbf{J}_{(O)}$ as

$$\boldsymbol{J}_{(O)} = \boldsymbol{L}\boldsymbol{J}_{(I)}. \tag{2.4.4}$$

**Definition of optical elements in Jones formalism**

| **optical element** | **non-rotated** | **rotated by angle $\zeta$** |
|---|---|---|
| Polarizer | $\begin{bmatrix}1 & 0\\ 0 & 0\end{bmatrix}$ | $\begin{bmatrix}\cos^2\zeta & \cos\zeta\sin\zeta\\ \cos\zeta\sin\zeta & \sin^2\zeta\end{bmatrix}$ |
| Modulator | $\begin{bmatrix}e^{i\frac{\varphi}{2}} & 0\\ 0 & e^{-i\frac{\varphi}{2}}\end{bmatrix}$ | $e^{i\frac{\varphi}{2}}\begin{bmatrix}\cos^2\zeta+\sin^2\zeta e^{-i\varphi} & \cos\zeta\sin\zeta\left(1-e^{-i\varphi}\right)\\ \cos\zeta\sin\zeta\left(1-e^{-i\varphi}\right) & \sin^2\zeta+\cos^2\zeta e^{-i\varphi}\end{bmatrix}$ |
| Compensator | $\begin{bmatrix}e^{i\frac{\delta}{2}} & 0\\ 0 & e^{-i\frac{\delta}{2}}\end{bmatrix}$ | $e^{i\frac{\delta}{2}}\begin{bmatrix}\cos^2\zeta+\sin^2\zeta e^{-i\delta} & \cos\zeta\sin\zeta\left(1-e^{-i\delta}\right)\\ \cos\zeta\sin\zeta\left(1-e^{-i\delta}\right) & \sin^2\zeta+\cos^2\zeta e^{-i\delta}\end{bmatrix}$ |

Table 2.1: Definition of Jones matrix for polarizer, modulator and compensator. In case of modulator $\varphi$ stands for phase of modulation, being generaly function of time. In case of compensator, $\delta$ stands for retardation angle, being a constant.

For example, if linearly polarized light at 45° pass through polarizer at 0 ° we will have

$$\begin{bmatrix}1\\ 0\end{bmatrix}=\begin{bmatrix}1 & 0\\ 0 & 0\end{bmatrix}\cdot\begin{bmatrix}1\\ 1\end{bmatrix} \tag{2.4.5}$$

Here it may seems that we forgot to write prefactor $1/\sqrt{2}$. Nevertheless, as Jones formalism does not treat the amplitude of light, we do not have to bother about such prefactors. It's just the ratio of the elements of Jones vectors that cary the information about the polarization state of light.

Now, if there is $n$ elements in the optical path, we can substitute all $n$ matrixes by one effective Jones matrix

$$\boldsymbol{L}_{\text{eff}}=\boldsymbol{L}_n\cdot\boldsymbol{L}_{n-1}\cdot\ldots\cdot\boldsymbol{L}_2\cdot\boldsymbol{L}_1. \tag{2.4.6}$$

Then, the propagation of light through such a train of optical elements write

$$\boldsymbol{J}_{(O)}=\boldsymbol{L}_{\text{eff}}\cdot\boldsymbol{J}_{(I)}. \tag{2.4.7}$$

Note that such a train of optical elements could be e.g. MOKE setup built on the optical table.

### 2.4.3 Description of MOKE by the Jones formalism

MOKE is described through Kerr rotation and Kerr ellipticity, thus we need description of the elliptical polarization in the Jones formalism using azimuth $\theta$ and ellipticity $\epsilon$.

Let's have elliptically polarized light where major axis is parallel with direction $s$ (see Appendix A). For such elliptically polarized light azimuth $\theta = 0$ and phase shift must be 90 degrees ($\delta = \frac{\pi}{2}$). From Eq. (2.4.1) we can see that in this special case ellipticity $\epsilon = \psi$, so

$$\mathbf{J}_\epsilon = \begin{bmatrix} \cos\epsilon \\ i\sin\epsilon \end{bmatrix}. \tag{2.4.8}$$

To rotate this ellipse by azimuth $\theta$, rotational matrix

$$\mathbf{R}_\theta = \begin{bmatrix} \cos\theta & -\sin\theta \\ \sin\theta & \cos\theta \end{bmatrix} \tag{2.4.9}$$

is applied, which will leave us with general description of polarized light through Jones vector using rotation $\theta$ and ellipticity $\epsilon$.

$$\mathbf{J}_{\theta\epsilon} = \begin{bmatrix} \cos\theta & -\sin\theta \\ \sin\theta & \cos\theta \end{bmatrix} \begin{bmatrix} \cos\epsilon \\ i\sin\epsilon \end{bmatrix} = \begin{bmatrix} \cos\theta\cos\epsilon - i\sin\theta\sin\epsilon \\ \sin\theta\cos\epsilon + i\cos\theta\sin\epsilon \end{bmatrix}. \tag{2.4.10}$$

The complex polarization parameter $\Phi$, that itself fully describe polarization state of light, is defined as the ratio of the second and first component of the Jones vector $\boldsymbol{J}_{\theta\epsilon}$.

$$\Phi = \frac{\sin\theta\cos\epsilon + i\cos\theta\sin\epsilon}{\cos\theta\cos\epsilon - i\sin\theta\sin\epsilon} = \frac{\tan\theta + i\tan\epsilon}{1 - i\tan\theta\tan\epsilon}. \tag{2.4.11}$$

If we consider small angle approximation ($\theta < 1^\circ$, $\epsilon < 1^\circ$) we can write

$$\Phi = \theta + i\epsilon. \tag{2.4.12}$$

Note that arbitrary polarization can be described through this notation, as linearly polarized light is actually elliptically polarized light with $\epsilon = 0$ and circularly polarized light is eliptically polarized light with $\epsilon = \frac{\pi}{4}$.

Now, the reflection of the incident $s$-polarized light from the sample is described as

$$\begin{bmatrix} r_{ss} \\ r_{ps} \end{bmatrix} = \begin{bmatrix} r_{ss} & r_{sp} \\ r_{ps} & r_{pp} \end{bmatrix} \begin{bmatrix} 1 \\ 0 \end{bmatrix}, \tag{2.4.13}$$

and the reflection of the $p$-polarized light from the sample is described as

$$\begin{bmatrix} r_{sp} \\ r_{pp} \end{bmatrix} = \begin{bmatrix} r_{ss} & r_{sp} \\ r_{ps} & r_{pp} \end{bmatrix} \begin{bmatrix} 0 \\ 1 \end{bmatrix}. \tag{2.4.14}$$

The Kerr angles are thus defined through the same way as is complex polarization parameter $\Phi$.

$$\Phi_s = -\frac{r_{ps}}{r_{ss}} = \theta_s + i\epsilon_s\,, \qquad \Phi_p = \frac{r_{sp}}{r_{pp}} = \theta_p + i\epsilon_p. \tag{2.4.15}$$

The minus sign for reflection of $s$-polarized light is stemming from historical MOKE sign conventions (see the Appendix A). Intuitively, the minus sign should be present with $\Phi_p$ as the positive direction of $p$-polarized light is changed upon reflection (consider, for example, reflection under normal incidence when both, incident and reflected beam, are described by right-handed system). Nevertheless, as definition of positive Kerr rotation is in fact in contrast with definition of positive rotation inside our coordinate systems (e.g. optical element rotation in coordinate system $s, p, k$), the negative sign is with the $\Phi_s$ instead.

## 2.5 Separation of linear and quadratic MOKE - concept of the 8-directional method

So far, we provided the theory on how to build the reflection matrix of the multilayer stack with FM layer in it. We also explain above that Kerr effect is described through those reflection coefficients. Thus, we posses tool that fully[12] describes Kerr reflection from the multilayer structure.

Although this description is well suitable for processing of our experimental data, it is too clumsy to express some equations in human-readable form. Also, note that for each sample the equations could differ according to number of layers in multilayer stack. But, for our understanding and to develop some measurement algorithm, it would be handy to have some more simplistic equations describing dependence of Kerr effect on the MO parameters, $\boldsymbol{M}$ direction and sample orientation. Here, we present an equations that are, to some extent, valid to any multilayer stack with FM layer of (001) oriented cubic crystal structure [13].

The analytical approximation for MOKE with the permittivity $\varepsilon'$ of the FM layer in the sample is [24]

$$\begin{aligned} \Phi_s &= -\frac{r_{ps}}{r_{ss}} = A_s\left(\varepsilon'_{yx} - \frac{\varepsilon'_{yz}\varepsilon'_{zx}}{\varepsilon_d}\right) + B_s\varepsilon'_{zx}, \\ \Phi_p &= \frac{r_{sp}}{r_{pp}} = -A_p\left(\varepsilon'_{xy} - \frac{\varepsilon'_{zy}\varepsilon'_{xz}}{\varepsilon_d}\right) + B_p\varepsilon'_{xz}, \end{aligned} \tag{2.5.1}$$

---

[12] Up to second order in magnetization.

where weighting optical factors $A_{s/p}$ and $B_{s/p}$ include influence of the other layers in the stack and they are very roughly even and odd functions of the AoI, respectively. The permittivity tensor of the FM layer is described by the Eq. (2.2.17). This permittivity tensor $\boldsymbol{\varepsilon}'$ covers any possible orientation of cubic crystal structure, including arbitrary rotation around its surface normal.

From now onwards, we will limit ourself to in-plane normalized magnetization

$$\frac{\boldsymbol{M}}{\|\boldsymbol{M}\|} = \begin{bmatrix} M_T \\ M_L \\ 0 \end{bmatrix} = \begin{bmatrix} \cos\mu \\ \sin\mu \\ 0 \end{bmatrix}, \tag{2.5.2}$$

with $\mu$ as the angle between $\boldsymbol{M}$ direction and $x$-axis of our coordinate system (see Appendix A). Then, for the FM layer of (001) oriented cubic crystal structure with sample orientation $\alpha$ (see Appendix A), the elements $\varepsilon'_{ij}$ of the Eq. 2.5.1 are

$$\begin{aligned} \varepsilon'^{(001)}_{yx/xy} &= \left[2G_{44} + \frac{\Delta G}{2}\left(1-\cos 4\alpha\right)\right] M_L M_T \\ &\quad + \frac{\Delta G}{4}\sin 4\alpha \left(M_T^2 - M_L^2\right), \end{aligned} \tag{2.5.3}$$

$$\varepsilon'^{(001)}_{zx/xz} = \; = \pm K M_L, \tag{2.5.4}$$

$$\varepsilon'^{(001)}_{yz/zy} = \; = \pm K M_T, \tag{2.5.5}$$

and, thus, from Eq. 2.5.1 Kerr amplitude is

$$\begin{aligned} \Phi_{s/p} = \pm A_{s/p} &\left[2G_{44} - \frac{K^2}{\varepsilon_d} + \frac{\Delta G}{2}\left(1-\cos 4\alpha\right)\right] M_L M_T \\ \pm A_{s/p} &\left[\frac{\Delta G}{4}\sin 4\alpha\right]\left(M_T^2 - M_L^2\right) \\ \pm B_{s/p} &K M_L\,. \end{aligned} \tag{2.5.6}$$

When $\boldsymbol{M}$ components are expressed through the angle $\mu$ of the $\boldsymbol{M}$ in-plane direction[13]

$$\begin{aligned} \Phi_{s/p} = \pm A_{s/p} &\left[\frac{2G_{44}}{2} - \frac{K^2}{2\varepsilon_d} + \frac{\Delta G}{4}\left(1-\cos 4\alpha\right)\right] \sin(2\mu) \\ \pm A_{s/p} &\left[\frac{\Delta G}{4}\sin 4\alpha\right]\cos(2\mu) \\ \pm B_{s/p} &K \sin\mu. \end{aligned} \tag{2.5.7}$$

---

[13] $M_L M_T = \cos\mu\sin\mu = \frac{1}{2}\sin(2\mu), \quad M_T^2 - M_L^2 = \cos^2\mu - \sin^2\mu = \cos(2\mu).$

This equation show dependence of Kerr angles on MO parameters $K$, $G_s$ and $2G_{44}$, on sample orientation $\alpha$ and on magnetization direction $\mu$, within validity of Eq. 2.5.1.

From those dependencies, the separation process known as 8-directional method can be developed [13]. In Eq. (2.5.6) we can distinguish three contributions with different dependence on the components of $\boldsymbol{M}$. Separation technique is based on appropriate summations of Kerr angles with eight different magnetization directions $\mu = k \cdot 45°$, where $k = 0, 1, ..., 7$. Those contributions are separated by 8-directional method:

$$\underbrace{\frac{1}{2}\left(\Phi_{s/p}^{\mu=90°} - \Phi_{s/p}^{\mu=270°}\right) = \pm B_{s/p} K,}_{\text{LinMOKE} \sim M_L \quad \text{(i.e. LMOKE)}} \tag{2.5.8a}$$

$$\underbrace{\frac{1}{2}\left(\Phi_{s/p}^{\mu=45°} + \Phi_{s/p}^{\mu=225°} - \Phi_{s/p}^{\mu=135°} - \Phi_{s/p}^{\mu=315°}\right) = \pm A_{s/p}\left[2G_{44} - \frac{K^2}{\varepsilon_d} + \frac{\Delta G}{2}\left(1 - \cos 4\alpha\right)\right],}_{\text{QMOKE} \sim M_L M_T} \tag{2.5.8b}$$

$$\underbrace{\frac{1}{2}\left(\Phi_{s/p}^{\mu=0°} + \Phi_{s/p}^{\mu=180°} - \Phi_{s/p}^{\mu=90°} - \Phi_{s/p}^{\mu=270°}\right) = \pm A_{s/p}\left[\frac{\Delta G}{2}\sin 4\alpha\right].}_{\text{QMOKE} \sim M_T^2 - M_L^2} \tag{2.5.8c}$$

Thus, with in-plane magnetization of the sample we can distinguish two different QMOKE contributions $\sim M_L M_T$ and $\sim (M_T^2 - M_L^2)$[14] and one LinMOKE contribution, being LMOKE. Note that due to optical interplay of two off-diagonal permittivity elements in Eq. (2.5.1), the QMOKE $\sim M_L M_T$ is partly stemming also from linear MO parameter $K$, i.e. contribution $K^2/\varepsilon_d$. Thus, due to this optically induced quadratic in magnetization contribution, the statement that QMOKE arise from quadratic MO tensor $\boldsymbol{G}$ is not completely accurate.

## 2.6 Conclusion

This chapter did provide sufficient theory to understand how the MO parameters $K$, $G_s$ and $2G_{44}$ can be yielded from the measurement of the Kerr angles. Section 2.5 did describe how to ensure that the Kerr angles we have measured are stemming from those MO parameters. When we posses the measurement of both, Kerr rotation and Kerr ellipticity, we can bound those to the reflection coefficients through Eq. (2.4.15). The reflection coefficients are then depending on many parameters, among them the MO

---

[14] Note that those two QMOKE contributions are analogous to d.c. magneto–transport effects known as anisotropic magnetoresistance (AMR) $\sim (M_T^2 - M_L^2)$ and planar Hall effect (PHE) $\sim M_L M_T$. See Tab.1.2.

parameters of the FM layer in the stack. Now, if we will posses knowledge of all the other parameters of the stack, the MO parameters can be set as free variables in the model based on Yeh's formalism described in Sec. 2.3. We may know some of those parameters directly from the experiment, auch as the photon energy (i.e. the radial frequency of the EM wave) or AoI. Others, that we do not directly know, such as the permittivity $\varepsilon_d$ and thickness of each layer in the multilayer stack, have to be actually obtained through some experimental techniques, e.g. x-ray reflectivity or ellipsometry. In the next chapter, we will take a look at this issue. Note also that the process can be reversed, i.e. if we posses all information about the multilayer stack, MO parameters included, we can simulate the Kerr angles from it.

# Chapter 3

# Experimental techniques, sample preparation and characterization

This chapter will introduce and describe the experimental MOKE techniques together with description of two MOKE setups, which were used to acquire experimental data for our research. A short discussion about the Python based numerical code used for the MOKE simulations and experimental data post-processing is presented as well. Further, we will briefly discuss the theory of thin film sample preparation and the theory of structural, optical and magnetic characterization. In the second half of this chapter we present all the samples investigated in this work. We discuss their preparation and all the characterization that is needed before we will start with LinMOKE and QMOKE investigations of those samples in the subsequent Chapter 4 and Chapter 5.

## 3.1 MOKE characterization techniques

In this section, we will look at methods and techniques used for MOKE experimental measurements and we will describe the setups used in our experiments. Furthermore, we will explain the MOKE techniques used for magnetic characterization together with loop symmetrization - a simple process that can, under some circumstances, separate QMOKE contributions from the hysteresis loops. Finally, we will discuss the numerical calculus that is used for the MOKE simulations.

### 3.1.1 MOKE detection techniques

There is several ways how to detect MOKE signal. We will briefly discuss some of those methods shortly, but before we would like to comment one thing that all of those MOKE detection techniques have in common. The Kerr angles are not measured absolutely, i.e. we do not directly measure Kerr rotation and/or ellipticity of incident $s$- or $p$- polarized wave upon reflection from sample that is magnetized into desired direction. Instead, we measure change in polarization state of light with change of $\boldsymbol{M}$ direction (in the LinMOKE case we usually just invert $\boldsymbol{M}$ direction).

There are two main reasons for this. (i) It is technically very hard to find absolute zero of MO signal. With majority of the setups (or at least with all the setups known to us) some offset is present, that depend on current setup alignment and sample alignment. The offset also often slowly drift in time. (ii) There could be other effects that cause change in the polarization state of light upon reflection, like natural anisotropy of the crystal (not the case of cubic crystals), strain etc. Thus, this differential measurement for two (or more) $\boldsymbol{M}$ directions can efficiently filter out those effects, as they are not $\boldsymbol{M}$ direction dependent. Although with measurements of hysteresis loops Kerr angles are measured directly, we are interested here in the shape of the loops and not in the exact value of the Kerr angles, where those loops usually posses considerable offset. In the case when we need to obtain exact value of Kerr angles from the loops, we must centre them around zero, which is in principle adequate to differential measurements when $\boldsymbol{M}$ is reversed.

Besides, there is one more thing that almost all MOKE measurement methods have in common.

### Measurement of Kerr ellipticity

All the methods described below are only able to directly detect change in the rotation of the plane of polarization, but are not able to directly detect ellipticity of the polarization. This should be common to all detection techniques that employ polarizers and are based on measurement of intensity change at the detector. Thus, to measure Kerr ellipticity, quarter-wave retarder (i.e. compensator $\delta = \frac{\pi}{2}$, see Tab.2.1) is employed in the optical pathway (in our case right behind the sample). Such a compensator will literary swap the ellipticity angle for the rotation angle and *vice versa*. Thus, with the compensator present, the setup is still only detecting changes in the rotation of the plane of polarization, but this rotation angle is now proportional to the ellipticity of polarized light that is reflected from the sample, but didn't pass through compensator yet. Hence the Kerr ellipticity is actually being measured.

In Jones formalism quarter-wave compensator writes:

$$\mathbf{C} = e^{i\frac{\delta}{2}} \begin{bmatrix} 1 & 0 \\ 0 & e^{-i\delta} \end{bmatrix} \overset{\delta=\frac{\pi}{2}}{=} e^{i\frac{\pi}{4}} \begin{bmatrix} 1 & 0 \\ 0 & -i \end{bmatrix} . \tag{3.1.1}$$

As discussed in previous chapter in Sec. 2.4, (i) in the Jones formalism we can discard the prefactors ($e^{i\frac{\pi}{4}}$ in this case) and (ii) we can join two or more Jones matrixes into one effective Jones matrix. We will do so for the reflection matrix of the sample and the Jones matrix of the compensator.

$$\mathbf{C}^{(\frac{\pi}{2})}\mathbf{R} = \begin{bmatrix} r_{ss} & r_{sp} \\ -ir_{ps} & -ir_{pp} \end{bmatrix} . \tag{3.1.2}$$

If we will now yield Kerr angles from this effective reflection matrix, we will have

$$\Phi_s^{\boldsymbol{C}(\frac{\pi}{2})} = i\frac{r_{ps}}{r_{ss}} = -\epsilon_s + i\theta_s\,, \qquad \Phi_p^{\boldsymbol{C}(\frac{\pi}{2})} = i\frac{r_{sp}}{r_{pp}} = -\epsilon_p + i\theta_p, \tag{3.1.3}$$

where we see that rotation have been swapped for ellipticity and *vice versa.*

### Nearly crossed polarizers

The simplest method for MOKE detection utilize so-called nearly crossed polarizers. One polarizer is in the incident beam pathway and the second polarizer (which we call analyzer) is in the reflected beam pathway. With crossed polarizers no light intensity get pass the analyzer to the detecetor. With magnetized sample the Kerr rotation is induced upon reflection and thus some of the light intensity will pass to the detector. Note that the rotation of analyzer and Kerr rotation of reflected beam, both have the very same effect on the intensity at the detector. This is being used to calibrate the setup and obtain volt-degree characterization for the measurement of Kerr angles. Because with completely crossed polarizer and analyzer the Kerr angle sign would be indistinguishable (from zero intensity we can go only up), the analyzer is slightly turn away from the crossed position (ca. 5° from crossed position), and therefore "nearly crossed polarizers". Then, the intensity drop or rise provide information on the sign, while absolute change in intensity give us information on the Kerr effect strength.

### Intensity differential measurement – use of Wollaston prism

Another technique for MOKE detection utilize Wollaston prism. Wollaston prism is a polarizer that split incoming light into two beams of linear polarizations orthogonal to each other, where both beams are deviated from the original path by an angle. How much intensity goes into each of the branch depends on how is the Wollaston prism balanced with respect to incoming polarization. If Wollaston prism will be balanced precisely at 0 degrees, the incoming $s$-polarized light will be split into two beams with linear polarization rotated by ±45°. Then, if we will turn Wollaston prism by 45°, one of the beam will be fully extinct and all the intensity will be in the other. Again, as in the previous case, rotation of Wollaston prism and rotation of polarization are relative to each other. Each of the beam is then detected by its own detector (usually some photodiode). With balanced Wollaston prism intensities on both diodes are the same. When Kerr effect is introduced through sample magnetization (or rather reversion of $\boldsymbol{M}$), intensity $I_1$ at one diode will rise whereas intensity $I_2$ at the other diode will fall. From the difference $I_1 - I_2$ we can calculate the Kerr angles. This technique is employed with the Vector MOKE setup based at Bielefeld University as will be discussed later in the text.

### Polarization modulation technique

This modulation techniques employ modulation of polarization state of light. This means that the polarization state of light will harmonically oscillate in time, producing also harmonic changes of the intensity at the detector. The signal is then being measured through lock-in amplifier. This provide us with much better signal-to-noise ratio, same as in the case of intensity modulation technique (where chopper is usually used), but furthermore filter out also effects as e.g. depolarization of the sample.

To modulate the ellipticity of polarization, photoelastic modulator (PEM) is used. The device act as a compensator with time-varying phase shift. Fused silica block inside the PEM is periodically compressed by a piezocrystal at frequency $\omega$ being usually 50 kHz. By the amplitude of compression, the amplitude of phase shift is given. To modulate rotation of polarized light, Faraday cell with capacitor (together forming LC oscillator) is used. Faraday cell consist of a coil with fused silica block inside. Magnetic field produced by the coil will induce Faraday rotation to the light passing through the fused silica. The higher the field the higher the Faraday rotation. These are the most conventional technique for modulation, but with rapid advance of technology there will be surely other approaches as is for example nematic liquid crystal modulator [105].

The measurement principle with modulation technique require more detailed treatment by Jones formalism to obtain Intensity dependencies of $I_{1\omega}$ and $I_{2\omega}$ being intensities at first and second harmonic of modulation frequencies measured by lock-in amplifier, respectively. With this technique it is actually possible to measure ellipticity without use of compensator, as the signal of $I_{1\omega}$ is usually proportional to Kerr ellipticity and $I_{2\omega}$ to Kerr rotation, yet the principle from point of physics is similar to the use of compensator (as PEM is compensator with time-varying phase shift). However measurement of Kerr ellipticity through $I_{1\omega}$ does not have to be a rule. With our Spectroscopy MOKE setup based at Technical University of Ostrava, that employ modulation technique through PEM, the Kerr ellipticity is still measured through use of compensator and detection of $I_{2\omega}$, as calibration of $I_{1\omega}$ is problematic in our case.

There is multiple way how to obtain calibration, i.e. volt-degree characterization of $I_{2\omega}$, of this technique. Similar calibration as in the case of nearly crossed polarizers could be done (i.e. by small analyzer rotation). Some setups may also employ null technique, that is described below, to measure Kerr effect.

#### Null technique

This technique is usually combined with the modulation technique using Faraday cell, although in principle could be used on its own. Another Faraday cell, so-called null cell, is employed within the setup, and is used to compensate Kerr effect from sample through feedback loop. Calibration of the null cell will provide us with ampere-degree characterization, i.e. we can calculate the Kerr angles from the current needed to compensate the Kerr effect from the sample.

### 3.1.2 Description of the MOKE setups

Here we will describe two setups used within our research.

The first setup, called Vector MOKE setup, is located at Bielefeld University and employ Wollaston prism based intensity differential method. Setup is well suitable for 8-directional method and for hysteresis loops and other Vector MOKE measurements due to its 3-axes electromagnet and rotational sample stage that allow precise alignment of the sample.

The second setup, MOKE spectroscopy setup, is located at Technical University of Ostrava, and employ PEM modulation technique. Setup can obtain LinMOKE and QMOKE spectra in spectral range 0.8 eV – 5.5 eV. Although measurement of 8-directional method is not so convenient here, still for some cases the samples could be align to run such a measurement. Setup use permanent magnets, thus no hysteresis loops can be obtained here.

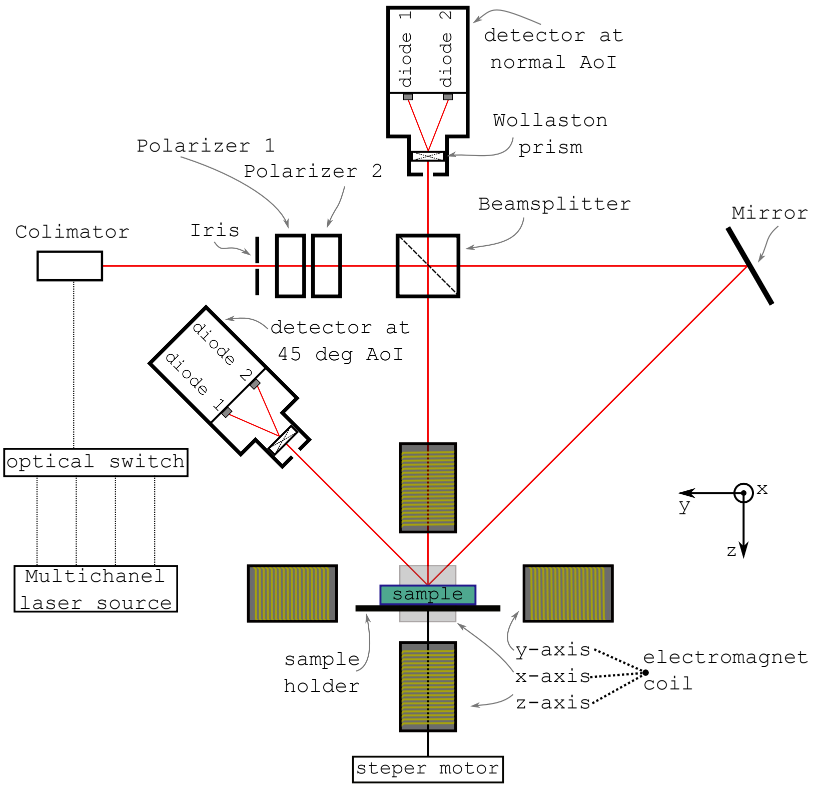

FIGURE 3.1: Sketch of the VectorMOKE setup from Bielefeld University. Multichannel source is connected by 4 fibres with optical switch, where each fibre is guiding one of the four wavelengths, being 670 nm, 636 nm, 488 nm and 406 nm, respectively. Through optical switch we then choose one wavelength, that is guided by single fibre to the collimator. Iris is used to control diameter of the beam, whereas polarizer 1 is used to control the intensity of the beam. Polarizer 2 is then used to yield *s*- or *p*- polarized light that is afterwards split by beamsplitter and hit the sample under normal incidence and angle of incidence 45°, respectively. Sample holder is mounted on the rotational axis, allowing full 360° rotation, and is placed inside 3-axis electromagnet. Reflected light from the sample is then detected by two detectors, each for one beam. Detectors consist of Wollaston prism and two photodiodes. In order to balance the Wollaston prism with photodiodes prior to measurement, detector itself can be rotated around axis given by incoming beam.

### Vector MOKE setup at Bielefeld University

This experimental setup consist of: multichannel fibre coupled laser source – collimator – polariser – beamsplitter – sample & electromagnet – two detectors. Source with 4 laser diodes can emit light at wavelengths 670 nm (1.85 eV), 635 nm (1.95 eV), 488 nm (2.54 eV) and 406 nm (3.05 eV), respectively. The laser light is guided to the collimator by fibre. Beamsplitter provide us with two probing beams, one is reflected from the sample under normal AoI, while the other is reflected under 45° AoI. The sample is placed on a rotational stage that can be tilted for adjustment so that the AoI is kept constant through full 360° rotation of the sample. The sample holder is mounted inside a 3-axes electromagnet. The maximum strength of the magnetic field is tuneable by poles of the magnets, that can be screwed in or out. With poles completely sheet in, we may apply field up to 381 mT. Nevertheless, in the case of $y$-axis magnets, the poles that are completely sheet in obstruct the beam at 45° incidence. Therefore, if we wish to probe the sample under 45° AoI, the maximum magnetic field we may apply in $y$-axis is 235 mT. The beam that is incident under normal AoI is passing through a drilled hole in the yoke of the $z$-axis coil of the electromagnet. Each of the beams reflected from a sample is detected by its own detector. Each of those two detectors consist of Wollaston prism with two balanced photodiodes. Stepper motor allow us to balance the detector by rotation around the propagating light axis. The setup is controlled via an in-house written code in Python language.

The Kerr rotation of the sample can then be determined by the difference of the intensity signal on those two diodes. Due to constant AoI with sample rotation, the setup is well suitable for 8-directional method measurement and, due to three axis electromagnet, for Vectorial magnetometry [17].

Detailed description of this setup can be found in literature [106] (written in german language).

#### Spectroscopy MOKE setup at Technical University of Ostrava

This experimental setup employ PEM modulation technique, and consist of: Lamp – monochromator – poalrasier – sample & magnets – (compensator) – PEM – analyzer – detectors.

The Xenon short arc lamp (extended to UV region, 300 W) is followed by a grid monochromator (Oriel Cornerstone 260 1/4 m) in Czerny-Turner optical configuration. A Rochon prism polarizer is then used to yield $s$-polarized or $p$-polarized incident wave. The sample is mounted on a holder that allow us to rotate the sample by an arbitrary angle $\alpha$ and is placed inside magnetic circuit with permanent magnets (300mT). Permanent magnets can be in-plane rotated by an arbitrary angle $\mu$. After reflection from the magnetized sample, the light travels through an optional optical element - quarter wave Fresnel rhomb (achromatic compensator). The light further propagates through a PEM (Hinds Instruments PEM-100) that is bound with an analyzer (Rochon prism) at 45° and they are as such mounted on the rotational stage. Afterwards, one of the three detectors, being infrared diode (Newport 7032 8NS) or photomultipliers for visible (Hamamatsu H7712-13) or ultra-violet (Hamamatsu H9307) light, detects the reflected light, respectively. To guide and focus the light through the setup only parabolic mirrors are used and hence our setup is completely chromatic-aberration free. The spectral range of the setup (determined by the spectral characteristics of lamp, monochromator

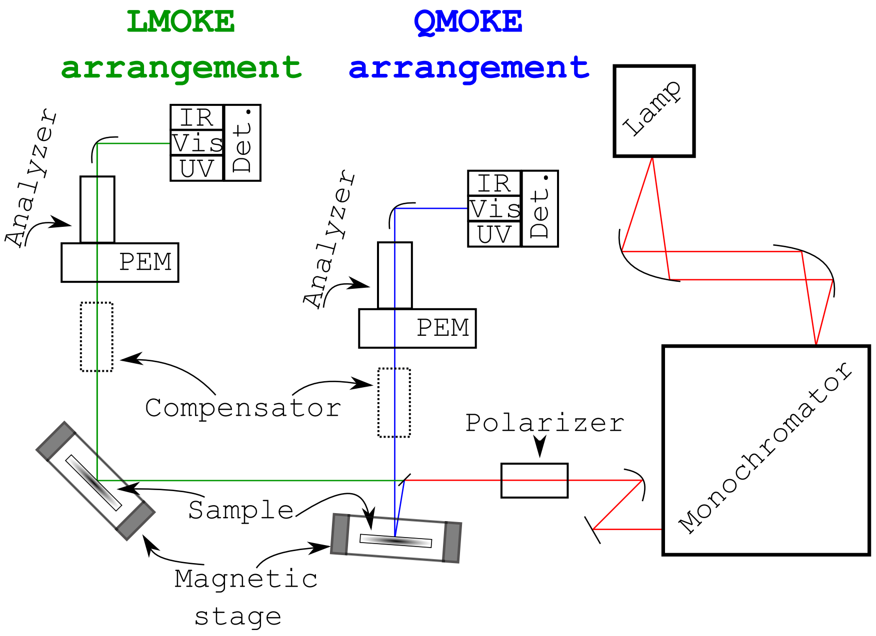

FIGURE 3.2: Sketch of the optical elements of the setup on the optical table. The optical elements are: lamp–monochromator–polarizer–sample with magnetic stage–(compensator)–PEM and analyzer–detectors. The optical path denoted by the red beam is stable for both, LMOKE and QMOKE configuration. To measure LMOKE, the green path is used while to measure QMOKE the blue path have to be arranged.

and detectors) is 0.8 eV – 5.5 eV. For the sketch of the setup's placement on the optical table, see Fig. 3.2.

Lock-in amplifier (Stanford Research System SR830) is used to process signal from the detector, where reference frequency bis provided by PEM. The setup is controlled via an in-house written code in Python language, using the pyVisa interface to communicate with the hardware of the setup.

We will now discuss measurement principle of this setup little bit more into detail. The response of the polarization state of light propagation through the setup is described in the Jones formalism as

$$\boldsymbol{J}_{\mathrm{det}} = \boldsymbol{A}\boldsymbol{P}(\boldsymbol{C}^{(\frac{\pi}{2})})\boldsymbol{R}\boldsymbol{J}_{\mathrm{in}}\,, \tag{3.1.4}$$

which can be written in matrix form as

$$\begin{aligned}\begin{bmatrix} E_s \\ E_p \end{bmatrix} = E_0 \begin{bmatrix} 1 & 1 \\ 1 & 1 \end{bmatrix} \begin{bmatrix} e^{i\frac{\varphi}{2}} & 0 \\ 0 & e^{-i\frac{\varphi}{2}} \end{bmatrix} \begin{bmatrix} \cos\beta & \sin\beta \\ -\sin\beta & \cos\beta \end{bmatrix} \\ \left(\begin{bmatrix} e^{i\frac{\pi}{4}} & 0 \\ 0 & e^{-i\frac{\pi}{4}} \end{bmatrix}\right) \begin{bmatrix} r_{ss} & r_{sp} \\ r_{ps} & r_{pp} \end{bmatrix} \begin{bmatrix} \cos\xi \\ \sin\xi \end{bmatrix}\,.\end{aligned} \tag{3.1.5}$$

$\boldsymbol{J}_{\mathrm{in}}$ is the Jones vector of the incident light, which is chosen by the polarizer at angle $\xi$. We use $\xi = 0°$, $\xi = 90°$, being $[1,0]$, $[0,1]$ for $s$-, $p$- polarized incident light, respectively. Reflection from the magnetized sample is described by reflection matrix $\boldsymbol{R}$. $\boldsymbol{C}^{(\frac{\pi}{4})}$ is the optional optical element - achromatic quarter-wave compensator. Analyzer $\boldsymbol{A}$ at 45° is bounded with PEM ($\boldsymbol{P}$) and they together can be rotated by an angle $\beta$. Phase of modulation is $\varphi = \varphi_S + \varphi_A \sin(\omega t)$, where $\varphi_S$ is phase shift constant in time, $\varphi_A$ is the modulation amplitude and $\omega$ is frequency of PEM. Finally, electric field amplitudes at the detector are described by $\boldsymbol{J}_{\mathrm{det}}$. $E_0$ is a constant prefactor and its absolute value is not important for our investigation.

Intensity at the detector is $I = |E|^2$, where $E = \sqrt{E_s^2 + E_p^2}$. But because analyzer is oriented at 45°, thus $E_s = E_p$, we can introduce the overall electric field intensity as $E = \sqrt{2}E_s = \sqrt{2}E_p$ and therefore write the intensity at the detector as $I = 2|E_s|^2$.

To analyze equations of intensity at the detector following steps and approximations are made: ($i$) We apply small angle approximations for Kerr angles $\theta_{s/p}$, $\epsilon_{s/p}$ and angle $\beta$. This imply that we neglect all the terms with square of the Kerr angle (i.e. with square of the off-diagonal reflection coefficients) and that $\cos\beta = 1$ and $\sin\beta = \beta$. ($ii$) We expand $e^{i\varphi}$ into Bessel functions [107] using terms up to $2\omega t$. The calibration of PEM provide us with $\varphi_S \approx 0$ which allow us to set $\sin\varphi_S = 0$ and $\cos\varphi_S = 1$. Then the expansion into the Bessel functions write $e^{i\varphi} = J_0(\varphi_A) + i2J_1(\varphi_A)\sin(\omega t) + 2J_2(\varphi_A)\cos(2\omega t)$.

We use second harmonic Intensity $I_{2\omega}$ to measure both , Kerr rotation and Kerr ellipticity alike, where compensator is add into the setup in order to detect Kerr ellipticity. The signal of $I_{2\omega}$ measured by lock-in amplifier for $s$-polarized incident beam with and without compensator and for $p$- polarized incident beam with and without compensator is

$$I_{2\omega}^{(s,c)} = -I_k|r_{ss}|^2(\epsilon_s + \beta_s) = \gamma^{(s,c)}(\epsilon_s + \beta) , \tag{3.1.6a}$$

$$I_{2\omega}^{(s)} = -I_k|r_{ss}|^2(\theta_s + \beta_s) = \gamma^{(s)}(\theta_s + \beta) , \tag{3.1.6b}$$

$$I_{2\omega}^{(p,c)} = -I_k|r_{pp}|^2(\epsilon_p - \beta_p) = \gamma^{(p,c)}(\epsilon_p - \beta) , \tag{3.1.6c}$$

$$I_{2\omega}^{(p)} = I_k|r_{pp}|^2(\theta_p + \beta_p) = \gamma^{(p)}(\theta_p + \beta) , \tag{3.1.6d}$$

respectively. Here superscript ($c$) denotes the presence of the quarter-wave compensator in the setup, $\omega$ is modulation frequency of the PEM and $I_k = 4J_2(\varphi_A)k_{2\omega}I_0$, where $k_{2\omega}$ is transmission coefficient for electronic equipment of the setup at $2\omega$ frequency and $I_0$ is intensity prefactor ($I_0 = |E_0|^2$).

| **Measurement techniques** | | |
|---|---|---|
| Measured Kerr effect | $\Phi_s$ | $\Phi_p$ |
| Polarizer orientation | $\xi = 0$ | $\xi = \frac{\pi}{2}$ |
| Rotation measurement | $\theta_s = \frac{\Delta I_{2\omega}^{(s)}}{2\gamma^{(s)}}$ | $\theta_p = \frac{\Delta I_{2\omega}^{(p)}}{2\gamma^{(p)}}$ |
| Ellipticity measurement | $\epsilon_s = \frac{\Delta I_{2\omega}^{(s,c)}}{2\gamma^{(s,c)}}$ | $\epsilon_p = -\frac{\Delta I_{2\omega}^{(p,c)}}{2\gamma^{(p,c)}}$ |

Table 3.1: The measurement techniques for the setup with arrangements of optical elements: polarizer–sample–(compensator)–PEM and analyzer–detector. The calibration slope $\gamma^{(s)/(s,c)/(p)/(p,c)}$ is obtained from a calibration measurement provided by precise PEM+analyzer rotation.

As can be seen $I_{2\omega}$ has a same linear dependence $\gamma$ for the Kerr angle and angle $\beta$. Thus, this volt-degree characterization factor $\gamma$ can be obtained through rotation by small angle $\beta$. With knowledge of $\gamma$ Kerr angles can be easily measured. Note that this volt-degree conversion factor $\gamma$ is unique for each wavelength. In ideal case $\gamma$ should be same for any sample orientation. But as the beam does a little bit travel on the surface upon the rotation of the sample and the sample is not ideal (reflectivity can be little bit different for different areas of the sample) and/or (in the case of small sample) the beam can be cut by the edge of the sample, we perform calibration of factor $\gamma$ also with each sample orientation.

The measurement method for both polarizations and for both Kerr angles are summarized in Tab. 3.1. Description of this setup with detailed calculation can be found in literature [31, 99].

### 3.1.3 MOKE for thin film magnetic characterization

The MOKE is powerful tool in investigation of magnetic properties of thin films. With use of the electromagnet the magnetic field strength can be modified at will, thus hysteresis curves, that provides information about remanence, coercivity or saturation value, can be measured. Magnetic properties of the sample are obtained through observation of the hysteresis curve shape and its change with the sample orientation $\alpha$ (see Appendix A for conventions).

Combination of electromagnet and rotational sample stage allow us to measure magnetic anisotropy – the position of easy and hard magnetic axes of the thin film FM layer. This is done through measurement of LMOKE hysteresis loop for each step in 360° rotation of the sample. The value of MOKE at remanence (i.e. at zero magnetic field) from each loop is then plotted against the angle $\alpha$ of the sample rotation. If the easy axis is align with the $y$-axis of our coordinate system, the sample will have $\boldsymbol{M} = [0, M_L, 0]$ at remanence, which will provide larger value of LMOKE than in case when easy axis is rotated e.g. by 45° with respect to $y$-axis of our coordinate system, where $\boldsymbol{M} = \frac{1}{\sqrt{2}}[M_T, M_L, 0]$ at remanence.

Note that not all samples posses a considerable remanence, which could make it problematic to probe magnetic anisotropy through the above mentioned manner. In the case of a very soft magnetic material the domain in the sample can close at zero magnetic field (i.e. order in such a manner that there is almost no net magnetization), which would provide random and negligible value of the MOKE. This can be easily fixed by taking the value of MOKE at some very weak magnetic field instead of zero magnetic field [1]. Thus, at such samples, a weak magnetic field will still produce net magnetization of the FM layer, but will not be strong enough to force $\boldsymbol{M}$ to tilt from its easy axis to align with the magnetic field (unless both are collinear). Technically, the strength of this " weak magnetic field" we need to use is unique for each sample and we have to find the right value from the measurement of hysteresis loop (preferably with the very fine step in the magnetic field strength.)

Further, note that there is also more comprehensive technique known as vectorial magnetometry MOKE measurement (Vector MOKE), which allow us to track the magnetization reversal in the sample and separately determine individual components of $\boldsymbol{M}$. The hysteresis curves with incident $s$- and $p$- polarized light are recorded for two external magnetic fields, one being parallel and one perpendicular to the plane of incidence. The details of this technique are well described in Ref. [17]. Nevertheless, note that in description of MOKE we use normalized magnetization $\boldsymbol{M}$, thus the quantitative information on $\boldsymbol{M}$ value cannot be extracted from MOKE investigations in contrast to e.g. vibrating sample magnetometry.

When the MOKE is employed for thin film magnetic characterization, QMOKE is actually unwanted artefact in our measurements, as we are interested solely in signal that is linearly proportional to $\boldsymbol{M}$. Thus if the QMOKE contribution (even in $\boldsymbol{M}$ part of the hysteresis loop) is substantial, we should separate the loop in its odd and even part [17, 18]

$$\Phi^{\text{odd}} = \frac{1}{2}\left[\Phi_{\text{inc}}(\boldsymbol{B}_0) - \Phi_{\text{dec}}(\boldsymbol{B}_0)\right] , \quad \Phi^{\text{even}} = \frac{1}{2}\left[\Phi_{\text{inc}}(\boldsymbol{B}_0) + \Phi_{\text{dec}}(\boldsymbol{B}_0)\right] , \tag{3.1.7}$$

---

[1] Note that we actually never took value of MOKE at zero magnetic field as the yoke of the electromagnet posses some small remanence as well, not to mention the Earth's magnetic field. Nevertheless those magnetic field can be usually neglected in such investigation.

where $\Phi_{\text{inc}}$ and $\Phi_{\text{dec}}$ corresponds to part of the loop with increasing and decreasing magnetic field $\boldsymbol{B}_0$, respectively. Then, $\Phi^{\text{odd}}$ corresponds to LinMOKE and $\Phi^{\text{even}}$ corresponds to QMOKE part of the loop. Note that if $\boldsymbol{M}$ reversal process is not fully antisymmetric, i.e. $\boldsymbol{M}$ is reversed through the same direction of $\boldsymbol{M}$ component $M_T$, this separation process can't be used anymore, thus one should be careful when putting this in use.

Measurements of hysteresis loops and remanence magnetic anisotropy are important to us as we need to be assured that we are saturated for any in-plane magnetization direction when performing 8-directional measurements or QMOKE spectroscopy measurements.

### 3.1.4 Python based numerical model for MOKE simulations

To analyze the measured MOKE data we use model that is described within Sec. 2.3 of Chapter 2, which can provide full reflection matrix of any planar multilayer system. The permittivity tensor of FM layer in this model is treated exactly as described in Sec. 2.2. Kerr angles are then obtained from reflection coefficients through Eq. (2.4.15). Note that if the small angle approximation would not suit us, we can always use exact formula of Eq. (2.4.11).

The model was coded using the Python programming language and we took advantage of the following libraries.

- *NumPy* - package contain powerful N-dimensional array object that was most useful for our numerical simulations.
- *SciPy* - fundamental library for scientific computing.
- *Matplotlib* - 2D plotting library used for visualisation in our numerical simulations. Furthermore, all the figures (except some sketches) presented in this work are plotted with use of this library (and occasionally finished in Inkscape - an open-source vector graphic editor).

Note that although we discuss this numerical model only briefly in this text, its creation was substantial part of this work and was considerably time-consuming especially when counting in its optimisation and debugging. Further, as the code is rather extensive, it is complicated to be ensured that no mistake is present in the code, and that computed outcome is in exact accordance with equations of Sec. 2.3. Thus, the code have been checked by multiple tests.

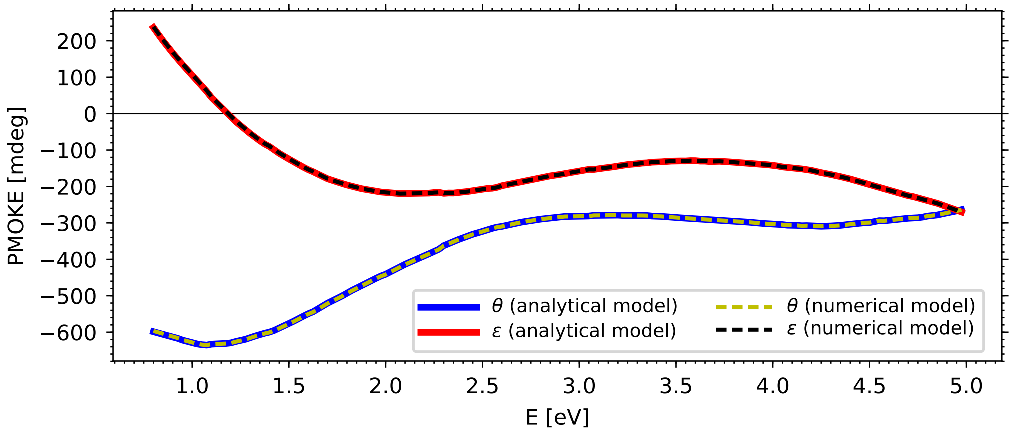

FIGURE 3.3: Simulation of PMOKE reflection at Fe/vacuum interface in spectral range 0.8 eV – 5.5 eV for normal AoI. Spectral values of $\varepsilon_d$ and $K$ of Fe was taken from investigation of our samples (sample with a nominal thickness of 12.5 nm as will be presented later in the text). Full lines are simulated according to Eq. (3.1.8), whereas dashed lines are simulated through our numerical model.

First part of the tests was to simulate well known physical phenomena as are e.g. total reflection and reflection under Brewstrew's angle [34], or to analyze amplitude and phase of the reflected wave. Second test, most suitable for our type of investigation, was to compare the simulated Kerr effect (spectra) with some analytical description. Such analytical description exist e.g. for single interface created by cubic FM material at Polar magnetization and vacuum [33].

$$\Phi = \frac{\varepsilon_{xy}}{\sqrt{\varepsilon_d}(1-\varepsilon_d)} \tag{3.1.8}$$

where $\varepsilon_{xy}$ and $\varepsilon_d$ are permittivity tensors elements of FM halfspace as defined in Sec. 2.2. Note, that this comparison will also attest the sign of computed Kerr angels, being quite important as will be shown in Sec. 5.2.5. In Fig. 3.3 we show comparison between our numerical model and analytical formula of Eq. (3.1.8) for simulation of PMOKE reflection from Fe / vacuum interface at normal AoI. The permittivity of Fe half-space is described solely by our data obtained from one of our samples, as will be described later in this text.

Finally, we would like to mention one imperfection that was deliberately introduced into the code. With transversal magnetization ($\mu = 0°, 180°$), the permittivity tensor of FM layer is of high symmetry which make it problematic to find polarization eigenmodes. The dynamical matrix become singular, which make it impossible to compute its inversion. The problem is not of physical nature, but rather of technical nature of the code.

The eigenmodes with transversal magnetization do exist, but we have to treat the situation as an exception and find them analytically. Nevertheless, we preliminary reach for easy solution – we deflect the $\boldsymbol{M}$ direction in the code by negligibly small and random angle $\Delta\mu = \pm(0.1 - 0.01)\,\mathrm{mdeg}$, which was very efficient and simple fix that survived to the current stage of the code. Nevertheless, when we will probe some very small and almost negligible effects of 8-directional method in the subsequent Chapter 4, this will result in some noise in numerically calculated data. Although this numerical noise may be suppress if the $\Delta\mu$ will not be random but static, we rather keep the deflection $\Delta\mu$ random, thus it cannot generate some artefact. Moreover, this imperfection of the code does not have to bother us very much as the numerical noise is deep below any realistic noise-to-signal ratio of the real experimental MOKE setup and in the real experiment the precision of $\boldsymbol{M}$ direction control is much less than this random number we implemented into the code. Further, with the QMOKE spectroscopy data processing, this fix does not have to be put into use, as we do not use transversal $\boldsymbol{M}$ directions where this problem occurs.

## 3.2 Optical characterization technique - ellipsometry

The Ellipsometry is powerful optical characterization technique that is well known in thin film samples characterization. It can provide information on permittivity, thickness and roughness of each layer in the multilayer stack. In the case of standard ellipsometry (our case), no conversion of *s*-polarized state into *p*-polarized state and *vice versa* is considered, thus it is suitable for isotropic and amorphous sample characterization. For anisotropic case, generalised ellipsometry have to be used. The standard ellipsometry measure ratio of diagonal reflection coefficients $r_{pp}/r_{ss}$. The linearly polarized light at 45°, i.e. composed of *s*- and *p*- polarized wave of the same amplitude and zero phase shift, is incident onto the sample. Each of polarization eigenmodes is then reflected with different amplitude and with different phase, providing elliptically polarized light upon reflection.

$$\frac{r_{pp}}{r_{ss}} = \tan\psi e^{i\delta} \tag{3.2.1}$$

where $\tan\psi$ is ratio of $E_s$, $E_p$ amplitudes upon reflection and $\delta$ shift between them [recall Eq. (2.4.1)].

We use ellipsometry to obtain $\varepsilon_d$ spectral dependence of layers in the sample. If perturbation of permittivity through magnetization is not considered, cubic samples are isotropic and thus ellipsometry is adequate technique for that. All the ellipsometry measurements were carried out on Mueller matrix ellipsometer Woolam RC2 with spectral range 0.7 – 6.4 eV. The measured data are processed within CompleteEASE software [108], that is based on multilayer optical model from Sec. 2.3. Note that there is no possibility to anyhow utilize this software for our MOKE measurements as the permittivity is treated here as scalar and the software is not open source, thus no customisation is possible to the code and only data from Woolam RC2 ellipsometer can be processed here.

To withdraw trustful information from the ellipsometry measurement we have to posses good information about the sample. If permittivity, thickness and roughness of each layer in the sample will be free variable of the fit, those parameters will strongly corelate between each other and the fit will be questionable. In our case we posses information on layers thicknesses and roughnesses from x-ray reflectivity method (described below) and the permittivity function of substrate and capping layer is taken from literature, or measured separately (for those purposes we prepared samples of substrate with capping layer only). Thus, in the ideal case, the permittivity $\varepsilon_d$ of FM layer in our sample is the only variable of the fit. To describe its spectral dependence we usually use B-spline method [109] accompanied with Kramers-Kronig relations. On one hand B-spline is a fast and sturdy method for determining spectra of $\varepsilon_d$, but on the other it does not provide direct information about the electronic structure of the material. This downside is of little importance to us as our data are accompanied by ab-initio calculations, and even so we are interested in MO investigation here. Yet, for such a purpose Lorentz-Drude model would be suitable in case of FM material.

## 3.3 Techniques for sample preparation and structural characterization

In this section we will describe some basic theory needed to understand the preparation process of our samples and the subsequent structural characterization.

### 3.3.1 Techniques for thin film preparation

There are various methods for thin film preparation, but the physical vapour deposition (PVD) and chemical vapour deposition (CVD) are the ones that allow layer-grow control on the atomic scale. The technological aspect of both methods is quite similar. The substrate, the medium on which the layer is growing, is placed into the vacuum chamber together with material precursors or targets. The targets are being vaporized, emitting its particles into the free space of the chamber, followed by deposition of those particles on every surface inside the chamber including the surface of the substrate. In the case of

CVD, there are more precursors that undergo some controlled chemical reaction during the deposition process, whereas in the case of PVD no chemical reaction is present. As we are probing here FM materials that consist of single elements (3d transition metals), or Heusler compounds, the PVD is the technique suitable for us.

The PVD methods are distinguished by the process used for the vaporization of the target's particles into the chamber. Most common methods are e.g. pulsed laser deposition, electron beam evaporation, molecular beam epitaxy or magnetron sputtering. The latter two are the techniques that were used for preparation of the samples investigated in this work and will be discussed below.

For the preparation of crystallographic layers, the substrate plays an important role for the epitaxial growth. Epitaxial means that there is a relation between crystal lattice of the layer and of the substrate. Thus, the layer is supposed to grow as a single crystal with the surface orientation given by the crystal lattice and surface orientation of the substrate. Such a growing process is a must in our case as the orientation of the crystal, thus, the orientation of the permittivity tensor, play a crucial role in our investigations.

### Magnetron sputtering

Magnetron sputtering[2] utilizes ions of inert gas (usually argon) to bombard the target of a material and sputter the atoms or cluster of atoms from the target. To ionize the Ar, the target is negatively charged, emitting high energy electrons into the chamber. Those electrons then ionize the Ar atoms, which become positively charged and are accelerated towards the negatively charged target by the electric field. The magnetron furthermore utilizes a strong magnetic field to trap those electrons in the vicinity of the target and force them to follow helical paths, which results in more ionizing collisions with Ar atoms near the target surface, providing significant boost in the efficiency of the sputtering process. To start the above described process, the right conditions in the chamber must be met, being mostly right Ar pressure and right power at the target. Furthermore, note that above described case is rather valid to well conducting materials, like metals. For dielectric targets, the argon must be ionized through radio frequency waves instead (so called RF sputtering).

In Fig. 3.4 two magnetron sputtering systems from Bielefeld University, which were used for preparation of some of our samples, are described in a nutshell. For further details about magnetron sputtering, see for for example Ref. [110, 111]

---

[2] The word originates from latin word "sputare", which mean "to spit".

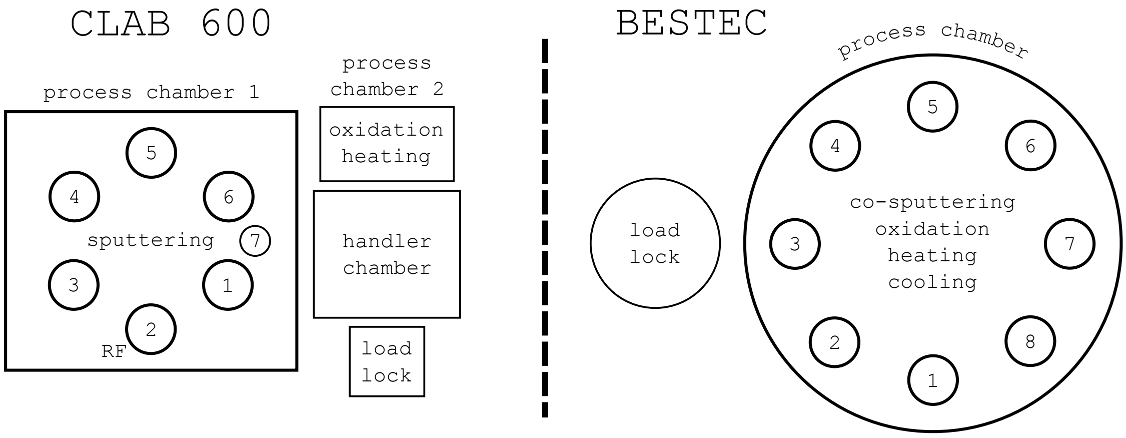

| | CLAB 600 | BESTEC |
|---|---|---|
| base pressure | $1{\cdot}10^{-7}$ mbar | $3{\cdot}10^{-9}$ mbar |
| working pressure | $1 - 25 \cdot 10^{-3}$ mbar | $1 - 25 \cdot 10^{-3}$ mbar |
| magnetrons | 6×4 inch:<br>3×DC for magnetic materials<br>2×DC for conducting materials<br>1×RF for insulating materials<br>1×2 inch:<br>DC for magnetic materials | 8×3 inch:<br>6×DC for magnetic materials<br>2×RF for insulating materials |
| e-beam evaporization | 0 | 1 |
| quartz micro balance | 0 | 1 |
| max. heating | ≈ 400°C | ≈ 1000°C |
| min. distance | <10 cm | 20 cm |

Figure 3.4: Sketch of the two sputtering systems from Bielefeld University and their tabular summary.

#### Molecular beam epitaxy

Molecular beam epitaxy is a method that employs heating of the targets (here rather called filaments) by a Knudsen cell. The material will thus sublime and condensate on the substrate. This method can grow the most pure films, as ultra high vacuum is needed in the chamber and no gasses are present as in case of magnetron sputtering. The deposition rate here is usually very low, allowing good epitaxial growth.

### 3.3.2 Techniques for thin film structural characterization

With the samples prepared by methods discussed above, we need to investigate if the samples grown truly epitaxially in the form of crystalline films. For this purpose, the x-ray diffraction (XRD) has been used. Further, we need to investigate the thicknesses of the layers in our samples for the purpose of further data processing in our optical and MO models. This has been done by x-ray reflectivity (XRR).

### X-ray diffraction

The wavelength of the x-ray radiation is in the range that the atomic structure of the material will serve as a grating on which diffraction of the x-ray EM wave occurs. Thus, each atom of the lattice will serve as a new source of radiation. This can be equivalently understood as x-ray radiation reflecting from each lattice plane in the sample and those reflected rays will interfere with each other. If the path difference of the rays reflected from different planes will induce constructive interference, we will observe diffraction peaks. This is described by the Bragg law

$$2a \sin \Theta = n\lambda \,, \tag{3.3.1}$$

with $a$ as the distance of lattice planes, $\Theta$ as the angle between incident ray and crystallographic planes, which distance is to be probed, and $\lambda$ as the x-ray wavelength (see Fig. 3.5).

The most common XRD measurement is a specular diffraction scan known as $\Theta$–$2\Theta$ scan. Here, the diffracted beam lies within the plane of incidence, spanned by the incident beam and the surface normal, and the condition $\Theta$–$2\Theta$ is fulfilled. Thus, we are sensitive to atomic planes parallel to the sample surface and perpendicular to the $z-$axis of the sample, although this claim is slightly simplified. Our substrates on which the layers are epitaxially grown, are not ideal, e.g. the MgO(001) substrate can have (001) planes slightly tilted with respect to its surface, which is called miscut. The difference is usually no more than a few tenths of degree, yet, if we will not consider the miscut during the alignment of the sample, the difference could cause significant drop in the measured Bragg peak intensity and, thus, it could be problematic to observe Bragg peaks for some thinner layers.

In some cases we also need to investigate the in-plane crystallographic ordering. For example, the Fe(011) layer grown on MgO(111) will have three possible growth directions each rotated by 120° from each other [112] (this is known as twinning). Note that for our 8-directional measurement, this in-plane crystallographic uniformity is quite important. In order to study this, off-specular scans using an Euler cradle can be used. The Euler cradle allows a tilt $\Psi$ of the sample and a rotation $\kappa$ around its normal axis. This actually allows us to probe the whole reciprocal space of the sample measuring $\Theta$–$2\Theta$ scans for a full 360° rotation of $\kappa$ and for every possible angles $\Psi$. However, such a

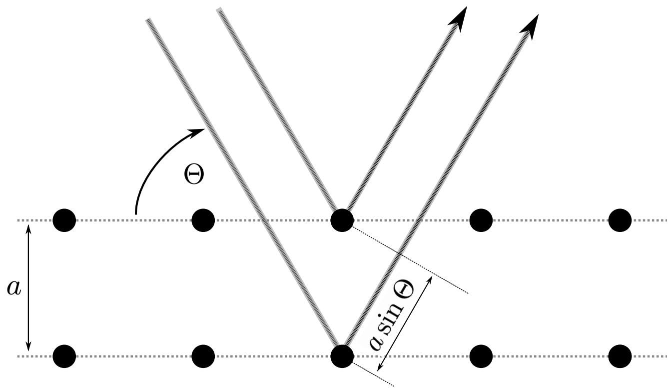

FIGURE 3.5: Sketch of the Bragg condition for x-ray diffraction. $a$ is lattice plane distance, $\Theta$ is angle of incidence with respect to probed crystallographic planes. $a \sin \Theta$ presents half of the path difference possessed by the beam reflected from lower crystallographic plane when compared to beam reflected from the upper crystallographic plane.

measurement would be time demanding. Thus, we usually choose $2\Theta$ to satisfy Bragg condition for a desired peak and then scan $\kappa$ for 360° or 180° rotation for each $\Psi$ that is in the range to cover the vicinity of the selected peak. Such a measurement is then usually graphically presented in a pole figure known as texture map. We will show and discuss those for some of our samples.

All our XRD measurements were carried out by a Phillips X'pert Pro MPD PW3040-60 machine using a Cu-$K_\alpha$ source ($\lambda = 1.5418$ Å).

### X-ray reflectivity

For this technique we use the same equipment as for the XRD method. The difference is that for small angles of incidence $\Theta$ (compared to XRD), ca. $0° - 10°$, the interference of the x-ray radiation on the layers in the multilayer stack will be observable (note that here in XRR we define $\Theta$ with respect to the surface plane and not with respect to surface normal as we do in optics for AoI). The XRR curve, the pattern created by the dependence of reflected intensity on $\Theta$, is defined by thickness, roughness and index of refraction of each layer (in principle the XRR reflection is described by same physics as was presented in Sec. 2.3 dealing with EM wave propagation in multilayers). Nevertheless, the periodicity of oscillation in the XRR curve is mainly given by layer thicknesses in the multilayer stack. Thus, this method is much more reliable for layer thickness investigation than ellipsometry, for example.

In Fig. 3.6 we present a sketch of XRR reflection, with scatering vector $\boldsymbol{q} = \boldsymbol{k}_r - \boldsymbol{k}_i$, where $\boldsymbol{k}_r$ and $\boldsymbol{k}_i$ being the wave vector of reflected and incident wave, respectively. The

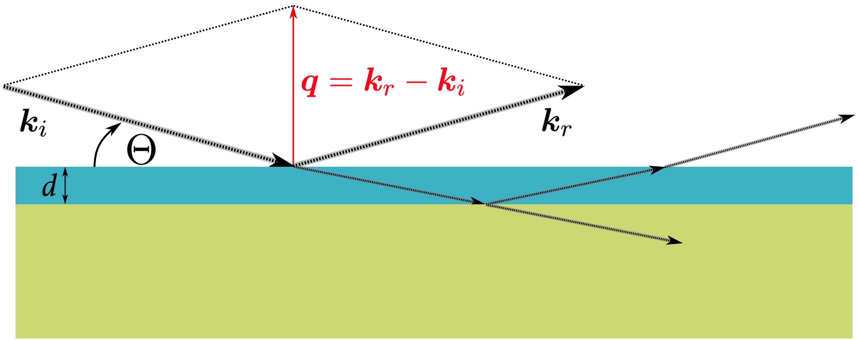

FIGURE 3.6: XRR reflection from a multilayer stack. $d$ is thickness of the layer, $\Theta$ is angle of incidence, $\boldsymbol{k}_r$, and $\boldsymbol{k}_i$ is wave vector of reflected and incident beam, $\boldsymbol{q}$ is scattering vector.

magnitude of $\boldsymbol{k}$ is $|\boldsymbol{k}| = \frac{\omega}{c} = \frac{2\pi}{\lambda}$, thus

$$\boldsymbol{q} = 2|\boldsymbol{k}|\sin\Theta = \frac{4\pi}{\lambda}\sin\Theta. \tag{3.3.2}$$

All our XRR curves will be plotted with dependence on scattering vector $\boldsymbol{q}$. The oscillations with length $\Delta q$ will then originate from the layer of thickness $d = \frac{2\pi}{\Delta q}$.

Further, all our XRR data are analyzed with the open-source program GenX [113] based on the Parratt algorithm [114].

## 3.4 Preparation and characterization of samples investigated in this work

Up to now, only the theory and the description of the experimental techniques and setups used in this work were discussed. In the rest of this chapter, the samples investigated in this work will be introduced. We will describe the preparation of samples and provide all the necessary characterization that is needed for the further MOKE data processing, being XRD, XRR, Ellipsometry and hysteresis loop measurements with remanence magnetic anisotropy measurements.

All the samples presented below are thin film multilayer stacks. In our investigation we probed the following samples or sample series:

- **MgO(001) / Fe(001) / Si** – sample series with variation of thickness (2.5 nm – 30 nm) of the Fe layer, prepared at Bielefeld University by magnetron sputtering. Samples were fabricated mainly to test the QMOKE spectroscopy in general, and to detect the QMOKE spectra of Fe in particular. This series was further accompanied by samples of the same stack composition prepared by MBE at Osnabrück Univeristy in order to compare the Fe MO parameters spectral dependencies obtained from samples prepared by different deposition methods.

- **MgO(001) / Cr(001) / Co$_2$MnSi(001) / Al** – Heusler compound sample series with variation of different post annealing temperatures ($300°C$ – $500°C$), mainly used for QMOKE spectroscopy. A different annealing temperature leads to different ordering ($B2 \rightarrow L2_1$) of this Heusler compound. The effect of different ordering on the spectral dependence of the MO parameters has been investigated. Samples were fabricated at Tohoku University in Sendai by Takahide Kubota.
- **MgO(111) / Fe(011)/ Pt** – several samples prepared by magnetron sputtering at Bielefeld University in order to probe the 8-directional method of FM layers with (011) oriented cubic crystal structures.
- **MgO(011) / Co(011) / Pt** – two samples prepared by magnetron sputtering at Bielefeld University in order to probe the 8-directional method of FM layers with (011) oriented cubic crystal structures.
- **MgO(111) / Ni(111) / Si** – sample prepared by magnetron sputtering at Bielefeld University in order to probe the 8-directional method of FM layers with (111) oriented cubic crystal structures.

The sample stacks are composed of MgO substrate, FM layer and capping layer (Si, Pt or Al) in order to prevent oxidation. In case of Co$_2$MnSi(001) a Cr buffer was used to improve the growth of the Heusler compound.

### 3.4.1 Fe(001) – layer thickness variation series

The series contains nine samples of MgO(001)/Fe(001)/Si/SiO$_x$ thin films multilayer structures. The thickness of the Fe layer vary across the samples in the range of 2.5 nm–30 nm. The Fe layers were grown on MgO(001) substrates at room temperature (RT) using magnetron sputtering (Leybold CLAB 600) in Ar atmosphere of $2.1\cdot10^{-3}$ mbar and with a growth rate of 0.25 nm per second. To prevent oxidation, the Fe layer was capped with approximately 2.5 nm of silicon under the same conditions and with a growth rate of 0.18 nm per second. The thicknesses of the Fe layers we were aiming for are: 2.5 nm, 5 nm, 7.5 nm, 10 nm, 12.5 nm, 15 nm, 20 nm, 25 nm, 30 nm. Those are the nominal thicknesses of the individual samples, which will be used to address the samples in the following. The real thickness of the Fe and Si layers of each sample was

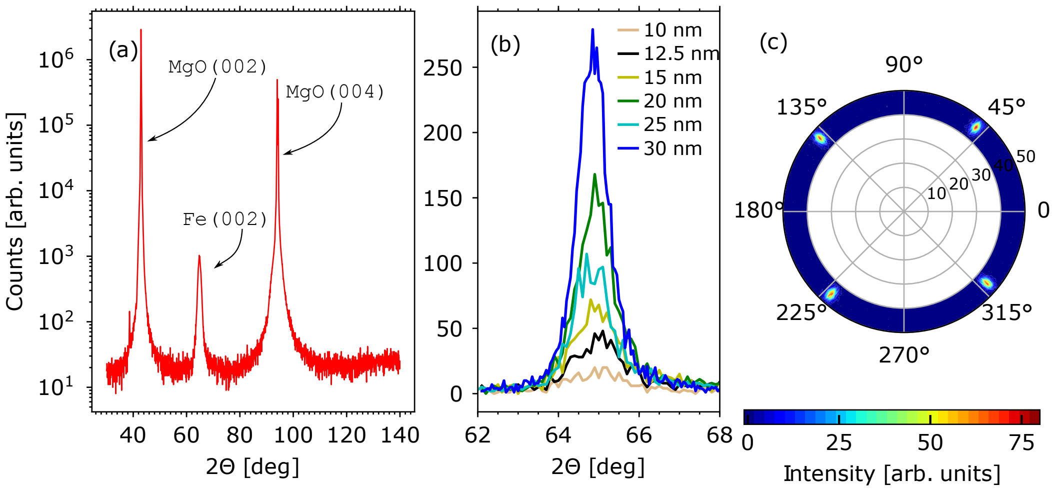

FIGURE 3.7: (a) $\Theta - 2\Theta$ scan of the sample with a nominal thickness of 20 nm for large range of $2\Theta = 30°$-$140°$ (b) XRD $\Theta - 2\Theta$ scans of the samples with a nominal thickness $\geq$ 10 nm. Thinner samples do not provide sufficient peak intensity, due to lack of material in the layer. (c) Off-specular XRD scan (Euler's cradle texture map) is presented for the Fe{110} peaks at $2\Theta = 44.738°$ of the sample with a nominal thickness of 20 nm. The measurement was performed for full 360° sample rotation (angular axis of the plot) with tilt of the sample $\Psi = \langle 40°, 50° \rangle$ (radial axis of the plot).

determined through XRR as will be discussed below. Further, an additional sample of the MgO substrate with only silicon capping was prepared in order to determine the optical parameters of the capping layer independently.

### XRD characterization

In Fig. 3.7 we present various XRD scans that have been performed on this sample series. In Fig. 3.7(a) we see a $\Theta - 2\Theta$ scan of the sample with a nominal thickness of 20 nm in the range of $2\Theta = 10°$-$140°$ and an integration time of 1 s. The peaks are described as marked in the graph. See that the characteristic peak of the Fe layer around $2\Theta = 65°$ is very well pronounced. In Fig. 3.7(b) we show scans around this characteristic peak for other samples in the series with sufficiently thick Fe layer providing a strong enough diffraction peak. For this measurement the integration time was 10 s, yet the intensity of the peaks is much lower than in Fig. 3.7(a). This is due to a lower width of the detector slits, which provide us a better resolution of the peak position. Finally, in Fig. 3.7(c) we show an off-specular texture map. We scan $\Psi$ in the range of 40°–50° for full 360° rotation of $\kappa$ when tuned to $2\Theta = 44.738°$ which corresponds to Fe{110} peak. The plot shows four peaks in 4-fold symmetry with no diffusion ring around. This indicates good epitaxial growth and good in-plane crystalline orientation that is necessary for our QMOKE investigation.

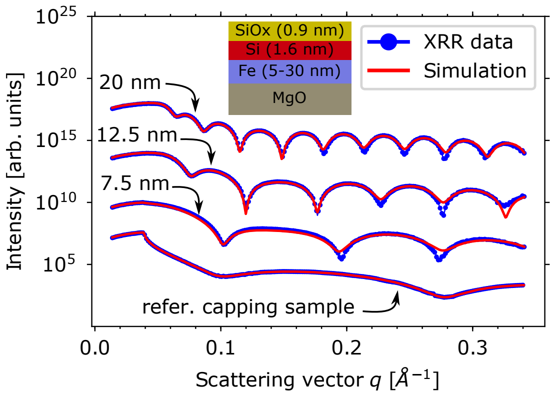

| Nom. thick.[nm] | $d_{\text{Fe}}$ [nm] | $d_{\text{cap}}$ [nm] | $\sigma_{\text{Fe}}$ [nm] | $\sigma_{\text{cap}}$ [nm] |
|---|---|---|---|---|
| 0.0 | - | 3.4 | - | 0.3 |
| 2.5 | 2.5 | 2.1 | 0.0 | 0.0 |
| 5.0 | 4.7 | 2.4 | 0.4 | 0.2 |
| 7.5 | 6.9 | 2.5 | 0.3 | 0.4 |
| 10.0 | 9.4 | 2.7 | 0.0 | 0.6 |
| 12.5 | 11.5 | 2.5 | 0.3 | 0.3 |
| 15.0 | 14.0 | 2.5 | 0.2 | 0.1 |
| 20.0 | 18.4 | 2.6 | 0.0 | 0.5 |
| 25.0 | 23.3 | 2.4 | 0.2 | 0.6 |
| 30.0 | 28.3 | 2.5 | 0.0 | 0.6 |

FIGURE 3.8: Exemplary XRR scans (blue dots) and their simulation (red line) for several samples from the series. The periodicity of oscillations is well described, providing us with reliable information about the thickness $d$ of the layers in the samples. The damping of oscillations is low, suggesting a low roughness $\sigma$ of the interfaces within the samples. The curves are shifted vertically for clarity.

Note that the orientation of the sample in the Euler cradle is rather random, as to align the height of the sample in the setup the sample stage has to be screwed up or down. Thus, the Fig. 3.7(c) cannot be used to determine the Fe[100] in plane direction in the layer (unless the sample position on the sample stage is marked for correction). Nevertheless, this is not necessary in this case, as from the lattice mismatch between Fe and MgO we know that Fe grows 45° rotated with respect to MgO[100] in-plane direction, which is given by the edge of the substrate.

### XRR characterization

Each sample in the series was characterized using XRR. In Fig. 3.8 XRR curves of some exemplary samples are shown. The periodicity of the oscillations is described very well by the model, which provides us with reliable information about the thicknesses of the Fe layers $d_{\text{Fe}}$ and the capping layers $d_{\text{cap}}$. The densities of the layers were fixed parameters of the fit and all values were taken from literature [115, 116]. Because Si and $\text{SiO}_x$ have very similar densities, the thickness of the native silicon oxide could not be clearly determined by XRR. The thickness of silicon oxide was estimated (0.9 nm) with respect to the growth dynamics of the native silicon oxide [117]. In the table presented in the right side of Fig. 3.8 we summarize all the thicknesses and the roughnesses provided by the XRR data fits.

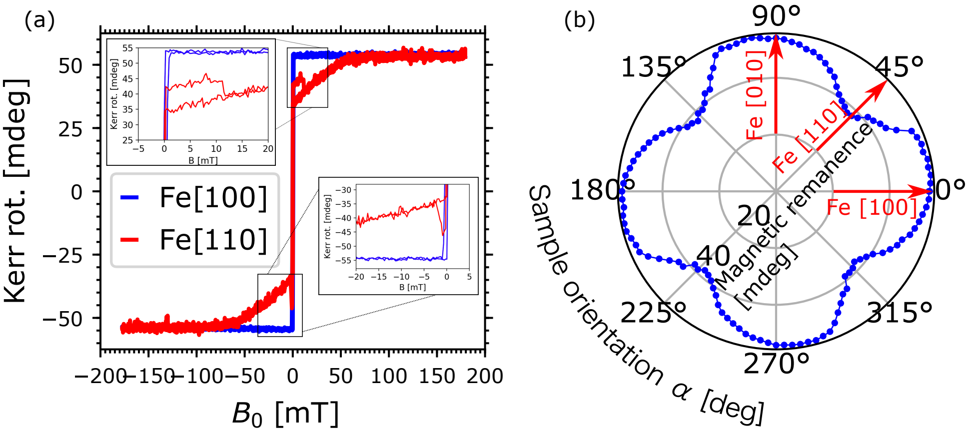

Figure 3.9: Magnetic characterization of the sample with a nominal thickness of 12.5 nm. (a) The LMOKE hysteresis loops at Fe[100] and Fe[110] external field directions. About 75 mT is sufficient to saturate the sample in the in-plane hard axis. (b) In-plane magnetic anisotropy, with the in-plane magnetic easy and hard axes along Fe⟨100⟩ and Fe⟨110⟩ directions, respectively.

### Hysteresis loops and magnetic anisotropy

In Fig. 3.9 (a) we present LMOKE hysteresis loops along Fe[100] and Fe[110] directions measured at $\lambda$=670 nm (1.85 eV). From Fig. 3.9(a), where anisotropy of magnetic remanence is shown, we identify the magnetic easy and hard axes along the Fe⟨100⟩ and Fe⟨110⟩ directions, respectively. From the plot it may be apparent that magnetic easy and hard axes are slightly counter-clockwise rotated with respect to the crystallographic directions. However, this is due to the QMOKE contributions in the MOKE loops as identified in the inset of Fig. 3.9(a), and possibly by slight misalignment of the sample in the setup with respect to $\alpha = 0°$. To keep the sample magnetically saturated in magnetic in-plane hard directions, a magnetic field of ≈75 mT is sufficient. Thus, the magnetic field of 300 mT used within QMOKE spectroscopy is by far enough to keep the sample saturated for any in-plane $\boldsymbol{M}$ direction.

### Optical characterization

The spectra of $\varepsilon_d$ of Fe were determined by a multilayer optical model [104] and processed using CompleteEASE software [108]. In the CompleteEASE software, thicknesses and roughnesses of the layers were stable parameters as determined by XRR measurements. The permittivity of MgO and native SiO$_x$ was taken from the literature [118]. From the measurement of the reference sample (MgO with the Si capping only, with nominal Fe thickness 0 nm), the permittivity of the Si layer was obtained. Thus, with all the Fe layered samples, $\varepsilon_d$ of the Fe layer was the only unknown and free variable of the fit. The spectral dependence of the imaginary part of $\varepsilon_d$ were described by B-spline [109],

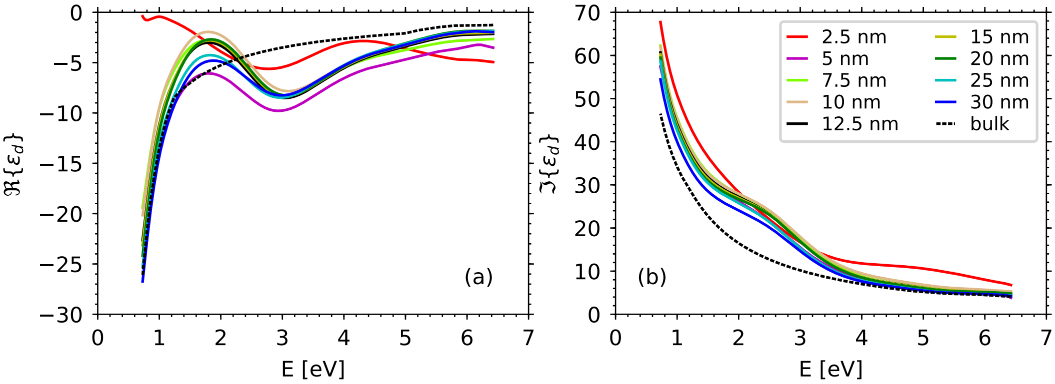

FIGURE 3.10: The (a) real and (b) imaginary part of $\varepsilon_d$ of the Fe layers. Black dashed lines are the $\varepsilon_d$ of Palik [118] and were used as an initial guess for the fit of the $\varepsilon_d$ of the Fe layers for all the samples (full, coloured lines).

while complementary spectra of the real part were determined through Kramers-Kronig relations.

The resulting spectra of the real and imaginary part of Fe layers are presented in Fig. 3.10 (a) and (b), respectively. Only the sample with a nominal thickness of 2.5 nm is deviating from the others, which could possibly be due to low crystallographic quality of the film. Note that the characteristic peak at 2.5 eV in the imaginary part of spectra is not present in the spectra taken from literature (by Palik [118]). Nevertheless, the presence and position of this peak is fully consistent with other reports and with our ab-initio calculations as shown in Fig. 5.6 presented in Chapter 5.

### Complementary samples prepared by MBE

Furthermore, another set of MgO(001)/Fe(001)/ Si samples were prepared by MBE method by our colleagues Jannis Thien and Olga Kuschel from Osnabrück University. The samples of that series were characterized in the same way as described above. Since the preparation and structural characterization of the MBE grown Fe films was the main part of Jannis Thien's Bachelor thesis [119], we just summarise the results here.

Fe and Si films were prepared on single crystalline MgO(001) substrates. Prior to deposition, the substrates were annealed at 400°C for 1h in a $1{\cdot}10^{-4}$ mbar oxygen atmosphere to remove carbon contamination and obtain defined surfaces. Fe films were deposited by thermal evaporation from a pure metal rod at a substrate temperature of 250°C. Silicon capping layers were evaporated at room temperature using a crucible. The deposition rates of 1.89 and 0.3 nm/min for Fe and Si, respectively, were used and controlled by a quartz microbalance next to the source. The base pressure in the UHV chamber was $10^{-8}$ mbar.

One of the samples from the this series was used for QMOKE spectroscopy processing in order to compare QMOKE spectroscopy results of samples prepared by two different techniques. Through XRR measurements we determined a thickness of the Fe layer to 12.6 nm and thickness of the Si+SiO$_x$ capping layer to 8.1 nm. XRD $\Theta - 2\Theta$ scan was performed to check that the sample is of good crystalline quality [119].

### 3.4.2 Co$_2$MnSi(001) – post annealing temperature variation series

The Heusler compound Co$_2$MnSi is a half-metallic ferromagnet [120, 121] with a band gap of 0.4 to 0.8 eV [122, 123] and Curie temperature of 985 K [124]. It was demonstrated that the magnetic properties of Heusler compounds depend on crystallographic ordering [125]. Co$_2$MnSi provides a transition from $B2$ to $L2_1$ crystallographic ordering with increasing annealing temperature [16, 29, 126]. In case of $L2_1$ the lattice is composed of four interpenetrating fcc sublattices, where two of them are occupied by Co atoms [positions ($\frac{1}{4}$, $\frac{1}{4}$, $\frac{1}{4}$) and ($\frac{3}{4}$, $\frac{3}{4}$, $\frac{3}{4}$)] and another two by Mn and Si atoms [positions (0,0,0) and ($\frac{1}{2}$, $\frac{1}{2}$, $\frac{1}{2}$)], respectively. The dependence of $L2_1$ ordering on annealing temperature for Co$_2$MnSi Heusler compounds has been reported in Ref. [16].

This sample series was prepared by Takahide Kubota from Tohoku University in Sendai. The samples consists of a 30 nm-thick Co$_2$MnSi layer grown on a MgO(001) crystal substrate with 40 nm thick Cr buffer layer. To prevent oxidation 1.3 nm thick Al capping layer is used. The samples were grown by inductively coupled plasma-assisted magnetron sputtering. Each sample was annealed *in situ* at different temperature, being 300°C, 350°C, 400°C, 450°C, 475°C and 500°C.

#### XRD & XRR characterization

The detailed structural characterization of those samples is discussed in detail in literature by Wolf *et al.* [29], where the information about Heusler compound ordering is obtained through off-specular Euler cradle measurements of Co$_2$MnSi {220} peaks and Co$_2$MnSi {111} peaks. The results of those XRD investigations show that annealing at higher temperatures promotes higher degree of $L2_1$ ordering. Namely, with samples annealed at 300°C and 350°C no $L2_1$ ordering was observed. First change of crystallographic ordering to $L2_1$ structure occurs at 400°C and gets stronger with higher annealing temperatures [16, 29]. Here, in Fig. 3.11, we show our $\Theta$-$2\Theta$ scan in the range of $2\Theta = 25° - 95°$ (140°) for the sample annealed at 300°C (500°C). From the description of peaks within the figure, we can see that samples are indeed of good crystalline quality.

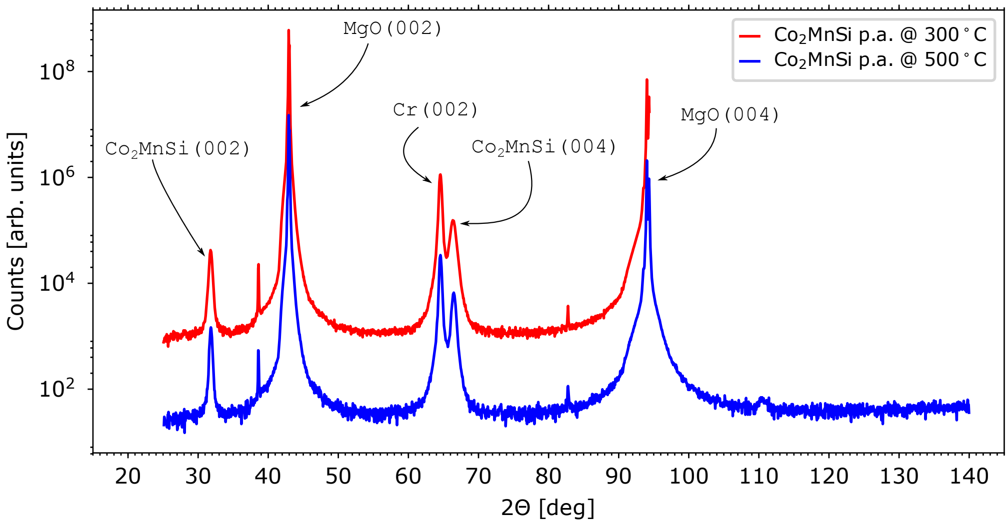

FIGURE 3.11: X-ray diffraction Θ-2Θ scan for the $Co_2MnSi$ samples annealed at 300°C and 500°C.

The thicknesses of the layers of the samples provided by Wolf *et al.* [29] and mentioned above in the text do not seem to be exact numbers, but rather estimated from growth rate and deposition time. However, small deviations from the reported values should not be too crucial for our investigation. In Fig. 3.12 we present XRR data for samples annealed at 300°C and 500°C. The thickness of the Cr buffer layer and of $Co_2MnSi$ is close to the estimated values, but the Al capping thickness is much larger than reported (see the table in the right side of the Fig. 3.12). This may be connected to the fact that the samples are already some years old, thus aluminium oxide has formed in the capping layer which could have lead to larger thicknesses. On the other hand, in the XRR curve of the 500°C annealed sample, the Kiessig oscillations with the longest period (presumably caused by the capping layer), are not described very well by the fit, thus the information on the Al cap thickness has some additional uncertainty.

### Hysteresis loops and magnetic anisotropy

In Fig. 3.13 (a) and (b) we show the hysteresis loops of the samples annealed at 300°C and 500°C, respectively. In Fig. 3.13 (c) the Kerr magnetic remanence pole figure is displayed. We can see in-plane magnetic easy and hard axes, parallel to $Co_2MnSi$ $\langle 110\rangle$ and $\langle 100\rangle$ directions, respectively (which is in agreement with previous findings [29]). Note that the orientation of the in-plane easy and hard axes does not change upon annealing. Further, a magnetic field of 300 mT used within our spectroscopic setup is by far enough to magnetically saturate the sample in any in-plane magnetization direction,

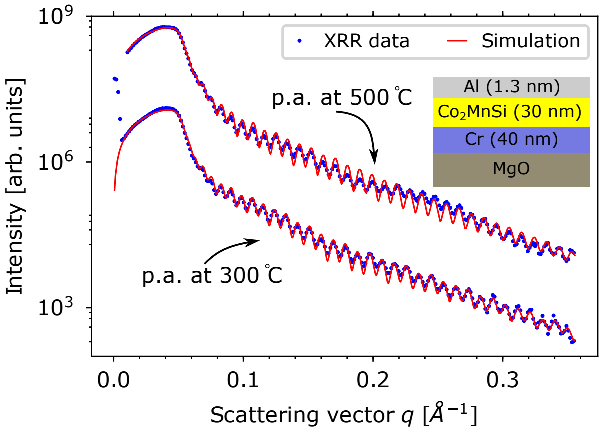

| | p.a. at 300°C | p.a. at 500°C |
|---|---|---|
| $d_{\mathrm{Cr}}$ [nm] | 38.5 | 37.1 |
| $d_{\mathrm{Co_2MnSi}}$ [nm] | 25.9 | 26.7 |
| $d_{\mathrm{Al}}$ [nm] | 5.1 | 3.7 |
| $\sigma_{\mathrm{Cr}}$ [nm] | 0.5 | 0.7 |
| $\sigma_{\mathrm{Co_2MnSi}}$ [nm] | 0.4 | 0.4 |
| $\sigma_{\mathrm{Al}}$ [nm] | 1.0 | 1.4 |

FIGURE 3.12: Exemplary XRR scans (blue dots) and their simulations (red lines) for two samples from the series. The damping of oscillations is low, suggesting a low roughness of the interfaces within the samples. The curves are shifted vertically for clarity.

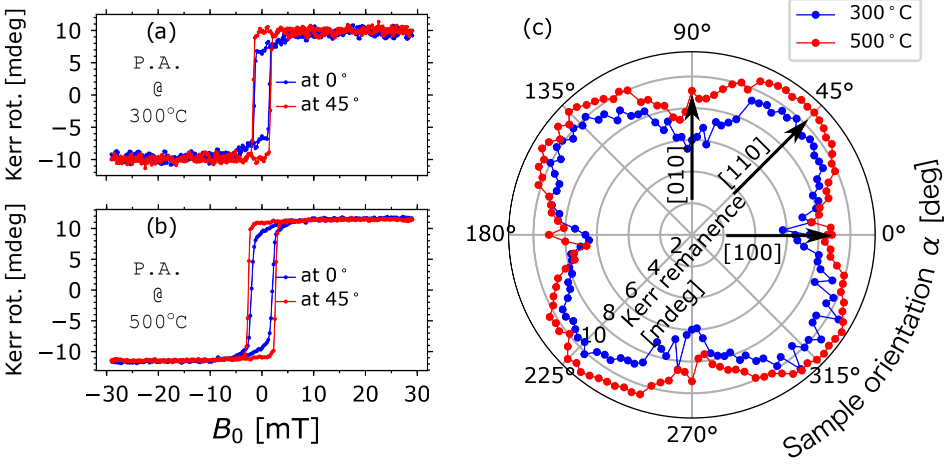

FIGURE 3.13: LMOKE loops at a wavelength of 670 nm of the sample that was post annealed at (a) 300°C and (b) 500°C. Loops were interpolated and divided into odd and even part, only odd part of the loop is shown here. (c) Kerr remanence pole figure of samples anealed at 300°C and 500°C. The crystallographic directions ⟨110⟩ and ⟨100⟩ in the $Co_2MnSi$ layer are directed towards the in-plane magnetic easy and hard axes, respectively.

since a magnetic field of less then 25 mT is needed to saturate the samples in its in-plane hard axis [Fig. 3.13 (a) and (b)].

### Optical characterization

The optical characterization of this samples were carried out by my colleague Daniel Král from Charles University in Prague. The optical response of the samples were measured using a dual rotating compensator RC2 Woollam ellipsometer. The measurements

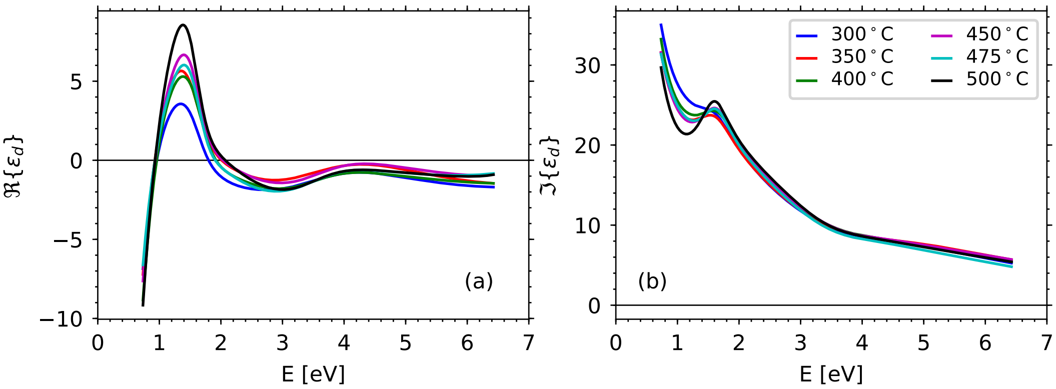

FIGURE 3.14: Real (a) and imaginary (b) part of the spectral dependence of $\varepsilon_d$ of all $Co_2MnSi$ samples.

were carried out in reflection mode with the angles of incidence 60°, 65°, 70°. Prior to each measurement, the samples were cleaned using UV spectroscopy-grade (99.8% purity) ethanol. The spectral dependencies of the ellipsometric parameters $\psi$ and $\delta$ were obtained in the spectral range of 0.7 eV–6.5 eV. The spectra of diagonal permittivity in the 0th order $\varepsilon_d$ were calculated from $\psi$ and $\delta$ using the Drude model and three Lorentzian oscillators to describe the electron transitions located at approximately 1.7, 1.8 and 5.5 eV. The spectra were processed using the CompleteEase software. The real part of the spectra of $\varepsilon_d$ is shown in Fig. 3.14(a) and the imaginary part of the spectra of $\varepsilon_d$ is shown in Fig. 3.14(b).

### 3.4.3 Fe(011) samples grown on MgO(111) substrates

Multiple samples of MgO(111)/Fe(011)/Pt (or Si) have been prepared by magnetron sputtering (Bestec system). For each sample, slightly different deposition conditions were chosen. We pick to present here three samples, named as RS210917, RS260917 and RS020718. Sample RS210917 seemed to be of very good crystalline quality, yet its MOKE investigations show some unexpected and interesting results, as will be discussed later in the text in Chapter 4.

The MgO(111) substrate treatment and Fe layer growth process was inspired by Ref. [127] and Ref. [112], respectively. Each of the MgO(111) substrates was ultrasonically cleaned in acetone, isopropanol and ethanol for 15-20 minutes in each of the solvents. Immediately after, the substrate was dried in $N_2$ atmosphere and transfered to the deposition chamber. Here, each substrate was annealed at ca. 700°C[3] for 120 min at a base pressure of $8{\cdot}10^{-8}$ mbar. From this point onwards the preparation of each sample varied.

---

[3] Temperature at heater set to 850°C, which should provide a temperature of ca. 700°C at the substrate carrier following the temperature calibration curve of the sample holder.

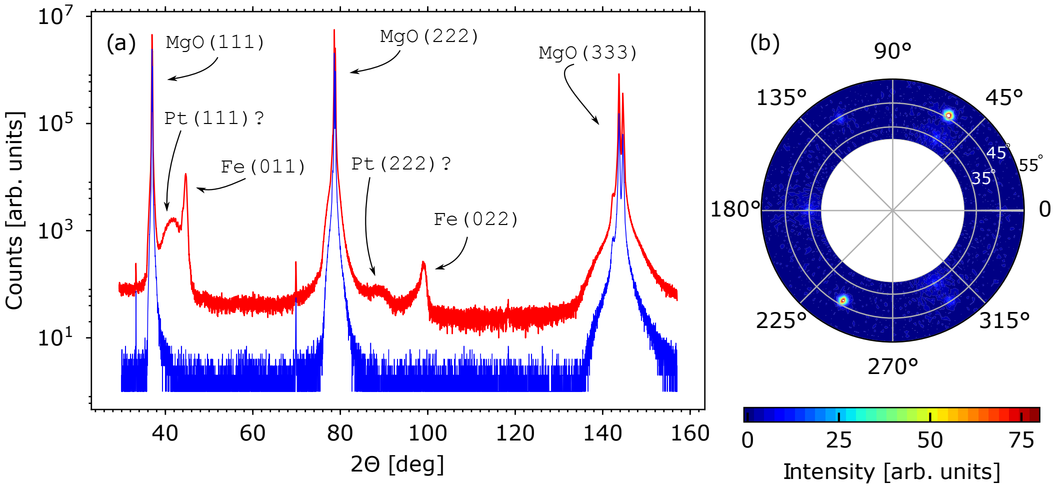

FIGURE 3.15: (a) XRD Θ–2Θ scan of the sample RS210917 (red colour). The scan represented by blue colour is of pure MgO(111) substrate. (b) The off-specular texture map of Fe{001} peaks with $\Psi = \langle 30°, 55° \rangle$ and $2\Theta = 65.518°$.

The Fe layer of the sample RS210917 was grown at 300°C with an Ar pressure of $2.2{\cdot}10^{-3}$ mbar. The deposition process took 390 s with a growth rate of 0.0512 nm/s providing us a ca. 20 nm thick layer. Afterwards, the sample was cooled down to RT and a Pt capping layer was sputtered for 22 s with a growth rate of 0.09 nm/s, which should result in a 2 nm thick Pt capping layer. In the case of the sample RS260917, the only difference was that the Fe layer was grown at 580°C and the deposition took 220 s (ca. 11 nm thick). Also, the capping layer was deposited at a slightly higher temperature of 40°C.

The third presented sample was prepared with time-distance of almost a year from the first two. The Fe layer was also grown at 580°C but the growth rate was not calibrated and only estimated from previous numbers. The Fe target was sputtered with half a power on the magnetron compared to previous samples. The deposition time was 1800 s, which should result in a Fe layer dozens of nm thick. The Ar pressure during the deposition was $9.7{\cdot}10^{-3}$ mbar and the Si capping layer was used instead of Pt.

For the Fe(011) layer grown on MgO(111) there are 3 possible in-plane growth directions rotated by 120° from each other. Nevertheless, it is possible that one of those direction could be preferable due to miscut of the substrate, as proposed by Mattson *et al.* [112]. Yet, all three samples were post annealed *ex-situ* at 500°C for 60 min in a magnetic field of 650 mT in hope of recrystallization towards a single in-plane Fe[011] direction.

### XRD & XRR

The XRD specular Θ–2Θ scan of the sample RS210917 is presented in Fig. 3.15(a). Characteristic peaks of the Fe(011) layer, located at $2\Theta = 44.65°$ and $2\Theta = 99.11°$

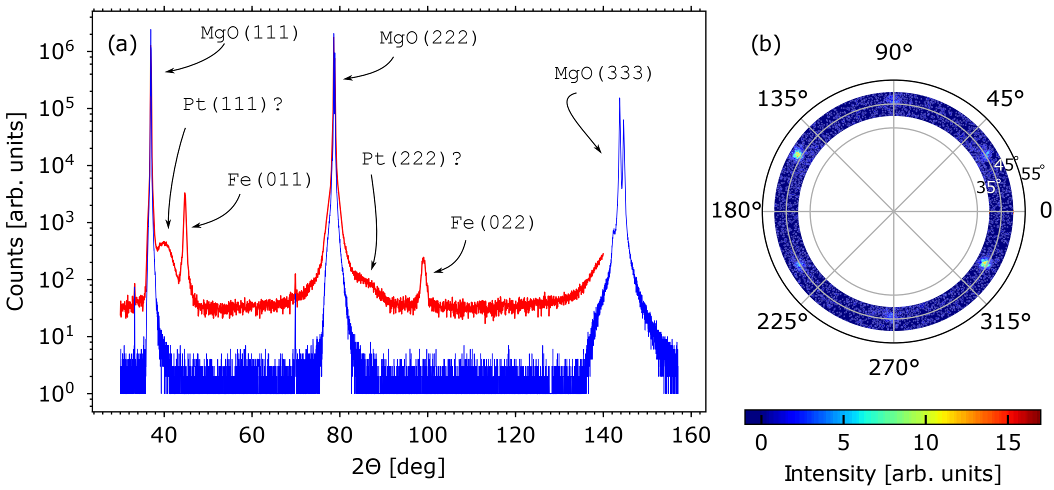

Figure 3.16: (a) XRD Θ–2Θ scan of the sample RS260917 (red colour). The scan represented by blue colour is of pure MgO(111) substrate. (b) The off-specular texture map of Fe{001} peaks with $\Psi = \langle 40°, 50° \rangle$ and $2\Theta = 65.096°$.

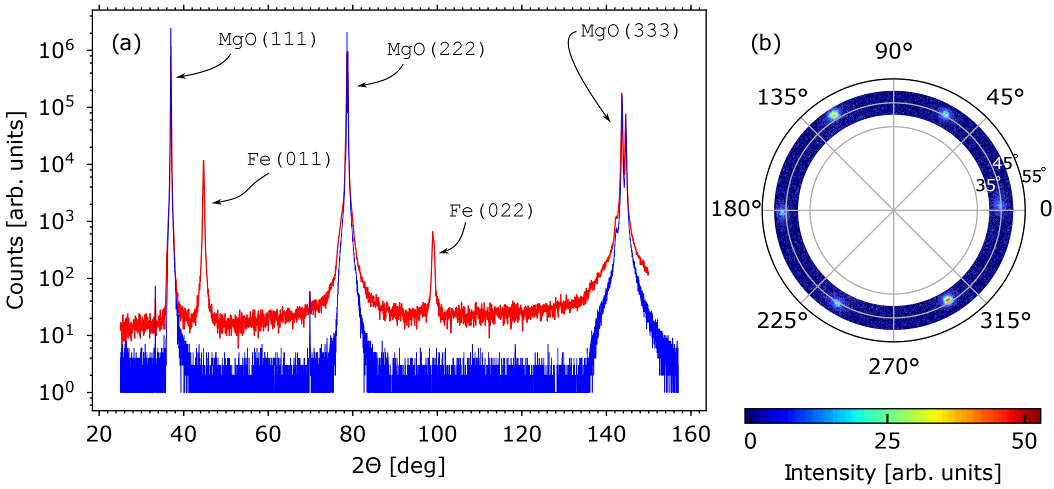

Figure 3.17: (a) XRD Θ–2Θ scan of the sample RS020718 (red colour). The scan represented by blue colour is of pure MgO(111) substrate. (b) The off-specular texture map of Fe{001} peaks with $\Psi = \langle 40°, 50° \rangle$ and $2\Theta = 65.082°$.

are very well pronounced. We attributed remaining two peaks at $2\Theta = 41.50°$ and $2\Theta = 89.20°$ to the Pt(111) capping layer, although those peaks are 1.3° and 5° away from the positions reported at the Materials Project website [128], respectively. Though, the crystallographic structure of the capping layer is of no significance to our research. In Fig. 3.15(b) we present an off-specular texture map. The scan is performed with $\Psi = \langle 30°, 55° \rangle$ and full 360° rotation of $\kappa$ when tuned to $2\Theta = 65.518°$ corresponding to Fe{001} peaks. Only two significant peaks are present at $\Psi = 45°$ separated by 180° in $\kappa$, confirming well grown Fe(011) layer with almost no in-plane twinning.

In Fig. 3.16(a), the specular Θ–2Θ scan of the sample RS260917 is presented. The scan is almost identical to the previous case with negligible change in the position of the Fe(011) characteristic peaks and minor change in the position of the first Pt(111) peak, being $2\Theta = 49.92°$. The second peak of Pt(111) is very broad and weak. The texture map of this sample, presented in Fig. 3.16(b), have been measured with $\Psi = \langle 40°, 50° \rangle$, full 360° rotation of $\kappa$ and $2\Theta$ fixed to 65.096°. In addition to a set of two pronounced peaks separated by 180° in $\kappa$ we may notice here additional 4 peak, where all 6 peaks are separated by 60° in $\kappa$. This indicate in-plane twinning in the layer, although one of the twins clearly predominates.

Finally, the XRD specular $\Theta$–$2\Theta$ scan of the sample RS020718 is presented in Fig. 3.17(a). The characteristic peaks of the Fe(011) layer are again well pronounced and with negligible change in peak positions with respect to previous samples. For the capping layer, Si was used, thus obviously no Pt(111) peaks can be observed. Figure 3.17(b) presents the texture map scan with $\Psi = \langle 40°, 50° \rangle$, full 360° rotation of $\kappa$ and $2\Theta$ fixed to $2\Theta = 65.082°$. In this case, the twinning in the sample is most pronounced, as all 6 peaks separated by 60° in $\kappa$ are of comparable amplitude. Thus, this sample is only presented here to show that substantial twinning can occur when Fe(011) layer is grown on MgO(111) substrate, and we will not use this sample in further investigations and analysis of the 8-directional method.

The XRR curves of all three samples are shown in Fig. 3.18. We were only able to extract reliable information from the sample RS210917, as the latter two samples seem to have too large roughnesses for any ongoing Kiessig oscillations to appear. Although we present the simulation for the XRR curve of the sample RS260917, it should be taken with care, as we have to change the density of the Fe layer by 30% and the extracted thickness of the Fe layer $d_{\mathrm{Fe}}$ does not correspond with thickness estimated through deposition time and growth rate. We ware not able to describe the XRR curve of RS020718 by any reasonable model.

### Magnetic characterization

The magnetic characterization through MOKE hysteresis loops and remanence magnetic anisotropy measurements is presented in Fig. 3.19 for the sample RS210917 and in Fig. 3.20 for the sample RS260917.

Figure 3.19(a) shows the hysteresis loops at the sample orientation $\alpha = 0°$ and $\alpha = 90°$. Both loops are clearly magnetically saturated at a magnetic field of 200 mT. In Fig. 3.19(b) we show the same loops for a smaller magnetic field region. Here one can clearly recognize that the loops are not symmetric. With the assumption of fully antisymmetric $\boldsymbol{M}$ reversal, this odd in $\boldsymbol{M}$ contribution to the loops can be attributed

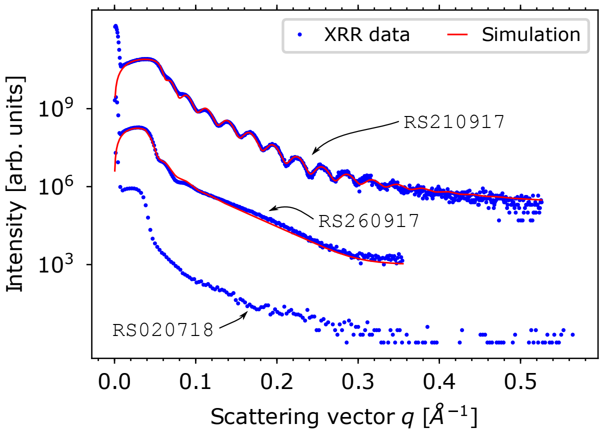

| | RS21. | RS26. |
|---|---|---|
| $d_{\mathrm{Fe}}$ [nm] | 20.1 | 18.4 (?) |
| $d_{\mathrm{Pt}}$ [nm] | 1.8 | 1.9 |
| $\sigma_{\mathrm{MgO}}$ [nm] | 0.6 | 1.7 |
| $\sigma_{\mathrm{Fe}}$ [nm] | 0.1 | 0.5 |
| $\sigma_{\mathrm{Pt}}$ [nm] | 0.9 | 0.4 |

FIGURE 3.18: XRR characterization of Fe(011) samples. The simulation of the RS210917 XRR curve provides reliable information, whereas the simulation of the RS260917 sample should be taken with care, as the fit parameters bounds have to be very loose to enable a sufficient matching between experimental data and simulation fit. We were not able to describe the XRR curve of RS020718 by any model.

to QMOKE. Thus, we separated the loops to its odd and even parts in $\boldsymbol{M}$ according to Eq. (3.1.7), being presented in Figs. 3.19(c) and (d), respectively. We show two magnetic field loops which have unusual remanence values with respect to the angular dependence presented in Fig. 3.20(e). The remanence magnetic anisotropy suggests one major easy in-plane axis and one hard in-plane axis rotated by 90° with respect to each other. In addition, there are two minor easy in-plane axes, each tilted by ca. 15° from the hard in-plane axis. We show comparison of remanence magnetic anisotropy yielded from raw loops of Fig. 3.19(a) and from odd loops from Fig. 3.19(c). Only negligible changes can be observed. However, we further applied a similar set of measurements as needed for the vector MOKE technique [17], i.e. measurements of loops with $s$- and $p$- polarized light for external magnetic field parallel and perpendicular to the plane of incidence and with AoI of 45° and 0°. Here, we found out that the magnetization reversal is not fully antisymmetric in the range of $\alpha = \langle 356°, 12° \rangle$ and $\alpha = \langle 174°, 192° \rangle$ as indicated in Fig. B.1 in the Appendix B. Therefore, it is not justified to use the separation process of Eq. (3.1.7) here, and loops that were separated as odd in $\boldsymbol{M}$ can still possess some QMOKE contribution. Nevertheless, the measurements of the hysteresis curves with normal AoI indicate that some out-of-plane component of $\boldsymbol{M}$ could be present during the magnetization reversal process for some sample orientations $\alpha$. This would contribute to the measured signal in form of PMOKE, which will have some implications for the 8-directional method measurement of this sample which will be discussed in Sec. 4.2.3. For more details concerning antisymmetric reversal process and contribution of PMOKE, see Appendix B.

In Fig. 3.20(a) we show hysteresis loops of the sample RS260917, which are surprisingly

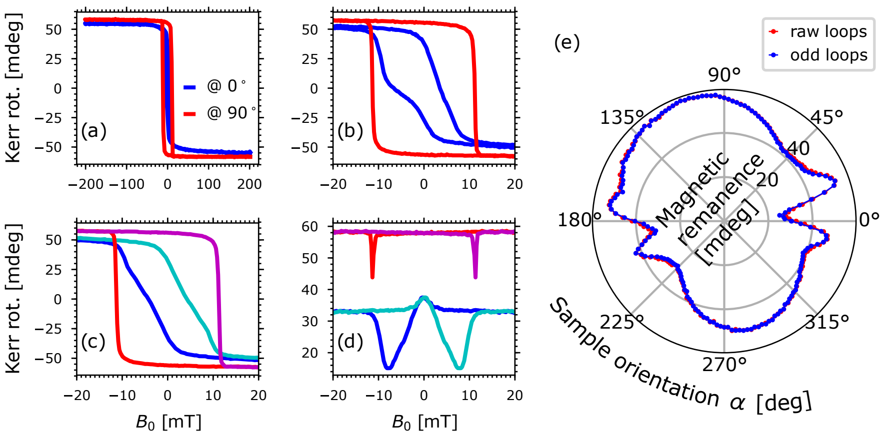

FIGURE 3.19: MOKE magnetic characterization of the sample RS210917 at a wavelength of 670 nm. (a) Hysteresis loops measured for the sample orientation $\alpha = 0°, 90°$. (b) Close-up of those loops. (c) Odd part of the loops and (d) even part of the loops. Remanence magnetic anisotropy presented in (e) when yielded from raw loops (b) and from odd loops (c).

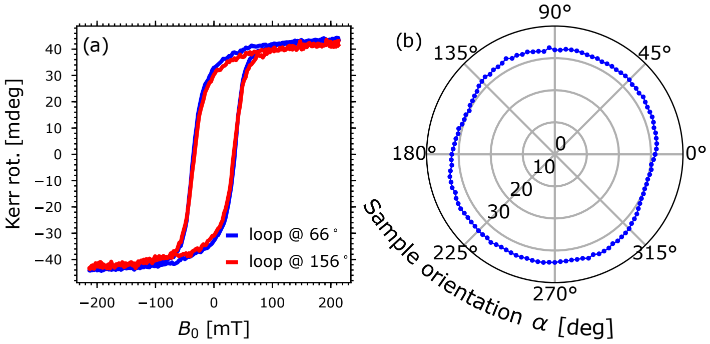

FIGURE 3.20: MOKE magnetic characterization of the sample RS260917 at a wavelength of 670 nm. (a) Hysteresis loops measured for the sample orientation $\alpha = 66°$ and 156°. (b) Remanence magnetic anisotropy.

substantially different from the loops of sample RS210917. It seems that the sample is not magnetically saturated even at a magnetic field of 200 mT and also its coercivity is considerably larger than for the previous sample. The shape of the remanence magnetic anisotropy does not posses such an unusual shape anymore, and we can identify a small difference between the remanence at $\alpha = 66°(+180°)$ and $\alpha = 156°(+180°)$, which may correspond to a magnetic easy and hard axis, respectively. Such a two fold magnetic anisotropy is expected for a (011) oriented surface and the fact that it is not much pronounced could be attributed to some twinning in the layer as indicated by Fig. 3.16(b). We did not apply decomposition of the loops into its odd and even parts in $\boldsymbol{M}$, as the loops look symmetric with respect to origin, thus the correction to the magnetic remanence plot would be negligible.

### 3.4.4 Co(011) samples grown on MgO(011) substrates

The deposition process of Co(011) epitaxial layers on Mg(011) substrates was inspired by Ref. [129]. The MgO(011) substrates were ultrasonically cleaned in acetone, isopropanol and ethanol for 15 minutes in each of the solvents and dried in $N_2$ atmosphere. Immediately afterwards, the substrates were transfered to the deposition chamber and *in situ* annealed at 660°C for 120 min. The Co layer was deposited at a substrate temperature of 300°C and Ar pressure of $2.1{\cdot}10^{-3}$ mbar and a growth rate of 0.064 nm/s. Two samples were prepared, one with a deposition time of 312 s and other with a deposition time of 110 s resulting in samples with ca. 20 nm and ca. 7 nm thick Co layer, respectively. The deposition of a 2 nm thick Pt capping layer (growth rate 0.09nm/s and deposition time 22 s) took place at RT. The samples were then *ex-situ* annealed at 500°C in a magnetic field of 650 mT.

In Fig. 3.21(a), we show the XRD $\Theta$–$2\Theta$ specular scans for both samples. The characteristic Co(011) peak is present only for the sample with a nominal thickness of 20 nm. In Fig. 3.21(b), the off-specular scan is presented for the sample with a nominal thickness of 20 nm. The sample was aligned on the Euler cradle in such a way that the MgO edge was parallel to the $y$ axis of our coordinate system at $\alpha = 0$. The $\Psi$ was scanned in the range $\langle 30°, 55° \rangle$ for full 360° rotation of $\kappa$, when tuned to the Co$\{200\}$ peaks at $2\Theta = 51.615°$. Two peaks at $\Psi = 45°$ in two-fold symmetry indicate a well grown Co (011) epitaxial layer. The XRR curve of the 20 nm thick Co(011) sample is presented in Fig. 3.22, where on the right side the results of the fit are summarized in the table.

The magnetic characterization is presented in Fig. 3.23. In Fig. 3.23(a) we show magnetic field loops at $\alpha = 12°$ and $\alpha = 102°$ and in Fig. 3.23(b) we show a close-up of the $\boldsymbol{M}$ reversal of the same loops. In Fig. 3.23(c) and (d) we present odd and even in $\boldsymbol{M}$ part of those loops, that were separated according to Eq. (3.1.7). The two loops were chosen with respect to the shape of the remanence magnetic anisotropy plot, presented in Fig. 3.23(e). Its shape has just minor correction when yielded from the raw loops from Fig. 3.23(a) or from odd loops from Fig. 3.23(c). The shape indicates well pronounced easy and hard in-plane magnetic axes, although 12° rotated from the position where we would expected it to be compared to the off-specular XRD scan presented in Fig. 3.21(b). It seems that for the magnetic hard axis at $\alpha = 12°(+180°)$, the sample is not yet fully saturated with a magnetic field of 235 mT, which will make it problematic to use this sample for 8-directional investigation in our vector MOKE setup.

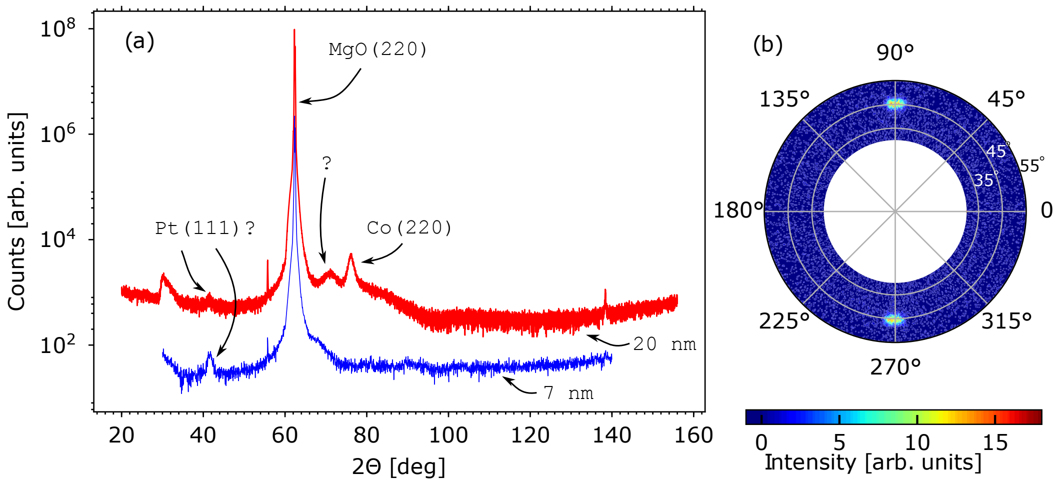

FIGURE 3.21: (a) XRD Θ–2Θ scan of the Co(011) sample with a nominal thickness of 20 nm (red colour) and with a nominal thickness of 7 nm (blue colour). Only the 20 nm thick sample provides a characteristic Co(011) peak. (b) The off-specular texture map of Co{002} peaks with $\Psi = \langle 30°, 55° \rangle$ and $2\Theta = 51.615°$.

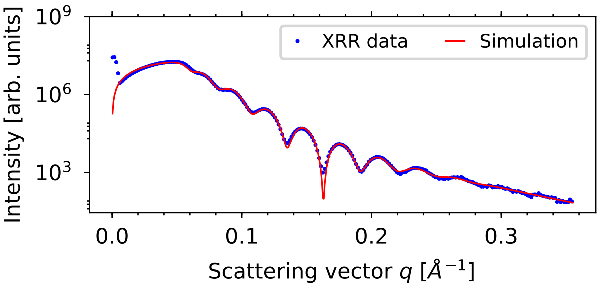

| | |
|---|---|
| $d_{\mathrm{Co}}$ [nm] | 18.0 |
| $d_{\mathrm{Pt}}$ [nm] | 2.6 |
| $\sigma_{\mathrm{MgO}}$ [nm] | 0.5 |
| $\sigma_{\mathrm{Co}}$ [nm] | 2.3 |
| $\sigma_{\mathrm{Pt}}$ [nm] | 1.3 |

FIGURE 3.22: XRR curve and its simulation of the Co(011) sample with a nominal thickness of 20 nm. Results of the fit are summarized in the table on the right side of the figure.

### 3.4.5 Ni(111) sample grown on MgO(111) substrate

For the (111) orientation, only a single sample was prepared. The deposition process was inspired by Ref. [127]. The substrate was ultrasonically cleaned in acetone, isopropanol and ethanol for 15 minutes in each of the solvents and dried in $N_2$ atmosphere. The substrate was then *in-situ* annealed for 60 min. at ca. 800°C – 850°C. The Ni layer was deposited 350°C with an Ar pressure of $2.1 \cdot 10^{-3}$ mbar and a growth rate of 0.066 nm/s resulting in ca. 22 nm thick layer after a deposition time of 333 s. An approximately 4 nm thick Si capping layer was sputtered at RT with a growth rate of 0.0374 nm/s and a deposition time of 107 s.

The XRD Θ–2Θ specular scan is shown in Fig. 3.24(a). The blue curve belongs to a pure MgO(111) substrate, whereas the red curve is of the Ni(111) sample. The characteristic peaks of Ni(111) at $2\Theta = 44.55°$ and Ni(222) at $2\Theta = 98.67°$ show good epitaxial growth

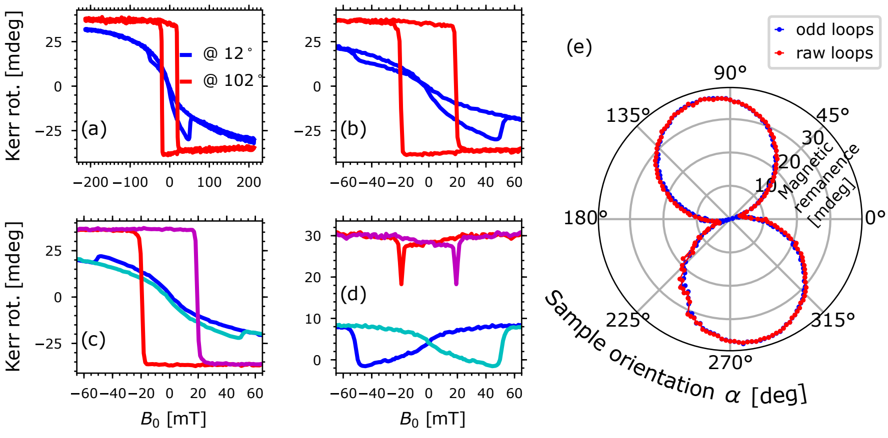

FIGURE 3.23: Magnetic characterization of Co(011) sample with a nominal thickness of 20 nm at a wavelength of 670 nm. (a) Magnetic field loops measured at a sample orientation of $\alpha = 12°$ and $\alpha = 102°$, which corresponds to magnetic in-plane hard and easy axis, respectively. (b) Close-up of the magnetic field loops which were separated into their (c) odd and (d) even parts. (e) Remanence magnetic anisotropy yielded from raw loops (a) and odd loops (c).

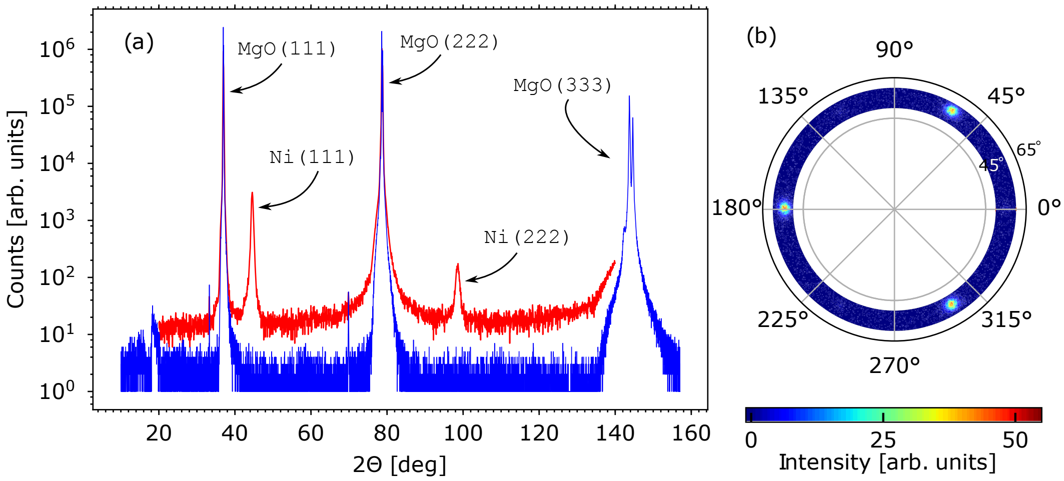

FIGURE 3.24: (a) XRD Θ–2Θ scan of the Ni(111) sample (red colour). The scan represented by blue colour is of a pure MgO(111) substrate. (b) The off-specular texture map of the Ni{002} peaks with $\Psi = \langle 50°, 60° \rangle$ and $2\Theta = 52.809°$.

of the Ni layer. In Fig. 3.24(b), we show the off-specular texture map for $\Psi = \langle 50°, 60° \rangle$ and full 360° rotation of $\kappa$ when tuned to $2\Theta = 52.809°$, which corresponds to the Ni{002} peaks. Three peaks in a three fold symmetry confirm that the layer has good in-plane uniformity.

The XRR curve with the simulation is shown in Fig. 3.25, where on the right side of the figure the values of the fit are summarized in the table. Although the simulation does not describe the experimental XRR curve very well, the periodicity of oscillations

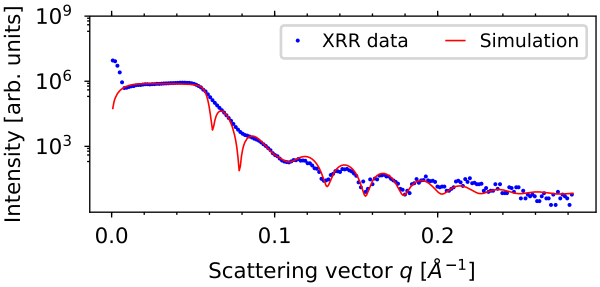

| | |
|---|---|
| $d_{\mathrm{Ni}}$ [nm] | 22.2 |
| $d_{\mathrm{Si}}$ [nm] | 3.5 |
| $\sigma_{\mathrm{MgO}}$ [nm] | 0.9 |
| $\sigma_{\mathrm{Ni}}$ [nm] | 1.9 |
| $\sigma_{\mathrm{Si}}$ [nm] | 0.1 |

FIGURE 3.25: XRR measurement and simulation of the Ni(111) sample.

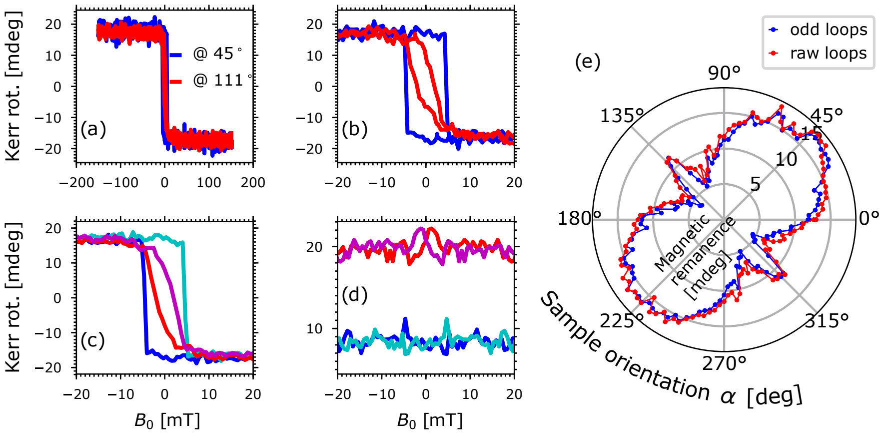

FIGURE 3.26: MOKE magnetic characterization of the Ni(111) sample at a wavelength of 488 nm. (a) Magnetic field loops measured at a sample orientation of $\alpha = 45°$ and $\alpha = 111°$. (b) Close-up of the magnetic field loops which were separated into their (c) odd and (d) even parts. (e) Remanence magnetic anisotropy yielded from raw loops (a) and odd loops (c).

is sufficiently described providing us with information about the layer thickness, which is in good match with our prediction from the deposition process. The first two dips that appear in the simulation are not that pronounced in the experimental data. This could be possibly addressed to slightly inaccurate densities of layers in the model.

The hysteresis loops and Kerr remanence magnetic anisotropy measured at a wavelength of 488 nm is shown in Fig. 3.26. As can be seen from Fig. 3.26(a) and (b), a magnetic field of ca. 10 mT is sufficient to magnetically saturate the sample in any in-plane direction. We also separated the loops into their odd and even parts, although the contribution of QMOKE is minimal here as shown in Fig. 3.26(c) and (d). In Fig. 3.26(e) the remanence magnetic anisotropy plot is shown. We observe a two-fold symmetry, indicating a clear magnetic easy in-plane axis. Additional peaks at $\alpha = 135°$ and 315° are present and have been observed already in literature as discussed in Ref. [130].

## 3.5 Conclusion

In this chapter, we introduced all the techniques and setups that have been used for the MOKE experimental data gathering. We also briefly introduced the techniques of thin films preparation and structural characterizations. Further, we have introduced all the samples that will be investigated from point of MOKE and QMOKE in particular. The Fe(001) thickness dependent sample series and $Co_2MnSi$ Heusler compound sample series are the two main sample sets used fro QMOKE spectroscopy investigations. The residual samples are used for the investigations of the 8-directional method of cubic crystal structures with various surface orientations.

# Chapter 4

# The 8-directional method of (001), (011) and (111) oriented thin films with cubic crystal structure

The 8-directional method of (001) oriented cubic crystal structures has been already introduced in Sec. 2.5. In this chapter, we will examine this method in more detail and we will further extend it to (011) and (111) oriented cubic crystal structures.

The derived equations for each surface orientation are compared to numerical simulations of the Python based code that was introduced in Sec. 3.1.4. Through this comparison we are testing approximative description of Kerr angles through Eq. (2.5.1), being

$$\Phi_s = -\frac{r_{ps}}{r_{ss}} = A_s \left( \varepsilon'_{yx} - \frac{\varepsilon'_{yz}\varepsilon'_{zx}}{\varepsilon_d} \right) + B_s \varepsilon'_{zx},$$

$$\Phi_p = \frac{r_{sp}}{r_{pp}} = -A_p \left( \varepsilon'_{xy} - \frac{\varepsilon'_{zy}\varepsilon'_{xz}}{\varepsilon_d} \right) + B_p \varepsilon'_{xz}.$$

Recall that this equation was adopted to obtain human-readable dependence of Kerr angles on MO parameters $K$, $G_s$, $2G_{44}$, on sample orientation $\alpha$ and on in-plane components of $\boldsymbol{M}$ or on $\mu$, the in-plane direction of $\boldsymbol{M}$. Thus, we will employ Eq. (2.5.1) again to derive equations of the 8-directional method of (011) and (111) oriented cubic crystal structures.

Further, we present here experimental measurements of the 8-directional method for all three surface orientations. The results are compared to derived equations and numerical simulations. Finally, the 8-directional method of each surface orientation is analyzed to be further utilized for the QMOKE spectroscopy measurement.

As a reminder, the 8-directional method assumes only in-plane $\boldsymbol{M}$ and thus $\boldsymbol{M} = [M_T, M_L, 0] = [\cos\mu, \sin\mu, 0]$, where $\mu$ is angle between $x$-axis of our coordinate system and in-plane $\boldsymbol{M}$ direction (see Appendix A). Measurements of Kerr angles for eight different magnetization directions ($\mu = k \cdot 45°$, where $k = 0, 1, 2, ..., 7$) provide basis of this method. Separation of individual contributions works as follows.

$$\frac{1}{2}\left(\Phi_{s/p}^{\mu=90°} - \Phi_{s/p}^{\mu=270°}\right) = \Phi_{M_L} \text{ contribution,} \tag{4.0.1a}$$

$$\frac{1}{2}\left(\Phi_{s/p}^{\mu=45°} + \Phi_{s/p}^{\mu=225°} - \Phi_{s/p}^{\mu=135°} - \Phi_{s/p}^{\mu=315°}\right) = \Phi_{M_L M_T} \text{ contribution,} \tag{4.0.1b}$$

$$\frac{1}{2}\left(\Phi_{s/p}^{\mu=0°} + \Phi_{s/p}^{\mu=180°} - \Phi_{s/p}^{\mu=90°} - \Phi_{s/p}^{\mu=270°}\right) = \Phi_{M_T^2 - M_L^2} \text{ contribution,} \tag{4.0.1c}$$

$$\frac{1}{2}\left(\Phi_{s/p}^{\mu=0°} - \Phi_{s/p}^{\mu=180°}\right) = \Phi_{M_T} \text{ contribution,} \tag{4.0.1d}$$

$$\frac{1}{8}\sum_{k=0}^{7} \Phi_{s/p}^{\mu=k\cdot 45°} = \Phi_{\text{Const.}} (\text{Constant Kerr contribution}). \tag{4.0.1e}$$

Here, we may see that two additional contributions $\Phi_{M_T}$ and $\Phi_{\text{Const.}}$ are added in comparison to description of the 8-directional method in Sec. 2.5. Although for (001) orientation those two contributions are zero, for (011) and (111) orientations they are not.

## 4.1 The 8-directional method of (001) orientation

### 4.1.1 Equations of 8-directional method of (001) orientation

The equations of 8-directional method of (001) oriented cubic crystal structures have already been discussed in Sec. 2.5 and were originally published in Ref. [13]. Kerr angles are described through Eq. (2.5.6):

$$\begin{aligned}
\Phi_{s/p}^{(001)} = & \pm A_{s/p}\left[2G_{44} - \frac{K^2}{\varepsilon_d} + \frac{\Delta G}{2}(1-\cos 4\alpha)\right] M_L M_T \\
& \pm A_{s/p}\left[\frac{\Delta G}{4}\sin 4\alpha\right]\left(M_T^2 - M_L^2\right) \\
& \pm B_{s/p} K M_L,
\end{aligned}$$

and when in-plane magnetization is expressed through $\mu$ (as shown in Eq. (2.5.2)), we obtain Eq. (2.5.7):

$$\begin{aligned}\Phi^{(001)}_{s/p} = &\pm A_{s/p}\left[\frac{1}{2}2G_{44} - \frac{K^2}{2\varepsilon_d} + \frac{\Delta G}{4}(1-\cos 4\alpha)\right]\sin(2\mu)\\ &\pm A_{s/p}\left[\frac{\Delta G}{4}\sin 4\alpha\right]\cos(2\mu)\\ &\pm B_{s/p}K\sin\mu.\end{aligned}$$

Three non-zero contributions to Kerr angles can be separated through Eqs.(2.5.8a)–(2.5.8c), being in analogy with Eqs.(4.0.1a)–(4.0.1c). The contributions are (i) LMOKE contribution $\Phi_{M_L}$ that is proportional to $\pm B_{s/p}K$. This contribution is isotropic, i.e. independent of sample orientation $\alpha$. (ii) QMOKE contribution $\Phi_{M_LM_T}$ that is proportional to $\pm A_{s/p}\left[2G_{44} - \frac{K^2}{\varepsilon_d} + \frac{\Delta G}{2}(1-\cos 4\alpha)\right]$. This contribution is composed of isotropic part and anisotropic part with $\cos 4\alpha$ dependency. (iii) The QMOKE contribution $\Phi_{M_T^2-M_L^2}$ proportional to $\pm A_{s/p}\frac{\Delta G}{2}\sin 4\alpha$. This contribution is purely anisotropic with dependency $\sin 4\alpha$.

### 4.1.2 Comparison of 8-directional equations of (001) orientation to numerical simulations

Within numerical code we simulate Kerr angels separately for eight $\boldsymbol{M}$ directions of the 8-directional method and then apply separation process as describe by Eqs. (4.0.1a) –(4.0.1e). When this is done for each sample orientation $\alpha$ in the full 360° rotation (e.g. with step of 1°), we can plot numerically calculated dependence of each contribution on the sample orientation $\alpha$. Thus, this way we can compare behaviour of numerically calculated contributions to their description through equations of 8-directional method and see if, or how much, do they comply.

Figure 4.1 shows the results of such numerical simulations. For all Figs. 4.1 (a) – (f) we hold constant only (i) photon energy of incidence light, being 1.85 eV, (ii) diagonal permittivity $\varepsilon_d = -3.02 + 28.24i$ (which is value of $\varepsilon_d$ of Fe at 1.85 eV that was obtained by ellipsometry measurements as described in Sec. 3.4.1) and (iii) linear MO parameter $K = 0.09\varepsilon_d$. Rest of the parameters were tuned for each of the subplot separately in order to observe changes and compare them to predictions of Eq. (2.5.6). The structure of the simulated sample is the bulk FM/air interface, except for the last graph [Fig. 4.1(f)], where the simulation of 20 nm thin film FM layer on MgO substrate is presented. Note that FM material of those calculations is not real as MO parameters are fabricated to our liking (all the MO parameters are chosen to be fraction of $\varepsilon_d$). Although we actually

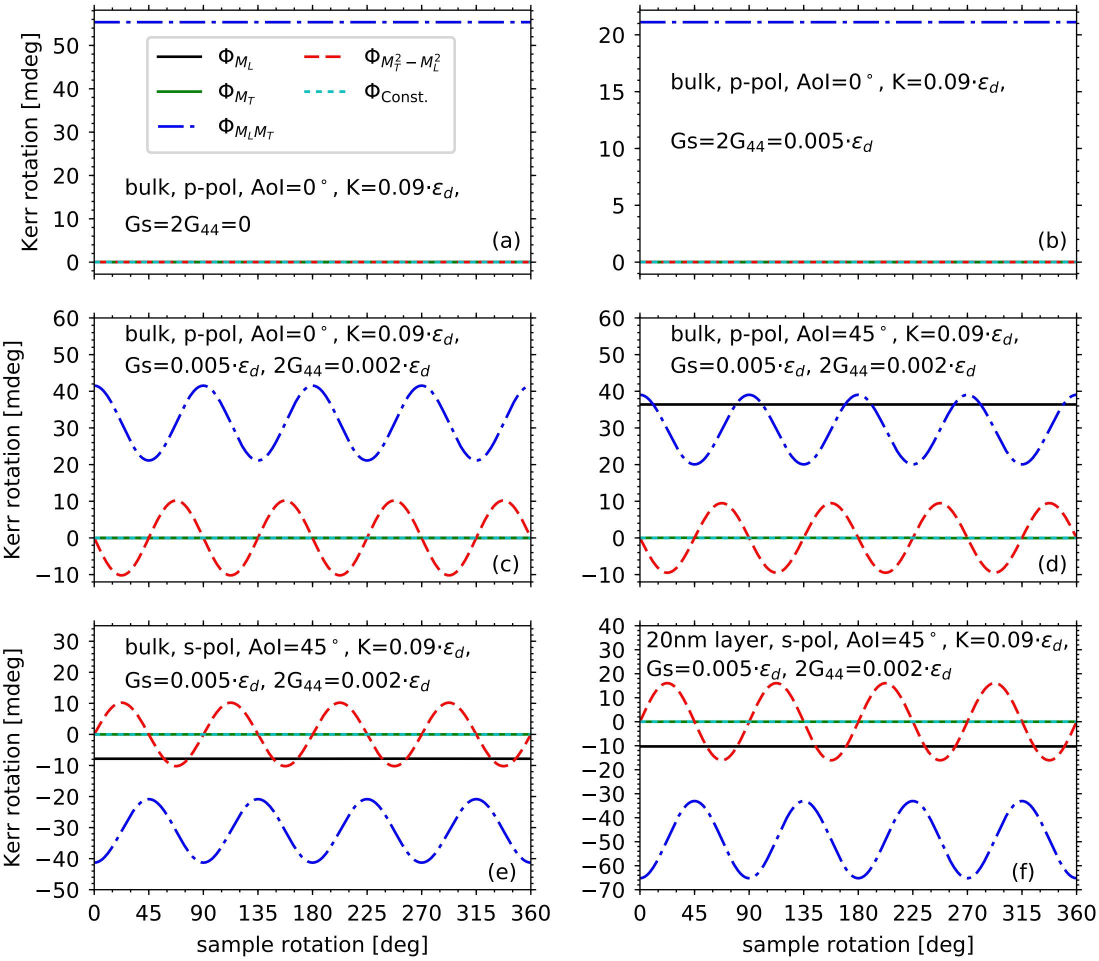

FIGURE 4.1: Numerical simulations of the 8-directional method of (001) oriented cubic crystal structures. For all six graphs we hold photon energy of incident light at 1.85 eV, $\varepsilon_d = -3.02 + 28.24i$ and $K = 0.09 \cdot \varepsilon_d$. Rest of the values are changed with each simulation, where all the values are stated as the text insets in the individual graphs. The text inset 'bulk' means that structure in the calculation is FM/air interface. In the last graph (f), MgO substrate/20nm FM layer/air structure is used instead with $\varepsilon_d$(MgO)=3.0+0i. AoI stands for angle of incidence.

posses values of all MO parameters in case of Fe (as will be presented in Chapter 5) it make more sense to use fabricated one, as we need to tune the values in this investigation.

In Fig. 4.1(a) we present simulation for *p*-polarized incident light under normal AoI. Quadratic MO parameters $G_s$ and $2G_{44}$ are "switched off", i.e. $G_s = 2G_{44} = 0$. Thus, we only see here $\Phi_{M_L M_T}$ contribution proportional to $A_p K^2/\varepsilon_d$. Note that LMOKE $\Phi_{M_L}$ contribution is zero due to normal AoI ($B_{s/p}^{\mathrm{AoI}=0} = 0$). In Fig. 4.1(b) we "switched on" quadratic MO parameters and set them both to equal value $G_s = 2G_{44} = 0.005\varepsilon_d$, thus $\Delta G = 0$. This means that $\boldsymbol{G}$ tensor is isotropic in this case. The value of $\Phi_{M_L M_T}$ contribution went down, being in accordance with Eq. (2.5.6) where $2G_{44}$ and $K^2/\varepsilon_d$ do posses opposite sign. In subsequent Fig. 4.1(c), $2G_{44}$ is lowered to $0.002\varepsilon_d$ which is providing us with $\Delta G = 0.003\varepsilon_d$ and, thus, the anisotropic part of QMOKE contributions has emerged. We can now observe $\cos 4\alpha$ and $\sin 4\alpha$ oscillations of contributions $\Phi_{M_L M_T}$ and $\Phi_{M_T^2-M_L^2}$, respectively. When AoI is raised to 45° [Fig. 4.1(d)] the LMOKE $\Phi_{M_L}$ contribution spring up as expected. Effect of polarization change from $p$-polarization to $s$-polarization is then presented in Fig. 4.1(e). Change of sign of individual contributions follow well predictions of Eq. (2.5.6). Note that also change of absolute values of individual contributions take place, because for AoI$\neq 0$ we have $A_p \neq A_s$ and $B_p \neq B_s$ [17]. In the last graph Fig. 4.1(f), we have changed the structure from FM(bulk)/air interface to MgO/FM(20nm)/air thin film layer. We may observe some change in the value of the contributions, but the symmetry remain the same as it should. All the changes described in graphs Figs. 4.1(a)–(f) follow very well all the predictions of Eq. (2.5.6). Although approximative relation of Eq. (2.5.1) was derived for thin FM layer [24], it obviously hold well for bulk material as well. Finally, note that contribution $\Phi_{M_T}$ and $\Phi_{\text{Const.}}$ are in all 6 graphs zero as expected.

Now, although from the graphs in Fig. 4.1 it looks like all the contributions follow well their symmetry and predictions of Eq. (2.5.6), we will examine these more thoroughly by means of the fast Fourier transform (FFT). The individual frequencies per 360° sample rotation of contributions $\Phi_{M_L}$, $\Phi_{M_L M_T}$, $\Phi_{M_T^2-M_L^2}$, $\Phi_{M_T}$ and $\Phi_{\text{Const.}}$ are shown in Figs. 4.2(a),(b),(c), (d) and (e), respectively, being the FFT of the individual contributions in Fig. 4.1(f). The value of amplitude in millidegrees is marked whenever the value rise above $10^{-3}$ mdeg. Smaller values can be safely omitted.

The analysis by FFT show us negligible discrepancy of contributions $\Phi_{M_L}$, $\Phi_{M_T}$ and $\Phi_{\text{Const.}}$ when compared to the theory, i.e. to Eq. (2.5.6). All the contributions have negligible anisotropic four-fold contribution that is not predicted by equations of 8-directional method.

In Figs. 4.2(f)–(j) we show zero-fold amplitude (i.e. isotropic part, or offset) dependence on AoI for each contribution separated by 8-directional method. In Figs. 4.2(k)–(o) their four-fold amplitude (i.e. anisotropic part) dependence on AoI is shown instead. We see that the four-fold dependence of contributions $\Phi_{M_L}$, $\Phi_{M_T}$ and $\Phi_{\text{Const.}}$ stay in negligible values for all the angles of incidence. However, as the dependence on AoI is clearly pronounced, we are assured that those contributions have real origin in the physical model. In contrary, the offset dependence on AoI for $\Phi_{M_T^2-M_L^2}$, $\Phi_{M_T}$ and $\Phi_{\text{Const.}}$, that is shown in Figs. 4.2(h)–(j), respectively, is just the noise of the calculations caused by deflection of $\boldsymbol{M}$ by random angle $\Delta\mu$ as was discussed in Sec. 3.1.4.

Nevertheless, we should keep in mind that MO parameters that were used in those simulations were fabricated. In case of a material with different MO parameters, this

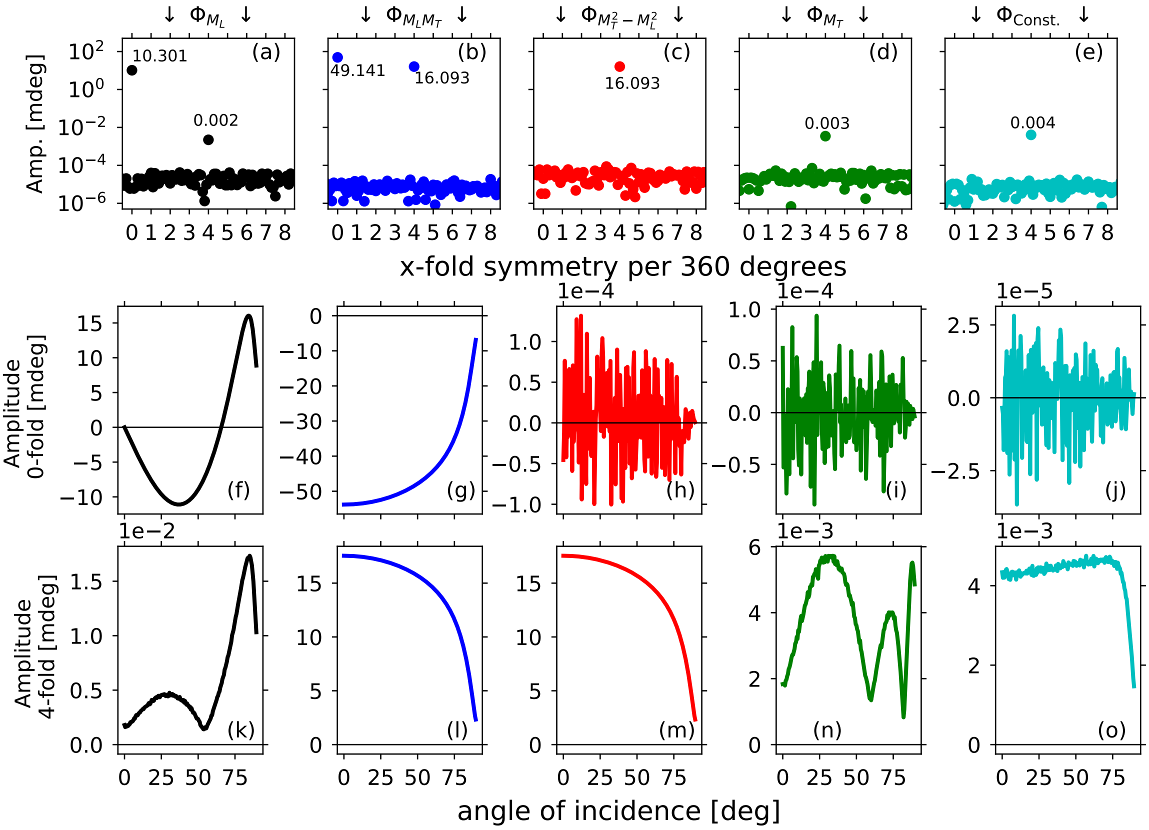

FIGURE 4.2: In (a) – (e) we show FFT of Fig. 4.1(f) contributions $\Phi_{M_L}$, $\Phi_{M_L M_T}$, $\Phi_{M_T^2-M_L^2}$, $\Phi_{M_T}$ and $\Phi_{\text{Const.}}$, respectively. Colours are in compliance. Rest of the graphs (f)–(o) are dependencies on angle of incidence of zero-fold and four-fold part of each contribution. The graphs are column and colour sorted.

four-fold behaviour of $\Phi_{M_L}$, $\Phi_{M_T}$ and $\Phi_{\text{Const.}}$ could be more pronounced[1]. From our experience, that we gained by debugging and "playing around" with numerical code, those four-fold oscillations of $\Phi_{M_L}$, $\Phi_{M_T}$ and $\Phi_{\text{Const.}}$ contributions get stronger whenever $\Delta G$ and/or $K$ is of higher value. Thus, we believe that those oscillations are stemming from some interplay of $K \cdot \Delta G$, although more rigorous examination should be done to make this claim sound. Further, note that the best of our experimental measurements does not have noise smaller than 0.5 mdeg, and usually the noise is rather around 1 mdeg or more. Thus, the oscillations would have to grow in amplitude by more than two orders to become visible in our experiments, otherwise they would be lost in noise.

---

[1] See e.g. Ref. [28] where such a behaviour of LMOKE is reported with cubic (001) system. Yet, we do not claim that this oscillations reported in this literature is of same origin as in our numerical calculations.

### 4.1.3 Experimental measurements of $Co_2MnSi(001)$ Heusler compound samples, comparison to the theory and to numerical calculations

To compare real experiment with the equations of 8-directional method and with numerical calculations is the next step in our investigations. In Fig. 4.3 we show 8-directional measurements of the $Co_2MnSi$ sample annealed at 500°C (introduced in Sec. 3.4.2) that were collected at vector MOKE setup (described in Sec. 3.1.2). The 8-directional method was measured with AoI=45° and with AoI=0° for both polarization of incident light, $s$ and $p$. The wavelength of the probing light was 670 nm.

Experimental data points are marked as crosses. The fit of the simple goniometrical function, $O + A\cos(4\alpha + \varphi)$ with $O$ as offset, $A$ as amplitude and $\varphi$ as phase shift, to the experimental data is draw by lines of the same colour as the experimental data points and denoted with suffix "fit" in the legend. Residual lines in Fig. 4.3, that are described in the legend with suffix "simulation", represent the numerical code simulations. The parameters used in numerical calculus were taken (i) directly from experiment (photon energy, AoI, polarization of incident wave) (ii) from investigations presented in Sec. 3.4.2 (thicknesses and $\varepsilon_d$ of each layer) and (iii) from QMOKE spectroscopy which will be described in Chapter 5 (MO parameters). Used optical and MO parameters of $Co_2MnSi$ are $\varepsilon_d = 1.21 + 22.61i$, $K = -0.1302 - 0.2238i$, $G_s = 0.002729 - 0.03244i$ and $2G_{44} = -0.0127 - 0.01457i$.

We can see that Figs. 4.3(a) and (c) have much better noise-to-signal ratio than Figs. 4.3(b) and (d). This is due to fact that detector at normal incidence was harder to calibrate than detector at AoI=45°. In the Tab. 4.1 we compare the values of numerical simulations to the values of fit to the experimental data. Each of contributions of every graph in Figs. 4.3(a)–(d) is described through its offset (i.e. zero-fold symmetry amplitude) and four-fold symmetry amplitude (i.e. amplitude of oscillations). From all the contributions in all the graphs the QMOKE $\Phi_{M_T^2-M_L^2}$ have best agreement between numerical simulation and experiment, with difference in amplitude of oscillations around 1 mdeg or less. For QMOKE contribution $\Phi_{M_L M_T}$ the compliance is not so good. The differences in offset are in the range of 1-4 mdeg and the differences in amplitude of oscillations are in the range of 0.4–1.1 mdeg. The larger discrepancy in graphs (b) and (d) can be, to some extend, assign to the large noise of the experimental data, but clearly the difference is there. The fit to experimental data of LMOKE contribution $\Phi_{M_L}$ at normal incidence [Figs. 4.3(b) and (d)] can be omitted, as it is just fit to noise around zero signal. The fit to LMOKE experimental data at AoI=45° [Fig. 4.3(c)] provide amplitude of oscillations 0.58 mdeg, but this again is rather fit to slightly noisier region $\alpha = \langle 135°, 315° \rangle$ of the experimental data. Otherwise the agreement between fit and simulation is in perfect match. On the other hand, in Fig. 4.3(a) there is about 1 mdeg shift in the LMOKE

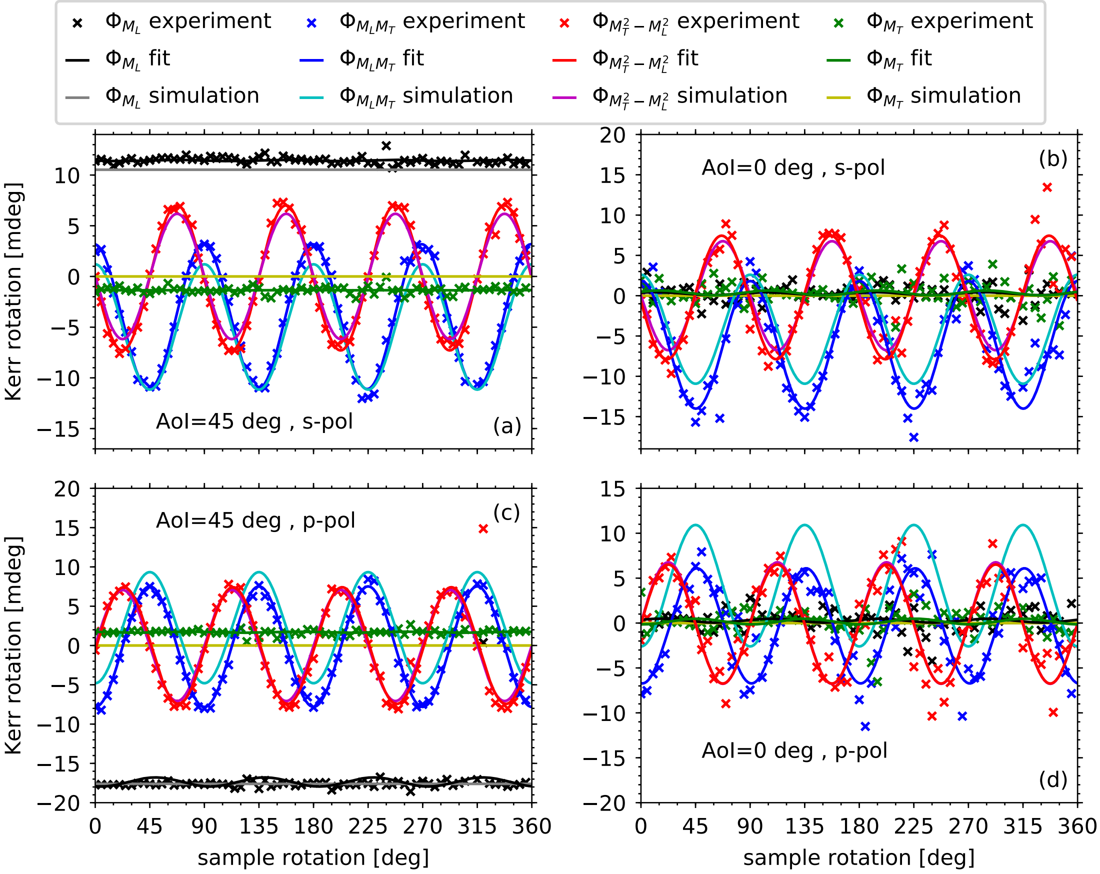

FIGURE 4.3: The measurements of the 8-directional method of $Co_2MnSi$ sample annealed at 500°C. All measurements were carried out at wavelength 670 nm. Polarization of incident wave and AoI is stated for each measurement as inset in the graph. Full lines designated as fit in the legend are fit of simple goniometrical function of four-fold symmetry to experimental data, where offset and amplitude were free parameters of that fit. Full lines designated as simulation in the legend are numerical calculations with the same parameters as in the experiment and with MO parameters obtained from QMOKE spectroscopy ($K = -0.1302 - 0.2238i$, $G_s = 0.002729 - 0.03244i$, $2G_{44} = -0.0127 - 0.01457i$).

offset. Finally, in the Figs. 4.3(a) and (c) the experimental $\Phi_{M_T}$ contribution have clear offset of ca. 1.5 mdeg, whereas simulation is sharp zero.

All those discrepancies can stem from multiple sources. (i) As will be explained below in the text, the MO parameters were obtained only from three experimental points from all the points shown in Fig. 4.3. (ii) The MO parameters were acquired on different setup than is the setup used for measurements presented in Fig. 4.3. (iii) In our numerical simulations we expect ideal sample with perfect cubic structure, with layers of homogenous thickness, etc., where all this is just approximation of the real sample that was measured. (iv) The setup does not have to be artefact-free. For example, the offset of $\Phi_{M_T}$ contribution in Figs. 4.3(a) and (c) could be explained by slight offset of magnets

| Contribution [mdeg] | Fig. 4.3(a) | Fig. 4.3(b) | Fig. 4.3(c) | Fig. 4.3(d) |
|---|---|---|---|---|
| $\Phi_{M_L}$ off. fit | 11.441 | 0.253 | -17.366 | 0.266 |
| $\Phi_{M_L}$ off. sim. | 10.527 | 0.000 | -17.605 | 0.000 |
| $\Phi_{M_L}$ amp. fit | 0.065 | 0.187 | 0.580 | 0.222 |
| $\Phi_{M_L}$ amp. sim. | 0.002 | 0.064 | 0.000 | 0.000 |
| $\Phi_{M_L M_T}$ off. fit | -3.961 | -6.098 | -0.147 | -0.314 |
| $\Phi_{M_L M_T}$ off. sim. | -4.979 | -4.159 | 2.269 | 4.159 |
| $\Phi_{M_L M_T}$ amp. fit | 7.141 | 7.913 | 7.670 | 6.409 |
| $\Phi_{M_L M_T}$ amp. sim. | 6.182 | 6.764 | 7.070 | 6.764 |
| $\Phi_{M_T^2-M_L^2}$ off. fit | -0.142 | -0.217 | -0.008 | -0.110 |
| $\Phi_{M_T^2-M_L^2}$ off. sim. | 0.000 | 0.000 | 0.000 | 0.000 |
| $\Phi_{M_T^2-M_L^2}$ amp. fit | 7.154 | 7.666 | 7.427 | 6.628 |
| $\Phi_{M_T^2-M_L^2}$ amp. sim. | 6.182 | 6.764 | 7.070 | 6.764 |
| $\Phi_{M_T}$ off. fit | -1.346 | 0.343 | 1.691 | 0.168 |
| $\Phi_{M_T}$ off. sim. | 0.000 | 0.000 | 0.000 | 0.000 |
| $\Phi_{M_T}$ amp. fit | 0.024 | 0.307 | 0.071 | 0.319 |
| $\Phi_{M_T}$ amp. sim. | 0.031 | 0.033 | 0.005 | 0.000 |

TABLE 4.1: The table compare offsets and amplitudes of individual contributions from Fig. 4.3 obtained from fit to experimental data and from numerical simulations.

with respect to the plane of incidence, thus, with magnetic field applied by $x$-axis magnets the sample may posses some small part of $M_L$ magnetization in reality. Note that alignment of the system is quite crucial with the MOKE measurements and realignment of the setup is often a must to obtain a good results. Thus, it could easily happen that the artefact that is present at one measurement is not present in the another one.

### 4.1.4 Utilizing 8-directional method of (001) orientation for spectroscopy

With QMOKE spectroscopic measurements, we are interested in such contributions to the MOKE signal, where only one of the quadratic MO parameters $G_s$ or $2G_{44}$ contribute to the signal. When processing the data of such a contribution, we can set only one of the quadratic MO parameters as free variable, whereas second one can be omitted and set to zero. Positions of those contributions in the 8-directional method can be easily found from Eq. (4.1.1), where MOKE dependence on sample orientation $\alpha$ and $\boldsymbol{M}$ direction $\mu$

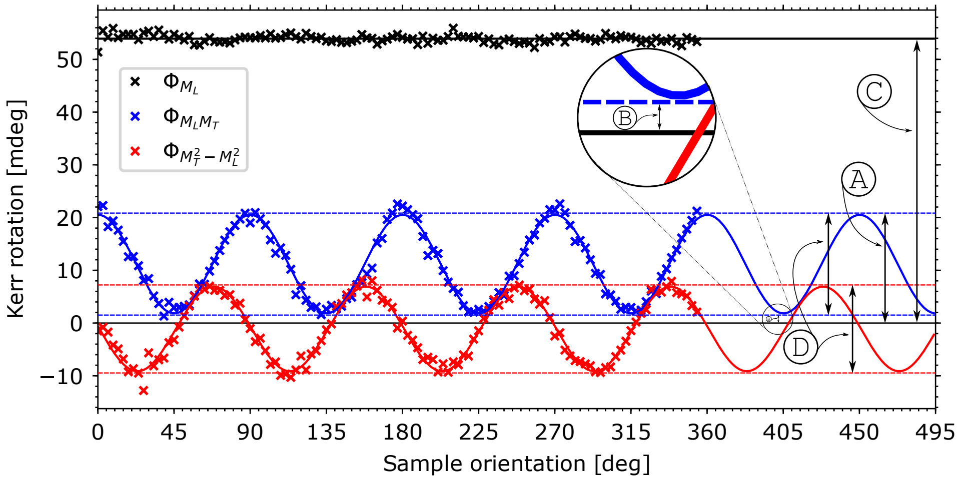

FIGURE 4.4: The 8-directional measurement at wavelength 670 nm (1.85 eV), with AoI=45° for the sample from Fe(001) series with a nominal thickness of 12.5 nm. Several MOKE values are designated in the graph, being Ⓐ $= A_s\left(2G_{44} - \frac{K^2}{\varepsilon_d}\right)$, Ⓑ $= A_s\left(G_s - \frac{K^2}{\varepsilon_d}\right)$, Ⓒ $= B_s K$ and Ⓓ $= A_s \Delta G$.

is shown separately for each MO parameter.

$$\begin{aligned}\Phi_{s/p}^{(001)} = \pm\, A_{s/p} \Bigg\{ & \frac{2G_{44}}{4}\left[(1+\cos 4\alpha)\sin 2\mu - \sin 4\alpha \cos 2\mu\right] \\ & + \frac{G_s}{4}\left[(1-\cos 4\alpha)\sin 2\mu + \sin 4\alpha \cos 2\mu\right] \\ & - \frac{K^2}{2\varepsilon_d}\sin 2\mu \Bigg\} \\ & \pm B_{s/p}\, K \sin \mu. \end{aligned} \tag{4.1.1}$$

In Fig. 4.4 we present 8-directional measurement of the sample from Fe(001) sample series with a nominal thickness of 12.5 nm (sample series described in Sec. 3.4.1). Several values are indicated in the graph. The value Ⓒ $= B_s K$ denote the LMOKE $\Phi_{M_L}$ contribution that originates only from MO parameter $K$. The value Ⓐ $= A_s\left(2G_{44} - \frac{K^2}{\varepsilon_d}\right)$ and Ⓑ $= A_s\left(G_s - \frac{K^2}{\varepsilon_d}\right)$ originates from quadratic MO parameters $2G_{44}$ and $G_s$, respectively. Thus, those points are ideal for QMOKE spectroscopy measurements. The contribution of $\frac{K^2}{\varepsilon_d}$ can be accounted for, as will be discussed in the Chapter 5. Value Ⓓ $= A_s \Delta G$ then stems from anisotropy of quadratic MO tensor $\boldsymbol{G}$. The measurement of values Ⓐ, Ⓑ and Ⓒ is thus used in QMOKE spectroscopy of cubic (001) oriented samples.

## 4.2 The 8-directional method of (011) orientation

### 4.2.1 Equations of 8-directional method of (011) orientation

In order to get cubic crystal structure from (001) orientation to (011) orientation, we have to rotate cubic crystal structure (i.e. permittivity tensor) around the $x$-axis of our coordinate system by angle $\vartheta_x = 45°$. Further, $\vartheta_y = 0°$ while $\vartheta_z = \alpha$, being the rotation of (011) surface oriented sample around its surface normal. Then, elements of the permittivity tensors that appear in Eq. (2.5.1) are [38]

$$\begin{aligned}\varepsilon'^{(011)}_{yx/xy} &= \left[2G_{44} + \frac{3}{8}\Delta G\,(1-\cos 4\alpha)\right] M_L M_T \\ &+ \left[\frac{3}{16}\Delta G\,(\sin 4\alpha)\right]\left(M_T^2 - M_L^2\right) \\ &+ \frac{1}{8}\Delta G \sin 2\alpha,\end{aligned} \tag{4.2.1}$$

$$\varepsilon'^{(011)}_{zx/xz} = \pm K M_L, \tag{4.2.2}$$

$$\varepsilon'^{(011)}_{yz/zy} = \pm K M_T. \tag{4.2.3}$$

We apply those permittivity tensor elements in Eq. (2.5.1) which give us

$$\begin{aligned}\Phi^{(011)}_{s/p} = &\pm A_{s/p}\left[2G_{44} - \frac{K^2}{\varepsilon_d} + \frac{3}{8}\Delta G\,(1-\cos 4\alpha)\right] M_L M_T \\ &\pm A_{s/p}\left[\frac{3}{16}\Delta G \sin 4\alpha\right]\left(M_T^2 - M_L^2\right) \\ &\pm A_{s/p}\ \frac{1}{8}\Delta G \sin 2\alpha \\ &\pm B_{s/p} K M_L.\end{aligned} \tag{4.2.4}$$

When $\boldsymbol{M}$ components are expressed through $\boldsymbol{M}$ angle $\mu$, Kerr angles are

$$\begin{aligned}\Phi^{(011)}_{s/p} = &\pm A_{s/p}\left[\frac{2G_{44}}{2} - \frac{K^2}{2\varepsilon_d} + \frac{3}{16}\Delta G\,(1-\cos 4\alpha)\right]\sin(2\mu) \\ &\pm A_{s/p}\left[\frac{3}{16}\Delta G \sin 4\alpha\right]\cos(2\mu) \\ &\pm A_{s/p}\ \frac{1}{8}\Delta G \sin 2\alpha \\ &\pm B_{s/p} K \sin\mu.\end{aligned} \tag{4.2.5}$$

If compared to Eq. (2.5.7) of the (001) oriented cubic crystal structures, we can observe two changes. First change is the different amplitude of anisotropic part of QMOKE contributions $\Phi_{M_L M_T}$ and $\Phi_{M_T^2-M_L^2}$, which is $\frac{3}{16}\Delta G$ in the case of (011) orientation compared to $\frac{1}{4}\Delta G$ in the case of (001) orientation. Thus, the amplitude of anisotropic oscillations in the case of the (011) oriented samples should be 75% of the amplitude of anisotropic oscillations in the case of the (001) oriented samples. Second change is that $\Phi_{\text{Const.}}$ is no more zero but has anisotropic behaviour with two-fold symmetry and with the amplitude $\frac{1}{8}\Delta G$.

### 4.2.2 Comparison of 8-directional equations of (011) orientation to numerical simulations

We again employ numerical code to make simulations of the 8-directional method of (011) oriented cubic crystal structures. All the used parameters in numerical code are the same as in the case of (001) orientation, we only rotated the crystallographic structure to (011) orientation. Thus, we can directly compare the changes.

As shown in Figs. 4.5(a)–(f) all the predictions of Eq. (4.2.5) are well in place. The LMOKE $\Phi_{M_L}$ contribution and isotropic part of QMOKE $\Phi_{M_L M_T}$ that stems from $2G_{44}+K^2/\varepsilon_d$ [Figs. 4.5(a) and (b)] are the same as for (001) orientation. In Figs. 4.5(c)–(f) the anisotropic oscillations of QMOKE $\Phi_{M_L M_T}$ and $\Phi_{M_T^2-M_L^2}$ contributions have lower amplitude than in the case of the (001) simulations. The $\Phi_{\text{Const.}}$ contribution with two-fold symmetry is well pronounced with all graphs where $\Delta G \neq 0$. For more detailed analysis and comparison, let's see the FFT analysis of Fig. 4.5(f)

First, let's discuss the well pronounced characteristics of contributions in 8-directional method. In Fig. 4.6(a) the offset (i.e. zero-fold symmetry amplitude) of LMOKE $\Phi_{M_L}$ contribution have the same value as for (001) orientation (if difference of 0.003 mdeg is neglected). The change of the prefactor of $\Delta G$ ($1/4^{(001)} \rightarrow 3/16^{(011)}$) affects the offset of the QMOKE $\Phi_{M_L M_T}$ contribution [Fig. 4.6(b)] and the amplitude of four-fold oscillations of QMOKE $\Phi_{M_L M_T}$ and $\Phi_{M_T^2-M_L^2}$ contributions, Figs. 4.6(b) and (c), respectively. Note that change of the amplitude from $16.093^{(001)}$ mdeg to $12.074^{(011)}$ mdeg is exactly[2] 75% as predicted by our equations. Furthermore, the amplitude of two-fold oscialtions of $\Phi_{\text{Const.}}$ contribution is exactly three times smaller then QMOKE $\Phi_{M_L M_T}$ and $\Phi_{M_T^2-M_L^2}$ four-fold oscillations amplitude. Although from equations above it seems that it should be only 3/2 times smaller, see Eqs. (4.0.1a)–(4.0.1e) on how those contributions are obtained and wherefrom the factor of 2 is stemming from.

Further, the FFT analysis also discovered some behaviour that is not predicted by Eq. (4.2.5). For $\Phi_{M_L}$ contribution [Fig. 4.6(a)] the four-fold symmetry oscillations hold the same amplitude compare to (001), but now also two-fold symmetry oscillations are

---

[2] When rounded to 3 decimals: 75,026%

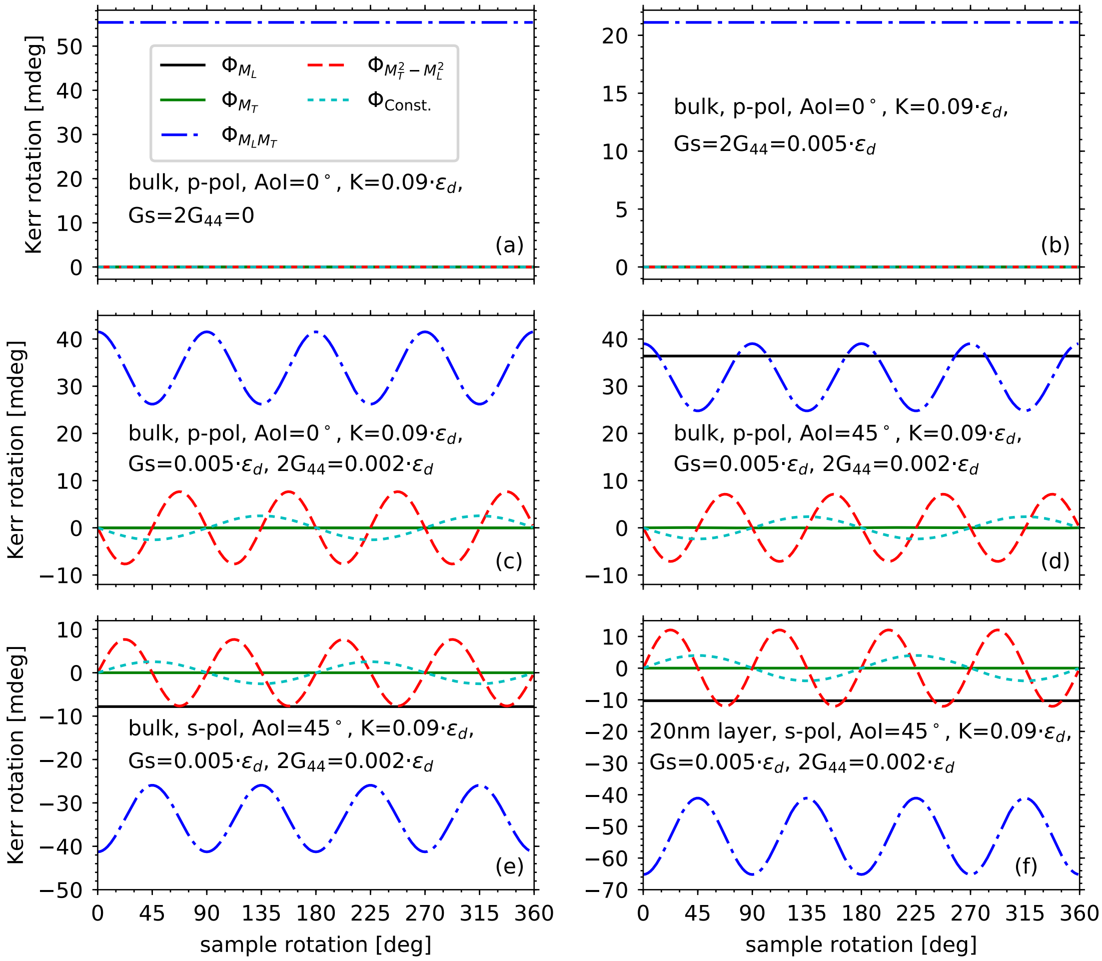

FIGURE 4.5: Numerical simulations of the 8-directional method of (011) oriented cubic crystal structures. For all six graphs we hold the same (i) the photon energy of the incident light at 1.85 eV, (ii) $\varepsilon_d = -3.02 + 28.24i$, (iii) $K = 0.09 \cdot \varepsilon_d$. Rest of the values were changed with each simulation and all the values are stated as the text inset in the individual graphs. Bulk means that structure in calculations is FM/air interface. In the last graph (f) MgO substrate/20nm FM layer/air structure was used instead with ($\varepsilon_d$(MgO)=3.0+0i). AoI stands for angle of incidence.

present as well. The exactly same behaviour is valid for $\Phi_{M_T}$ contribution shown in Fig. 4.6(d). Furthermore two-fold symmetry and six-fold symmetry oscillations emerged for the QMOKE contributions $\Phi_{M_L M_T}$ and $\Phi_{M_T^2-M_L^2}$, Figs. 4.6(b) and (c), respectively. The four-fold symmetry oscillations of $\Phi_{\mathrm{Const.}}$ contribution are again in the same magnitude as in the previous (001) case. Nevertheless, all of those oscillations, that are not covered by Eq. (4.2.5), are of negligible amplitudes and most probably would not be observable in the experimental data.

Furthermore in Figs. 4.6(f)–(j) we show dependence of the offset of each contribution on AoI and in Figs. 4.6(k)–(o) we show dependence of amplitude of superposition of all the oscillations on AoI.

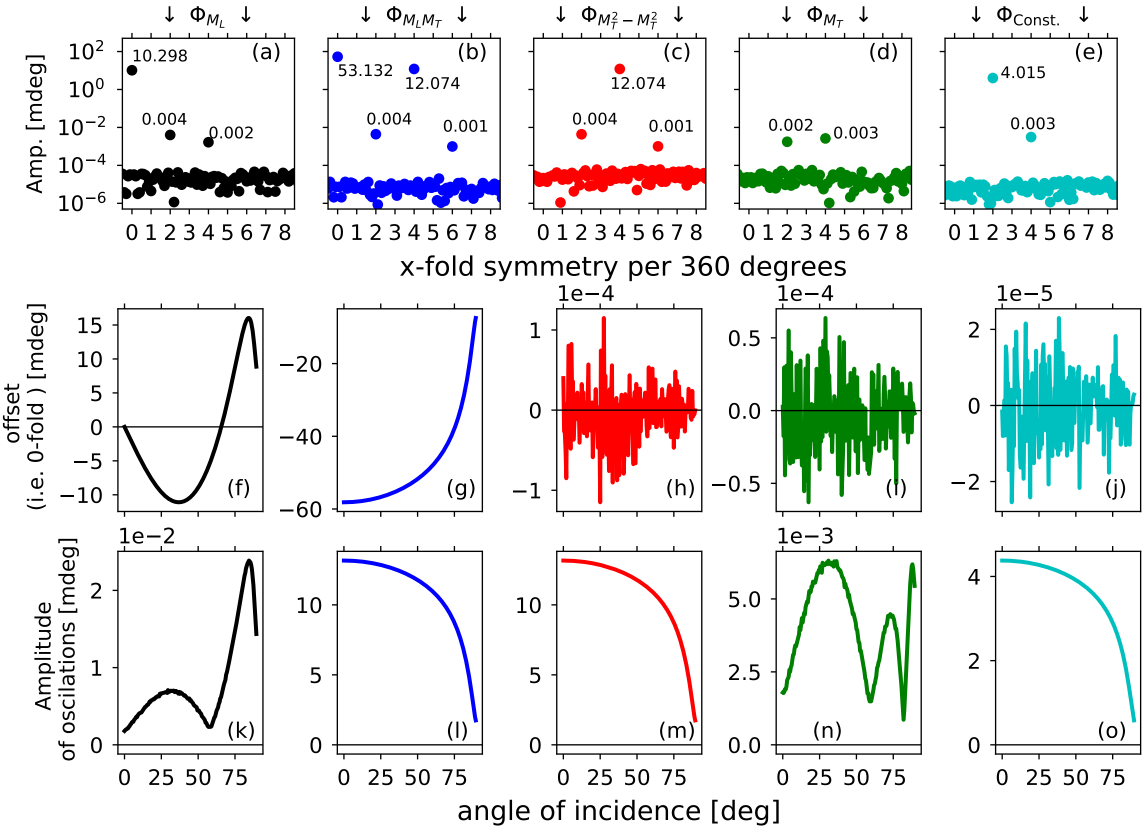

FIGURE 4.6: In (a) – (e) we show FFT of Fig. 4.5(f) contributions $\Phi_{M_L}$, $\Phi_{M_L M_T}$, $\Phi_{M_T^2-M_L^2}$, $\Phi_{M_T}$ and $\Phi_{\mathrm{Const.}}$, respectively. Colours are in compliance. Rest of the graphs (f) – (o) are dependencies on angle of incidence of each contribution, separated to offset (zero-fold amplitude) (f) – (j) and amplitude of superposition of all oscillations (k)–(o). The graphs are column and colour sorted.

### 4.2.3 Experimental measurements of the Fe(011) samples, comparison to the theory and to numerical calculations

For the means of 8-directional method measurements of (011) oriented cubic crystal structures we are in possession of Fe(011) and Co(011) samples, as discussed in Sec. 3.4. Nevertheless, as the Co(011) sample is not saturated with all in-plane directions at maximum magnetic field of our vector MOKE setup (235 mT), we will present here 8-directional measurements of Fe(011) samples only. Also, from the QMOKE spectroscopy of the Fe(001) oriented sample series (presented in subsequent Chapter 5), we are in possession of spectral dependence of all MO parameters of Fe, hence we may compare our measurements with numerical model in this case.

In Fig. 4.7 we present 8-directional measurement of the sample RS210917 (for its characterization see Sec. 3.4.3) at wavelength 670 nm. Polarization and AoI of each measurement is stated as the text insets in the graphs (a)–(d). To check the symmetry of

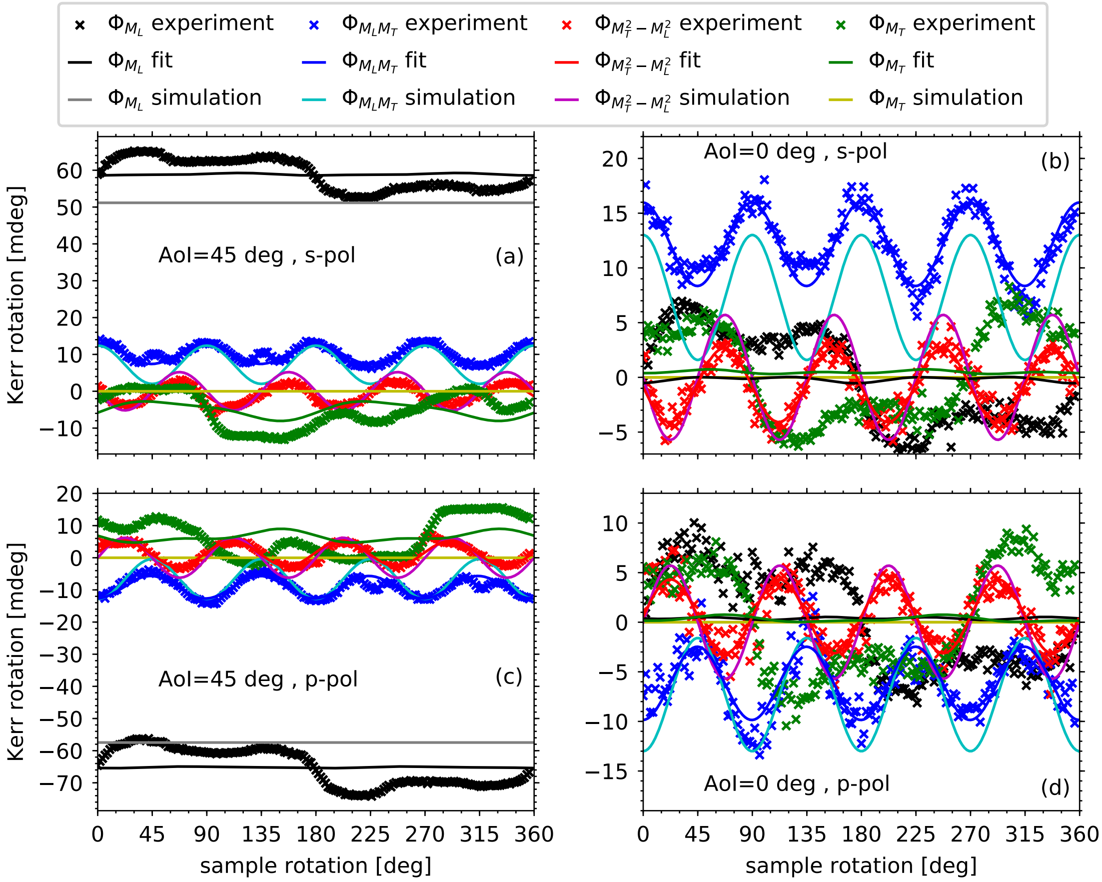

FIGURE 4.7: The 8-directional measurements of Fe(011) sample RS210917 at wavelength 670 nm (1.85 eV). Polarization of incident wave and AoI is stated as text inset in each subplot. Optical and MO parameters used in numerical simulations are $\varepsilon_d(\mathrm{Pt}) = 12.89 + 21.22i$, $\varepsilon_d(\mathrm{MgO}) = 3.0 + 0i$, $\varepsilon_d(\mathrm{Fe}) = -3.02 + 28.24i$, $K = -1.356 + 0.2604i$, $G_s = 0.001862 - 0.05277i$, $2G_{44} = -0.01075 - 0.01489i$.

individual contributions, as predicted by Eq. (4.2.4) and by numerical calculations, we further present fit of function $O + A\cos(4\alpha + \varphi)$ to the experimental data of $\Phi_{M_L M_T}$ and $\Phi_{M_T^2-M_L^2}$ and of function $O + A_1\cos(4\alpha + \varphi_1) + A_2\cos(2\alpha + \varphi_2)$ to experimental data of $\Phi_{M_L}$ and $\Phi_{M_T}$, where offset $O$, amplitude $A$, $A_{1,2}$ and phase shift $\varphi$, $\varphi_{1,2}$ were free variables of the fit. Finally, the numerical simulations for each measurement is provided. Thicknesses of layers in the sample was used as obtained from XRR, optical and magnetooptic parameters were obtained from ellipsometry and MOKE spectroscopy of Fe(001) oriented sample, (the values are stated in the caption of Fig. 4.7), photon energy and AoI is known directly from the experiment.

We may immediately notice strange behaviour of LMOKE $\Phi_{M_L}$ contribution in all the measurements of Figs. 4.7(a)–(d). From prediction of Eq. (4.2.4) this contribution should be isotropic, but from prediction of numerical calculus some (negligible) oscillations of two-fold and four-fold symmetry may be present. Nevertheless, the fit of function with such a symmetry was not able to describe experimental data, and our numerical calculations also do not posses any oscillations observable by a naked eye. Note that oscillations of $\Phi_{M_L}$ contribution do not vanish with the normal AoI, therefore we may exclude anisotropic LMOKE (more precisely anisotropic MO tensor $\boldsymbol{K}$) as the origin. Furthermore, the same behaviour is displayed also for $\Phi_{M_T}$ contribution (that is expected to be zero), although shifted by ca. 90° in $\alpha$. The contributions $\Phi_{M_L}$ and $\Phi_{M_T}$ from Figs. 4.7(a) – (d) were centred around zero and fit with function $A_1 \cos(\alpha + \varphi_1) + A_3 \cos(3\alpha + \varphi_3)$ as shown in the Figs. 4.8(a) – (d), respectively. We see that function of such a symmetry can describe the contributions perfectly, except small discrepancy in $\Phi_{M_T}$ contribution at AoI of 45°. The results of fit are summarized in the table that is part of the Fig. 4.8. We can see that for each measurement the amplitudes of one-fold and three-fold oscillations are the same for $\Phi_{M_L}$ and $\Phi_{M_T}$. In both cases dependence on AoI is very shallow. With change of polarization the sign is not reversed and only small change in amplitude is observable.

We propose explanation of this behaviour as additional PMOKE contribution that is caused by easy magnetic plane which is tilted from the surface plane of the sample. See Fig. B.3 from Appendix B, where this idea is proposed and discussed. Our external magnetic field is not strong enough to force the magnetization off the tilt of the easy magnetic plane, thus the $\boldsymbol{M}$ posses some out-of-plane component $M_z$. Exception is the intersection of the surface plane and the easy magnetic plane, which would correspond to $y$-axis direction when the sample is at $\alpha = 0°$ or $\alpha = 180°$ as indicated by dependence of $\Phi_{M_L}$ in Fig. 4.8 and by discussion in Appendix B. The reversal of sign with sample rotation by 180° is in agreement with this theory, as $M_z$ component will reverse its direction upon such a rotation, providing opposite sign of PMOKE. Further, PMOKE do not change sign with the change of incident light polarization and its dependence on AoI is very shallow [33], which is exactly the behaviour we observe here. Finally, the 90° shift between $\Phi_{M_L}$ and $\Phi_{M_T}$ is also in perfect match with this prediction as well as one-fold symmetry of those contributions. On the other hand, this tilted easy magnetic plane do not explain three-fold symmetry of $\Phi_{M_L}$ and $\Phi_{M_T}$ contributions, unless some curvature of the plane is taken into account. Small change in the amplitude upon change of polarization of the incident light can be explained by slight deviation from normal AoI.

When we will get back to Fig. 4.7, notice that mean value of $\Phi_{M_L}$ contribution in Figs. 4.7(a) and (c) is roughly given by fit to the experimental data and correspond to the $\Phi_{M_L}$ value when magnetization is align with intersection of surface and magnetic easy plane. The difference of ca. 10 mdeg from numerically calculated value may seemed a lot, but keep in mind that the value of $K$ and other MO parameters were acquired on completely different sample of Fe.

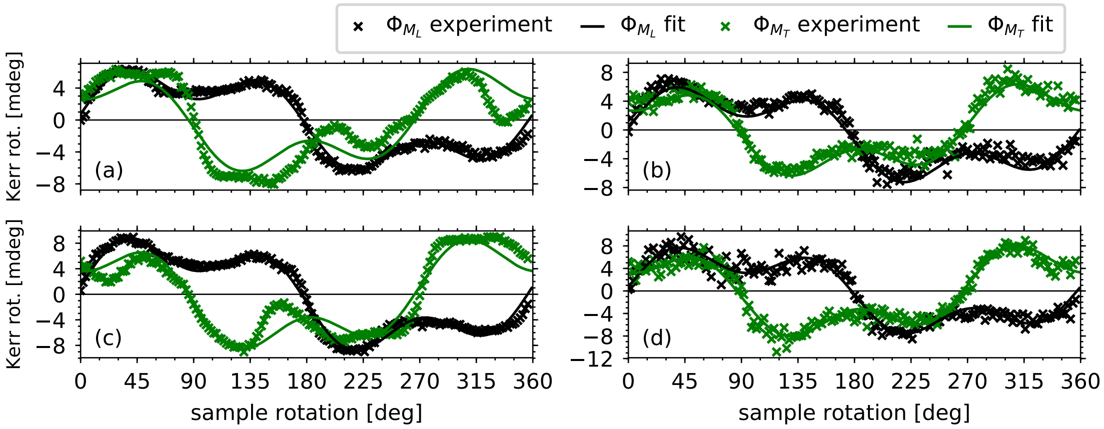

| Amplitudes [mdeg] | (a) | (b) | (c) | (d) |
|---|---|---|---|---|
| $\Phi_{M_L}$ Amp. 1-fold | 5.322 | 5.378 | 7.322 | 6.374 |
| $\Phi_{M_L}$ Amp. 3-fold | 2.612 | 2.688 | 3.470 | 3.111 |
| $\Phi_{M_T}$ Amp. 1-fold | 5.311 | 5.339 | 7.201 | 6.640 |
| $\Phi_{M_T}$ Amp. 3-fold | 2.610 | 2.554 | 3.442 | 3.238 |
| $\varphi_1(\Phi_{M_L}) - \varphi_1(\Phi_{M_T})$ | 88.6° | 91.5° | 89.1° | 88.3° |
| $\varphi_3(\Phi_{M_L}) - \varphi_3(\Phi_{M_T})$ | 88.2° | 90.2° | 88.0° | 92.5° |

FIGURE 4.8: Contributions $\Phi_{M_L}$ and $\Phi_{M_T}$ taken from the Figs. 4.7 (a) – (d) are shown here in subplots (a) – (d), respectively. Contribution $\Phi_{M_L}$ was centred around zero. Fit of function $A_1 \cos(\alpha + \varphi_1) + A_3 \cos(3\alpha + \varphi_3)$ to both contributions is presented, where $A_{1,3}$ are amplitudes of one-fold and three-fold oscillations and $\varphi_{1,3}$ is phase shift of one-fold and three-fold oscillations. Results of the fit are summarized in the table.

The QMOKE $\Phi_{M_L M_T}$ and $\Phi_{M_T^2 - M_L^2}$ contributions in Fig. 4.7 follow predicted four-fold symmetry. Evaluated comparison of experimental data fit with numerical model is presented in Tab. 4.2. If we consider that MO parameters were obtained from different sample, the agreement in case of $\Phi_{M_T^2 - M_L^2}$ contribution is perfect. In the case of $\Phi_{M_L M_T}$ contribution the amplitude of oscillations is also not in such a bad agreement, but the offset is off quite a bit, maybe except Fig. 4.7(c). Also, notice that the four-fold oscillation of this contribution are not so regular as in the case of $\Phi_{M_T^2 - M_L^2}$ oscillations. First of all, there are those dips at at sample orientation $\alpha$ of 45° and 135°, 225° and 315° in Figs. 4.7(a), (c), respectively. Then, it seems that amplitude of oscillations is not same for full 360° rotation. It seems that those irregularities are to some extent in correlation with one-fold and three-fold oscillations of $\Phi_{M_L}$ contribution. If we would lower one-fold amplitude and then superimpose those oscillations on the regular four-fold shape of $\Phi_{M_L M_T}$ curve, the outcome should be somewhat similar to the measured experimental data. Only exception is in Fig. 4.7(d), where this trend is opposite then in the rest of the subplots, which may be related to the opposite sign of $\Phi_{M_L M_T}$ contribution in

| Contribution [mdeg] | Fig. 4.7(a) | Fig. 4.7(b) | Fig. 4.7(c) | Fig. 4.7(d) |
|---|---|---|---|---|
| $\Phi_{M_L M_T}$ off. fit | 10.195 | 12.157 | -9.172 | -6.163 |
| $\Phi_{M_L M_T}$ off. sim. | 7.197 | 7.299 | 6.617 | -7.230 |
| $\Phi_{M_L M_T}$ amp. fit | 2.793 | 3.81 | 3.511 | 3.693 |
| $\Phi_{M_L M_T}$ amp. sim. | 5.198 | 5.708 | 6.217 | 5.708 |
| $\Phi_{M_T^2-M_L^2}$ off. fit | -0.965 | -0.718 | 1.309 | 0.591 |
| $\Phi_{M_T^2-M_L^2}$ off. sim. | 0.000 | 0.000 | 0.000 | 0.000 |
| $\Phi_{M_T^2-M_L^2}$ amp. fit | 3.154 | 3.369 | 3.941 | 3.721 |
| $\Phi_{M_T^2-M_L^2}$ amp. sim. | 5.198 | 5.704 | 6.213 | 5.704 |

TABLE 4.2: The table compare offsets and amplitudes of $\Phi_{M_L M_T}$ and $\Phi_{M_T^2-M_L^2}$ contributions from Fig. 4.7 obtained from fit to experimental data and from numerical simulations.

this case. Note that tilted easy plane of the sample would not explain this behaviour, as $\Phi_{M_L M_T}$ contribution is obtain through Eq. (4.0.1c), which would effectively filter out this PMOKE contribution. Introducing some curvature to magnetic easy plane, as suggested before, could explain such behaviour due to different magnitude of $M_z$ component with each of four directions required by Eq. (4.0.1c) (and thus the PMOKE contribution would not be filter out in $\Phi_{M_L M_T}$), but then the same behaviour should be observed with $\Phi_{M_T^2-M_L^2}$ (with 45° phase shift in $\alpha$), which is not the case of our measurements.

To ensure that we are not observing just some artefact of the vector MOKE setup, we are showing here measurements of the same sample at MOKE spectroscopic setup (described in Sec. 3.1.2), where we were able to align the sample well enough to provide measurement with full 360° rotation of the sample. The results for several wavelengths are shown in Fig. 4.9. The values of optical and MO parameters used in numerical simulations are summarized in the table that is part of the figure. We will not discuss comparison of fit to experimental data with numerical calculations in such a detail as before, but note that when experimental results are compare to numerical simulations, the offset of $\Phi_{M_L M_T}$ have perfect match in Fig. 4.9(c), but is completely off in Fig. 4.9(d). This just show that spectra of MO parameters yielded from Fe(001) sample with nominal thickness 12.5 nm are in good match with MO parameters of Fe(011) sample (RS210917) at some photon energies, but quite off at others photon energies. Overall comparison is then summarized and evaluated in Tab. 4.3. Furthermore, we would like to point out two things: (i) the irregularities in $\Phi_{M_L M_T}$ contribution present with measurements on vector MOKE setup, which slightly questioned our theory of tilted magnetic easy plane, are not present in those measurements anymore, (ii) one-fold and three-fold oscillations of $\Phi_{M_L}$ and $\Phi_{M_T}$ contribution do not vanish even in Fig. 4.9(d) where $\Phi_{M_L M_T}$ and

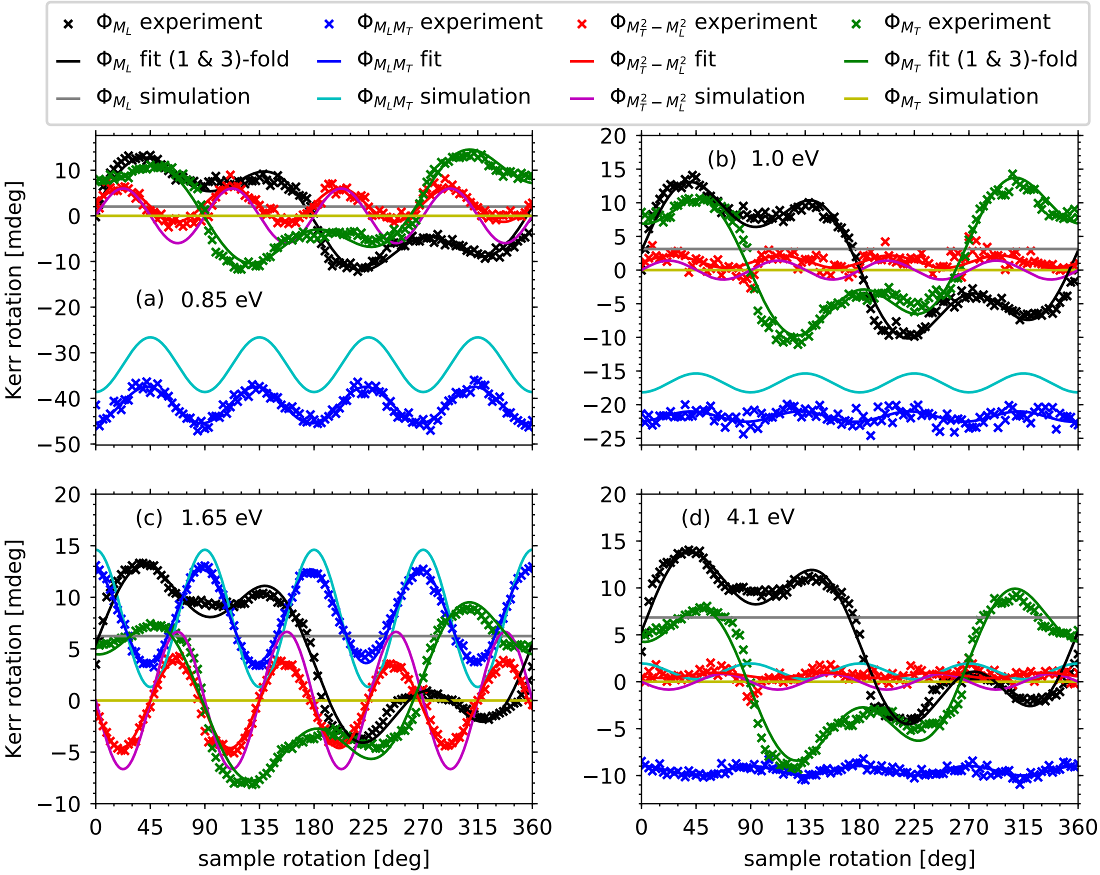

| | (a) | (b) | (c) | (d) |
|---|---|---|---|---|
| $\varepsilon_d$(MgO) | 2.94+0i | 2.95+0i | 2.99+0i | 3.25+0i |
| $\varepsilon_d$(Fe) | -16.64+51.27i | -11.17+44.10i | -3.23+30.00i | -5.21+8.27i |
| $\varepsilon_d$(Pt) | -23.25+70.44i | -25.76+56.27i | -15.13+25.48i | -2.64+6.44i |
| $K$ | -3.616+2.558i | -2.912+1.819i | -1.562+0.467i | -0.159-0.107i |
| $G_s$ | -0.2111-0.0449i | -0.1416-0.0613i | -0.0172-0.0633i | 0.0025-0.0028i |
| $2G_{44}$ | -0.0611-0.0450i | -0.0290-0.0203i | -0.0140-0.0096i | 0.0024+0.0024i |

Figure 4.9: 8-directional measurement of Fe(011) sample RS210917 executed on Spectroscopy MOKE setup. Incident wave was $s$-polarized and AoI=5°. Photon energies of probing light is sated as insets in each graph. Table summarize optical and MO parameters used in numerical simulations.

$\Phi_{M_T^2-M_L^2}$ oscillations are almost extinguished due to small $\Delta G$ parameter. This also further supports our assumption of tilted magnetic easy plane.

Now, we take a look on another Fe(011) sample to see if the behaviour of sample RS210917 is consistent. In Fig. 4.10 we present the 8-directional measurements of the sample RS260917 measured on the vector MOKE setup for all 4 available wavelengths, where used optical and MO parameters for numerical simulation are summarized in the table that is part of the figure.

| Contribution [mdeg] | Fig. 4.9(a) | Fig. 4.9(b) | Fig. 4.9(c) | Fig. 4.9(d) |
|---|---|---|---|---|
| $\Phi_{M_L M_T}$ off. fit | -41.471 | -21.711 | 8.163 | -9.484 |
| $\Phi_{M_L M_T}$ off. sim. | -32.620 | -16.766 | 7.957 | 1.109 |
| $\Phi_{M_L M_T}$ amp. fit | 4.002 | 0.772 | 4.537 | 0.510 |
| $\Phi_{M_L M_T}$ amp. sim. | 5.991 | 1.409 | 6.653 | 0.837 |
| $\Phi_{M_T^2-M_L^2}$ off. fit | 2.384 | 1.251 | -0.441 | 0.681 |
| $\Phi_{M_T^2-M_L^2}$ off. sim. | 0.000 | 0.000 | 0.000 | 0.000 |
| $\Phi_{M_T^2-M_L^2}$ amp. fit | 3.712 | 0.924 | 4.177 | 0.287 |
| $\Phi_{M_T^2-M_L^2}$ amp. sim. | 5.991 | 1.409 | 6.653 | 0.837 |
| $\Phi_{M_L}$ fit 1-fold Amp. | 10.257 | 9.816 | 7.217 | 7.621 |
| $\Phi_{M_L}$ fit 3-fold Amp. | 5.032 | 4.66 | 3.498 | 3.902 |
| $\Phi_{M_T}$ fit 1-fold Amp. | 10.264 | 9.768 | 7.243 | 7.514 |
| $\Phi_{M_T}$ fit 3-fold Amp. | 4.874 | 4.590 | 3.473 | 3.866 |

TABLE 4.3: Offsets and amplitudes of $\Phi_{M_L M_T}$ and $\Phi_{M_T^2-M_L^2}$ contributions from Fig. 4.9 obtained from fit to experimental data and from numerical simulations. In case of contributions $\Phi_{M_L}$ and $\Phi_{M_T}$ we show only outcome of the fit to experimental data.

| Contribution [mdeg] | Fig. 4.10(a) | Fig. 4.10(b) | Fig. 4.10(c) | Fig. 4.10(d) |
|---|---|---|---|---|
| $\Phi_{M_L}$ off. fit | 37.194 | 40.508 | 43.200 | 41.952 |
| $\Phi_{M_L}$ off. sim. | 34.238 | 36.809 | 41.506 | 41.328 |
| $\Phi_{M_L M_T}$ off. fit | 1.221 | 0.247 | -1.878 | -2.007 |
| $\Phi_{M_L M_T}$ off. sim. | 3.083 | 3.729 | 8.348 | 9.233 |
| $\Phi_{M_L M_T}$ amp. fit | 0.370 | 0.183 | 0.908 | 1.199 |
| $\Phi_{M_L M_T}$ amp. sim. | 1.417 | 0.342 | 5.441 | 6.165 |
| $\Phi_{M_T^2-M_L^2}$ off. fit | -0.366 | -0.344 | -0.692 | -0.865 |
| $\Phi_{M_T^2-M_L^2}$ off. sim. | 0.000 | 0.000 | 0.000 | 0.000 |
| $\Phi_{M_T^2-M_L^2}$ amp. fit | 0.105 | 0.147 | 1.017 | 1.033 |
| $\Phi_{M_T^2-M_L^2}$ amp. sim. | 1.417 | 0.342 | 5.441 | 6.165 |
| $\Phi_{M_L}$ fit 2-fold Amp. | 0.572 | 0.600 | 0.720 | 0.774 |
| $\Phi_{M_L}$ fit 4-fold Amp. | 0.034 | 0.230 | 0.182 | 0.164 |
| $\Phi_{M_T}$ fit 2-fold Amp. | 0.756 | 0.929 | 0.873 | 0.801 |
| $\Phi_{M_T}$ fit 4-fold Amp. | 0.153 | 0.042 | 0.0413 | 0.074 |

TABLE 4.4: The table compare experimental values (fit to experimental values) and values of numerical simulation from Fig. 4.10. We show only comparison for QMOKE contribution $\Phi_{M_L M_T}$ and $\Phi_{M_T^2-M_L^2}$. In case of contribution $\Phi_{M_L}$ and $\Phi_{M_T}$ we compare only offset. The values from fit to the oscillations of $\Phi_{M_L}$ and $\Phi_{M_T}$ contribution are then presented in the lower part of the table.

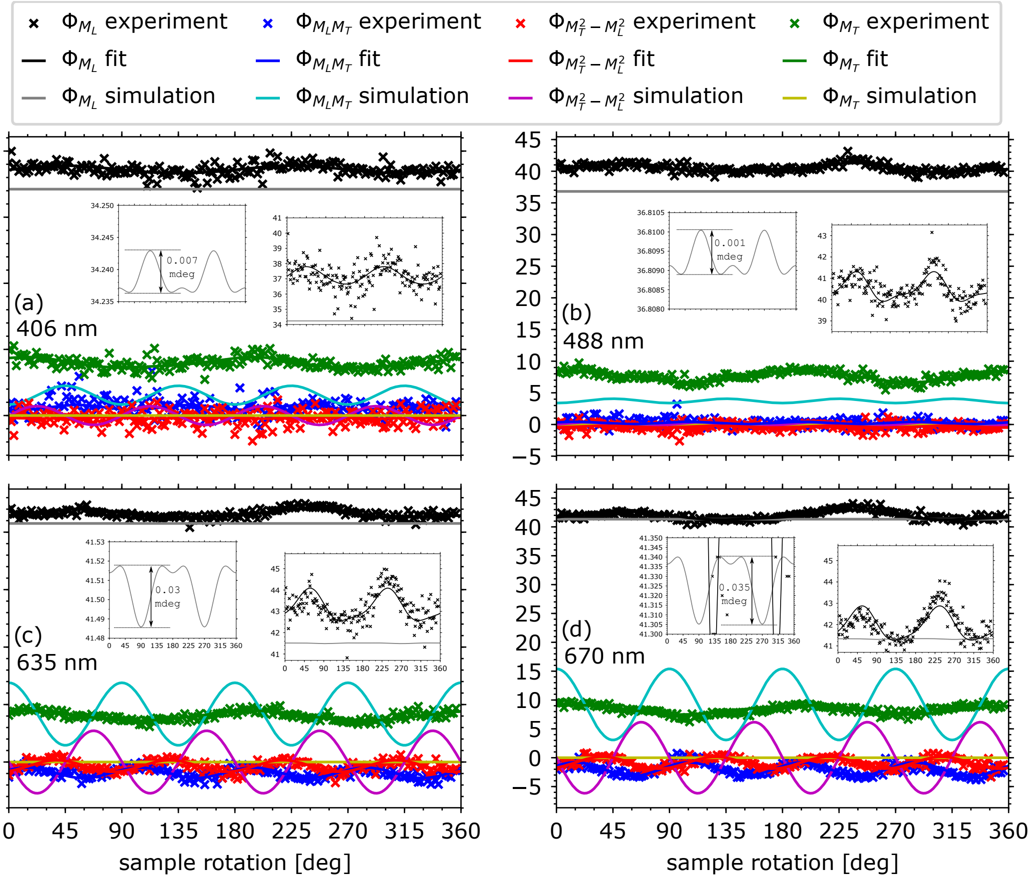

| | (a) | (b) | (c) | (d) |
|---|---|---|---|---|
| $\varepsilon_d$(MgO) | 3.10+0i | 3.05+0i | 3.01+0i | 3.00+0i, |
| $\varepsilon_d$(Fe) | -8.51+16.23i | -6.70+22.63i | -3.18+27.51i | -3.02+28.25i |
| $\varepsilon_d$(Pt) | -5.27+9.97i | -7.60+13.07i | -11.87+19.49i | -12.89+21.22i |
| $K$ | -0.398-0.210i | -0.735-0.198i | -1.266+0.173i | -1.356+0.260i |
| $G_s$ | 0.0058+0.0019i | 0.0220-0.0054i | 0.0086-0.0475i | 0.0019-0.0528i |
| $2G_{44}$ | 0.0111-0.0012i | 0.0086-0.0145i | -0.0074-0.0163i | -0.0108-0.0149i |

FIGURE 4.10: 8-directional measurement of sample RS260917 with incident $s$-polarized light. Used wavelength is stated in each graph as text inset. Experimental points of $\Phi_{M_L}$ and $\Phi_{M_T}$ contributions are fitted with goniometrical function of two-fold and four-fold symmetry. Further, a detail of experiment with fit and numerical simulation of LMOKE $\Phi_{M_L}$ contribution is shown in each graphs in form of two insets, respectively.

The scenario of $\Phi_{M_L}$ and $\Phi_{M_T}$ contributions is now different from the previous case. We observe no one-fold or three-fold oscillations anymore with this sample, but contributions are not isotropic either. The fit of function $O + A_1 \cos(4\alpha + \varphi_1) + A_2 \cos(2\alpha + \varphi_2)$ describes now the experimental data well. The amplitudes of two-fold and four-fold oscillations of $\Phi_{M_L}$ and $\Phi_{M_T}$ contributions from Figs. 4.10(a)–(d) are summarized in Tab. 4.4. In all the measurements the amplitudes are <1 mdeg, which is "small enough" to possibly have the same origin as the two-fold and four-fold oscillations in our numerical model. But, on the other hand, the oscillations simulated using MO parameters of Fe are in all four cases about 1–2 orders lower than the one observed in the experiment, as indicated by the insets in Fig. 4.10. Thus, it is also plausible that the correlation here is rather random and further systematic investigation is needed to provide evidence that this two-fold and four-fold anisotropy of $\Phi_{M_L}$ and $\Phi_{M_T}$ contributions are of MO origin same as in our numerical simulations. The isotropic part (offset) of LMOKE $\Phi_{M_L}$ contribution is here in much better agreement with numerical simulation than within sample RS210917, especially in case of measurements at wavelength 635 nm and 670 nm, being presented in Figs. 4.10 (c) and (d), respectively. Contribution $\Phi_{M_T}$ have in all graphs clear offset, that is too strong to be explained by misaligned $x$- axis magnets. All this together may be caused by the fact that the sample is not 100% saturated with any sample orientation $\alpha$ as Fig. 3.20 suggest. Non of the two loops measured in the magnetic in-plane easy and hard axis (although the difference between easy and hard magnetic axis is quite small here) are in full saturation. Concerning this issue, we would like to mention here rotating field separation method [19], allowing the separation also for sample that are not fully saturated. But note that this would not solve the problem with the saturation in this case, as even rotating field method require full saturation at least with magnetic easy axis, which is not the case of sample RS260917.

Figure 4.10 (d) and Figure 4.7 (a) show measurements of smaple RS260917 and RS210917 under same conditions, respectively. The oscillations of $\Phi_{M_L M_T}$ and $\Phi_{M_T^2 - M_L^2}$ contributions are half that strong in the case of the sample RS260917. This may be connected with different thickness of the samples, but also with some in-plane twinning of the sample RS260917 as was shown in Fig. 3.16 presented in Sec. 3.4.3. Nevertheless, the substantial difference in offset of $\Phi_{M_L M_T}$ should not be affected by twinning to any extent, as this isotropic part of QMOKE should be independent of crystal orientation and should be present even with polycrystalline samples. Note that prediction of numerical model are also quite higher than the real experimental values.

At the end of this discussion about experimental results of Fe(011) samples, we would like to comment on the results of Liang *et al.* from Ref. [36], where the measurements of Fe(011)/GaAs(011) sample by rotating field method are discussed. In their study they experimentally show that LMOKE contribution posse two-fold anisotropy. Furthermore, they also present that contribution $\Phi \sim M_T^2$ (contribution they use in contrast to our $\Phi_{M_T^2-M_L^2}$ contribution) poses strong four-fold as well as strong two-fold anisotropy. They support the findings with the theoretically predicted dependence of the off-diagonal permittivity tensor elements [Eq. (4.2.1) at the beginning of this section]. But interestingly, their equations have a different shape than ours, although the reference is given to the same literature [38].

We believe that two-fold anisotropy of their $\Phi \sim M_T^2$ contribution originate from what we present as $\Phi_{\mathrm{Const.}}$ contribution. Nevertheless, this would suggest that their measurement is not differential and they are able to measure MOKE signal absolutely instead. In our case, measurements of contributions $\Phi_{M_L}$, $\Phi_{M_L M_T}$, $\Phi_{M_T^2-M_L^2}$ and $\Phi_{M_T}$ according to Eqs. (4.0.1a)–(4.0.1c), respectively, all are differential measurements, i.e. filter out any static contribution that is not dependent on $\boldsymbol{M}$ direction as is e.g. $\Phi_{\mathrm{Const.}}$ contribution. The reason why we did not show $\Phi_{\mathrm{Const.}}$ contribution in any of our experimental measurements is that absolute measurement of MOKE signal is technically very demanding, and although we tried to do so, we were not able to conclusively separate which part of the measured signal is originating from MO effects, i.e. $\Phi_{\mathrm{Const.}}$ contribution, and which is caused by e.g. negligible sample wobbling upon its rotation by angle $\alpha$.

The two-fold symmetry of LMOKE contribution measured on Fe(011)/GaAs(011) has roughly same amplitude as the amplitude of two-fold oscillations of $\Phi_{M_L}$ experimentally observed on the sample RS260917. Thus, the origin of those two-fold oscillations could be the same in both cases, although in our case we would need more satisfying evidence that those oscillations are really of MO origin. Further, in the case of Fe(011)/GaAs(011) we would suggest to consider also contribution of interface, which was recently reported to be source of two-fold anisotropy of PMOKE measured on Fe/GaAs system [131].

Finally, Liang *et al.* also used numerical calculations based on Yeh's formalism to describe their experimental observations. The numerical calculus indeed described those LMOKE two-fold oscillations, but the result posses also four-fold oscillations – same as is the case of our numerical simulations. The shape of the numerically calculated curve describing LMOKE dependence on sample orientation $\alpha$ presented by Liang *et al.* is in exact match with shape of our numerically calculated LMOKE $\Phi_{M_L}$ contribution (see insets in Fig. 4.10). Note that if we would not use MO parameters obtained by QMOKE spectroscopy of Fe(001) samples, but instead fit the numerical model into the measured 8-directional method (for this we would need measurement of Kerr ellipticity as well) with MO parameters as free variable of the fit, we would also probably obtain result that would describe those oscillations, but from our point of view the MO parameters that would be found by the fit would be questionable. Although MO parameters of Fe may quantitatively differ from sample to sample (as will be shown in Chapter 5), the qualitative aspect of MO tensors $\boldsymbol{K}$ and $\boldsymbol{G}$ should be in principle same and independent from surface orientation.

### 4.2.4 Utilizing 8-directional method of (011) orientation for spectroscopy

Although we do not present any spectroscopy of (011) oriented cubic crystal samples in this work, we offer here an idea how the measurement process should be done. Same as in the case of cubic (001) oriented samples we present here in Eq. (4.2.6) description of MOKE with dependence on individual MO parameters.

$$\begin{aligned}\Phi_{s/p} = \pm A_{s/p}\Bigg\{ & 2G_{44}\left[\left(\frac{5}{16}+\frac{3}{16}\cos 4\alpha\right)\sin 2\mu - \frac{3}{16}\sin 4\alpha\cos 2\mu\right] \\ & + G_s\left[\frac{3}{16}(1-\cos 4\alpha)\sin 2\mu + \frac{3}{16}\sin 4\alpha\cos 2\mu\right] \\ & -\frac{K^2}{2\varepsilon_d}\sin 2\mu\Bigg\} \\ \pm B_{s/p}\ & K\sin\mu.\end{aligned} \tag{4.2.6}$$

Here we can see that with sample orientation $\alpha = 0°$ the $\Phi_{M_L M_T}$ contribution is dependent only on $2G_{44}$. But there is no point in the 8-directional method of (011) oriented cubic crystal structures, where the MOKE would stem from $G_s$ without any contribution of $2G_{44}$. Nevertheless, if we extract value of $K$ from the LMOKE measurement, and then the value of $2G_{44}$ from the QMOKE measurement at $\alpha = 0°$, we may then measure QMOKE response with some other sample orientation where $G_s$ contribute to the MOKE signal and include the contribution of $K$ and $2G_{44}$ from previous measurements, thus extract solely value of $G_s$.

On the other hand, if there is such a anisotropic contribution to LMOKE signal as was presented within the samples above, this process will not be valid anymore. Of course, we can always run fit to whole 8-directional method measurement at each wavelength and set all the MO parameters as free variables of the fit, yet, such an access would be considerably time demanding for experimental data gathering.

## 4.3 The 8-directional method of (111) orientation

### 4.3.1 Equations of 8-directional method of (111) orientation

In order to get permittivity tensor of (111) oriented cubic crystal structure, we have to rotate (001) oriented cubic crystal structure (i.e. permittivity tensor) around the $x$-axis of our coordinate system by angle $\vartheta_x = 45°$ [which get us to (011) orientation] and subsequent rotation around $y$-axis by angle $\vartheta_y = 35.26°$ [$\arcsin(\vartheta_y) = 1/\sqrt{3}$] will get us to (111) orientation. Another possibility is to make single rotation of (001) oriented cubic crystal structure by angle $\vartheta_{-xy} = 54.73°$ [$\arcsin(\vartheta_{-xy}) = \sqrt{2}/\sqrt{3}$] around $-xy$ axis. The latter approach was used in the Ref. [38], which provide us with

$$\varepsilon'^{(111)}_{yx/xy} = \left[2G_{44} + \frac{1}{3}\Delta G\right] M_L M_T, \tag{4.3.1}$$

$$\begin{aligned}\varepsilon'^{(111)}_{zx/xz} = & -\frac{1}{3}\Delta G\left(\cos 3\alpha + \sin 3\alpha\right) M_L M_T \\ & +\frac{1}{6}\Delta G\left(\cos 3\alpha - \sin 3\alpha\right)\left(M_T^2 - M_L^2\right) \\ & \pm K M_L,\end{aligned} \tag{4.3.2}$$

$$\begin{aligned}\varepsilon'^{(111)}_{yz/zy} = & -\frac{1}{3}\Delta G\left(\cos 3\alpha - \sin 3\alpha\right) M_L M_T \\ & -\frac{1}{6}\Delta G\left(\cos 3\alpha + \sin 3\alpha\right)\left(M_T^2 - M_L^2\right) \\ & \pm K M_T.\end{aligned} \tag{4.3.3}$$

The permittivity tensor element $\varepsilon_{yx/xy}$ is now isotropic, i.e. independent on the sample orientation $\alpha$. However, the rest of the off-diagonal elements $\varepsilon_{zx/xz}$ and $\varepsilon_{yz/zy}$, that were in all previous cases only linear in $\boldsymbol{M}$, are now, for the first time, also quadratic in $\boldsymbol{M}$ and dependent on the sample orientation $\alpha$. This is making things more interesting, because those elements are intermixing in the cross-term of Eq. (2.5.1). In the previous cases this intermixing only caused optically induced quadratic in $\boldsymbol{M}$ contribution $K^2/\varepsilon_d$ to QMOKE. But now, we should see optically induced contributions of 3rd and 4th orders in $\boldsymbol{M}$. The outcome of Eq. (2.5.1) for (111) oriented cubic crystal structures is

$$
\begin{aligned}
\Phi_{s/p}^{(111)} &= \pm A_{s/p}\left(2G_{44}+\frac{\Delta G}{3}-\frac{K^2}{\varepsilon_d}\right)M_L M_T\\
&\quad + B_{s/p}\Bigg[\pm K M_L-\frac{\Delta G}{3}\left(\cos 3\alpha+\sin 3\alpha\right)M_L M_T\\
&\qquad +\frac{\Delta G}{6}\left(\cos 3\alpha-\sin 3\alpha\right)\left(M_T^2-M_L^2\right)\Bigg]\\
\begin{matrix}\text{Optically induced}\\ 3^{\text{rd}}\text{ order}\end{matrix}\quad &\begin{cases} -A_{s/p}\Bigg\{\dfrac{K\Delta G}{2\varepsilon_d}\left[\left(\cos 3\alpha+\sin 3\alpha\right)M_L M_T^2+\left(\cos 3\alpha-\sin 3\alpha\right)M_L^2 M_T\right]\\[2ex] \qquad -\dfrac{K\Delta G}{6\varepsilon_d}\left[\left(\cos 3\alpha+\sin 3\alpha\right)M_L^3+\left(\cos 3\alpha-\sin 3\alpha\right)M_T^3\right]\Bigg\}\end{cases}\\
\begin{matrix}\text{Optically induced}\\ 4^{\text{th}}\text{ order}\end{matrix}\quad &\begin{cases} \pm A_{s/p}\Bigg\{\dfrac{\Delta G^2}{9\varepsilon_d}\sin 6\alpha\left(M_L M_T^3-M_L^3 M_T\right)\\[2ex] \qquad +\dfrac{\Delta G^2}{36\varepsilon_d}\left[2\cos 6\alpha M_L^2 M_T^2-\cos 6\alpha\left(M_T^4+M_L^4\right)\right]\Bigg\}.\end{cases}
\end{aligned}
\tag{4.3.4}
$$

When this is expressed through in-plane $\boldsymbol{M}$ direction angle $\mu$ we have

$$
\begin{aligned}
\Phi_{s/p}^{(111)} &= \pm A_{s/p}\left(\frac{2G_{44}}{2}+\frac{\Delta G}{6}-\frac{K^2}{2\varepsilon_d}\right)\sin 2\mu\\
&\quad + B_{s/p}\Bigg[\pm K\sin\mu-\frac{\sqrt{2}}{6}\Delta G\sin\left(3\alpha+\frac{\pi}{4}\right)\sin 2\mu\\
&\qquad +\frac{\sqrt{2}}{6}\Delta G\cos\left(3\alpha+\frac{\pi}{4}\right)\cos 2\mu\Bigg]\\
\begin{matrix}\text{Optically induced}\\ 3^{\text{rd}}\text{ order}\end{matrix}\quad &\begin{cases} -A_{s/p}\dfrac{\sqrt{2}}{6\varepsilon_d}K\Delta G\left[\sin\left(3\alpha+\dfrac{\pi}{4}\right)\sin 3\mu+\cos\left(3\alpha+\dfrac{\pi}{4}\right)\cos 3\mu\right]\end{cases}\\
\begin{matrix}\text{Optically induced}\\ 4^{\text{th}}\text{ order}\end{matrix}\quad &\begin{cases} \pm A_{s/p}\left[\dfrac{\Delta G^2}{36\varepsilon_d}\sin 6\alpha\sin 4\mu-\dfrac{\Delta G^2}{72\varepsilon_d}\cos 6\alpha\cos 4\mu-\dfrac{\Delta G^2}{72\varepsilon_d}\cos 6\alpha\right].\end{cases}
\end{aligned}
\tag{4.3.5}
$$

The scenario is now very much different from the two previous cases. Isotropic part of contribution $\Phi_{M_L M_T}$ is still proportional to optical weighting factor $A_{s/p}$, i.e. is maximal with normal AoI, but the anisotropic part is now dependent on optical weighting factor $B_{s/p}$, thus is extinct with normal AoI. Contribution $\Phi_{M_T^2 - M_L^2}$ is now dependent on $B_{s/p}$ and same as in previous cases do not posses any isotropic contribution (i.e. offset). Now, we are getting to the optically induced 3rd and 4th order in $\boldsymbol{M}$ contributions. From their dependence on $\boldsymbol{M}$ direction we can see that optically induced 3rd order, that is odd in $\boldsymbol{M}$, will be imposed to $\Phi_{M_L}$ and $\Phi_{M_T}$ contributions, whereas optically induced contribution of 4th order, that is even in $\boldsymbol{M}$, will be imposed to $\Phi_{M_L M_T}$ and $\Phi_{M_T^2 - M_L^2}$ contributions.

This may introduce little bit of confusion into the denomination of $\Phi_{M_L}$, $\Phi_{M_L M_T}$, $\Phi_{M_T^2 - M_L^2}$ and $\Phi_{M_T}$, which are contributions separated directly from 8-directional method as described in Eqs. (4.0.1a)–(4.0.1d), respectively. In the case of (001) and (011) orientations, the denomination of those contributions through $\boldsymbol{M}$ components is in perfect match with their $\boldsymbol{M}$ dependence. But this is no more true for the (111) oriented cubic crystal structures due to additional contribution of those optically induced 3rd and 4th orders in $\boldsymbol{M}$, where their true dependence on $\boldsymbol{M}$ can be seen in Eq. (4.3.4) and Eq. (4.3.5). Yet, to keep things consistent, we will hold the denomination of those contributions same as in previous sections.

However, note that an objection is in place that our approach to approximations of MOKE is not consistent with (111) oriented cubic crystal structures. On the one hand we acknowledge "only" contributions up to 2nd order in $\boldsymbol{M}$ to the permittivity tensor $\boldsymbol{\varepsilon}$, but then, on the other hand, we acknowledge optically induced contributions of 3rd and 4th order in $\boldsymbol{M}$. As will be shown below, the contribution of 4th order can be safely omitted, but this is no more true for the contribution of 3rd order. If we would neglect it as well, we would not be able to explain some features in the experimental observations of 8-directional measurements. Thus, if we do acknowledge optically induced contribution of 3rd order, we should also acknowledge some contribution of 3rd order in $\boldsymbol{M}$ to the permittivity tensor, i.e. some cubic MO tensor that would together with $\boldsymbol{M}^3$ give rise to $\boldsymbol{\varepsilon}^{(3)}$. However, all the experimental observations are qualitatively explained here just by this optically induced contribution of 3rd order and, thus, it seems that contribution of such cubic MO tensor to permittivity tensor would only contribute quantitatively into the signal. Thus, in this work we will acknowledge optically induced contribution of 3rd order in the case of (111) oriented cubic crystal structure although no cubic MO tensor have been introduced, and in the final conclusion of this work we will provide some ideas on how to resolve this issue in the future.

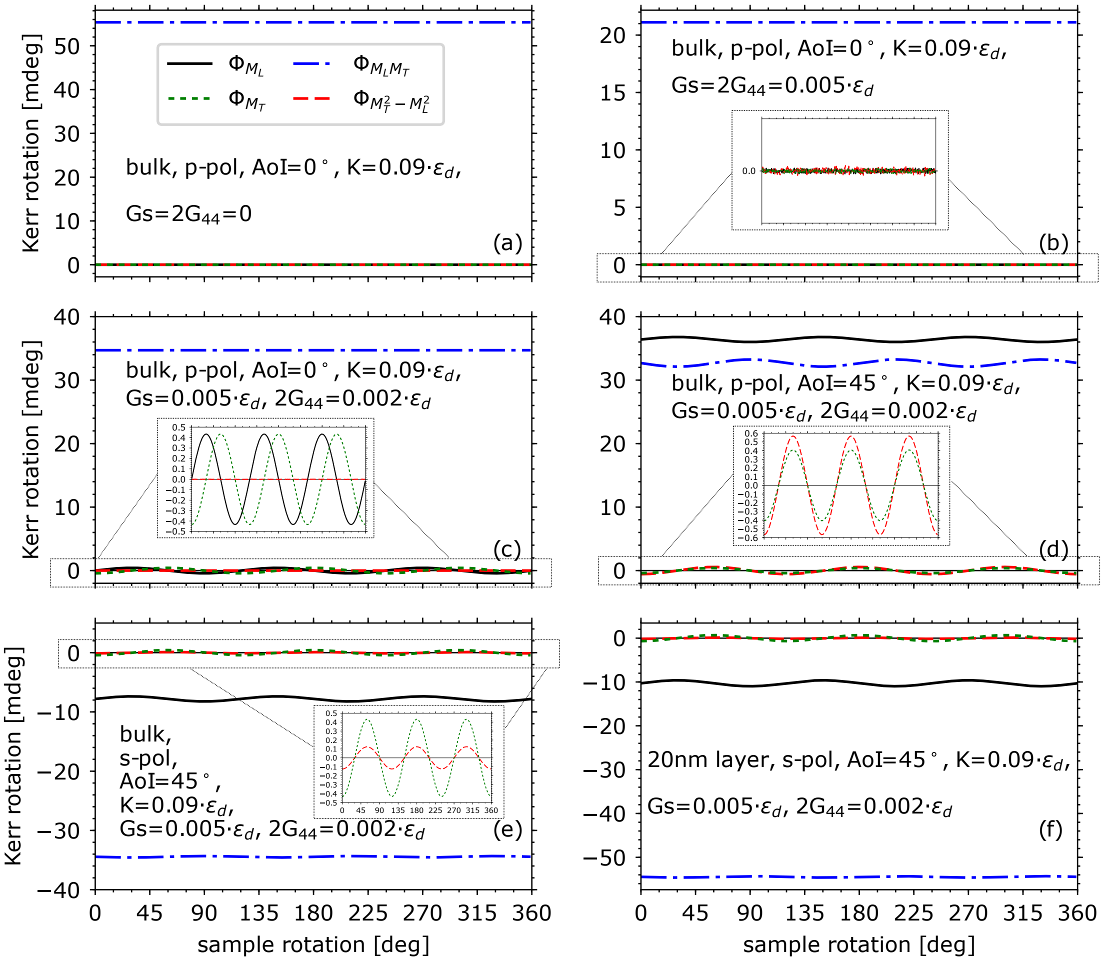

FIGURE 4.11: Numerical simulations of the 8-directional method of (111) oriented cubic crystal structures. For all six graphs we hold photon energy of incident light at 1.85 eV, $\varepsilon_d = -3.02 + 28.24i$ and $K = 0.09 \cdot \varepsilon_d$. Rest of the values was changed with each simulation, and all the values are stated as the text inset in the individual graphs. Bulk means that structure in calculations is FM/air interface. In last graph (f) MgO substrate/20nm FM layer/air structure was used instead with ($\varepsilon_d$(MgO)=3.0+0i). AoI stands for angle of incidence.

### 4.3.2 Comparison of 8-directional equations of (111) orientation to numerical simulations

We will again compare predictions of Eq. (4.3.5) with numerical simulations. In Figs. 4.11(a) – (e) we show numerical calculations of contributions separated by the 8-directional method of (111) oriented cubic crystal structures. We are holding the parameters of numerical model same as they were with previous (001) and (111) orientations. Figures 4.11(a) and (b), where only $K^2/\varepsilon_d$ and $2G_{44} - K^2/\varepsilon_d$ contributes, respectively, are in exact match with previous cases. LMOKE $\Phi_{M_L}$ is here extinct due to normal AoI. The noise presented in inset of Fig. 4.11(b) is due to deflection of $\boldsymbol{M}$ by random angle

$\Delta\mu$ as is discussed in Sec. 3.1.4. In Fig. 4.11(c), where $\Delta G \neq 0$, we may see that $\Phi_{M_L M_T}$ and $\Phi_{M_T^2 - M_L^2}$ contributions still do not posses any oscillations, as their anisotropic part is now $\sim B_{s/p}$ and thus is suppressed by normal AoI. Contribution of optically induced $4^{\text{th}}$ order is not pronounced here, and we will take a closer look on it later. On the other hand, optically induced contribution of $3^{\text{rd}}$ order is well pronounced with $\Phi_{M_L}$ and $\Phi_{M_T}$ contributions. The oscillations are not very strong and the inset of Fig. 4.11(c) is presenting their close-up. When AoI is raised to 45° in Fig. 4.11(d), the anisotropic part of $\Phi_{M_L M_T}$ and $\Phi_{M_T^2 - M_L^2}$ spring up as expected. We may see that those oscillations are slightly stronger than that of $\Phi_{M_L}$ and $\Phi_{M_T}$. Thus, in this case $B_{s/p} > A_{s/p}K/\varepsilon_d$, but this does not have to be rule in all cases, as is shown in Fig. 4.11(e), where change of polarization of incident wave is enough to reverse the situation. Further, note that sign changes of individual contributions are well in accordance with change of incident wave polarization as is predicted by Eq. (4.3.5). When we switch from bulk material to 20 nm thin layer, only absolute values of contributions are affected [Fig. 4.11(f)]. Finally, when we compare Fig. 4.11 were anisotropic oscillations occur with Eq. (4.3.5), there is 45° (i.e. $\pi/4$) phase shift discrepancy. This is caused by fact that Eq. (4.3.5) was derived from permittivity tensor elements of cubic (111) surface orientation to which we get through rotation around $-xy$ axis as mentioned above [38]. But in our numerical calculations we rotate permittivity by $\vartheta_x = 45°$ and then by $\vartheta_y = 35.26°$. Both approaches will provide permittivity tensor of cubic (111) surface orientation, but with 45° shift in $\alpha$ with respect to each other. We could provide numerical simulations using rotation around $-xy$ axis to hold this consistent, but the 45° shift does not play any important role at this stage, and the plots are more clear and organised without the shift.

The FFT analysis of data from Fig. 4.11(f) is shown in Fig. 4.12. The amplitudes of three-fold symmetry oscillation in all contributions are much lower then amplitudes of four-fold oscillations with (001) and (011) oriented cubic crystal structures. Of course, the strength of this amplitude will be dependent on many factors, mostly values of MO parameters, but it seems that in general those three-fold oscillations will be much lower in amplitude and, thus, harder to observe in the experiment. Further, we do not observe any six-fold symmetry with $\Phi_{M_L M_T}$ nor $\Phi_{M_T^2 - M_L^2}$ contributions. This is due to fact that those oscillations are so negligible that they get lost in the noise of simulation from random deflection of $\boldsymbol{M}$ by $\Delta\mu$. Note that $\Delta G \ll 1$ and $\varepsilon_d \gg 1$ thus $\Delta G^2/(36\varepsilon_d)$ is truly negligible in its value.

In Fig. 4.13 we show detail of numerical simulation of $\Phi_{M_L M_T}$, $\Phi_{M_T^2 - M_L^2}$ and $\Phi_{\text{Const.}}$ contributions when we kept constant deflection $\Delta\mu = 0.1$ mdeg. Nice six-fold pattern is observable with $\Phi_{M_L M_T}$ contribution as shown in Fig. 4.13(a). Contributions $\Phi_{M_T^2 - M_L^2}$ and $\Phi_{\text{Const.}}$ also poses six-fold symmetry, as indicated in insets of Fig. 4.13(b), but as those contributions are extracted from afflicted $\boldsymbol{M}$ directions $\mu = 0°, 180°$ (as discussed

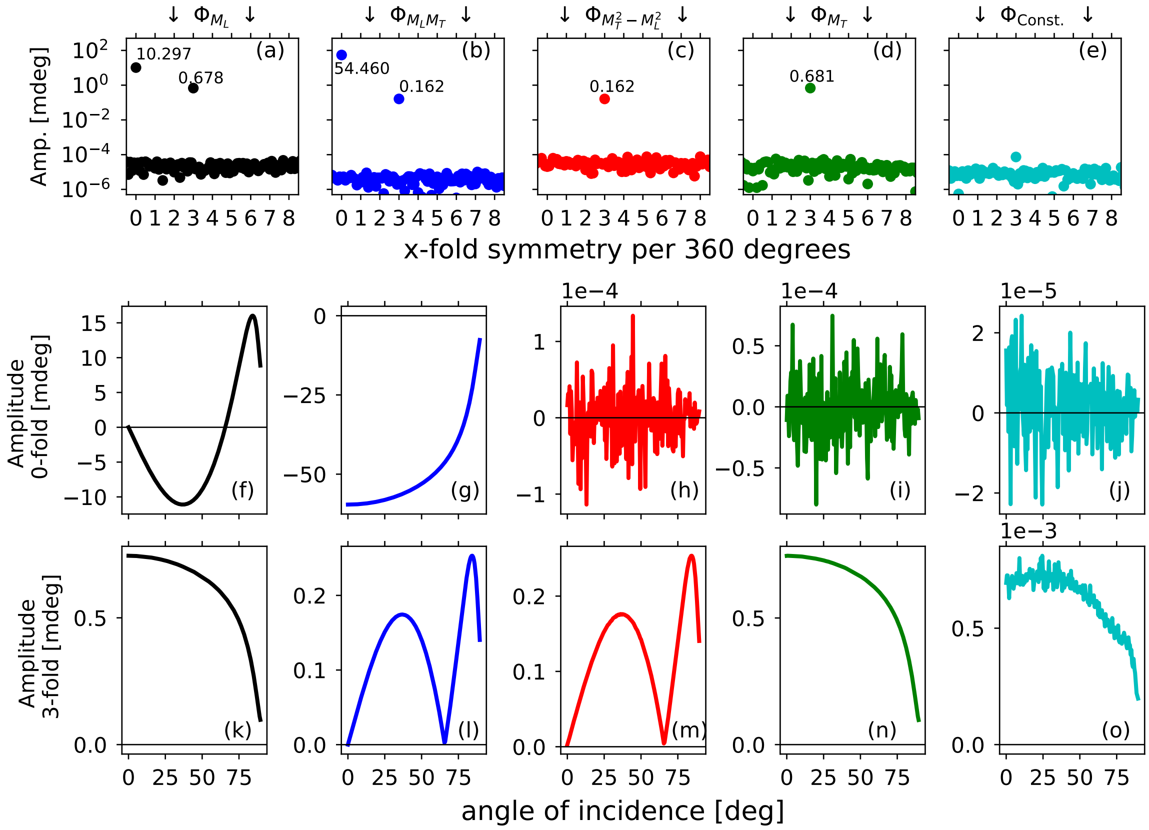

FIGURE 4.12: In (a)–(e) we show FFT of Fig. 4.11(f) contributions $\Phi_{M_L}$, $\Phi_{M_LM_T}$, $\Phi_{M_T^2-M_L^2}$, $\Phi_{M_T}$ and $\Phi_{\mathrm{Const.}}$, respectively. Colours are in compliance. Rest of the graphs (f)–(o) are dependencies on angle of incidence of each contribution, separated to offset (zero-fold amplitude) (f)–(j) and to three-fold oscillations amplitude (k)–(o). The graphs are column and colour sorted.

in Sec. 3.1.4) we may see some numerical instability at certain sample orientations, indicated by the strong peaks. Further, although we do not present exact numbers here, the amplitudes of oscillations are very different for each of those 3 contributions, contrary to predictions of Eq. (4.3.5). This may be attributed to approximative Eq. (2.5.1) from which Eq. (4.3.5) stems, or, of course, we could make a mistake during its derivation.

Nevertheless, this optically induced contributions of 4th order are so negligible that can be safely omitted and, thus, we will not further investigate wherefrom the inconsistency between derived equations and numerical simulations is stemming from. Further, regarding the numerical instability, note that maximum strength of those peaks is ca. 0.002 mdeg, which is deep below our experimental signal-to-noise ratio. Also, $\boldsymbol{M}$ directions used to yield $\Phi_{M_LM_T}$ contribution are clearly not affected by this numerical instability (and those are $\boldsymbol{M}$ directions used with our QMOKE spectroscopy technique discussed in Chapter 5).

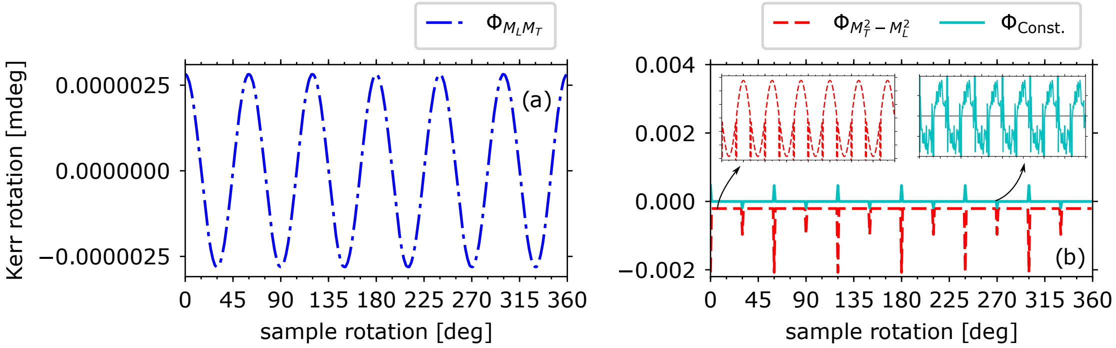

Figure 4.13: Detail of the 8-directional simulation with parameters taken from Fig. 4.11(f), but with AoI=0. The random deflection of $\boldsymbol{M}$ in-plane direction was switched off and kept to $\Delta\mu = 0.1\,$mdeg.

### 4.3.3 Experimental measurements of the Ni(111)/MgO(111) sample, comparison to the theory

Here we present 8-directional measurements of Ni(111) sample epitaxially grown on MgO(111) substrate (as presented in Sec. 3.4.5). All measurements were carried out on the vector MOKE setup. In Figs. 4.14(a) and (b) we present measurement with AoI=45° at wavelength 488 nm for $p$-polarized and $s$- polarized incident wave, respectively. In Figs. 4.14(c) and (d) same set of measurements at wavelength 670 nm is shown. Clear three-fold symmetry is observable as predicted by the theory. Note that changes in signs of individual contributions with change of polarization of incident wave are in exact match with the predictions of Eq. (4.3.5) and predictions of numerical simulations. Strength of amplitudes is summarized in the table that is part of Fig. 4.14. The amplitudes of oscillations are very weak. To carry out those measurements, we actually had to align sample and the setup very carefully and run the measurements multiple times in a row, thus each presented data point is a mean value from multiple measurements. We do not present any numerical calculations for Ni(111) sample, as we are not in possession of MO parameters for this material yet.

Experimental data from second detector, i.e. detector at AoI=0°, are then presented in Fig. 4.15. As all the contributions are quite noisy and with small or any offset, we split contributions by set of two and plot them separately for better clarity of the graphs. The labels of subplots in Fig. 4.15 are chosen with respects to labels of subplots in Fig. 4.14. Figures 4.15(a1) and (a2) refer to the same measurement (except AoI) as is shown in Fig. 4.14(a) and *et cetera*. The amplitude of three-fold oscillations is again summarized in the table that is part of the Fig. 4.15. The oscillations of $\Phi_{M_L}$ and $\Phi_{M_T}$ contributions are clearly pronounced as predicted by the theory. The theory also predicts no oscillations (neglecting optically induced 4th order) for $\Phi_{M_L M_T}$ and $\Phi_{M_T^2-M_L^2}$

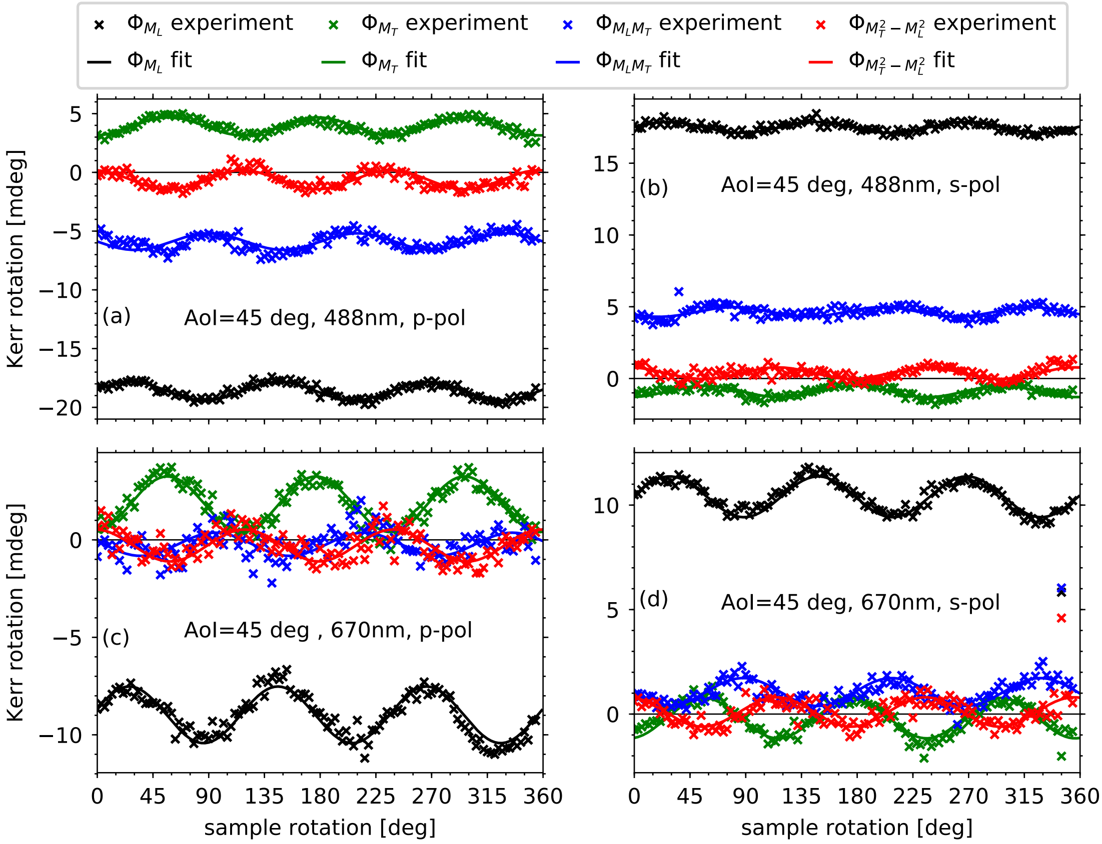

| 3-fold Amp. [mdeg] | (a) | (b) | (c) | (d) |
|---|---|---|---|---|
| $\Phi_{M_L}$ | 0.796 | 0.380 | 1.453 | 0.975 |
| $\Phi_{M_T}$ | 0.769 | 0.396 | 1.427 | 0.967 |
| $\Phi_{M_L M_T}$ | 0.708 | 0.336 | 0.595 | 0.668 |
| $\Phi_{M_T^2-M_L^2}$ | 0.811 | 0.403 | 0.818 | 0.703 |

FIGURE 4.14: Measurements of the 8-directional method of the 22 nm thick Ni(111) layer grown on MgO(111) substrate and capped with ca. 4 nm of Si. Measurements were carried our under AoI of 45° for two different wavelengths and different polarizations of incident light, exactly as stated in the text insets of graphs (a) – (d). The amplitude of three-fold oscillations of each of contributions is summarized in the table that is part of this figure.

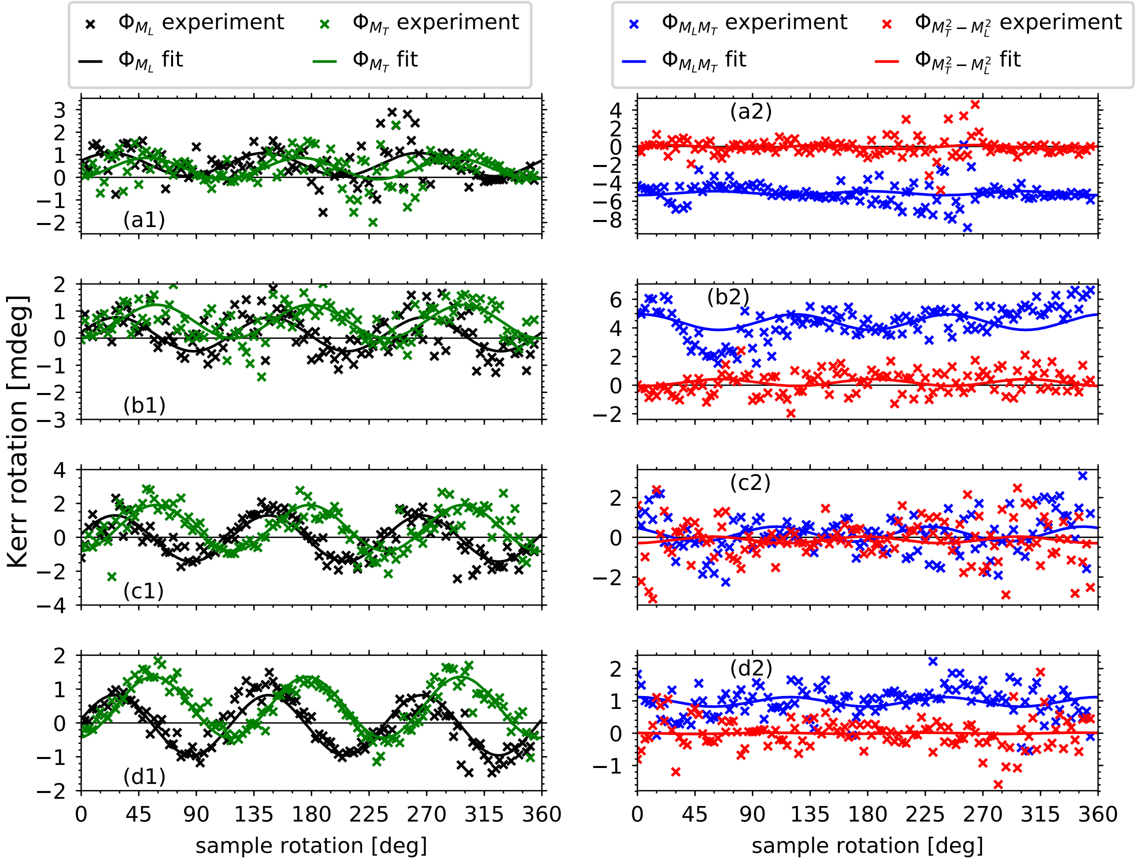

| 3-fold Amp. [mdeg] | (a1) | (b1) | (c1) | (d1) |
|---|---|---|---|---|
| $\Phi_{M_L}$ | 0.517 | 0.629 | 1.364 | 0.890 |
| $\Phi_{M_T}$ | 0.476 | 0.620 | 1.366 | 0.903 |

| 3-fold Amp. [mdeg] | (a2) | (b2) | (c2) | (d2) |
|---|---|---|---|---|
| $\Phi_{M_LM_T}$ | 0.221 | 0.544 | 0.375 | 0.148 |
| $\Phi_{M_T^2-M_L^2}$ | 0.220 | 0.240 | 0.167 | 0.023 |

FIGURE 4.15: Measurements of the 8-directional method of the 22 nm thick Ni(111) layer grown on MgO(111) substrate and capped with ca. 4 nm of Si. Measurements were carried our under AoI of 0°. Otherwise, the conditions of the measurement in (a1) and (a2) are identical as in the Fig 4.14(a) and *et cetera*. Table that is part of the figure summarizes amplitude of three-fold oscialtions from the fit to experimental data.

oscillations. In case of $\Phi_{M_T^2-M_L^2}$ contribution the signal is truly noise around zero, whereas for $\Phi_{M_LM_T}$ contribution, we may see some hint of oscillations in Figs. 4.15(b2) and (d2). The fit to experimental data should not be much trusted here, as the data are quite noisy, and the hint of the oscillations here may be attributed to some small misalignment or artefact of the setup.

### 4.3.4 Utilizing 8-directional method of (111) orientation for spectroscopy

In the case of the 8-directional method of (111) oriented cubic crystal structures, we may isolate contribution of MO parameter $K$ from contribution $\Phi_{M_L}$ at $\alpha = 0°$ ($\pi/4$ shift is not considered). Nevertheless, there is no such a sample orientation $\alpha$ where we could isolate quadratic MO parameters from each other. Thus, at each photon energy we would have to measure $\Phi_{M_L M_T}$ contribution for several sample orientation $\alpha$ in the range of $\alpha = \langle 0°, 120° \rangle$ in order to extract value of $\Delta G$ from amplitude of oscillations and value of $2G_{44}$ from its offset (and thus obtain value of $G_s = \Delta G - 2G_{44}$).

## 4.4 Conclusion

In this chapter, we introduced the equations of the 8-directional method of (011) and (111) oriented cubic crystal structures in addition to the well known description of the (001) oriented cubic crystal structures. The comparison with the numerical model, in which the dependence of individual contributions of the 8-directional method is tested concerning the change of MO parameters, change of AoI and change of polarization of the incident wave, suggests that the equations are derived correctly. Only negligible discrepancies may be found, which can be attributed to an approximative relation of Eq. (2.5.1).

The comparison to the experiment was rather complicated in the case of cubic (011) oriented samples. The contributions $\Phi_{M_L}(\alpha)$ and $\Phi_{M_T}(\alpha)$ posses quite unexpected behaviour of one- and three-fold symmetry for one of the Fe(011) samples. We explained the one-fold symmetry oscillation by a PMOKE contribution caused by a magnetic easy plane that is tilted from the surface of the sample. In the case of three-fold symmetry oscillation, we were not able to provide reliable explanation, but it can be possibly connected to MgO(111) substrate that could induce some additional magnetic anisotropy of three-fold symmetry. The second Fe(011) sample demonstrates a weak two-fold symmetry regarding the sample rotation $\alpha$, which is not predicted by the equations of cubic (011) oriented 8-directional method, but very weak oscillations of such a symmetry have emerged in the numerical model, as well. A correlation between those two-fold oscillations in experiment and numerical model will be subject of future systematic investigations.

In case of experimental measurements of Ni(111) thin film samples, the results qualitatively support predictions of the theory. The complications here are that the anisotropic behaviour for cubic (111) oriented samples is less pronounced than for other surface orientations. Note that we probed a few others cubic (111) oriented samples and the oscillations were usually even less pronounced than in case of Ni(111) at 670 nm. Nevertheless, the noise-to-signal ratio could be still quite improved, especially with measurements at a single wavelength where a stable laser light source can be used.

# Chapter 5

# QMOKE spectroscopy of (001) oriented thin films with cubic crystal structure

In this chapter technique of QMOKE spectroscopy is presented. The aim of QMOKE spectroscopy is to obtain spectral dependence of quadratic MO parameters $G_s$ and $2G_{44}$ in addition to linear MO parameter $K$, that is necessary for QMOKE spectra processing. Thin films of Fe and $Co_2MnSi$ are investigated and results are discussed. We would like to recall here requirements that are presumed for QMOKE spectroscopy technique. (i) The sample is of cubic structure, (ii) surface orientation is (001) (at least for now), (iii) the sample is in-plane magnetically saturated for any in-plane direction of external magnetic field.

## 5.1 Measurement principles and data processing

The separation process of the 8-directional method of (001) oriented cubic crystal structures, discussed in detail in previous Chapter 4, separate LMOKE $\Phi_{M_L}$ contribution and two QMOKE contributions $\Phi_{M_L M_T}$ and $\Phi_{M_T^2 - M_L^2}$. For QMOKE spectroscopy measurement we need to isolate QMOKE contribution where only $G_s$ or $2G_{44}$ contributes to the signal. This can be done through measurement of $\Phi_{M_L M_T}$ contribution under specific sample orientations, as is discussed in Sec. 4.1.4. Thus, in our QMOKE spectroscopy technique we measure three kind of spectra.

$$\text{QMOKE} \sim G_s = Q_s :$$

$$\Phi_{s/p}^{\mu=45^\circ} + \Phi_{s/p}^{\mu=225^\circ} - \Phi_{s/p}^{\mu=135^\circ} - \Phi_{s/p}^{\mu=315^\circ} = \pm 2A_{s/p}\left(G_s - \frac{K^2}{\varepsilon_d}\right), \quad \begin{array}{r} \alpha = 45^\circ, \\ \text{AoI} = 5^\circ, \end{array} \tag{5.1.1a}$$

$$\text{QMOKE} \sim 2G_{44} = Q_{44} :$$

$$\Phi_{s/p}^{\mu=45^\circ} + \Phi_{s/p}^{\mu=225^\circ} - \Phi_{s/p}^{\mu=135^\circ} - \Phi_{s/p}^{\mu=315^\circ} = \pm 2A_{s/p}\left(2G_{44} - \frac{K^2}{\varepsilon_d}\right), \quad \begin{array}{l} \alpha = 0^\circ, \\ \text{AoI} = 5^\circ, \end{array} \tag{5.1.1b}$$

$$\text{LMOKE} \sim K :$$

$$\Phi_{s/p}^{\mu=90^\circ} - \Phi_{s/p}^{\mu=270^\circ} = \pm 2B_{s/p}K, \quad \begin{array}{l} \alpha = \text{arb. angle}, \\ \text{AoI} = 45^\circ. \end{array} \tag{5.1.1c}$$

Here, we are introducing abbreviation $Q_s$ and $Q_{44}$ for QMOKE spectra originating from $G_s$ and $2G_{44}$, respectively. Note that the AoI conditions in the equations above were chosen with respect to the AoI dependence of the optical weighting factors $A_{s/p}$ and $B_{s/p}$. Thus, AoI will only affects the amplitude of the acquired spectra and is not essential for the spectra separation process. On the other hand, sample orientation $\alpha$ and the magnetization directions $\mu$ are vital to the measurement sequences.

Now, if we will bind Eqs. (5.1.1a)–(5.1.1c) with Tab. 3.1 (table summarizes the measurement techniques of our spectroscopy MOKE setup), we will understand how $\theta_s$, $\theta_p$, $\epsilon_s$ and $\epsilon_p$ for all those three spectra are measured. For measurement of $Q_s$ or $Q_{44}$ spectra we set $\Delta I_{2\omega} = I_{2\omega}^{\mu=45^\circ} + I_{2\omega}^{\mu=225^\circ} - I_{2\omega}^{\mu=135^\circ} - I_{2\omega}^{\mu=315^\circ}$ and for measurement of LMOKE spectra we set $\Delta I_{2\omega} = I_{2\omega}^{\mu=90^\circ} - I_{2\omega}^{\mu=270^\circ}$.

The right side of Eqs. (5.1.1a)–(5.1.1c) shows outcome of those measurement sequences when using approximative description of MOKE through Eq. (2.5.1). Note that this approximation is not used in the next step, that is to extract MO parameters $G_s$, $2G_{44}$ and $K$. However, this approximative outcome of measurement sequences suggests in which order to proceed. We have to extract spectral dependence of MO parameter $K$ from the LMOKE spectra first, to be able to compensate for the $K^2/\varepsilon_d$ contribution[1] when processing $Q_s$ and $Q_{44}$ spectra for extraction of spectral dependence of $G_s$ and $2G_{44}$, respectively.

The extraction process works as follow. Through Python based numerical model, discussed in Sec. 3.1.4, we reproduce measurement sequence of LMOKE [left side of Eq. (5.1.1c)]

---

[1] Recall that this quadratic-in-magnetization contribution to MOKE arises from optical interplay of two off-diagonal elements, both being linear in magnetization.

with $K$ set as a free parameter and $G_s = 2G_{44} = 0$. All other parameters required in the numerical code are known from investigations presented in Sec. 3.4 or directly known from the experiment. This model is then fitted into the LMOKE spectra obtained experimentally, which will yield us spectral dependence of $K$. Then, we reproduce measurement sequence of $Q_s$ [left side of Eq. (5.1.1a)] in numerical code with $K$ spectra included, where $G_s$ is set as a free parameter whereas $2G_{44} = 0$. The fit of this model to experimental spectra $Q_s$ provide us with spectral dependence of $G_s$. Finally, we reproduce measurement sequence of $Q_{44}$ [left side of Eq. (5.1.1b)] in numerical model with $2G_{44}$ used as a free parameter and where all other parameters are already known. This provide us with spectral dependence of $2G_{44}$. Note that we are always processing Kerr rotation and Kerr ellipticity of each measurement sequence at once and, thus, we are yielding both, real and imaginary part of the MO parameters.

Now, there is one final thing that remains to be tested. Because right side of Eqs. (5.1.1a)–(5.1.1c) provides selectivity to $G_s$, $2G_{44}$ and $K$ only within validity of Eq. (2.5.1), we should try to do the extraction process iteratively. Thus, we will repeat the extraction process described in the paragraph above, but this time we will use all the MO parameters from the first iteration and non of them will be set to zero. We tested this for several samples and there was no difference between spectra from first and second iteration. This again confirms that Eq. (2.5.1) is a fine approximation, as is shown in Chapter 4 as well.

Finally, we will presented spectra of extracted MO parameters in two possible forms. (i) The spectra will be presented in its pure shape, i.e. dependence of $K$, $G_s$ or $2G_{44}$ on photon energy $E$ [eV]. (ii) For better clarity, the spectra will be presented in the form multiplied by its photon energy, i.e. dependence of $K \cdot E$ [eV], $G_s \cdot E$ [eV] or $2G_{44} \cdot E$ [eV] on photon energy E [eV]. Note that this second expression is alternative expression of the conductivity spectra, being analogous[2] to well-known relation of conversion between complex permittivity and complex conductivity tensor [Eq. (2.2.3)].

## 5.2 Quadratic and linear MOKE spectroscopy of Fe(001) epitaxial films on MgO(001) substrates

We present here LinMOKE and QMOKE spectroscopic investigations of Fe(001) thickness dependent sample series [32]. The details on this samples with all necessary characterization can be found in Sec. 3.4.1.

---

[2] There is difference in the factor $\hbar/\varepsilon_0$.

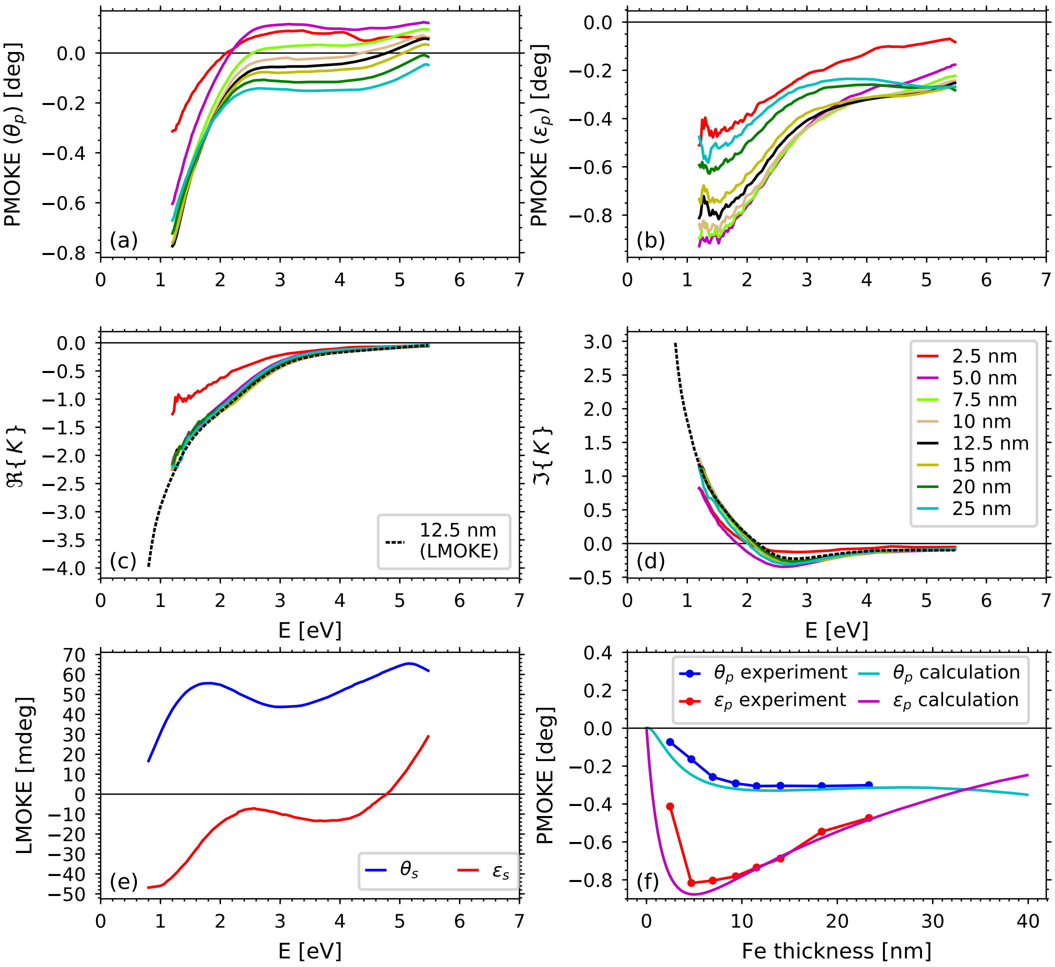

FIGURE 5.1: PMOKE spectra of (a) Kerr rotation $\theta_p$ and (b) Kerr ellipticity $\epsilon_p$ at AoI=5°, scaled to magnetization saturation. Spectra of (c) real and (d) imaginary part of MO parameter $K$ yielded from the saturated PMOKE spectra and, in case of the sample with a nominal thickness of 12.5 nm, from LMOKE spectra. (e) LMOKE spectra of the sample with a nominal thickness of 12.5 nm. (f) Thickness dependence of PMOKE at a photon energy of 1.85 eV at AoI=5°.

### 5.2.1 Linear MOKE spectroscopy

Although PMOKE spectroscopy was not discussed in the text of this work, we present PMOKE spectra for this sample series. Measurement process is technically similar to LMOKE, but we use out-of plane magnetic external field, thus PMOKE=$\frac{1}{2}(\Phi_{s/p}^{M_P} - \Phi_{s/p}^{-M_P})$. The PMOKE spectra for all the samples are presented in Figs. 5.1 (a), (b) and were measured on the setup at Charles University in Prague (not described within this work) by my colleague Lukáš Beran. In Figs. 5.1(c) and (d), we present the $K$ spectra obtained from the PMOKE spectroscopy and in case of the sample with a nominal thickness of 12.5 nm also from the LMOKE spectroscopy. The LMOKE spectra were obtained at our spectroscopic MOKE setup and are shown in Figs. 5.1(e).

Note that PMOKE spectra were measured with the magnetic field of 1.2 T which is not enough to magnetically saturate the samples out-of-plane[3]. We were able to compensate this through multiplicative factor 2.2, which was found through scaling of $K$ spectra from PMOKE to the $K$ spectra from LMOKE (where the sample was fully saturated) of sample with a nominal thickness of 12.5 nm. In Figs. 5.1(c) and (d) we may see that the scaled $K$ spectra extracted from PMOKE are in perfect match with $K$ spectra from LMOKE. We find this excellent agreement and linear dependence of $K$ on $\boldsymbol{M}$ as (i) confirmation of sample quality, i.e. linear tensor $\boldsymbol{K}$ is truly isotropic for this sample, (ii) another confirmation of the correctness of the determination of the optical constants of $\varepsilon_d$ and $K$ from experimental data. The $K$ spectra of the sample with a nominal thickness of 2.5 nm are deviating from others, which is not surprising as its $\varepsilon_d$ spectral dependence (Fig. 3.10) from ellipsometry is also quite off with respect to other samples in the series.

Finally, we present another test in Fig. 5.1(f), which is the dependence of the PMOKE (scaled to the magnetization saturation) on the Fe layer thickness at a photon energy of 1.85 eV. The predicted dependence is calculated by numerical model using all the parameters of the sample with a nominal thickness 12.5 nm (MO parameter $K$ is taken from the LMOKE measurement) and only Fe layer thickness is used as variable. The experimental data follows well the predicted dependence. There is small disagreement between some experimental and calculated values which can be explained by slightly different $\varepsilon_d$ and $K$ for each sample from a series, as well as probable small difference in the scaling factor for different Fe layer thicknesses.

### 5.2.2 Quadratic MOKE spectroscopy

We measured $Q_s$ and $Q_{44}$ spectra for all the samples at our spectroscopic MOKE setup in the range of 1.6 eV – 4.8 eV. When the spectral range of the setup was upgraded to 0.8 eV – 5.5 eV, the sample with a nominal thickness of 12.5 nm was remeasured. Kerr rotation and Kerr ellipticity of $Q_s$ is presented in Figs. 5.2(a) and (b), respectively. The rotation and ellipticity of $Q_{44}$ is presented in Figs. 5.2(c) and (d), respectively. All the measured spectra were digitally processed by Savitzky-Golay filter over the photon energy to improve signal-to-noise ratio. Again, the thinnest sample with a nominal thickness of 2.5 nm shows the largest deviation compared to the other samples of the thickness dependent series.

---

[3] Due to high demagnetizing field in the case of out-of-plane magnetization of thin layer.

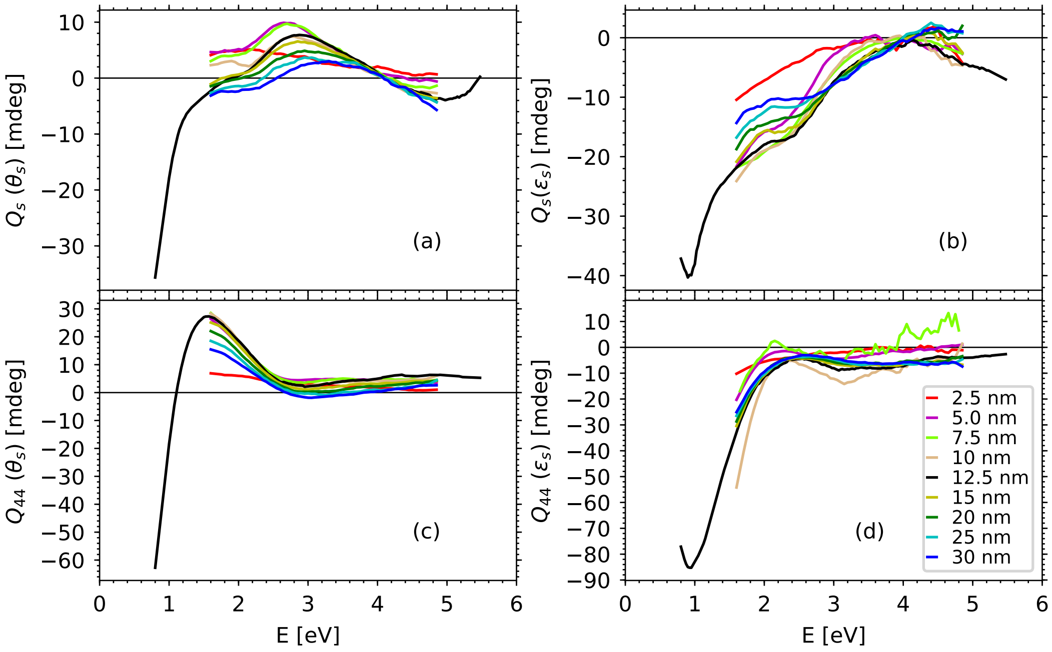

FIGURE 5.2: (a) Kerr rotation $\theta_s$ and (b) Kerr ellipticity $\epsilon_s$ of $Q_s$ spectra. (c) Kerr rotation $\theta_s$ and (d) Kerr ellipticity $\epsilon_s$ of $Q_{44}$ spectra.

The extracted spectra of the quadratic MO parameters $G_s$ and $2G_{44}$ are then shown in Figs. 5.3(a)–(d). The spectral dependence do not substantially change with the thickness, showing that there is no substantial contribution from the interface. Only exception, excluding the sample with nominal thickness 2.5 nm that is deviating also in all previous measurements, is the sample with a nominal thickness 10 nm, where its real part of MO parameter $2G_{44}$ is strongly deviating in spectral range below 2 eV. The source of this deviation is interplay of two facts: (i) Kerr ellipticity of $Q_{44}$ spectra is almost twice as large compared to samples with neighbouring nominal thickness. (ii) The absolute value of $K$ is above value of 1 (real and imaginary part alike) and thus the $K^2/\varepsilon_d$ is dominant contribution to $Q_{44}$ spectra below 2 eV. As a result the extraction of $2G_{44}$ is not very stable with small changes in $Q_{44}$ spectra.

The spectral dependence of parameter $\Delta G = G_s - 2G_{44}$ is shown in Figs. 5.3 (e) and (f). The parameter provides information about the anisotropy strength of the quadratic MO tensor $\boldsymbol{G}$. Thus from its spectral dependence we may estimate at which photon energies the oscillations in the 8-directional method measurement will be stronger and at which will be weaker.

Further, in Fig. 5.4 we present similar test as in the cae of LinMOKE spectroscopy. Value of Kerr rotation and Kerr ellipticity of $Q_s$ [Fig. 5.4(a)] and of $Q_{44}$ [Fig. 5.4(b)] at 1.85 eV is plotted against the thickness of the Fe layer in the sample. Full lines are predictions of numerical model, where all the parameters were taken from the sample

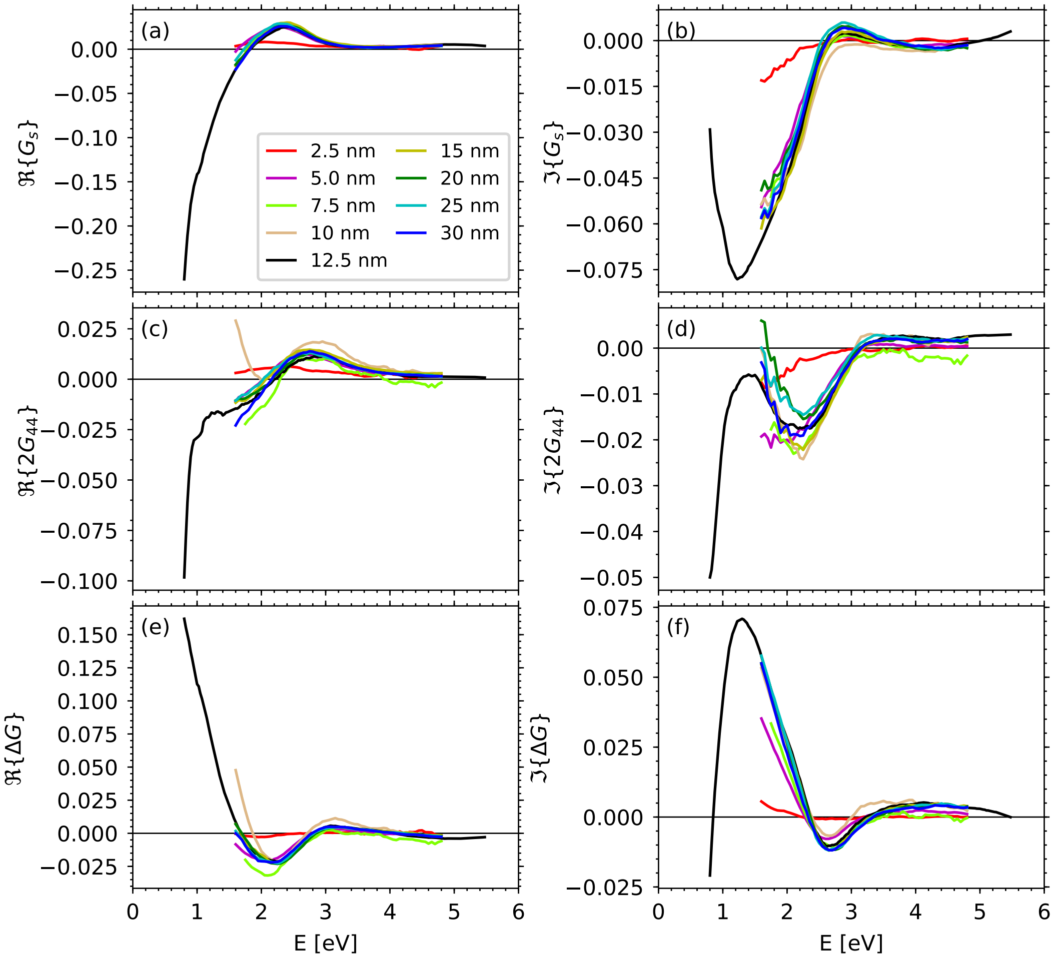

FIGURE 5.3: Spectra of (a) real and (b) imaginary part of the quadratic MO parameter $G_s$ and (c) real and (d) imaginary part of the quadratic MO parameter $2G_{44}$ for all the samples of the series.

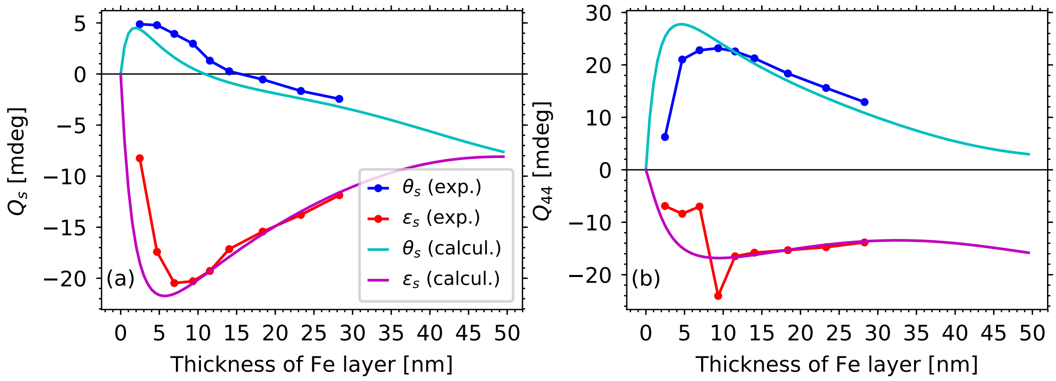

FIGURE 5.4: (a) QMOKE ~ $G_s$ thickness dependence and (b) QMOKE ~ $2G_{44}$ thickness dependence, both for a photon energy of 1.85 eV. Calculated lines were provided by Yeh's 4×4 matrix calculus. Both thickness dependencies are for AoI = 5°. (c) The spectral dependence of real and imaginary part of $\Delta G = G_s - 2G_{44}$ represents the anisotropy strength of the quadratic MO tensor across the whole spectral range. Every point is weighted by its photon energy for clarity.

with a nominal thickness 12.5 nm. Bullets connected by lines are then experimental values. The experimental results slightly differs from theoretical dependence for thinner Fe layers. This should be caused by slightly different $\varepsilon_d$, $K$, $G_s$ and $2G_{44}$ for the thinner Fe layers as shown in Figs. 3.10 , 5.1 and 5.3, respectively, as well as slightly different material properties of capping layers in each sample.

### 5.2.3 Comparison of the samples grown by molecular beam epitaxy and by magnetron sputtering

The Fe(001) samples prepared by MBE were subjected to the same MOKE spectral investigations in order to compare spectral dependence of $K$, $G_s$ and $2G_{44}$ of two Fe(001) layers prepared by different deposition techniques. We made all necessary characterization to provide sample's original parameters to the numerical calculus for the MO parameters extraction. In Figs. 5.5(a)–(c) we show comparison of all three MO parameters between sample prepared by MBE and sample with nominal thickness 12.5 nm prepared by magnetron sputtering. For better clarity in the UV part of the spectra, we present MO parameters in the form multiplied by its photon energy. The spectral dependence of both samples is very similar in all three cases, except for the real part of $2G_{44}$ spectra at lower photon energies ($< 2$ eV). Note that the same discrepancy has already been discussed for the case of the sample with nominal thickness 10 nm. Thus, the explanation here remain the same.

Otherwise, the differences of absolute values across the spectra is probably connected with slightly different crystalline qualities of the Fe layers. Those differences are not surprising, as the experimental values of MO parameters reported in literature differ in a similar manner, as will be shown below in the text.

### 5.2.4 Comparison of experimental spectra with ab-initio models and literature

Here we will show and discuss comparison of our experimental data with ab-initio calculated spectra and with the data available in the literature. The ab-initio calculations are work of my colleagues Jaroslav Hamrle and Ondřej Stejskal. All the representative experimental data within this section are from the sample with a nominal thickness of 12.5 nm. Further, all the spectra will be shown in form multiplied by its photon energy.

The electronic structure calculations of bcc Fe [100] were performed using the WIEN2k code [132]. For all the calculations we used the bulk value of lattice constant, being 2.8665 Å. The electronic structure was calculated twice, once with $\boldsymbol{M}$ parallel to Fe[100]

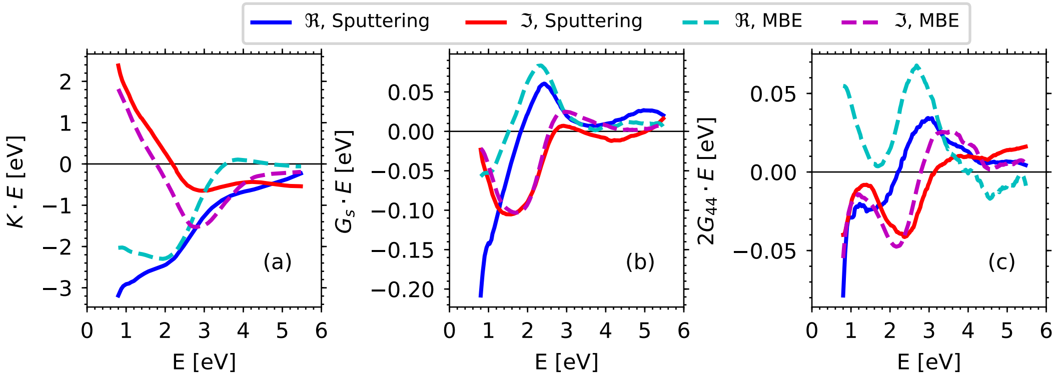

FIGURE 5.5: Comparison of the spectra of the MO parameters (a) $K$, (b) $G_s$ and (c) $2G_{44}$ of two samples, one prepared by magnetron sputtering and the other by MBE. For each of the samples, all the data used within numerical calculations were obtained from the original measurements of the particular sample.

direction and once with $\boldsymbol{M}$ parallel to Fe[110] direction. For both calculations we used $90^3 = 729000$ $k$-points in the full Brillouin zone. Further, the product of the smallest atomic sphere and the largest reciprocal space vector was set to $R_{\mathrm{MT}}K_{\mathrm{max}} = 8$ with the maximum value of the partial waves inside the spheres, $l_{\mathrm{max}} = 10$, where the largest reciprocal vector in the charge Fourier expansion was set to $G_{\mathrm{max}} = 12\,\mathrm{Ry}^{1/2}$. The exchange correlation potential LDA was used within all calculations and convergence criteria were $10^{-6}$ electrons for charge convergence and $10^{-6}\,\mathrm{Ry}{=}1.410^{-5}\,\mathrm{eV}$ for energy convergence. The spin-orbit coupling is included in the second variational method. We used broadening 0.001 Ry (0.014 eV) to determine Fermi level by temperature broadened eigenvalues.

The optical properties were determined within electric dipole approximation using the Kubo formula [60, 133]. The Drude term (intraband transitions) is omitted in the ab-initio calculated optical and MO properties. Full permittivity tensor $\boldsymbol{\varepsilon}$ for each of two directions of $\boldsymbol{M}$ is obtained by broadening the spectra and applying Kramers-Kronig relations. The spectra for $K$, $G_s$ and $2G_{44}$ are obtained directly from the permittivity tensors $\boldsymbol{\varepsilon}$ as[134]

$$K = \frac{1}{2}\left(\varepsilon_{yz}^{([100])} - \varepsilon_{zy}^{([100])}\right), \tag{5.2.1a}$$

$$G_s = \varepsilon_{xx}^{([100])} - \varepsilon_{yy}^{([100])}, \tag{5.2.1b}$$

$$2G_{44} = \varepsilon_{xy}^{([110])} + \varepsilon_{yx}^{([110])}, \tag{5.2.1c}$$

where the superscript denotes the $\boldsymbol{M}$ direction in the crystallographic structure.

Figures 5.6 (a) and (b) present experimental spectra of $\varepsilon_d - 1$[4] compared to our ab-initio

---

[4] Here -1 is to subtract contribution of vacuum, which is present only in the real part of $\varepsilon_d$.

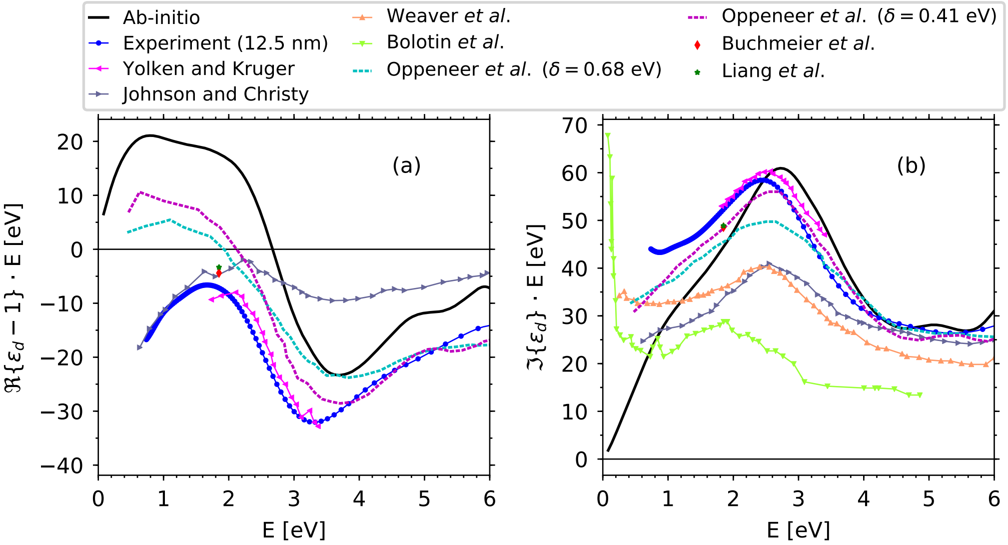

FIGURE 5.6: Experimental (markers) and ab-initio calculated interband spectra (lines) of (a) real and (b) imaginary part of $(\varepsilon_d - 1) \cdot E$ [eV]. Experimental spectra acquired in this work have marker every 10 experimental points (blue bullets). The remaining spectra are taken from literature [19, 35, 60, 135, 136].

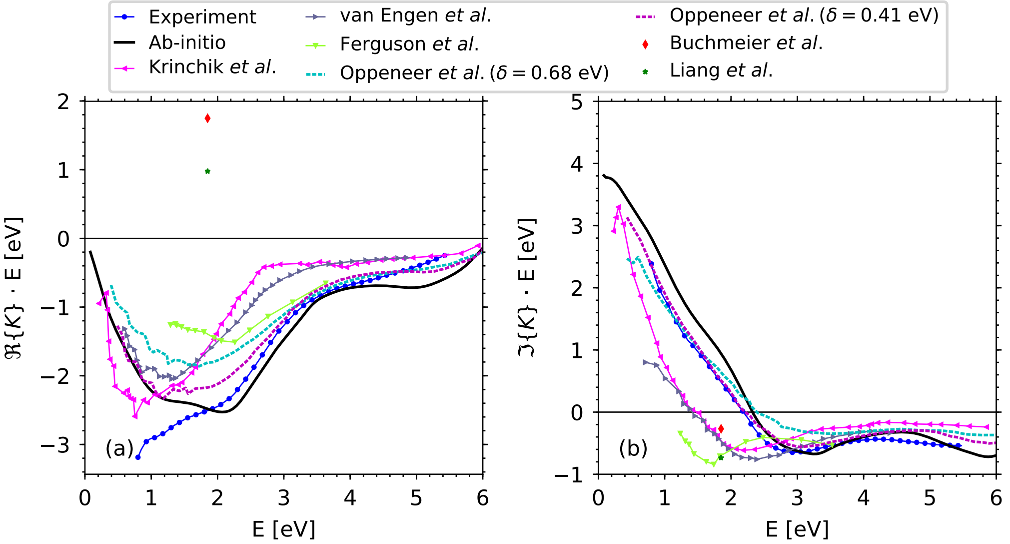

FIGURE 5.7: Experimental (markers) and ab-initio calculated interband spectra (lines) of the (a) real and (b) imaginary part of $K$·E [eV]. Experimental spectra acquired in this work have a marker every 5 experimental points (blue bullets). The remaining spectra are taken from the literature [19, 35, 54, 55, 60].

calculations, to data from the literature [60, 135, 136] and to ab-initio calculations by Oppeneer *et al.* [60]. Absorption part of the diagonal permittivity $\mathrm{Im}(\varepsilon_d)$ is dominated by the absorption peak at 2.4 eV, which originates from transitions of mostly-3d down electrons above and below the Fermi level. The ab-initio calculated peak position is very stable with small changes of the lattice constant, magnetization direction, or small distortion of the Fe lattice. Nevertheless, peak's position is determined by the selected exchange potential, where LDA provides the closest match to the experimental results and other potentials (GGA, LDA+U, GGA+U) display larger deviation from the experimental peak position. Although LDA still overestimates the width of the occupied 3d bands, the width of the occupied 3d bands can be corrected using dynamical mean-field theory (DMFT) [137]. Therefore we choose the LDA exchange potential to calculate the electronic structure of bcc Fe. Further, as the peak amplitude depends on the smearing parameter [60], we tuned smearing to $\delta = 0.6\,\mathrm{eV}$ in the case of $\varepsilon_d$ to adjust the peak height.

In Figs. 5.7 (a) and (b) we show a similar comparison for linear MO parameter $K$. Excellent agreement between experiment and ab-initio is demonstrated. Note that the absorption part corresponds here to $\mathrm{Re}(K)$, with two peaks at 1.1 and 2.0 eV. The amplitude of the latter peak is ca. -2.5 eV, i.e. about 4% of the maximal value of $\mathrm{Im}(\varepsilon_d \cdot E)$ (which is ca. 60 eV). If we compare spectra reported in the literature with our experimental and theoretical spectra and among themselves their absolute values differ by dozens of percent at some photon energies in both figures (Figs. 5.6 and 5.7). Nevertheless, the characteristics features as are the peaks and courses of spectra are very similar for all the presented data, both experimental and theoretical (note that disagreement with the reported values at single wavelength [19, 35] is probably due to sign inconsistency). Furthermore, the anomalous Hall conductivity actually corresponds to the d.c. limit of the imaginary part of the $K$ spectra. Its value extracted from the ab-initio calculation is 512 $(\Omega\mathrm{cm})^{-1}$ (760 $(\Omega\mathrm{cm})^{-1}$ without broadening) which agree very well with the value provided in Ref. [138]. Finally, note that sign of ab-initio calculated $K$-spectra have to be reversed to agree with the sign of the experimental $K$-spectra[5].

Experimental spectra of the real and imaginary part of $G_s \cdot E$ are shown and compared with the ab-initio calculations in Figs. 5.8 (a) and (b) respectively. The fundamental (imaginary) part of $G_s$ has a well pronounced peak at 1.6 eV with the amplitude $\mathrm{Im}(G_s \cdot E) = -0.11\,\mathrm{eV}$ in the experimental spectra. The main features of $G_s$ spectra are well-described ab-initio, however, the ab-initio calculated peak at 1.6 eV has about half that amplitude. Real and imaginary part of the experimental and ab-initio spectra of $2G_{44}$ is shown in Figs. 5.8 (c) and (d), respectively. The ab-initio calculations describe very well

---

[5] We have reported this issue to Wien2k developers and the sign of off-diagonal components have been corrected in the Wien2k version 19.1.

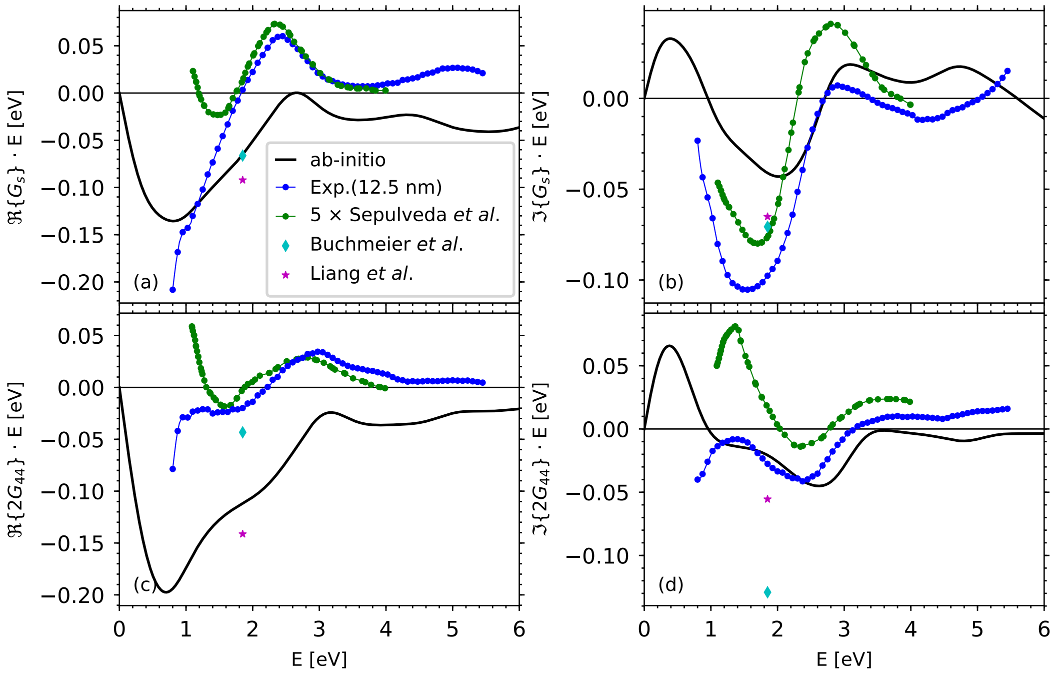

FIGURE 5.8: The experimental $G_s$ spectra (a, b) and the experimental $2G_{44}$ spectra (c,d) compared with the ab-initio calculations. $G_s$ spectra are calculated for $\vec{M} \parallel [001]$ and $2G_{44}$ spectra calculated for $\vec{M} \parallel [110]$ both with smearing of FWHM=1.2 eV and with $90^3 = 729000$ $k$-points in the full Brillouin zone. Further, we show a comparison with data taken from the literature [19, 35, 92]. The spectra taken from Sepúlveda *et al.*[92] have been multiplied by a factor of 5 to be comparable with our experimental spectra.

fundamental (imaginary) part of $2G_{44}$ spectra, where both, shape and amplitude, are in a good match. The real part of $G_s$ and $2G_{44}$ spectra have a larger disagreement between experiment and ab-initio description, particularly for small photon energies. This could stem from the missing Drude term, which is omitted in the ab-initio calculations, and which mainly contributes to the real part of the permittivity at small photon energies. Finally, note that in case of $2G_{44}$ the convergence (for example on density of the $k$-mesh) of ab-initio calculations is much better compared to $G_s$, as $G_s$ is calculated as a small change of the diagonal permittivities [Eq. (5.2.1b)] whereas $2G_{44}$ is calculated from off-diagonal permittivity [Eq. (5.2.1c))].

Furthermore, we present comparison of the spectral dependence of $G_s$ and $2G_{44}$ from Sepúlveda *et al.* [92]. The original spectra of Sepúlveda *et al.* were not very much pronounced and had to be multiplied by a factor of 5 to be comparable to our experimental and ab-initio spectra as is shown in Figs. 5.8(a)–(d). Then, the agreement is perfect for the real part of both $G_s$ and $2G_{44}$ in the spectral range 1.5 – 4.0 eV, whereas disagreement of spectral dependence under 1.5 eV can be explained by different sample quality; as the same behaviour was already experienced for $2G_{44}$ in the case of the sample with a nominal thickness of 10 nm and also in the case of the sample prepared by the MBE.

The imaginary part of $G_s$ and $2G_{44}$ spectra still agrees very well when our data are compared to the scaled data of Sepúlveda *et al.* [92], except for some offset and also different amplitude of peaks, especially in case of the $\mathrm{Im}(2G_{44})$ peak at 1.5 eV. We do not know wherefrom the scaling factor 5 between our data and data of Sepúlveda *et al.* is stemming, but in the case of Sepúlveda *et al.* the data were obtained from experimental measurement of variation of reflectivity with quadratic dependence on magnetization. The bad crystallinity of the samples should not be a problem here as in case of polycrystalline material $\Delta G = 0$, i.e. $G_s = 2G_{44}$, which is not the case here. However, note that our optical spectra of $\varepsilon_d$, $K$, $2G_{44}$ and $G_s$ well describe their experimental reflectivity spectra using our numerical model.

### 5.2.5 Consequences of the MOKE sign disagreement between the experiment and numerical model

The correct sign of the measured MOKE spectra is given by the conventions used. Nevertheless, the correct sign of MO parameters $K$, $G_s$ and $2G_{44}$ is no more subject of conventions, as they describe material properties[6]. To obtain the correct spectra of MO parameters $K$, $G_s$ and $2G_{44}$ from the measured experimental MOKE spectra, the same conventions must be adopted within the numerical model and the experiment. Here, one would intuitively expect only the reversed sign of yielded MO parameters when the sign conventions of the experiment and the numerical model do not comply. However, this is true only for linear MO parameter $K$, whereas completely incorrect values are yielded in this case for the quadratic MO parameters $G_s$ and $2G_{44}$.

In the experiment there is numerous points where we can go wrong and thus measure the MOKE spectra of the incorrect sign according to our conventions. For example, wrong direction of in-plane $\boldsymbol{M}$ rotation (i.e. $\mu \to -\mu$), wrong direction of positive external field and thus opposite direction of $\boldsymbol{M}$ (i.e. $\mu \to \mu + 180^\circ$), error in the calibration process of the setup itself (note that the positive direction of the optical element rotation and the positive direction of the Kerr rotation have opposite conventions) or some quirk in the processing algorithm of the measured data itself (usually we measure change of intensity, which has to be converted to Kerr angles). Furthermore, we can also make a sign error in the code of the numerical model, but this was already discussed and checked for in the Sec. 3.1.4.

Above mentioned sign mistakes in the experiment will not always lead to the same error. The wrong direction of positive external magnetic field will affect the sign of LMOKE spectra but not the sign of QMOKE spectra, whereas wrong direction of $\boldsymbol{M}$

---

[6] Sign between real and imaginary part is given by time convention, but this sign should not be attributed to the spectra itself.

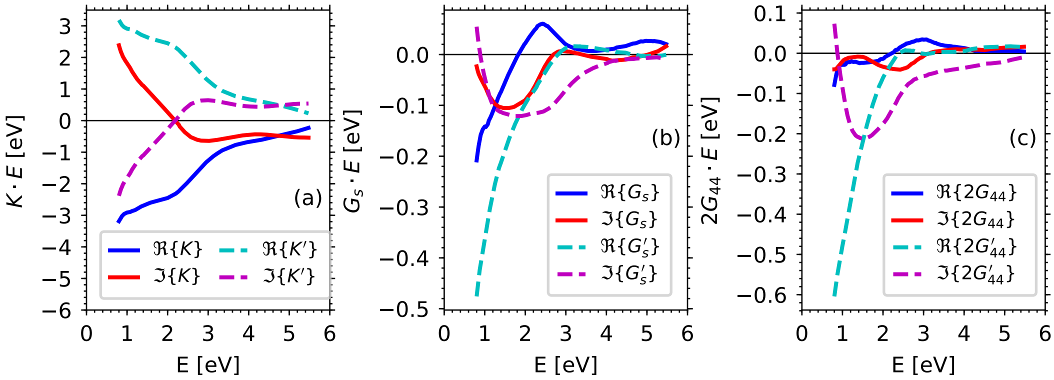

FIGURE 5.9: Comparison of the spectra of MO parameters (a) $K$, (b) $G_s$ and (c) $2G_{44}$ to the MO parameters yielded from the experimental spectra with the wrong (reversed) sign of $\mu$ ($K'$, $G'_s$ and $2G'_{44}$).

rotation will produce a wrong sign of both spectra, LMOKE and QMOKE alike - see the Eqs.(5.1.1a)–(5.1.1c).

Now we will discuss the latter case, when the direction of $\boldsymbol{M}$ rotation has the opposite direction, $\mu' \to -\mu$ leading to a wrong sign of experimental spectra measured according to Eqs.(5.1.1a)–(5.1.1c). The linear MO parameter $K'$, yielded from the LMOKE spectra with a reversed sign, will only have the opposite sign compared to the true MO parameter $K$. But the quadratic MO parameters $G'_s$ and $2G'_{44}$, yielded from the $Q_s$ and $Q_{44}$ spectra with the opposite sign, will be completely different from the true MO parameters $G_s$ and $2G_{44}$, respectively. This is caused by the contribution of $K^2/\varepsilon_d$, which is invariant to the sign of $K$ itself, to the $Q_s$ and $Q_{44}$ spectra. Thus, the MO parameters yielded from sign-reversed experimental spectra are bound with the true MO parameters by following equations.

$$K' = -K \tag{5.2.2}$$

$$G'_s = -G_s + 2\frac{K^2}{\varepsilon_d} \tag{5.2.3}$$

$$2G'_{44} = -2G_{44} + 2\frac{K^2}{\varepsilon_d} \tag{5.2.4}$$

In Fig. 5.9 we show the wrong MO parameters $K'$, $G'_s$ and $2G'_{44}$ compared to the true MO parameters $K$, $G_s$ and $2G_{44}$, respectively.

We recall that neither the shape nor the sign of the true MO parameters is given by the convention used. Any sign conventions can be adopted, but the crucial point is that the conventions used in real experiments and in numerical calculus are the same. Obviously, this issue applies to any error in the experimental setup or the numerical code that would unintentionally reverse the sign of the measured or calculated MOKE spectra, respectively.

## 5.3 Quadratic and linear MOKE spectroscopy on partially ordered $Co_2MnSi$ Heusler compounds

Effect of crystallographic ordering on QMOKE have been already lately studied with $Co_2MnSi$ Heusler compound [29], but only from point of view of 8-directional method at single wavelength (1.95 eV). Here we present LMOKE and QMOKE spectroscopy and its dependence on the crystallographic ordering. Experimental results will be accompanied by theoretical ab-initio calculations that are again work of my colleagues Jaroslav Hamrle and Ondřej Stejskal.

### 5.3.1 Linear MOKE spectroscopy

The LMOKE spectra were measured according to Eq. (5.1.1c) with AoI of 45° and $p$-polarized incident wave in spectral range of 0.8 eV – 5.5 eV. LMOKE rotation and ellipticity is presented in Figs. 5.10(a) and (b), respectively. The extracted spectra of linear MO parameter $K$ are then presented in Figs. 5.10(a) and (b). Here we can see a new peak forming with the presence of $L2_1$ ordering in the spectral region of 1.5 eV and 1.3 eV in real and imaginary part, respectively. Note that this peak was not easily observable in the LMOKE spectra itself. Otherwise there is no substantial change of position of peaks with annealing temperature and thus with increased $L2_1$ ordering. On the other hand the amplitude of peaks is more pronounced with higher annealing temperature.

### 5.3.2 Quadratic MOKE spectroscopy

The QMOKE spectra were further measured on the samples according to Eqs. (5.1.1a) and (5.1.1b) with AoI of 5° and $p$-polarized incident light. In Figs. 5.11(a) and (b) we show Kerr rotation and Kerr ellipticity of $Q_s$ spectra, respectively, and in Figs. 5.11(c) and (d) we show Kerr rotation and Kerr ellipticity of $Q_{44}$ spectra, respectively. The sharp oscillations presented in both quadratic spectra are quite unique for metallic material.

In Fig. 5.12 we then show extracted quadratic MO parameters of $Co_2MnSi$ layer. The real and imaginary spectra of MO parameter $G_s$ are presented in Figs. 5.12(a) and (b), respectively. The real and imaginary spectra of $2G_{44}$ are presented in Figs. 5.12(c) and

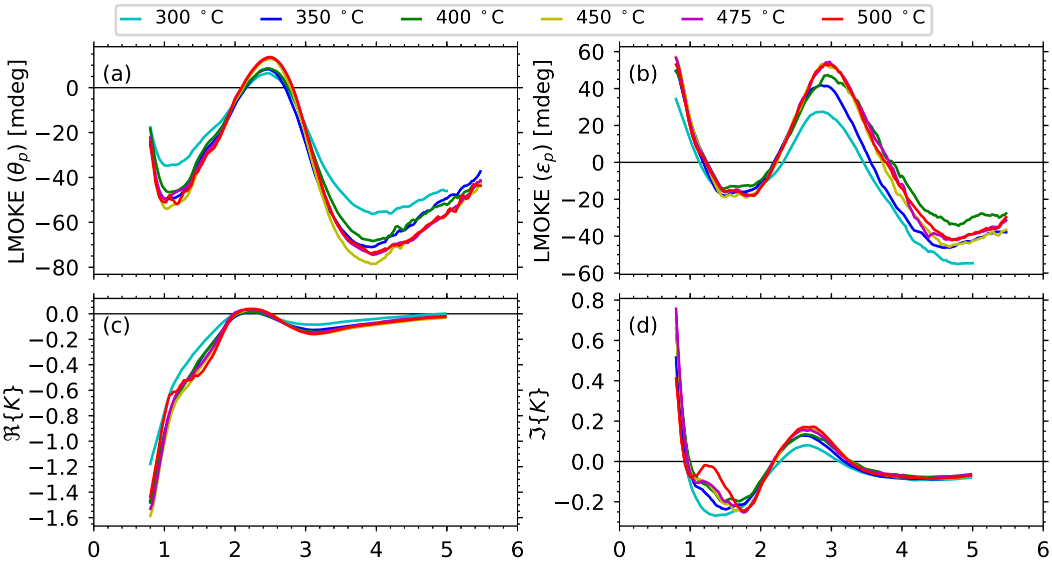

FIGURE 5.10: LMOKE (a) rotation (b) ellipticity measured with $p$-polarized incident light under angle of incidence 45°. Spectra of real (c) and imaginary (d) linear MO parameter $K$.

(d), respectively. Furthermore, we present spectra of $\Delta G = G_s - 2G_{44}$, denoting the anisotropy strength of quadratic MO tensor $\boldsymbol{G}$ of Co$_2$MnSi layer. Real and imaginary part of $\Delta G$ spectra is then shown in Figs. 5.12(e) and (f), respectively.

The degree of $L2_1$ ordering obviously affect amplitude of peaks, same as was the case in the linear MO parameter $K$. This effect seems to be most pronounced with the spectra of $G_s$, where also a new peak arise with $L2_1$ ordering in the spectral range 2–3 eV and around 4 eV for both, real and imaginary part. Again, the position of the peaks is the same for all the samples and only change of the amplitude occurs with the different amount of $L2_1$ ordering in the sample. This is consistent with all the MO parameters $K$, $G_s$, $2G_{44}$. Because it does not appear that the change of amplitude gets stronger at the lower energies, we can assume that transition from $B2$ to $L2_1$ affects mainly the interband contribution to the MO parameters, while intraband contribution (Drude) is not affected by this change of ordering.

### 5.3.3 Comparison to ab-initio calculations

The electronic structure of Co$_2$MnSi was calculated by the Linearized Augmented Plane Wave (LAPW) method using the DFT-based WIEN2k [139] code with lattice parameter of 5.656 Å. We chose LDA as the exchange-correlation potential in this case as it performs even better than LDA+U for optical and MO calculations. $L2_1$ crystal structure represented by space group Fm$\bar{3}$m was assumed in all calculations. The electronic

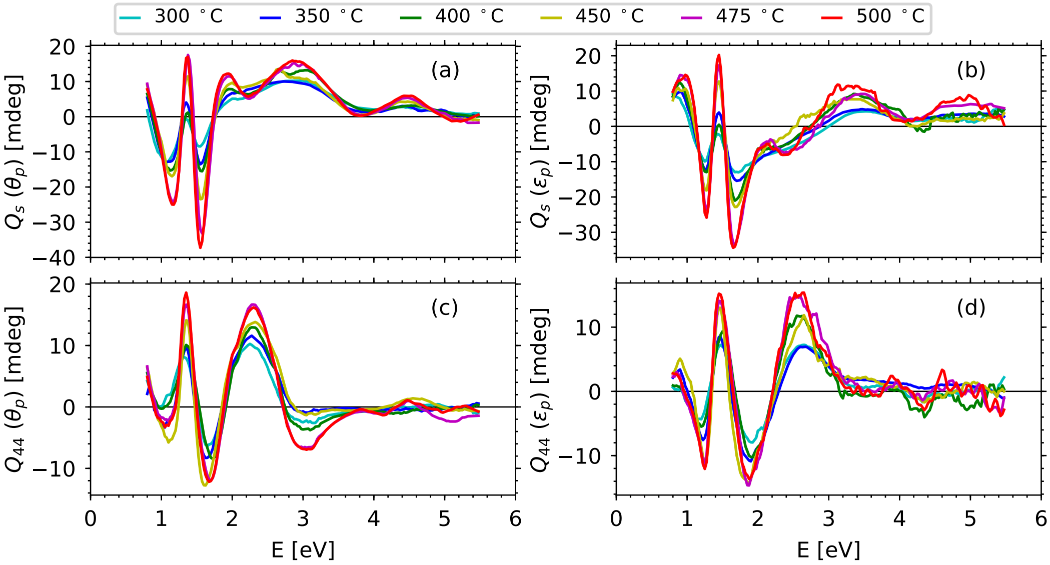

FIGURE 5.11: Spectra of $Q_s$ (a) rotation (b) ellipticity and spectra of $Q_{44}$ (e) rotation and (f) ellipticity. All spectra are measured with $p$-polarized incident light and with angle of incidence 5°.

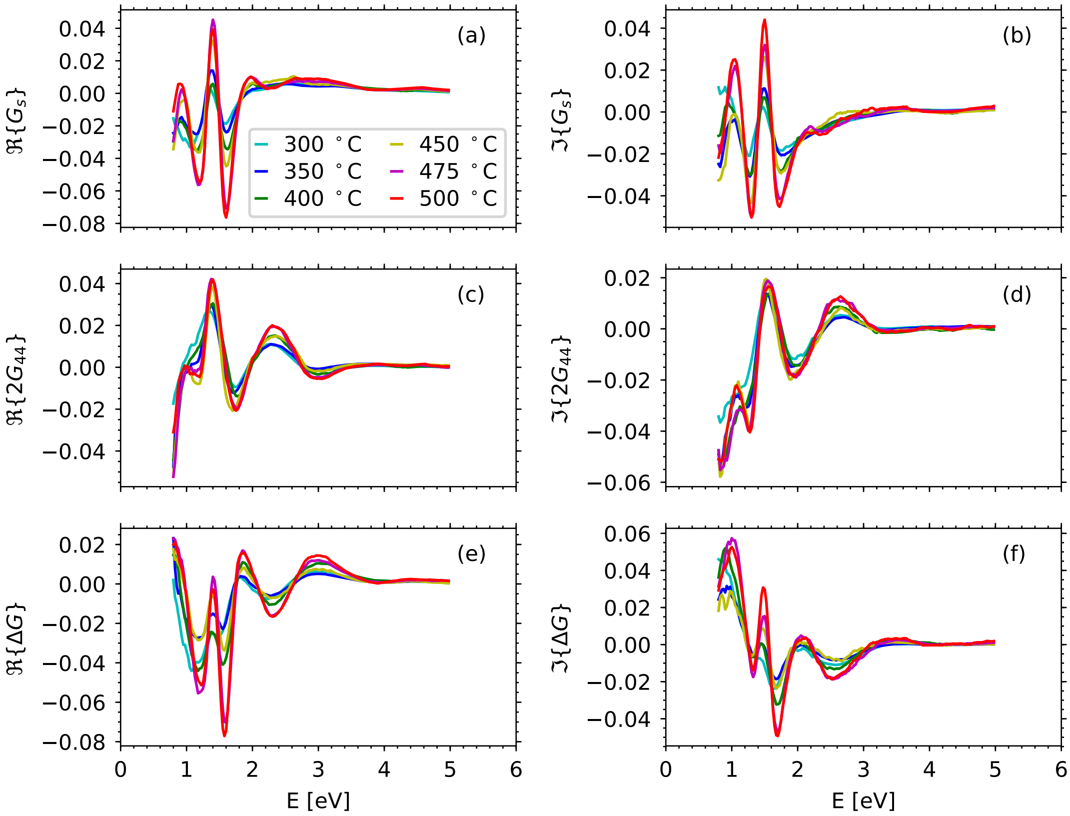

FIGURE 5.12: Spectral dependence of extracted quadratic MO parameters $G_s$ [(a) real and (b) imaginary] and $2G_{44}$ [(c) real and (d) imaginary]. In (e) and (f) we present real and imaginary part of parameter $\Delta G = G_s - 2G_{44}$, respectively. The parameter $\Delta G$ denotes anisotropy strength of quadratic MO tensor $\boldsymbol{G}$.

structure was calculated with a mesh of 27000 $k$-points in the full Brillouin zone and with the product of the smallest atomic sphere radius and the largest reciprocal space vector set to $R_{\mathrm{MT}}K_{\mathrm{max}} = 7$. The maximum value of partial waves inside the spheres was $l_{\mathrm{max}} = 10$ and the largest reciprocal vector in the charge Fourier expansion was set to $G_{\mathrm{max}} = 12\,\mathrm{Ry}^{\frac{1}{2}}$. These are default values for standard calculations and determine the LAPW basis in which the solution is searched for.

The optical and MO spectra were calculated using the Kubo formula [58, 133] on a finer mesh of 216000 $k$-points in the full Brillouin zone. By Lorentz broadening the spectra with 0.5 eV and applying the Kramers-Kronig relations, the full permittivity tensor is obtained. Same as in the case of Fe, we obtain only interband contributions to the permittivity tensor and the Drude term is omitted.

The calculations were performed for two magnetization directions, namely [100] and [111] relative to the crystallographic axes. Similar as in the case of bcc Fe, the MO parameters are obtained directly from the permittivity tensor as [134]

$$K = \frac{1}{2}\left(\varepsilon_{yz}^{([100])} - \varepsilon_{zy}^{([100])}\right), \tag{5.3.1a}$$

$$G_s = \varepsilon_{xx}^{([100])} - \varepsilon_{yy}^{([100])}, \tag{5.3.1b}$$

$$2G_{44} = \frac{3}{2}\left(\varepsilon_{xy}^{([111])} + \varepsilon_{yx}^{([111])}\right), \tag{5.3.1c}$$

where the superscript denotes the magnetization direction relative to the crystal axes.

The theoretical spectra of $\varepsilon_d$ are shown in Figs. 5.13 (a) and (b). The major optical transitions appear for higher energies, which is apparent from Fig. 5.13(b). This discrepancy can be arguably attributed to the employed exchange-correlation potential as the major approximation present in the Density functional theory, which does not accurately describe actual exchange-correlation energy of the true many-electron system [140, 141].

In Figs. 5.13(c) and (d) comparison of the experimental and theoretical spectra of linear MO parameter $K$ are presented. The experimental spectra are well described ab-initio, but the peak at 1.3 eV that appear with $L2_1$ ordering is not very much pronounced. In Figs. 5.13(e)–(h) we show the complex spectra of $G_s$ and $2G_{44}$. The amplitude and period of oscillations in those spectra are well described ab-initio, which we find to be a success. In the case of $2G_{44}$ spectra the theory is in excellent match with experiment. On the other hand, for spectra of $G_s$, which are calculated as small variation of diagonal permittivity [Eq. (5.3.1b)], the ab-initio optical transitions appear for higher energies same as in the case of $\varepsilon_d$. Note that theoretical spectra of $K$ and $2G_{44}$ are calculated

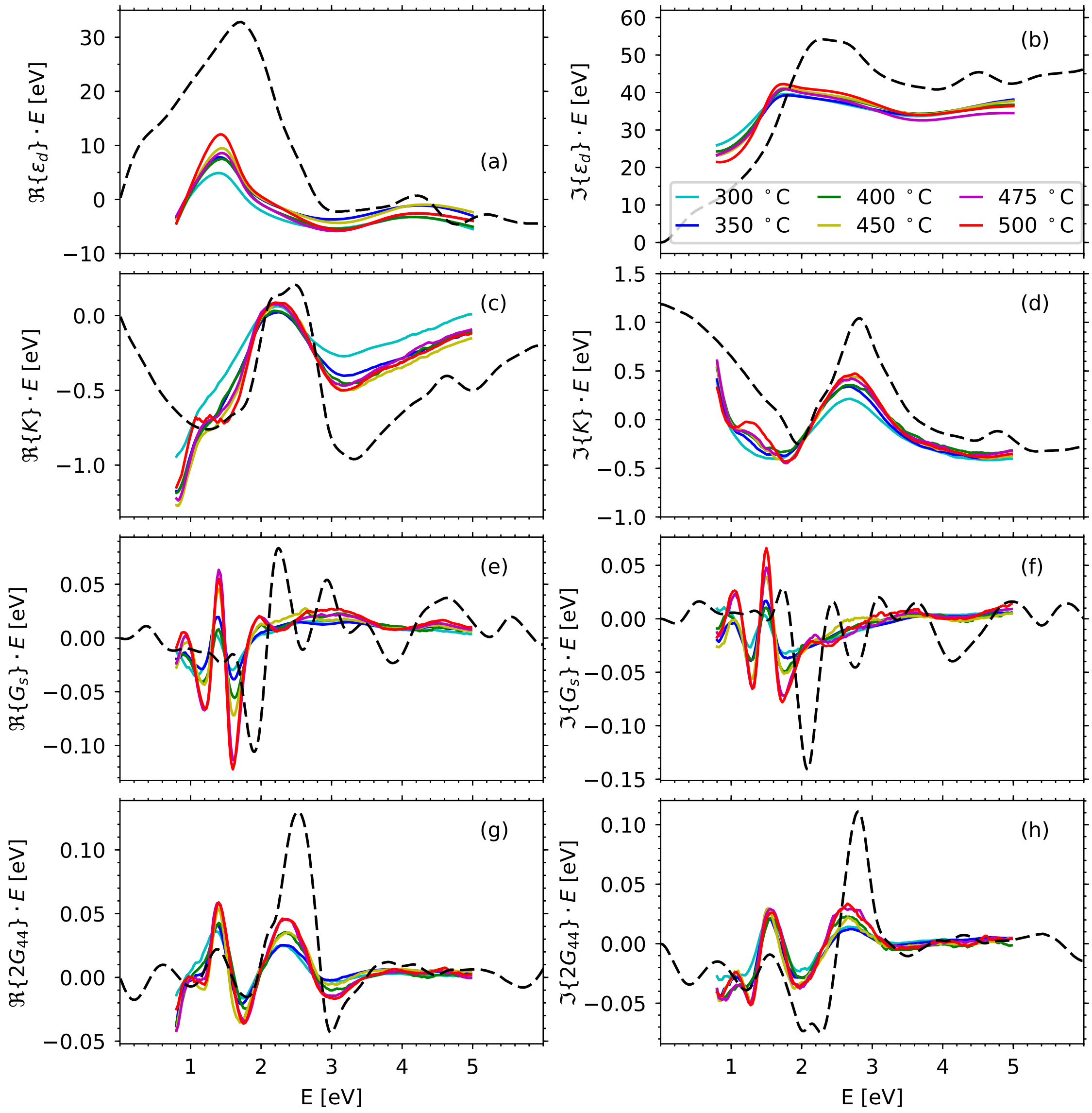

FIGURE 5.13: Spectral dependence of the ($i$) permittivity in the 0th order in $\boldsymbol{M}$ $\varepsilon_d$((a) real, (b) imaginary), ($ii$) linear MO parameter $K$ ((c) real, (d) imaginary), ($iii$) quadratic MO parameter $G_s$ ((e)real, (f) imaginary) and ($iv$) quadratic MO parameter $2G_{44}$ ((g) real, (h) imaginary). Coloured, full lines are the experiment. The black, dashed lines are the theoretical ab-initio calculations.

from off-diagonal elements of the permittivity tensor [Eqs. (5.3.1a) and (5.3.1c)], and the position of all peaks follow very well the experiment here.

## 5.4 Conclusion

In this chapter, we provided a description of our approach to QMOKE spectroscopy, which allows us to obtain quadratic MO parameters in the extended visible spectral range. The spectral dependence of $K$, $G_s$ and $2G_{44}$ is experimentally determined in the spectral range of 0.8 – 5.5 eV for two materials, the prototypical ferromagnetic Fe grown on MgO substrates and $Co_2MnSi$ Heusler compounds.

In the case of the thickness dependent sample series of Fe thin films the dependence of the obtained spectra on Fe layer thickness is small, indicating small contribution of the interface. The spectra of $G_s$ and $2G_{44}$ were successfully described ab-initio using the electric dipole approximation with the electronic structure of bcc Fe calculated by DFT with LDA exchange-correlation potential and spin-orbit coupling. Further, $G_s$ and $2G_{44}$ were compared to the single report that we found in the literature, where multiplicative factor of 5 had to be introduced to the spectra from literature to obtain a good match with our experimental and theoretical spectra.

In the case of $Co_2MnSi$ Heusler compounds we investigated the effect of transition from $B2$ to $L2_1$ ordering on the spectra of linear and quadratic MO parameters. Higher degree of $L2_1$ ordering promotes higher amplitude at MO resonant frequencies. As this change is not further pronounced at lower photon energies, we assume that the transition from $B2$ to $L2_1$ affects mainly interband contribution to the MOKE signal. All the experimental spectra were described well ab-initio, although in the case of $\varepsilon_d$ and $G_s$ the optical transitions appear for higher photon energies, which was attributed to the exchange-correlation potential.

Further, in the Appendix C we provide preliminary results of LinMOKE and QMOKE spectroscopy of epitaxial magnetite $Fe_3O_4$ thin films. The spectral dependence of $K$, $G_s$ and $2G_{44}$ is presented for series of four samples, where the partial pressure of oxygen was varied for deposition of each of the magnetite films.

# Final conclusion, remarks and perspectives of the presented work

In this work, we have introduced the topic of QMOKE for cubic crystal structures. After comprehensive introduction the theory based on electromagnetic optics has been discussed and the phenomenological origin of MOKE has been explained as perturbation of the permittivity tensor by magnetization. This perturbation of permittivity is described up to the second order in magnetization by the linear MO parameter $K$ and two quadratic MO parameters $G_s$ and $2G_{44}$. With the use of Yeh's 4×4 matrix calculus, assuming a coherent propagation of monochromatic EM waves in a multilayer structure, we are able to precisely describe the Kerr reflection from the sample by those MO parameters. For this purpose we developed a code in Python language based on the Yeh's 4×4 matrix calculus that was subsequently used for various simulations of the 8-directional method and for spectroscopy data processing. In order to make experimental investigations, multiple sets of samples were prepared and characterized through methods such as XRD, XRR and ellipsometry. The magnetic characterization of those samples was done by MOKE magnetic loops measurements.

The first goal of this work was the extension of the 8-directional method of (001) oriented cubic crystal structures to (011) and (111) oriented cubic crystal structures. The equations for each surface orientation ware derived using approximative analytical relation that binds the Kerr angles to the permittivity tensor elements of the ferromagnetic layer. The derived equations were compared to the simulations provided by numerical code. We found only very negligible discrepancies, which do not play any important role with current experimental setups and measurement principles. Nevertheless, if noise-to-signal ratio will be dramatically improved with our future experimental equipment, those discrepancies should be revisited and probed again carefully.

The 8-directional method of the (011) oriented cubic crystal structures has been experimentally investigated for Fe(011) oriented thin films grown on MgO(111) substrates. Here, the experimental results reveal some interesting behaviour of one-fold and three-fold symmetry that was not predicted by the derived equations nor numerical model simulations. Yet, this behaviour was observed for a single sample only and can be reasonably explained by out-of-plane component of the magnetization produced by magnetic anisotropy of the sample. For the second Fe(011) sample we observed some two-fold symmetry of the LMOKE $\Phi_{M_L}$ effect, which is predicted by the numerical model and has been lately discussed in the literature. Yet, we are not convinced that this behaviour is truly of MO origin, as from our numerical simulations, in which MO parameters of Fe where used, this two-fold symmetry should be substantially lower in the amplitude. We further fabricated Co(011) thin film samples grown on MgO(011) substrates, but unfortunately we were not able to saturate them in any of our MOKE setups. Because the experimental results of the 8-directional method of (011) oriented samples were only partly conclusive, our plan is to continue with systematic studies, where further samples will be prepared and we will upgrade the MOKE setups with magnets providing stronger field.

In order to experimentally probe the 8-directional method of (111) oriented cubic structures, we fabricated Ni(111) thin film sample grown on MgO(111) substrate. The experimental results were qualitatively well in line with the derived equations and numerical simulations. The observed three-fold oscillation of contributions $\Phi_{M_L}$ and $\Phi_{M_T}$ were predicted by theory as optically induced contribution of 3rd order in $\boldsymbol{M}$. Yet, from quantitative point of view it is a question if the description by MO parameters $K$, $G_s$ and $2G_{44}$ would be sufficient, or if we should introduce a cubic MO tensor of 3rd order in $\boldsymbol{M}$ as additional contribution to the permittivity tensor. Through the measurement of Kerr rotation as well as Kerr ellipticity of one of the contributions separated by 8-directional method of (111) oriented cubic structures, we can extract the value of MO parameters $K$, $G_s$ and $2G_{44}$ and then use those MO parameters to simulate the residual contributions and analyze if the amplitude and offset fit well to the experimental values. If the discrepancy here would be only a few percent, it will not be so crucial to introduce a cubic MO tensor as contribution of 3rd order in $\boldsymbol{M}$ to the permittivity tensor.

The second goal of this work was the development of QMOKE spectroscopy for (001) oriented cubic crystal structures. The separation process is stemming from the classical 8-directional method, but we use just a combination of four magnetic field directions and a sample rotation by 45° [31]. This way we are able to separate two QMOKE spectra which are stemming from quadratic MO parameters $G_s$ and $2G_{44}$, entitled $Q_s$ and $Q_{44}$, respectively. To extract those quadratic MO parameters from the experimental QMOKE spectra we employ Python based numerical calculus, in which the measurement process is fully reproduced. Here we showed that consensus of sign between experiment and numerical calculus is of crucial importance in case of quadratic MO parameters extraction due to the contribution of $K^2/\varepsilon_d$ to the $Q_s$ and $Q_{44}$ spectra. All the experimental data were collected on our own in-house built MOKE spectroscopy setup.

The QMOKE spectroscopy has been applied to bcc Fe(001) thin film samples of various thickness grown on MgO(001) substrates [32]. Spectra of the MO parameters $K$, $G_s$ and $2G_{44}$ were successfully extracted from the experiment in the spectral range $0.8 - 5.5\,\mathrm{eV}$. The dependence of $Q_s$ and $Q_{44}$ on Fe layer thickness follow well numerical prediction, which indicates small contribution of the interface to the value of MO parameters. We also compared $K$, $G_s$ and $2G_{44}$ spectra of Fe(001) samples prepared by magnetron sputtering to the spectra of Fe(001) samples prepared by MBE, where we showed that the course of the spectra holds well between both samples, but the absolute value can differ by a bit. Finally, the experimental spectra of MO parameters were compared to ab-initio calculations [100] and available data in the literature.

Furthermore, we investigated the QMOKE spectra of a thin films $Co_2MnSi$ Heusler compounds, for which different temperatures of post annealing promote different degree of $L2_1$ ordering. The extraction of the spectral dependencies of the MO parameters $K$, $G_s$ and $2G_{44}$ in the spectral range of $0.8 - 5.5\,\mathrm{eV}$ was already routine work in this case, as the method have been well established with the Fe(001) sample set. We found out that a higher degree of $L2_1$ ordering considerably promotes the amplitude in the peaks of the spectra. As this effect is not more pronounced at lower photon energies, we assume that the Drude contribution is not affected by this change of ordering. The spectra of $G_s$ and $2G_{44}$ posses unique rapid oscillations that are not very typical for metallic material and thus it is already a success that amplitude and period of those oscillations were well described ab-initio.

With the well established technique of QMOKE spectroscopy, we can now easily apply it to any other ferri- or ferromagnetic material as shown in the Appendix C for epitaxial magnetite $Fe_3O_4$ thin films. Furthermore, one of our future goals is to apply this method to AFM. The challenge here is to align the magnetic moments in the AFM to four directions in order to separate the QMOKE spectra. Our idea is to start with NiO(111) easy-plane AFM, where sufficiently large magnetic field will align the moments perpendicular to the magnetic field due to the Zeeman energy reduction by a small canting of the moments [94]. To reduce the requirement on the magnetic field strength, we may also take advantage of the exchange coupling to an adjacent ferri- or ferromagnetic layer which we can easily align by the external magnetic field [142, 143]. In the latter case the contribution of ferri- or ferromagnetic layer has to be studied separately through the same manner as we did in case of Fe or $Co_2MnSi$ samples. Nevertheless, to apply

QMOKE spectroscopy on a NiO(111) surface oriented layer, we have to first conclusively solve the above mentioned issue of $3^{\mathrm{rd}}$ order contribution to the 8-directional method measurements.

In this final paragraph we would like to conclude our plans for future work in the field of QMOKE investigations. First of all, our plan is to improve the numerical code. This includes the implementation of a proper solution for the magnetization direction at $\mu = 0°$ and $\mu = 180°$. Also, the numerical precision of the numerical solution of the wave equation (i.e. when code is searching for $N_{z,j}$ components of the wave-vector) could be improved, which would make the code more suitable also for the characterization of MO effects in the x-ray spectral region and we could employ the description of XMLD spectra through the MO parameters $G_s$ and $2G_{44}$. From experimental point of view we plan to rebuild the MOKE spectroscopy setup with the use of a spectrometer that will employ a diffraction grating in combination with a CCD camera, as the measurement of the QMOKE spectra at the current spectroscopy MOKE setup, which is scanning each wavelength separately, is still quite slow. Further, we plan to considerably improve noise-to-signal ratio of our vector MOKE setup. Then, we can make a more detailed investigation of the 8-directional method of (011) and particularly (111) oriented samples. We will further test, whether we need to extend our theoretical description of MOKE by a MO tensor cubic in magnetization in order to successfully describe the experimental data of (111) oriented samples.

# Appendix A

# Sign conventions

Within the fields of optics and magnetooptic, there is a vast amount of conventions. As there is no generally accepted system of conventions, we define here all conventions adopted within this work.

To describe reflection on the sample, three cartesian systems are needed, one for incident light beam, one for reflected light beam and one for the sample. All those cartesian systems are defined in Fig. A.1.

**Time convention**

Electric field vector of electromagnetic wave is described by negative time convention as $\boldsymbol{E}(\boldsymbol{r},t) = \boldsymbol{E}(\boldsymbol{r})e^{-i\omega t}$, providing permittivity in form $\varepsilon = \mathrm{Re}(\varepsilon) + i\,\mathrm{Im}(\varepsilon)$, where imaginary part of complex permittivity $\mathrm{Im}(\varepsilon) > 0$.

**Cartesian referential of the sample**

The cartesian system describing the sample is the right-handed $\hat{x}$, $\hat{y}$, $\hat{z}$ system, where $\hat{z}$-axis is normal to the surface of the sample and points into the sample. The $\hat{y}$-axis is parallel with the plane of light incidence and with the sample surface, while its positive direction is defined by the direction of $k_y$, being the $\hat{y}$-component of the wave vector of incident light as shown in Fig. A.1. In this system, rotations of the crystallographic structure and magnetization take place.

**Cartesian referential of light**

We use right-handed cartesian system $\hat{s}$, $\hat{p}$, $\hat{k}$ for description of the incident and reflected light beam. The direction of vector $\hat{k}$ defines the direction of propagation of light. Vector $\hat{p}$ lies in the incident plane, i.e. a plane defined by incident and reflected beam. Vector $\hat{s}$ is perpendicular to this plane and corresponds to $\hat{x}$. This convention is the same for both incident and reflected beams (Fig. A.1).

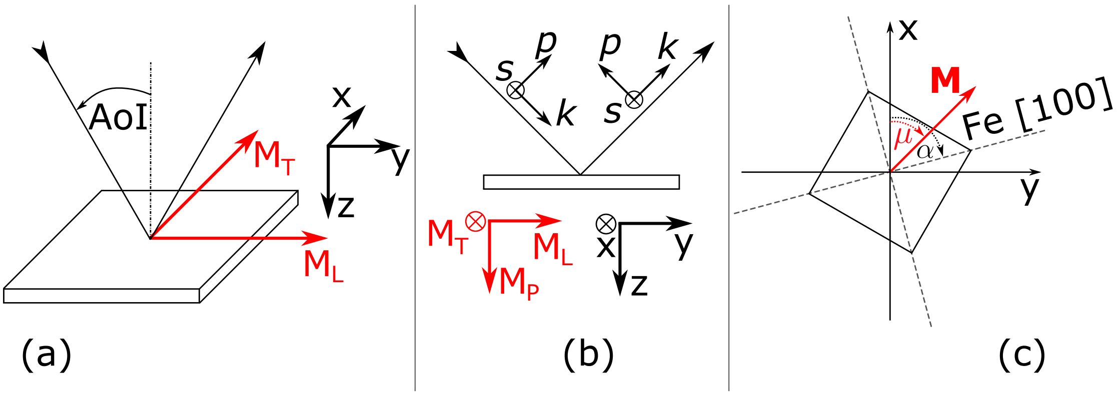

FIGURE A.1: (a) The right-handed coordinate system $\hat{x}$, $\hat{y}$, $\hat{z}$ is established with respect to the plane of incidence and surface of the sample. Components of the in-plane normalized magnetization $M_T$ and $M_L$ are defined along the axes $\hat{x}$ and $\hat{y}$ of the coordinate system, respectively. (b) Definition of the right-handed Cartesian system $\hat{s}$, $\hat{p}$, $\hat{k}$ of incident and reflected beam. (c) Definition of positive in-plane rotation of the sample and magnetization within the $\hat{x}$, $\hat{y}$, $\hat{z}$ coordinate system, described by angle $\alpha$ and $\mu$, respectively.

### Convention of the Kerr angles

The Kerr rotation $\theta$ is positive if azimuth $\theta$ of the polarization ellipse rotates clockwise, when looking into the incoming light beam. The Kerr ellipticity $\epsilon$ is positive if electric field vector $\boldsymbol{E}$ rotates clockwise when looking into the incoming light beam.

**Rotation of the optical elements and the sample** The rotation is defined as positive, if the rotated vector pointing in $\hat{x}$ ($\hat{s}$) direction rotates towards $\hat{y}$ ($\hat{p}$) direction. The sample orientation $\alpha$=0 corresponds to Fe[100] direction being parallel to $\hat{x}$-axis and, when looking at the top surface of the sample, the positive rotation of the sample is clockwise. Further, when looking into the incoming beam, the positive rotation of the optical elements is counter-clockwise, being in contrast to the positive Kerr angles, defined by the historical convention.

# Appendix B

# Magnetic anisotropy of Fe(011)/MgO(111) sample RS210917

In order to probe magnetization reversal process of the sample RS210917 in more detail, we performed set of MOKE measurements that is adequate to vector MOKE technique described in Ref. [17].

In Fig. B.1 we show hysteresis loops recorded with external magnetic field parallel ($B_{0y}$) and perpendicular ($B_{0x}$) to the plane of incidence, i.e. longitudinal and transversal external magnetic field, respectively. With $B_{0y}$ standard LMOKE hysteresis curves are measured. With external magnetic field $B_{0x}$, the loops are recorded for the sample rotated by $-90°$ with respect to the sample's position where LMOKE loops were recorded. Then, if $\boldsymbol{M}$ posses some $M_y$ component during reversal, we will measure it as LMOKE signal. Note that this $M_y$ component is in fact analogous to $M_x$ component during reversal of LMOKE loop measured with $B_{0y}$ external field. Sample orientation written as a text insets in subplots of the Fig. B.1 refer to position of the sample when LMOKE hysteresis loop was measured.

From Figs. B.1 (a)–(e) and (g)–(k) we may see that $\boldsymbol{M}$ reversal is not fully antisymmetric in the range of $\alpha = \langle 356°, 12° \rangle$ and $\alpha = \langle 174°, 192° \rangle$, respectively. This actually disable us to apply symmetrization and antisymmetrization of the loops as described by Eq. (3.1.7), which make it complicated to use vector MOKE technique to fully reconstruct the reversal process in the sample.

In Fig. B.2 we present another set of loops measurements, where the loops were measured with normal AoI, but the rest was exactly the same as in the previous case, i.e. loops

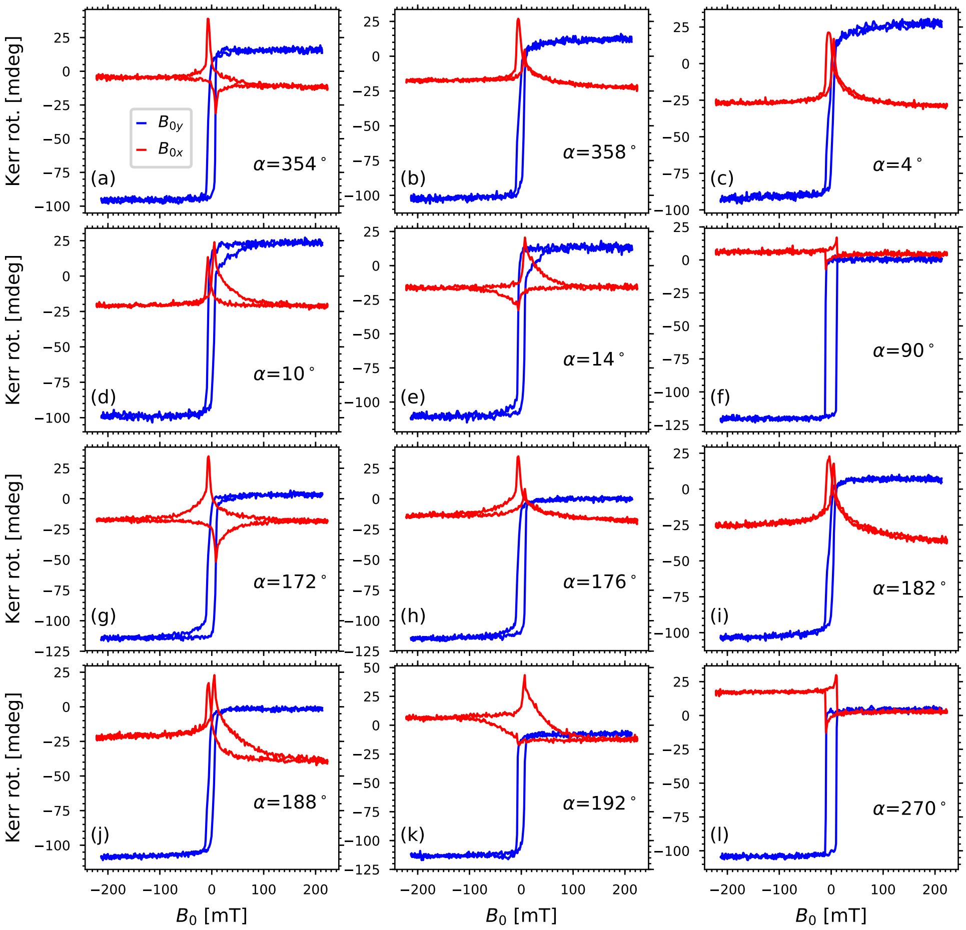

FIGURE B.1: Measurement of LMOKE hysteresis curves of sample RS210917 with AoI of 45° and $s$-polarized incident light are plotted with the blue colour. Text inset in each subplot denote orientation of the sample. The loops plotted with the red colour are measurements with transversal external field $B_{0x}$ when sample was rotated by $-90°$ with respect to the sample position writen in the subplot as text inset.

recorded with $B_{0y}$ external magnetic field and upon rotation by $-90°$ with $B_{0x}$ external magnetic field. Here, we may conclude that some out-of-plane (OOP) $\boldsymbol{M}$ component $M_z$ is present.

The LMOKE contribution does extinct with normal AoI, thus the loops observed in Figs. B.2 (a)–(l) should be of PMOKE contribution. Although we do not apply any OOP external magnetic field $B_{0z}$, the magnetic anisotropy of the sample could force the $\boldsymbol{M}$ to posses some component of $M_z$. From the shape of the loops, we propose an easy magnetic plane that is tilted in the OOP direction. When the sample posses orientation ca. $\alpha = 90°$ and $\alpha = 270°$ the tilt of the plane is parallel with the direction of $y$-axis [see the sketch in Fig. B.3(a)]. When the external magnetic field is applied in the direction of this tilt, the $\boldsymbol{M}$ is forced to be slightly OOP, producing PMOKE contribution as shown in Figs. B.2 (d)–(f) and (j)–(l). If we rotate the sample together with the direction of an external magnetic field, the loops should stay the same, as the external magnetic field

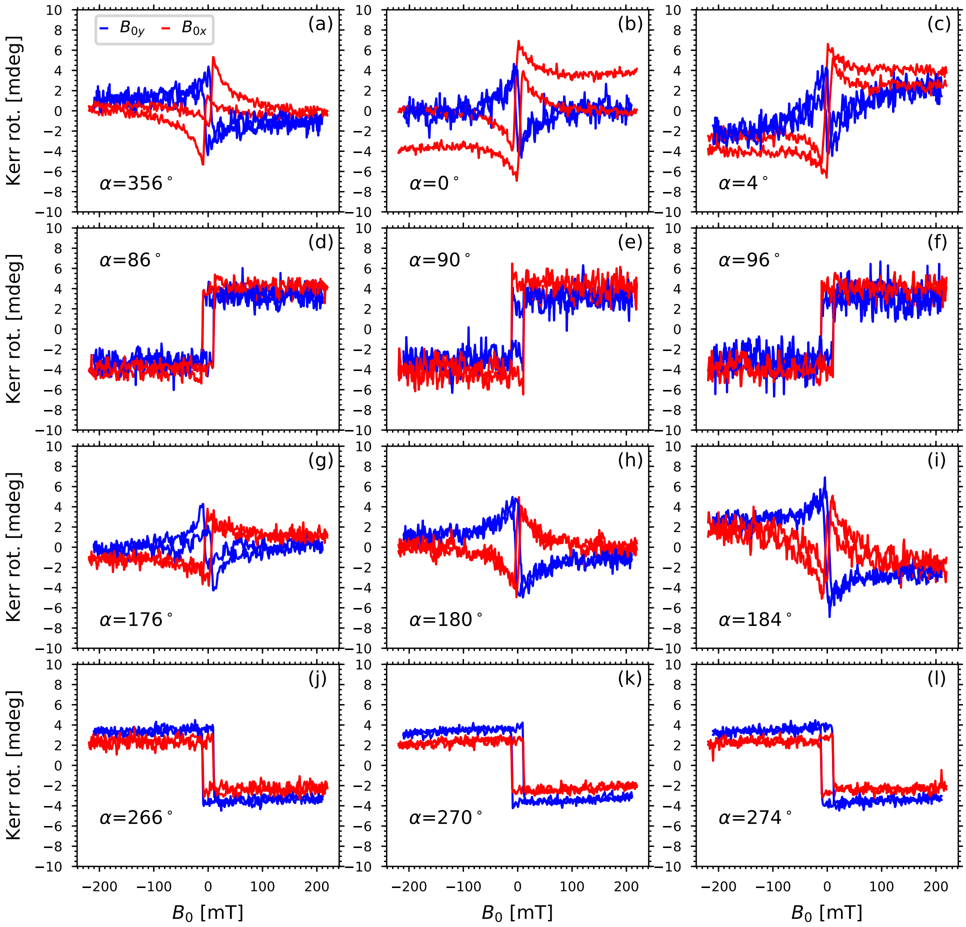

FIGURE B.2: Measurements of hysteresis loops with in plane external magnetic field $B_{0y}$ and $B_{0x}$. The orientation of the sample is stated in each subplot as text inset. With the mesaurement of loop with external magnetic field $B_{0x}$, sample was rotated by $-90°$.

and the magnetic easy plane did not change orientation with respect to each other and, thus, the induced $M_z$ component must be the same. Such a behaviour is exactly what we observe in Figs. B.2 (d)–(f) and (j)–(l).

When the sample posses orientation ca. $\alpha = 0°$ and $\alpha = 180°$, the intersection of the surface plane and the magnetic easy plane is parallel to $y$-axis [see the sketch in Fig. B.3(b)]. For the external magnetic field applied along this intersection, nothing force $\boldsymbol{M}$ to posses OOP component $M_z$. However, OOP component $M_z$ may be induced during $\boldsymbol{M}$ reversal, when $\boldsymbol{M}$ rotates in the direction of the tilt of the magnetic easy plane. Such a behaviour can be observed with Figs. B.2 (a)–(c) and (g)–(i). It seems that in this case $\boldsymbol{M}$ reverse in opposite direction when loop is measured with $B_{0y}$ external magnetic field and when the sample is rotated by $-90°$ and the loop is measured with $B_{0x}$ external magnetic field.

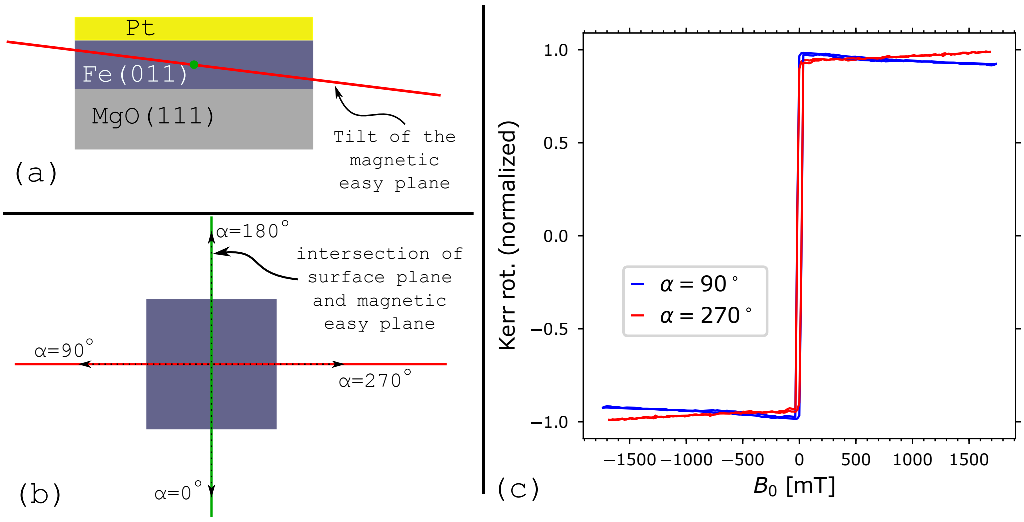

FIGURE B.3: (a),(b) sketch of tilted magnetic easy plane in the RS210917 sample. (c) Measurements of hysteresis loops with longitudinal external field under AoI of 60°.

To test this theory, we further employ MOKE setup where external magnetic field can go as high as 2 T. If the sample truly posses OOP tilted easy magnetic plane as discussed above and as shown in Figs. B.3(a) and (b), we should be able to force the $\boldsymbol{M}$ off this easy magnetic plane by sufficiently large external magnetic field. In Fig. B.3(c) we present two loops measured with $B_{0y}$ external magnetic field and AoI of roughly 60°.

The contribution of LMOKE will not change its sign upon rotation of sample by 180° (i.e. from $\alpha = 90°$ to $\alpha = 270°$). But the contribution of PMOKE should change its sign, as the slope of the tilt of magnetic easy plane is reversed upon rotation and, thus, opposite component of $M_z$ is generated. We may observe that with loop measured at $\alpha = 90°$ the value of Kerr rotation is decreasing with stronger external magnetic field. The positive PMOKE contribution to the loop is decreasing as the external magnetic field force the $\boldsymbol{M}$ to align within the surface plane of the sample and, thus, the $M_z$ component is decreased. On the other hand, with the loop measured at $\alpha = 270°$, the value of Kerr rotation is increasing with the stronger external magnetic field. Here, the negative contribution of PMOKE to the loop is decreasing as the external magnetic field force the $\boldsymbol{M}$ to align within the surface plane of the sample and, thus, the amount of $-M_z$ component is decreased.

To make this kind of investigation complete, we should also present those loops for sample orientation $\alpha = 0°$ and $\alpha = 180°$, where we should observe no change of Kerr rotation with the increasing external magnetic field, but unfortunately we do not have those measurements in hand. But either way, the presented data support well this theory of tilted magnetic easy plane in the sample, and it also well explain some behaviour in the 8-directional measurements of this sample presented in Sec. 4.2.3.

# Appendix C

# QMOKE spectroscopy of the epitaxial magnetite $Fe_3O_4$ thin films

We present here preliminary results of LinMOKE and QMOKE spectroscopy on epitaxial magnetite $Fe_3O_4$ thin films grown by reactive molecular beam epitaxy on MgO(001) single crystal substrates. Before deposition process, the substrates were cleaned by heating up to 400 C° for 60 min in UHV chamber in oxygen atmosphere of 10 mPa. Magnetite layers were grown at 250 C° under different oxygen pressure ranging from 0.1 to 10 mPa. The thickness of the deposited layers were monitored using quartz crystal oscillator. Magnetite exhibits inverse spinel structure with lattice constant of 8.396 Å, while MgO crystallises in a rock salt structure with lattice constant 4.212 Å, hence the lattice mismatch is only 0.33 %. After the deposition the crystalline order and stoichiometry were checked at RT in-situ by the X-ray photon electron spectroscopy (XPS) and low energy electron diffraction (LEED), where the results are summarized in Ref. [144]. The samples were further ex-situ studied by XRR, AFM and Ellipsometry. Some of the results are briefly summarized in Tab. C.1. We acknowledge Michaela Tomíčková and Jari Rodewald for the sample preparation and characterization.

We measured LMOKE and QMOKE spectroscopy according to Eqs.(5.1.1a)–(5.1.1c). The LMOKE spectra measured with AoI of 45° and $s$-polarized incident beam are shown in Figs. C.1(a) and (b). Spectra of all samples are quite similar, only the sample with lowest partial pressure of oxygen have more pronounced peaks. The QMOKE spectra $Q_s$ and $Q_{44}$ are presented in Figs. C.1(c)–(f) and were measured with $s$- polarized incident beam under AoI=5°. The sample prepared with the lowest partial pressure of oxygen during deposition again deviate the most.

| pressure of $O_2$ [mPa] | Thickness XRR [nm] | Roughness XRR [nm] | Roughness AFM RMS [nm] |
|---|---|---|---|
| 10 | 63.8 | 2.6 | 3 |
| 1 | 50.4 | 2.5 | 0.8 |
| 0.5 | 56.5 | 2.5 | 0.3 |
| 0.1 | 65.9 | 2.5 | 1.9 |

TABLE C.1: The thicknesses and roughnesses as obtained from the XRR curves and roughnesses as obtained from the AFM measurements.

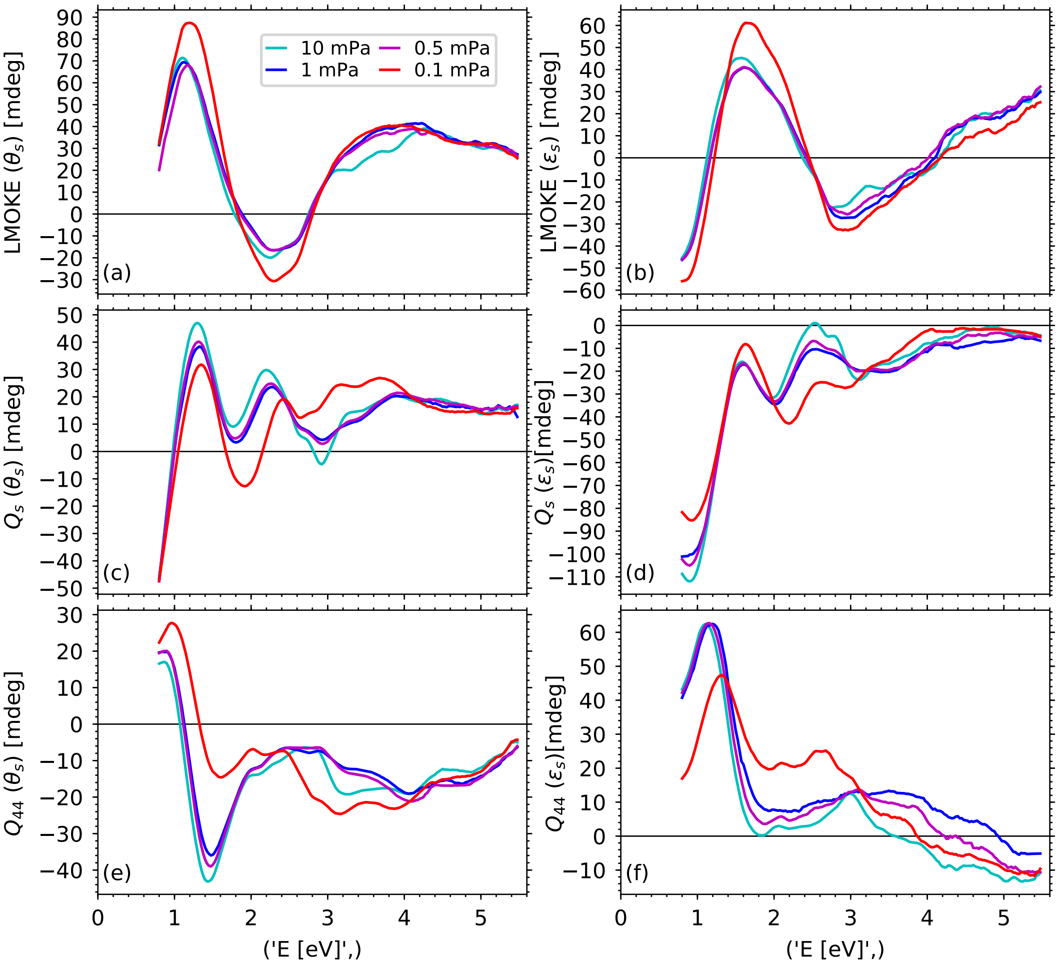

FIGURE C.1: LMOKE and QMOKE spectroscopy of epitaxial magnetite $Fe_3O_4$ thin films. The legend refers to different partial pressures of $O_2$ atmosphere in the chamber during deposition. LMOKE (a) rotation and (b) ellipticity measured with *s*- polarized incident light and under AoI of 45°. (c) Rotation and (d) ellipticity of $Q_s$ spectra and (e) rotation and (f) ellipticity of $Q_{44}$ spectra. The QMOKE spectra were measured with AoI of 5° and with *s*-polarized incident beam.

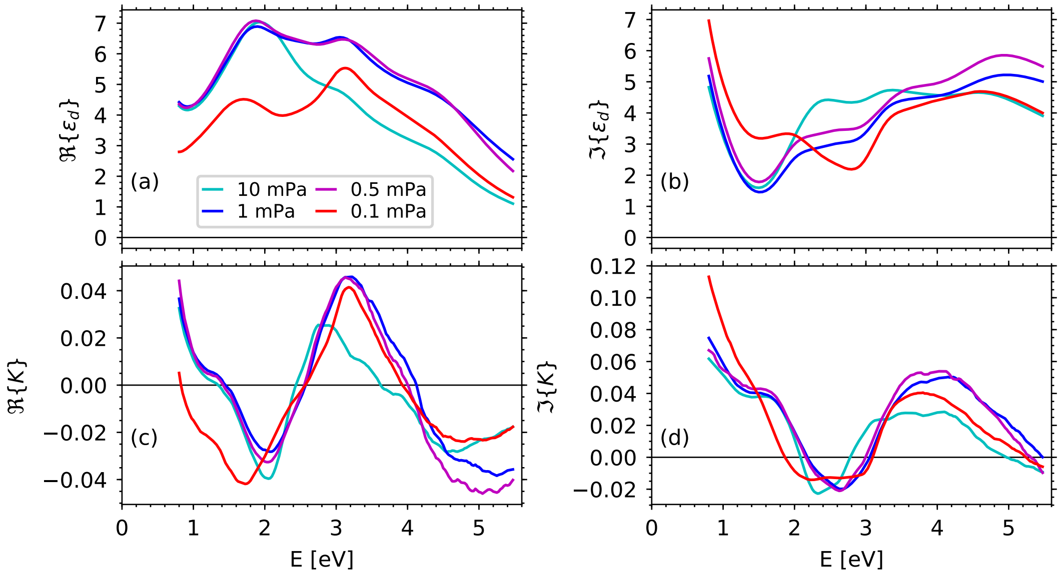

FIGURE C.2: Spectral dependencies of optical and MO parameters of epitaxial magnetite $Fe_3O_4$ thin films. The legend refers to different partial pressures of $O_2$ atmosphere in the chamber during deposition. Spectra of (a) real and (b) imaginary part of $\varepsilon_d$. Spectra of (c) real and (d) imaginary part of linear MO parameter $K$.

In Figs. C.2(a) and (b) we show spectra of $\varepsilon_d$ as obtained from ellipsometry measurements using B-spline method. In Figs. C.2(c) and (d) spectra of linear MO parameter $K$ extracted from LMOKE spectra are presented.

In Figs. C.3(a) and (b) we show spectra of $G_s$ that were extracted from $Q_s$ spectra, whereas in Figs. C.3(c) and (d) we show spectra of $2G_{44}$ that were extracted from $Q_{44}$ spectra. Furthermore, spectra of quadratic MO parameter $\Delta G$ are shown in Figs. C.3(e) and (f).

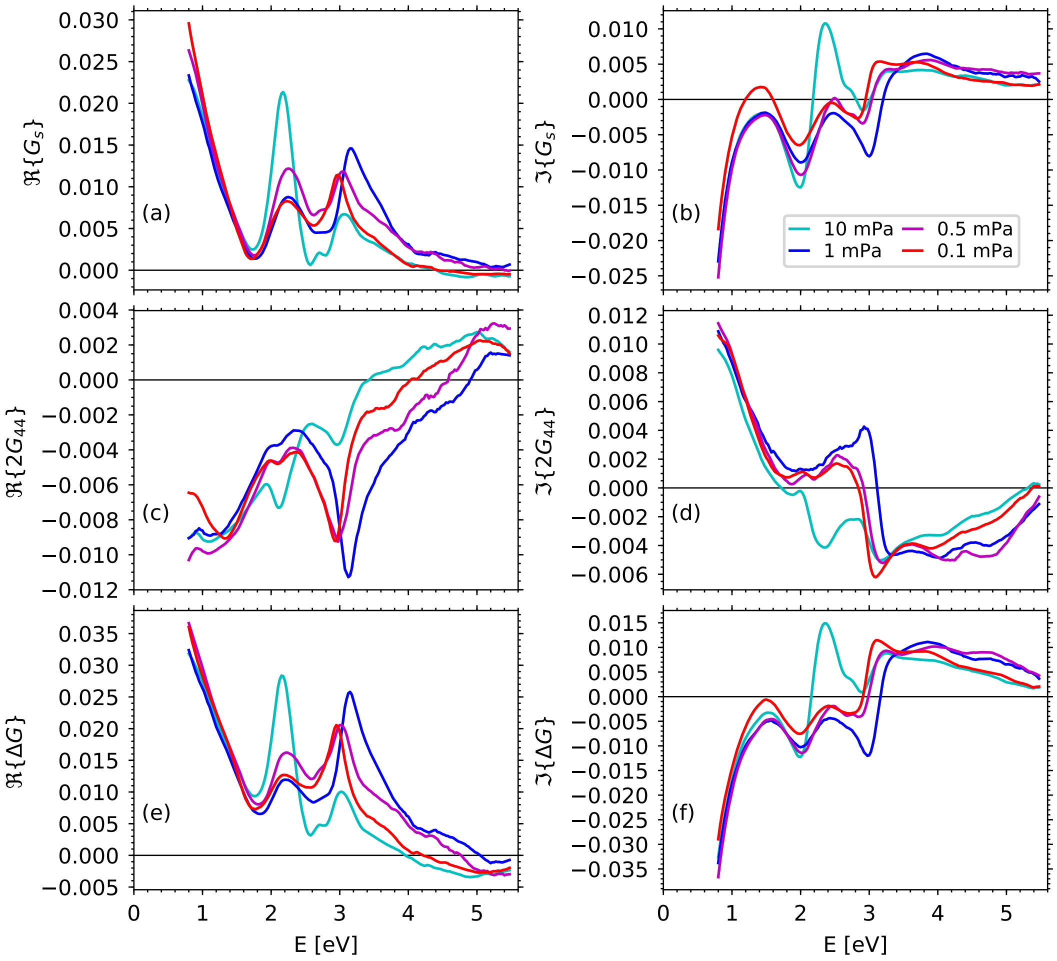

FIGURE C.3: Spectral dependencies of quadratic MO parameters of epitaxial magnetite $Fe_3O_4$ thin films. The legend refers to different partial pressures of $O_2$ atmosphere in the chamber during deposition. Spectra of (a) real and (b) imaginary part of $G_s$. Spectra of (c) real and (d) imaginary part of $2G_{44}$. Spectra of (e) real and (f) imaginary part of $\Delta G = G_s - 2G_{44}$.

# Bibliography

[1] J. Kerr, *On rotation of the plane of polarization by reflection from the pole of a magnet*, Philos. Mag. **3**, 321 (1877).

[2] A. K. Zvezdin and V. A. Kotov, *Modern Magnetooptics and Magnetooptical Materials* (Institute of Physics Publishing, Dirac House, Temple Back, Bristol BS1 6BE, UK, 1997).

[3] J.-m. Liu, *Photonic Devices* (Cambridge University Press, ADDRESS, 2005).

[4] Q. M. Zhong, A. S. Arrott, B. Heinrich, and Z. Celinski, *Surface magneto-optical Kerr effect for ultrathin Ni-Fe bilayers*, J. Appl. Phys. **67**, 4448 (1990).

[5] Q. Zhong, A. Arrott, B. Heinrich, and Z. Celinski, *Magneto-Optic response in ultrathin Ni-Fe bilayers*, J. Magn. Magn. Mater. **104**, 1837 (1992).

[6] R. M. Osgood, R. L. White, and B. M. Clemens, *Asymmetric magneto-optic response in epitaxial Fe(110)/Mo(110) thin films*, IEEE Trans. Magn. **31**, 3331 (1995).

[7] R. M. Osgood, B. M. Clemens, and R. L. White, *Asymmetric magneto-optic response in anisotropic thin films*, Phys. Rev. B **55**, 8990 (1997).

[8] K. Postava, H. Jaffres, A. Schuhl, F. Nguyen Van Dau, M. Goiran, and A. R. Fert, *Linear and quadratic magneto-optical measurements of the spin reorientation in epitaxial Fe films on MgO*, J. Magn. Magn. Mater. **172**, 199 (1997).

[9] R. M. Osgood, S. Bader, B. M. Clemens, R. L. White, and H. Matsuyama, *Second-order magneto-optic effect in anisotropic thin films*, J. Magn. Magn. Mater. **182**, 297 (1998).

[10] R. Carey, D. Newman, and M. Wears, *Asymmetric nonlinear magneto-optic effects in PtMnSb thin films*, J. Appl. Phys. **83**, 6739 (1998).

[11] R. Mattheis and G. Quednau, *Separation of Voigt Effect in Longitudinal Kerr Magnetometry*, Phys. Status Solidi A **172**, R7 (1999).

[12] R. Mattheis and G. Quednau, *Determination of the anisotropy field strength in ulrta-thin magnetic films using longitudinal MOKE and a rotationg field: the ROTMOKE method*, J. Magn. Magn. Mater. **205**, 143 (1999).

[13] K. Postava, D. Hrabovský, J. Pištora, A. R. Fert, Š. Višňovský, and T. Yamaguchi, *Anisotropy of quadratic magneto-optic effects in reflection*, J. Appl. Phys. **91**, 7293 (2002).

[14] T. Mewes, *Separation of the first- and second-order contributions in magneto-optic Kerr effect magnetometry of epitaxial FeMn/NiFe bilayers*, J. Appl. Phys. **95**, 5324 (2004).

[15] D. Berling, S. Zabrocki, R. Setphan, G. Garreau, J. Bubendroff, D. Mehdaoui, A. Bolmont, P. Wetzel, and G. Pirri, C. Gewinner, *Accurate measurement of the in-plane magnetic anisotropy energy function $E_a(\theta)$ in ultrathin films by magneto-optics*, J. Magn. Magn. Mater. **297**, 118 (2006).

[16] O. Gaier, J. Hamrle, S. J. Hermsdoerfer, H. Schultheiss, B. Hillebrands, Y. Sakuraba, M. Oogane, and Y. Ando, *Influence of the $L2_1$ ordering degree on the magnetic properties of $Co_2MnSi$ Heusler films*, J. Appl. Phys. **103**, 103910 (2008).

[17] T. Kuschel, H. Bardenhagen, H. Wilkens, R. Schubert, J. Hamrle, J. Pištora, and J. Wollschläger, *Vectorial magnetometry using magnetooptic Kerr effect including first- and second-order contributions for thin ferromagnetic films*, J. Phys. D: Appl. Phys. **44**, 265003 (2011).

[18] T. Kuschel, J. Hamrle, J. Pištora, K. Saito, S. Bosu, Y. Sakuraba, K. Takanashi, and J. Wollschläger, *Magnetic characterization of thin $C0_{50}Fe_{50}$ films by magnetooptic Kerr effect*, J. Phys. D: Appl. Phys. **45**, 495002 (2012).

[19] J. H. Liang, J. Z. Cau, J. X. Li, and Y. Z. Wu, *Separation of linear and quadratic magneto-optic Kerr effects in ultra-thin Fe films using a rotating field method*, J. Appl. Phys. **117**, 17E129 (2015).

[20] M. Montazeri, P. Upadhyaya, M. C. Onbasli, G. Yu, K. L. Wong, M. Lang, Y. Fan, X. Li, P. Khalili Amiri, R. N. Schwartz, C. A. Ross, and K. L. Wang, *Magneto-optical investigation of spin-orbit torques in metallic and insulating magnetic heterostructures*, Nat. Commun. **6**, 8958 (2015).

[21] V. Saidl, P. Němec, P. Wadley, V. Hills, R. P. Campion, V. Novák, K. W. Edmonds, F. Maccherozzi, S. S. Dhesi, B. L. Gallagher, F. Trojánek, J. Kuneš, J. Železný, P. Malý, and T. Jungwirth, *Optical determination of the Néel vector in a CuMnAs thin-film antiferromagnet*, Nat. Photonics **11**, 91 (2017).

[22] P. Němec, M. Fiebig, T. Kampfrath, and A. V. Kimel, *Antiferromagnetic opto-spintronics*, Nat. Phys. **14**, 229 (2018).

[23] J. Hamrle, S. Blomeier, O. Gaier, B. Hillebrands, H. Schneider, G. Jakob, B. Reuscher, A. Brodyanski, M. Kopnarski, K. Postava, and C. Felser, *Ion beam induced modification of exchange interaction and spin-orbit coupling in the $Co_2FeSi$ Heusler compound*, J. Phys. D: Appl. Phys. **40**, 1558 (2007).

[24] J. Hamrle, S. Blomeier, O. Gaier, B. Hillebrands, H. Schneider, G. Jakob, K. Postava, and C. Felser, *Huge quadratic magneto-optical Kerr effect and magnetization reversal in the $Co_2FeSi$ Heusler compound*, J. Phys. D: Appl. Phys. **40**, 1563 (2007).

[25] P. Muduli, W. Rice, L. He, and F. Tsui, *Composition dependence of magnetic anisotropy and quadratic magnetooptical effect in epitaxial films of the Heusler alloy $Co_2MnGe$*, J. Magn. Magn. Mater. **320**, L141 (2008).

[26] P. Muduli, W. Rice, L. He, B. Collins, Y. Chu, and F. Tsui, *Study of magnetic anisotropy and magnetization reversal using the quadratic magnetooptical effect in epitaxial $Co_xMn_yGe_z$(111) films*, J. Phys.: Condens. Matter **21**, 296005 (2009).

[27] S. Trudel, J. Hamrle, B. Hillebrands, T. Taira, and M. Yamamoto, *Magneto-optical investigation of epitaxial nonstoichiometric $Co_2MnGe$ thin films*, J. Appl. Phys. **107**, 043912 (2010).

[28] S. Trudel, G. Wolf, J. Hamrle, B. Hillebrands, P. Klaer, M. Kallmayer, H.-J. Elmers, H. Sukegawa, W. Wang, and K. Inomata, *Effect of annealing on $Co_2FeAl_{0.5}Si_{0.5}$ thin films: A magneto-optical and x-ray absorbtion study*, Phys. Rew. B **83**, 104412 (2011).

[29] G. Wolf, J. Hamrle, S. Trudel, T. Kubota, Y. Ando, and B. Hillebrands, *Quadratic magneto-optical Kerr effect in $Co_2MnSi$*, J. Appl. Phys. **110**, 043904 (2011).

[30] Š. Višňovský, *Magneto-Optical Permittivity tensor in crystals*, Czech. J. Phys B **36**, 1424 (1986).

[31] R. Silber, M. Tomíčková, J. Rodewald, J. Wollschläger, J. Pištora, M. Veis, T. Kuschel, and J. Hamrle, *Quadratic magnetooptic spectroscopy setup based on photoelastic light modulation*, Phot. Nano. Fund. Appl. **31**, 60 (2018).

[32] R. Silber, O. Stejskal, L. Beran, P. Cejpek, R. Antoš, T. Matalla-Wagner, J. Thien, O. Kuschel, J. Wollschläger, M. Veis, T. Kuschel, and J. Hamrle, *Quadratic magneto-optic Kerr effect spectroscopy of Fe epitaxial films on MgO(001) substrates*, Phys. Rev. B **100**, 064403 (2019).

[33] Š. Višňovský, *Optics in Magnetic Multilayers and Nanostructures* (CRC Press, Boca Raton, 2006).

[34] E. Hecht, *Optics, fourth edition* (Addison Wesley, San Francisco, 2002).

[35] M. Buchmeier, R. Schreiber, D. E. Bürgler, and C. M. Schneider, *Thickness dependence of linear and quadratic magneto-optical Kerr effects in ultrathin Fe(001) films*, Phys. Rev. B **79**, 064402 (2009).

[36] J. H. Liang, Y. L. Chen, L. Sun, C. Zhou, Y. Yang, and Y. Z. Wu, *The anisotropic linear and quadratic magneto-optical Kerr effects in epitaxial Fe/GaAs(110) film*, Appl. Phys. Lett. **108**, 3 (2016).

[37] B. Cullity and C. Graham, *Introduction to magnetic materials (second edition)* (Institute of Electrical and Electronics Engineers, New Jersey, 1997).

[38] J. Hamrlová, J. Hamrle, K. Postava, and J. Pištora, *Quadratic-in-magnetization permittivity and conductivity tensor in cubic crystals*, Phys. Status Solidi B **250**, 2194 (2013).

[39] M. Faraday, *I. Experimental research in Electricity.–Nineteenth Series*, Phil. Trans. Roy. Soc. **136**, 1 (1846).

[40] J. Kerr, *On reflection of polarized light from the equatorial surface of a magnet*, The London, Edinburgh, and Dublin Philosophical Magazine and Journal of Science **5**, 161 (1878).

[41] A. Righi, Ann. Chim. Phys. **9**, 120 (1886).

[42] P. Zeeman, , Leiden Commun. **15**, (1895).

[43] P. Zeeman, *XXXII. On the influence of magnetism on the nature of the light emitted by a substance*, Phil.Mag. **43**, 226 (1897).

[44] P. Zeeman, *Measurements concerning the influence of a magnetization, perpendicular to the plane of incidence on the light reflected from an iron mirror*, Leiden Commun. **29**, 3 (1896).

[45] C. H. Wind, Verhandl. Amsterdam Acad. **5**, 91 (1896).

[46] H. A. Lorentz, Arch. Néel **19**, 123 (1884).

[47] P. Drude, *Zur Elektronentheorie der Metalle; I. Teil*, Ann. Physik **1**, 566 (1900).

[48] P. Drude, *Zur Elektronentheorie der Metalle; II. Teil*, Ann. Physik **3**, 369 (1900).

[49] H. R. Hulme, *The Faraday effect in ferromagnetics*, Proc. Roy. Soc. (London) **135**, 237 (1932).

[50] O. Halpern, *Notiz über die Rotationspolarisation ferromagnetischer Körper*, Ann. Physik **12**, 181 (1932).

[51] C. Kittel, Phys. Rev. **83**, 208A (1951).

[52] P. N. Argyres, *Theory of the Faraday and Kerr Effects in Ferromagnetics*, Phys. Rev. **97**, 334 (1955).

[53] G. S. Krinchik, *Ferromagnetic Hall Effect at Optical Frequencies and Inner Effective Magnetic Field of Ferromagnetic Metals*, J. Appl. Phys. **35**, 1089 (1964).

[54] G. S. Krinchik and V. A. Artemjev, *Magneto-optic Properties of Nickel, Iron, and Cobalt*, J. Appl. Phys. **39**, 1276 (1968).

[55] P. E. Ferguson and R. J. Romagnoli, *Transverse Kerr Magneto–Optic Effect and Optical Properties of Transition–Rare–Earth Alloys*, J. Appl. Phys. **40**, 1236 (1969).

[56] P. Hohenberg and W. Kohn, *Inhomogeneous Electron Gas*, Phys. Rev. **136**, B864 (1964).

[57] W. Kohn and L. Sham, *Self-Consistent Equations Including Exchange and Correlation Effects*, Phys. Rev. **140**, A1133 (1965).

[58] R. Kubo, *Statistical-Mechanical Theory of Irreversible Processes. I. General Theory and Simple Applications to Magnetic and Conduction Problems*, J. Phys. Soc. Jpn. **12**, 570 (1957).

[59] E. R. Moog and S. D. Bader, Superlattices Microstruct. **1**, 543 (1985).

[60] P. M. Oppeneer, T. Maurer, J. Sticht, and J. Kübler, *Ab initio calculated magneto-optical Kerr effect of ferromagnetic metals: Fe and Ni*, Phys. Rev. B **45**, 10924 (1992).

[61] P. M. Oppeneer, J. Sticht, T. Maurer, and J. Kübler, *Ab initio investigation of microscopic enhancement factors in tuning the magneto-optical Kerr effect*, Z. Phys. B **88**, 309 (1992).

[62] Š. Višňovský, M. Nývlt, V. Prosser, R. Lopušník, R. Urban, J. Ferré, G. Pénissard, D. Renard, and R. Krishnan, *Polar magneto-optics in simple ultrathin-magnetic-film structures*, Phys. Rev. B **52**, 1090 (1995).

[63] S. Uba, L. Uba, A. N. Yaresko, A. Ya. Perlov, V. N. Antonov, and R. Gontarz, *Optical and magneto-optical properties of Co/Pt multilayers*, Phys. Rev. B **53**, 6526 (1996).

[64] Š. Višňovský, R. Lopušník, M. Nývlt, A. Das, R. Krishnan, M. Tessier, Z. Frait, P. Aitchison, and J. N. Chapman, *Magneto-optic studies of Fe/Au multilayers*, J. Magn. Magn. Mater. **198**, 480 (1999).

[65] J. Hamrle, M. Nývlt, Š. Višňovský, R. Urban, P. Beauvillain, R. Mégy, J. Ferré, L. Polerecký, and D. Renard, *Magneto-optical properties of ferromagnetic/non-ferromagnetic interfaces: Application to Co/Au(111)*, Phys. Rev. B **64**, 155405 (2001).

[66] J. Hamrle, J. Ferré, M. Nývlt, and Š. Višňovský, *In-depth resolution of the magneto-optical Kerr effect in ferromagnetic multilayers*, Phys. Rev. B **66**, 224423 (2002).

[67] J. Gřondilová, M. Rickart, J. Mistrík, K. Postava, Š. Višňovský, T. Yamaguchi, R. Lopušník, S. O. Demokritov, and B. Hillebrands, *Anisotropy of magneto-optical spectra in ultrathin Fe/Au/Fe bilayers*, J. Appl. Phys. **91**, 8246 (2002).

[68] Š. Višňovský, M. Veis, E. Lišková, V. Kolinský, D. Kulkarni, Prasanna, N. Venkataramani, S. Prasad, and R. Krishnan, *MOKE spectroscopy of sputter-deposited Cu-ferrite films*, J. Magn. Magn. Mater. **290**, 195 (2005).

[69] M. Veis, L. Beran, R. Antoš, D. Legut, J. Hamrle, J. Pištora, Ch. Sterwerf, M. Meinert, J.-M. Schmalhorst, T. Kuschel, and G. Reiss, *Magneto-optical spectroscopy of Co$_2$FeSi Heusler compound*, J. Appl. Phys. **115**, 17A927 (2014).

[70] K. H. J. Buschow, *Handbook of Magnetic Materials* (Elsevier Science B. V., Sara Burgerhartstraat 25 P.O. Box 211, 1000 AE Amsterdam, The Netherlands, 2001), Vol. 13.

[71] G. Metzger, P. Pluvinage, and R. Torguet, *Termes linéaires et quadratiques dans l'effet mgnéto-optique de Kerr*, Ann. Phys. **10**, 5 (1965).

[72] C. Stamm, C. Murer, M. Berritta, J. Feng, M. Gabureac, P. Oppeneer, and P. Gambardella, *MAgneto-Optical Detection of the Spin Hall Effect in Pt and W Thin Films*, Phys. Rev. Lett. **119**, 087203 (2017).

[73] A. Hirohata, Y. Baba, B. A. Murphy, B. Ng, Y. Yao, K. Nagao, and J.-y. Kim, *Magneto-optical detection of spin accumulation under the influence of mechanical*, Sci. Rep. **8**, (2018).

[74] J. Nogués and I. K. Schuller, *Exchange bias*, J. Magn. Magn. Mater. **192**, 203 (1999).

[75] T. Jungwirth, X. Marti, P. Wadley, and J. Wunderlich, *Antiferromagnetic spintronics*, Nat. Nano. **11**, 231 (2016).

[76] P. Wadley, B. Howells, J. Železný, C. Andrews, V. Hills, R. P. Campion, V. Novák, K. Olejník, F. Maccherozzi, S. S. Dhesi, S. Y. Martin, T. Wagner, J. Wunderlich, F. Freimuth, Y. Mokrousov, J. Kuneš, J. S. Chauhan, M. J. Grzybowski, A. W. Rushforth, K. W. Edmonds, B. L. Gallagher, and T. Jungwirth, *Electrical switching of antiferromagnet*, Science **351**, 587 (2016).

[77] S. Baierl, M. Hohenleutner, T. Kampfrath, A. K. Zvezdin, A. V. Kimel, R. Huber, and R. V. Mikhaylovskiy, *Nonlinear spin control by terahertz-driven anisotropy fields*, Nat. Photonics **10**, 715 (2016).

[78] A. V. Kimel, B. A. Ivanov, R. V. Pisarev, P. A. Usachev, A. Kirilyuk, and T. Rasing, *Inertia-driven spin switching in antiferromagnets*, Nat. Phys. **5**, 727 (2009).

[79] T. Kampfrath, A. Sell, G. Klatt, A. Pashkin, S. Ma, T. Dekorsy, M. Wolf, M. Fiebig, A. Leitenstorfer, and R. Huber, *Coherent terahertz control of antiferromagnetic spin waves*, Nat. Photonics **5**, 31 (2011).

[80] G. A. Prinz, *Magnetoelectronics*, Science **282**, 1660 (1998).

[81] M. I. Daykonov, *Spin physics in Semiconductors* (Springer International Publishing AG, Gewerbestrasse 11, 6330 Cham, Switzerland, 2017).

[82] A. von Ettingshausen and W. Nernst, *Ueber das Auftreten electromotorischer Kräfte in Metallplatten, welche von einem Wärmestrome durchflossen werden und sich im magnetischen Felde befinden*, Ann. Phys. Chem. **265**, 343 (1886).

[83] S. Y. Huang, W. G. Wang, S. F. Lee, J. Kwo, and C. L. Chien, *Intrinsic Spin-Dependent Thermal Transport*, Phys. Rev. Lett. **107**, 216604 (2011).

[84] D. Meier, T. Kuschel, L. Shen, A. Gupta, T. Kikkawa, K. Uchida, E. Saitoh, J.-M. Schmalhorst, and G. Reiss, *Thermally driven spin and charge currents in thin* $NiFe_2O_4$*/Pt films*, Phys. Rev. B **87**, 054421 (2013).

[85] M. Schmid, S. Srichandan, D. Meier, T. Kuschel, J.-M. Schmalhorst, M. Vogel, G. Reiss, C. Strunk, and C. H. Back, *Transverse Spin Seebeck Effect versus Anomalous and Planar Nernst Effects in Permalloy Thin Films*, Phys. Rev. Lett. **111**, 187201 (2013).

[86] D. Meier, D. Reinhardt, M. Schmid, C. H. Back, J.-M. Schmalhorst, T. Kuschel, and G. Reiss, *Influence of heat flow directions on Nernst effects in Py/Pt bilayers*, Phys. Rev. B **88**, 184425 (2013).

[87] O. Reimer, D. Meier, M. Bovender, L. Helmich, J.-O. Dreessen, J. Krieft, A. S. Shestakov, C. H. Back, J.-M. Schmalhorst, A. Hütten, G. Reiss, and T. Kuschel, *Quantitative separation of the anisotropic magnetothermopower and planar Nernst effect by the rotation of an in-plane thermal gradient*, Sci. Rep. **7**, 40586 (2017).

[88] N. Nagaosa, J. Sinova, S. Onoda, A. H. MacDonald, and N. P. Ong, *Anomalous Hall effect*, Rev. Mod. Phys **82**, 1539 .

[89] W. Thomson, *On the electro-dynamic qualities of metals: Effects of magnetization on the electric conductivity of nickel and of iron*, Proc. R. Soc. London **8**, 546 (1856).

[90] S. Valencia, A. Kleibert, A. Gaupp, J. Rusz, D. Legut, J. Bansmann, W. Gudat, and P. M. Oppeneer, *Quadratic x-ray magneto-optical effect upon reflection in a near-normal-incidence configuration at the M edges of 3d-transition metals*, Phys. Rev. Lett. **104**, 187401 (2010).

[91] H.-Ch. Mertins, P. M. Oppeneer, J. Kuneš, A. Gaupp, D. Abramsohn, and F. Schäfers, *Observation of the X-Ray Magneto-Optical Voigt Effect*, Phys. Rev. Lett. **87**, 47401 (2001).

[92] B. Sepúlveda, Y. Huttel, C. Martínez Boubeta, A. Cebollada, and G. Armelles, *Linear and quadratic magneto-optical Kerr effects in continuous and granular ultrathin monocrystalline Fe films*, Phys. Rev. B **68**, 064401 (2003).

[93] I. D. Lobov, A. A. Makhnev, and M. M. Kirillova, *Optical and magnetooptical properties of Heusler alloys XMnSb (X = Co, Pt)*, Phys. Met. Metalloved. **113**, 135 (2012).

[94] G. R. Hoogeboom, A. Aqeel, T. Kuschel, T. T. M. Palstra, and B. J. van Wees, *Negative spin Hall magnetoresistance of Pt on the bulk easy-plane antiferromagnet NiO*, Appl. Phys. Lett. **111**, 052409 (2017).

[95] T. Higuchi and M. Kuwata-Gonokami, *Control of antiferromagnetic domain distribution via polarization-dependent optical annealing.*, Nat. Commun. **7**, 10720 (2016).

[96] A. V. Kimel, A. Kirilyuk, A. Tsvetkov, R. V. Pisarev, and T. Rasing, *Laser-induced ultrafast spin reorientation in the antiferromagnet TmFeO3*, Nature **429**, 850 (2004).

[97] A. V. Kimel, A. Kirilyuk, P. A. Usachev, R. V. Pisarev, A. M. Balbashov, and T. Rasing, *Ultrafast non-thermal control of magnetization by instantaneous photomagnetic pulses*, Nature **435**, 655 (2005).

[98] N. Kanda, T. Higuchi, H. Shimizu, K. Konishi, K. Yoshioka, and M. Kuwata-Gonokami, *The vectorial control of magnetization by light*, Nat. Commun. **2**, 362 (2011).

[99] R. Silber, *Quadratic-in-magnetization magneto-optical spectroscopy*, Master's thesis, VŠB - Technical University of Ostrava, 2014.

[100] O. Stejskal, R. Silber, J. Pištora, and J. Hamrle, *Convergence study of the ab-initio calculated quadratic magneto-optical spectra in bcc Fe*, Phot. Nano. Fund. Appl. **32**, 24 (2018).

[101] O. Stejskal, *Microscopic Origin of Linear Magneto-Optical Effect in bcc Fe*, Ph.D. thesis, VŠB - Technical University of Ostrava, 2019.

[102] R. Feynman, R. Leighton, and M. Sands, *The Feynman lectures on physics; The new millennium Edition. Volume II: Mainly electromagnetism and matter* (Basic Books, 1290 Avenue of Americans, New York, NY 10104, 2011).

[103] K. Postava, T. Yamaguchi, and K. Roman, *Matrix description of coherent and incoherent light reflection and transmission by anisotropic multilayer structures*, Appl. Opt. **41**, 2521 (2002).

[104] P. Yeh, *Optics of anisotropic layered media: A new 4×4 matrix algebra*, Surf. Sci. **96**, 41 (1980).

[105] R. Ciprian, F. Loi, E. Busetto, V. Bonanni, B. Casarin, A. Caretta, M. Solzi, and M. Malvestuto, *MOKE setup exploiting a nematic liquid crystal modulator*, Rev. Sci. Instrum. **89**, 105107 (2018).

[106] G. Götz, *Aufbau eines multichromatischen Zwei-Strahl-Magnetometers mit einem dreiachsigen Magneten auf Grundlage des magnetooptischen Kerr-Effekts*, Bachelor's thesis, Bielefeld University, 2012.

[107] G. B. Arfken and H. J. Weber, *Mathematical methods for physicists, fourth edition* (Academic Press, San Diego, 1995).

[108] J. A. Woollam Co., Inc., *CompleteEASE$^{TM}$ Data Analysis Manual*, 2008.

[109] B. Johs and J. S. Hale, *Dielectric function representation by B-splines*, Phys. Status Solidi A **205**, 715 (2008).

[110] D. Depla, S. Mahieu, *et al.*, *Reactive sputter deposition* (Springer, ADDRESS, 2008), Vol. 109.

[111] S. M. Rossnagel and J. Hopwood, *Magnetron sputter deposition with high levels of metal ionization*, App. Phys. Lett. **63**, 3285 (1993).

[112] J. Mattson, E. E. Fullerton, C. Sowers, and S. Bader, *Epitaxial growth of body-centered-cubic transition metal films and superlattices onto MgO (111), (011), and (001) substrates*, J. Vac. Sci. Technol. A **13**, 276 (1995).

[113] M. Björck and G. Andersson, *GenX: an extensible X-ray reflectivity refinement program utilizing differential evolution*, J. Appl. Crystallogr. **40**, 1174 (2007).

[114] L. G. Parratt, *Surface Studies of Solids by Total Reflection of X-Rays*, Phys. Rev. **95**, 359 (1954).

[115] W. M. Haynes, David. R. Lide, and Thomas. J. Bruno, *Handbook of chemistry and physics, 95th edition* (CRC press, Boca Raton, 2014).

[116] J. S. Custer, M. O. Thompson, D. C. Jacobson, J. M. Poate, S. Roorda, W. C. Sinke, and F. Spaepen, *Density of amorphous Si*, Appl. Phys. Lett. **64**, 437 (1994).

[117] G. Mende, J. Finster, D. Flamm, and D. Schulze, *Oxidation of etched silicon in air at room temperature; Measurements with ultrasoft X-ray photoelectron spectroscopy (ESCA) and neutron activation analysis*, Surf. Sci. **128**, 169 (1983).

[118] E. D. Palik, *Handbook of Optical Constants of Solids* (Academic Press, San Diego, 1985).

[119] J. Thien, Bachelor's thesis, University Osnabrück, 2015.

[120] W. H. Wang, M. Przybylski, W. Kuch, L. I. Chelaru, J. Wang, Y. F. Lu, J. Barthel, H. L. Meyerheim, and J. Kirschner, *Magnetic properties and spin polarization of* $\mathrm{Co_2MnSi}$ *Heusler alloy thin films epitaxially grown on GaAs(001)*, Phys. Rev. B **71**, 144416 (2005).

[121] M. Jourdan, J. Minár, J. Braun, A. Kronenberg, S. Chadov, B. Balke, A. Gloskovskii, M. Kolbe, H. Elmers, G. Schönhense, H. Ebert, C. Felser, and M. Kläui, *Direct observation of half-metallicity in the Heusler compound* $Co_2MnSi$, Nat. Commun. **5**, 3974 (2014).

[122] S. Picozzi, A. Continenza, and J. Freeman, A, *$Co_2MnX$ (X = Si, Ge, Sn) Heusler compounds: An ab-initio study of their structural, electronic, and magnetic properties at zero and elevated pressure*, Phys. Rev. B **66**, 094421 (2002).

[123] S. Fuji, S. Sugimura, S. Ishida, and S. Asano, *Hyperfine fields and electronic structures of the Heusler alloys Co2MnX (X=Al, Ga, Si, Ge, Sn)*, J. Phys.: Condens. Matter **2**, 8583 (1990).

[124] J. Brown, P, U. Neumann, K, J. Webster, P, and R. A. Ziebeck, K, *The magnetization distributions in some Heusler alloys proposed as half-metallic ferromagnets*, J. Phys.: Condens. Matter **12**, 1827 (2000).

[125] S. Rodan, A. Alfonsov, M. Belesi, F. Ferraro, J. T. Kohlhepp, H. J. M. Swagten, B. Koopmans, Y. Sakuraba, S. Bosu, K. Takanashi, B. Büchner, and S. Wurmehl, *Nuclear magnetic resonance reveals structural evolution upon annealing in epitaxial* $Co_2$*MnSi Heusler films*, **102**, (2013).

[126] S. Trudel, O. Gaier, J. Hamrle, and B. Hillebrands, *Magnetic anisotropy, exchange and damping in cobalt-based full-Heusler compounds: an experimental review*, J. Phys. D: Appl. Phys. **43**, 193001 (2010).

[127] P. Sandström, E. B. Svedberg, J. Brich, and J. E. Sundgren, *Time-resolved measurements of the formation of single domain epitaxial Ni films on MgO(111) substrates using in-situ RHEED analysis*, Surf. Sci. **437**, L767 (1999).

[128] A. Jain, S. P. Ong, G. Hautier, W. Chen, W. D. Richards, S. Dacek, S. Cholia, D. Gunter, D. Skinner, G. Ceder, and K. Persson, *The Materials Project: A materials genome approach to accelerating materials innovation*, APL Materials **1**, 011002 (2013).

[129] Y. Nukaga, M. Ohtake, M. Futamoto, F. Kirino, N. Fujita, and N. Inaba, *Structure and Magnetic Properties of Co Epitaxial Thin Films Grown on MgO Single-Crystal Substrates*, IEEE Trans. Magn. **45**, 2519 (2009).

[130] T. Kuschel, T. Becker, D. Bruns, M. Suendorf, F. Bertram, and J. Fumagalli, P. Wollschläder, *Uniaxial magnetic anisotropy for thin Co films on glass studied by magnetooptic Kerr effect*, J. Appl. Phys. **109**, 093907 (2011).

[131] M. Buchner, P. Högl, S. Putz, M. Gmitra, S. Günther, M. A. W. Schoen, M. Kronseder, D. Schuh, D. Bougeard, J. Fabian, and C. H. Back, *Anisotropic Polar Magneto-Optic Kerr Effect of Ultrathin* Fe/GaAs(001) *Layers due to Interfacial Spin-Orbit Interaction*, Phys. Rev. Lett. **117**, 157202 (2016).

[132] P. Blaha, K. Schwarz, G. Madsen, D. Kvasnicka, and J. Luitz, *User's Guide, WIEN2k_16.1 (Release 10/15/2014)*, Vienna University of Technology, Austria, 2014.

[133] C. Ambrosch-Draxl and J. O. Sofo, *Linear optical properties of solids within the full-potential linearized augmented planewave method*, Comput. Phys. Commun. **175**, 1 (2006).

[134] J. Hamrlová, D. Legut, M. Veis, J. Pištora, and J. Hamrle, *Principal spectra describing magnetooptic permittivity tensor in cubic crystals*, J. Magn. Magn. Mater. **420**, 143 (2016).

[135] H. T. Yolken and J. Kruger, *Optical Constants of Iron in the Visible Region*, J. Opt. Soc. Am. **55**, 842 (1965).

[136] P. B. Johnson and R. W. Christy, *Optical constants of transition metals: Ti, V, Cr, Mn, Fe, Co, Ni, and Pd*, Phys. Rev. B **9**, 5056 (1973).

[137] O. Miura and T. Fujiwara, *Electronic structure and effects of dynamical electron correlation in ferromagnetic bcc Fe, fcc Ni, and antiferromagnetic NiO*, Phys. Rev. B **77**, 195124 (2008).

[138] Y. Yao, L. Kleinman, A. H. MacDonald, J. Sinova, T. Jungwirth, D.-s. Wang, E. Wang, and Q. Niu, *First Principles Calculation of Anomalous Hall Conductivity in Ferromagnetic bcc Fe*, Phys. Rev. Lett. **92**, 037204 (2004).

[139] P. Blaha, K. Schwarz, G. K. H. Madsen, D. Kvasnicka, and J. Luitz, *WIEN2K, An Augmented Plane Wave + Local Orbitals Program for Calculating Crystal Properties* (Karlheinz Schwarz, Techn. Universität Wien, Austria, ADDRESS, 2001).

[140] A. J. Cohen, P. Mori-Sánchez, and W. Yang, *Insights into Current Limitations of Density Functional Theory*, Science **321**, 792 (2008).

[141] C. J. Cramer and D. G. Truhlar, *Density functional theory for transition metals and transition metal chemistry*, Phys. Chem. Chem. Phys. **11**, 10757 (2009).

[142] W. Lin and C. L. Chien, *Electrical Detection of Spin Backflow from an Antiferromagnetic Insulator $Y_3Fe_5O_{12}$ Interface*, Phys. Rev. Lett. **118**, 067202 (2017).

[143] D. Hou, Z. Qiu, J. Barker, K. Sato, K. Yamamoto, S. Vélez, J. M. Gomez-Perez, L. E. Hueso, F. Casanova, and E. Saitoh, *Tunable Sign Change of Spin Hall Magnetoresistance in Pt/NiO/YIG Structures*, Phys. Rev. Lett. **118**, 147202 (2017).

[144] M. Tomíčková, *Structural, optic and magnetooptic properties of epitaxial thin film ferrites*, Master's thesis, VŠB - Technical University of Ostrava, 2016.

# List of publications

- **Robin Silber**, Ondřej Stejskal, Lukáš Beran, Petr Cejpek, Roman Antoš, Tristan Matalla-Wagner, Jannis Thien, Olga Kuschel, Joachim Wollschläger, Martin Veis, Timo Kuschel, Jaroslav Hamrle, *Quadratic magnetooptic Kerr effect spectroscopy of Fe epitaxial films on MgO(001) substrates*, Phys. Rev. B **100**, 064403, (2019).

- Ramakanth Illa, Radek Ješko, **Robin Silber**, Ondřej Životský, Katerina Mamulová Kutláková, Lenka Matějová, Marek Kolečník, Jaromír Pištora, Jaroslav Hamrle *Structural, magnetic, optical, and magneto-optical properties of $CoFe_2O_4$ thin films fabricated by a chemical approach*, Mater. Res. Bull. **117**, 96 (2019).

- **Robin Silber**, Michaela Tomíčková, Jari Rodewald, Joachim Wollschläger, Jaromír Pištora, Martin Veis, Timo Kuschel, Jaroslav Hamrle, *Quadratic magnetooptic spectroscopy setup based on photoelastic light modulation*, Phot. Nano. Fund. Appl. **31**, 60 (2018).

- Ondřej Stejskal, **Robin Silber**, Jaromír Pištora, Jaroslav Hamrle, *Convergence study of the ab-initio calculated quadratic magneto-optical spectra in bcc Fe*, Phot. Nano. Fund. Appl. **32**, 24 (2018).

- Alessia Niessen , Jana Ludwig, Manuel Glas, **Robin Silber**, Jan-Michael Schmalhorst, Elke Arenholz and Günter Reiss, *Perpendicular magnetic anisotropy of TiN buffered $Co_2FeAl/MgO$ bilayers*, J. Appl. Phys. **121**, 223902 (2017).

# *Acknowledgements*

This Ph.D. thesis is a result of the collaboration between the Center of Spinelectronic Materials and Devices from Bielefeld University and the Nanotechnology Centre from VŠB–Technical University of Ostrava. As a Ph.D. student of both Universities I worked for half the time (4×6 months) at Bielefeld University and for half the time at the University in Ostrava. As the focus of expertises in each group was slightly different, this collaboration provided me with much experience, which I'm truly grateful for.

My deepest thanks belong to Mgr. Jaroslav Hamrle, Ph.D. and Dr. Timo Kuschel who guided me through the whole process of my Ph.D. work. Thanks to them I adopted principles of independent scientific working, from carrying out the experiment in the lab, over processing and analysis of experimental data, to the preparation of decent manuscripts presenting a meaningful piece of scientific work. I'm also very grateful to Prof. Dr. Günter Reiss and doc. Dr. Ing. Michal Lesňák that they shielded me in my Ph.D. work and provided me with help whenever it was necessary.

My further thanks go to my colleagues from Bielefeld University that introduced me to several techniques and setups and always offer an advice or help when asked for. Special thanks go to Tristan Matalla-Wagner who did pattern Hall-bar structures on my samples and helped with the preparation of some substrate surfaces and to Jan Krieft who introduced me to the off-specular XRD measurements by using Euler cradle and the magnetron sputtering system. Further, I would like to explicitly mention Niclas Teichert, Christoph Klewe, Alex and Birte Böhnke, Alessia Niesen, Panagiota "Polina" Bougiatioti, Orestis Manos and Anastasiia Moskaltsova, who became my friends rather than colleagues. I spent a great time with them, starting with a trip to Hawaii up to skiing in Alps and becoming one of the Hiking victims. My thanks also go to Riechers family and Alex and Birte Böhnke, for the accommodation they offer me during my time in Bielefeld. I will also remember interesting discussion with Jungwoo "Jay" Koo and Andreas "Manni" Becker when we were having a beer after work in our coffee-room. Furthermore my thanks go to Jan Schmalhorst, who advised me with some technical aspects of several setups in the group and also helped me with with some of the administration stuff. He also invited me to join the Futsal matches he organised, and which we had play almost every week. Last but not least, I would like to thank to Aggi Windmann, who helped me a lot with all the administration stuff that was necessary to manage during my stays in Bielefeld.

For the time I spend in Ostrava, I would like to acknowledge all my colleagues from Nanotechnology centre at VŠB-TUO that provided any help, discussion or motivation during my Ph.D. study. Special thanks go to the colleagues from my office: Ondřej

Stejskal, Radek Ješko, Tibor Fördos and Zuzana Mrázková, with whom I had have many interesting discussions over the passed years, where the subject was not always from the realm of physics or science in general. I would like to highlight the help of Radek Ješko, for his assistance with some of the ellipsometry measurements, and the help of Ondřej Stejskal, for his ab-initio calculations that are showed and discussed in Chapter 5 of this work.

Further, I would like to acknowledge and thank the group of Martin Veis from Faculty of Mathematics and Physics of Charles University in Prague. The group's focus is also in the field of magnetooptics, so I had a lot of collaboration spending several weeks in their lab for various measurements. Here, I would like to highlight the help of Lukáš Beran for his advise with technical aspect of the setups I have used, of Daniel Král, who processed and measured ellipsometry on $Co_2MnSi$ Heusler alloys and, of course, of Martin Veis, who provided lots of help, discussion and ideas during my Ph.D. work.

My thanks also goes to the group of Joachim Wollschläger from Osnabrück University. Here, I would like to mention Jannis Thien and Olga Kuschel for the Fe/MgO samples preparation by MBE used for comparison with the Fe/MgO samples prepared by magnetron sputtering, and Jari Rodewald and Michaela Tomíčková (a student from VŠB-TUO who was on an internship in Osnabrück) who prepared and characterized magnetite thin films that are shortly discussed in the appendix of this work.

Furthermore, I'd like to thank to many of my friends from Ostrava, most of which I know since I was a kid. I have a lots of great memories with them and lot more is to come. Particularly, I would like to acknowledge Sandra Svobodová for some of the grammar corrections in the text of this work. I would also like to thank Kuba Výtisk and Lucie Doležilová (soon to be Výtisková) that they did always accommodate me with "bed and breakfast" in Prague on my regular ways Ostrava–Prague–Berlin–Bielefeld and vice versa.

Finally, I would like to acknowledge my entire family, especially my parents, grandparents and my brother. They always supported me in my studies and secure me from existential, financial and emotional sides. They have a great deserve in what kind of man I'm today, for what I'm entirely grateful and would like to express them my deepest thanks.